

Molecular dynamics simulations of enzymes on surfaces

vorgelegt von
Master of Science
Tillmann Utesch
Berlin

Von der Fakultät II – Mathematik und Naturwissenschaften
der Technischen Universität Berlin
zur Erlangung des akademischen Grades

Doktor der Naturwissenschaften
– Dr. rer. nat. –

genehmigte Dissertation

Promotionsausschuss:

Vorsitzender: Prof. Dr. Roderich Süßmuth
Berichter/Gutachter: Prof. Dr. Maria Andrea Mroginski
Berichter/Gutachter: PD Dr. Peter Hildebrand

Tag der wissenschaftlichen Aussprache: 11. April 2013

Berlin 2013
D 83

*Measure what is measurable,
and make measurable what is not so.*

Galileo Galilei¹

¹Der Ursprung dieses Zitats ist nicht belegt. Es wird aber mit Galileo in Verbindung gebracht [1]

Abstract

The immobilization of biomolecules on various surface materials plays an important role in a wide field of research. The interaction of large enzymes with organic and inorganic devices is, *inter alia*, relevant in the sectors of alternative energies, biomedicine, biocatalysis, cell signalling, and basic research.

One major drawback in this context is the lacking of structural and dynamic details on the atomic level. Closing this gap is a very important challenge because many processes accounting for the correct protein functionality or for the proper adsorbant–surface interaction are still elusive. Unfortunately, the experimental access and determination of these properties is extremely difficult and expensive. Therefore, theory, namely, classical all–atom molecular dynamics (MD) simulations, is needed to investigate these issues. Classical MD simulations are a potential and established technique to describe the initial adsorption of biomolecules onto surface materials on the atomic level and offer, additionally to these dynamics insights, information about the protein stability, which constitutes a crucial point upon surface contact.

In this work, the surface interaction dynamics of cytochrome *c*, bone morphogenetic protein-2 (BMP-2), sulfite oxidase (SO), [NiFe] hydrogenases and Ciona intestinalis voltage-sensing phosphatase (Ci-VSP) was investigated by classical all-atom MD simulations. The widely scattered projects are motivated by different goals and are settled in diverse fields of research, but all deal with protein–surface interactions that are not completely understood.

The simulations demonstrated that even small changes in the model could strongly affect the adsorption and conformation of biomolecules on surfaces. The variations included mutations in the enzyme, modifications of the surface by coating it with differently functionalized self-assembled monolayers (SAMs) and alterations of environmental parameters, such as the pH value and ionic strength. In doing so, structural rearrangements within the enzyme leading to different interactions with the surface, reorientations of the adsorbate with respect to the surface and the formation of stable water or ion layers on the device competing with the biomolecule in adsorption were observed.

Comparison between these findings of the molecular modelling approach and experimental data measured by cooperation partners showed a good agreement and offered a more precise way to improve surface immobilization and to understand protein functionality in more detail. Nevertheless, the potential of classical MD simulations combined with experimental work has to be treated carefully, because both methods analyse systems on different time scales.

Zusammenfassung

Die Immobilisierung von Biomolekülen auf verschiedenen Oberflächenmaterialien spielt eine bedeutende Rolle in einem weiten Forschungsfeld. Die Wechselwirkung zwischen großen Enzymen und organischen und anorganischen Materialien ist, unter anderem, entscheidend bei der Entwicklung von alternativen Energiequellen, der Biomedizin, der Biokatalyse, bei der Zelltransduktion und in der Grundlagenforschung.

Ein Hauptproblem in diesem Zusammenhang ist das Fehlen von strukturellen und dynamischen Details auf atomarer Ebene. Das Schließen dieser Lücke ist eine äußerst wichtige Herausforderung, da viele Prozesse, die für die korrekte Proteinfunktion und Oberflächeninteraktion verantwortlich sind, immer noch schwer zu fassen und im Detail unbekannt sind. Leider ist die experimentelle Zugänglichkeit dieser Eigenschaften extrem schwierig und aufwendig. Aus diesem Grund sind theoretische Ansätze wie klassische Moleküldynamiksimulationen (MD Simulationen) zur Bestimmung dieser Kenngrößen von großem Nutzen. Klassische Moleküldynamik ist eine potentielle und etablierte Technik, um die Adsorption von Biomolekülen auf Oberflächenmaterialien zu beschreiben, und bietet zusätzlich zu diesen Einsichten in die Dynamik Informationen über die Proteinstabilität, die einen entscheidenden Punkt bei Oberflächenkontakt darstellt.

In dieser Arbeit wurden die Interaktionsdynamiken von Cytochrom *c*, dem knochenbildenden Protein BMP-2, der Sulfitoxidase (SO), [NiFe] Hydrogenasen und der spannungsabhängigen Phosphatase von *Ciona intestinalis* (Ci-VSP) mit klassischen Moleküldynamiksimulationen untersucht. Trotz der weiten Streuung der Projekte und deren unterschiedlicher Motivation und Zielsetzung, stehen dennoch bei allen ungeklärte Protein-Oberflächeninteraktionen im Vordergrund.

Die Simulationen zeigten, dass sogar kleine Variationen in einem Modell große Auswirkungen auf das Adsorptionsverhalten und die Konformation eines Biomoleküls an Oberflächen haben kann. Die hier untersuchten Änderungen umfassten Mutationen in den Enzymen, Modifikationen an den Oberflächen durch Beschichtung mit unterschiedlich funktionalisierten selbst-assemblierten Monoschichten (SAMs) und Unterschiede an Deskriptoren, die die Umgebungsbedingungen innerhalb des Modells beschreiben, wie beispielsweise der pH Wert oder die Ionenstärke. Hierdurch wurden strukturelle Reorganisationen innerhalb der Enzyme, die zu unterschiedlichen Interaktionen mit den Oberflächen führten, Reorientierungen der Adsorbaten bezüglich der Oberflächen und die Ausbildung von stabilen Wasser- oder Ionenschichten auf den Oberflächen beobachtet.

Der Vergleich von diesen Ergebnissen der molekularen Modellierung mit experimentell bestimmten Daten von Kooperationspartnern zeigte eine gute Übereinstimmung und bot die Möglichkeit, Immobilisierungen an Oberflächen gerichtet zu verbessern und Proteinfunktionen detaillierter zu verstehen. Dennoch muss dieser vielversprechende Ansatz aus klassischen MD Simulationen in Kombination mit Experimenten vorsichtig behandelt werden, da sich die Zeitskalen der beiden Methoden, auf denen sie das System analysieren, stark von einander unterscheiden.

Publications

Parts of this work have been published in the following articles:

1. T. Utesch and M. A. Mroginski. “Three-Dimensional Structural Model of Chicken Liver Sulfite Oxidase in its Activated Form. ” *J Phys Chem Lett* **2010** 1 (23): 2159–2164.
2. T. Utesch, G. Daminelli, M. A. Mroginski. “Molecular Dynamics Simulations of the Adsorption of Bone Morphogenetic Protein-2 on Surfaces with Medical Relevance.” *Langmuir* **2011** 27 (21): 13144–13153
3. Y. Rippers, T. Utesch, P. Hildebrandt, I. Zebger, M. A. Mroginski. “Insights into the structure of the active site of the O₂-tolerant membrane bound [NiFe] hydrogenase of *R. eutropha* H16 by molecular modelling.” *Phys. Chem. Chem. Phys.* **2011** 13, 16146–16149
4. T. Utesch, M. Sezer, I. M. Weidinger, M. A. Mroginski. “Adsorption of Sulfite Oxidase on Self-Assembled Monolayers from Molecular Dynamics Simulations.” *Langmuir* **2012** 28 (13): 5761–5769
5. T. Utesch, D. Millo, M. A. Castro, P. Hildebrandt, I. Zebger, M. A. Mroginski. “Effect of the protonation degree of a self-assembled monolayer on the immobilization dynamics of a standard [NiFe] hydrogenase.” *Langmuir* **2013** 29 (2): 673–682
6. K. Hobiger, T. Utesch, M. A. Mroginski, G. Seebohm, T. Friedrich. “The linker pivot in Ci-VSP: the key to unlock catalysis.” *PLoS ONE* **2013**, 8(7): e70272. doi:10.1371/journal.pone.0070272
7. N. Heidary, T. Utesch, D. Millo, J. Fritsch, O. Lenz, P. Hildebrandt, A. Fischer, M. A. Mroginski, I. Zebger. “An integral, rational strategy for immobilizing oxygen tolerant [NiFe] hydrogenases on electrode surface” *in preparation - close to submission*

Other publications during this work:

1. J. J. Feng, D. H. Murgida, U. Kuhlmann, T. Utesch, M. A. Mroginski, P. Hildebrandt, I. M. Weidinger. "Gated Electron Transfer of Yeast Iso-1 Cytochrome *c* on Self-Assembled Monolayer-Coated Electrodes." *J Phys Chem B* **2008** 47: 15202–15211
2. D. Millo, M. E. Pandelia, T. Utesch, N. Wisitruangsakul, M. A. Mroginski, W. Lubitz, P. Hildebrandt, I. Zebger. "Spectroelectrochemical Study of the [NiFe] Hydrogenase from *Desulfovibrio vulgaris* Miyazaki F in Solution and Immobilized on Biocompatible Gold Surfaces." *J Phys Chem B* **2009** 113: 15344–15351
3. M. Sezer, R. Spricigo, T. Utesch, D. Millo, S. Leimkuehler, M. A. Mroginski, U. Wollenberger, P. Hildebrandt, I. M. Weidinger. "Redox properties and catalytic activity of surface-bound human sulfite oxidase studied by a combined surface enhanced resonance Raman spectroscopic and electrochemical approach." *Phys Chem Chem Phys* **2011** 12: 7894–7903
4. M. Sezer, S. Frielingsdorf, D. Millo, N. Heidary, T. Utesch, M. A. Mroginski, B. Friedrich, P. Hildebrandt, I. Zebger, I. M. Weidinger. "Role of the HoxZ subunit in the electron transfer pathway of the membrane-bound [NiFe]-hydrogenase from *Ralstonia eutropha* immobilized on electrodes." *J Phys Chem B* **2011** 115: 10368–10374
5. K. Hobiger, T. Utesch, M. A. Mroginski, T. Friedrich. "Coupling of Ci-VSP modules requires a combination of structure and electrostatics within the linker." *Biophys J* **2012** 102 (6):1313–1322
6. G. Schkolnik, T. Utesch, J. Salewski, K. Tenger, D. Millo, A. Kranich, I. Zebger, C. Schulz, L. Zimanyi, G. Rakhely, M. A. Mroginski, P. Hildebrandt. "Mapping local electric fields in proteins at biomimetic interfaces." *Chem Commun* **2012** 48: 70–72
7. H. K. Ly, T. Utesch, I. Diaz-Moreno, J. M. Garcia-Heredia, M. A. De La Rosa, P. Hildebrandt. "Perturbation of the Redox Site Structure of Cytochrome *c* Variants upon Tyrosine Nitration." *J Phys Chem B* **2012** 116 (19): 5694–5702
8. G. Schkolnik, T. Utesch, J. Zhao, S. Jiang, M. K. Thompson, M. A. Mroginski, P. Hildebrandt, S. Franzen. "Catalytic efficiency of dehaloperoxidase A is controlled by electrostatics – application of the vibrational Stark effect to understand enzyme kinetics." *Biochem Biophys Res Commun* **2012** 430 (3): 1011–1015

Talks and selected poster contributions:

1. *MD simulations of immobilised proteins*
ITQB Workshop: Structure, dynamics and function of proteins, 17.–19. September 2008, Lissabon, Portugal (talk)
2. Tillmann Utesch, Maria Andrea Mroginski, Grazia Daminelli, and Peter Hildebrandt.
Adsorption of bone morphogenetic protein 2 (BMP-2) onto surfaces with medical relevance
German Biophysical society Meeting, 28. September – 1. October 2008, Berlin, Germany (poster)
3. Tillmann Utesch and Maria Andrea Mroginski.
MD simulation and electron transfer in the sulfite oxidase
Workshop on Computer Simulation and Theory of Macromolecules 2010, 16.–18. April 2010, Hünfeld, Germany (poster)
4. Tillmann Utesch and Maria Andrea Mroginski.
Molecular Dynamics Simulations on the Sulfite Oxidase on SAM coated electrode surfaces at different ino concentrations
47th Symposium on Theoretical Chemistry: Designing Molecular Funtionality: Challenges for Theoretical Approaches, 21.–25. August 2011, Sursee, Switzerland (poster)
5. Yvonne Rippers, Tillmann Utesch, Peter Hildebrandt, Ingo Zebger and Maria Andrea Mroginski.
Development and validation of the homology model for the active site of the O₂-tolerant [NiFe] MBH of R. eutropha H16 by MD and QM/MM calculations
XV. International Symposium on Relations between Homogeneous and Heterogeneous Catalysis, 11.–16. September 2011, Berlin, Germany (poster)
6. Tillmann Utesch and Maria Andrea Mroginski.
Ionic strength dependent dependent immobilization of the sulfite oxidase
Workshop on Computer Simulation and Theory of Macromolecules 2012, 20.–21. April 2012, Hünfeld, Germany (poster)
7. Tillmann Utesch, Nina Heidary, Maria Ana Castro, Diego Millo, Peter Hildebrandt, Anna Fischer, Ingo Zebger, and Maria Andrea Mroginski.
Adsorption of the membrane-bound [NiFe] hydrogenase on SAM coated gold electrodes
Annual Meeting of the German Biophysical Society, 23.–26. September 2012, Göttingen, Germany (poster)
8. *Adsorption simulations of enzymes on modified surfaces*
PhD-Symposium on Complex enzymes for biosensor application, 29.–30. November 2012, Luckenwalde, Germany (talk)
9. *Adsorption simulations of biomolecules on SAM coated surfaces*
Molecular Modelling Workshop 2013, 25.–27. February, Erlangen, Germany (talk)

List of abbreviations

APBS	Adaptive Poisson-Boltzmann Solver
BMP-2	Bone morphogenetic protein 2
CB	covalent bond
CD	catalytic domain
CHARMM	Chemistry at HARvard Molecular Mechanics
Ci-VSP	<i>Ciona intestinalis</i> voltage-sensing phosphatase
COG	centre of geometry
COM	centre of mass
cSO	chicken sulfite oxidase
EPR	electron paramagnetic resonance
ET	electron transfer
FC	Franck-Condon
FeS	iron sulphur
FEtk	Finite Element ToolKit
GPU	graphic processing unit
HB	hydrogen bond
HMM	Hidden Markov model
hSO	human sulfite oxidase
IET	intra molecular electron transfer
MBH	membrane bound hydrogenase
MD	molecular dynamics
MM	Molecular Mechanics
Moco	molybdopterin cofactor
ms	millisecond
NAD ⁺	nicotinamide adenine dinucleotide
ns	nanosecond
PBC	periodic boundary conditions
PC	phosphatidylcholine
PD	phosphatase domain
PDB	Protein database
PE	phosphatidylethanolamine
PIP2	phosphatidylinositol 4,5-bisphosphate
PME	particle mesh Ewald
PTEN	phosphatase and tensin homologue

List of abbreviations

QM	quantum mechanical
radgyr	radius of gyration
RH	regulatory hydrogenase
rmsd	root mean square deviation
rmsf	root mean square fluctuation
SAM	self-assembled monolayer
SEIRA	surface enhanced infrared absorption
SERR	surface enhanced resonance Raman
SH	soluble hydrogenase
SMD	steered molecular dynamics
SO	sulfite oxidase
TEVC	Two Electrode Voltage Clamp
TGF- β	transforming growth factor β
TS	through space
vdW	van der Waals
VSD	voltage sensory domain
WT	wild type

List of symbols

β	isothermic compressibility
ΔG	driving force
ε	vdW energy minimum
η	dielectric constant
γ	phase shift
\hbar	Planck constant $\hbar = 6.626068 \cdot 10^{-34} \text{ m}^2 \text{ kg s}^{-1}$
ι	chemical potential
κ'	Boltzmann term
λ_p	volume rescaling factor
λ_r	reorganization energy
λ_T	velocity rescaling factor
$\langle O \rangle_{ensemble}$	ensemble average of observable
$\langle O \rangle_{time}$	time average of observable
μ	dipole moment
ν	frequency
ω	improper torsion
ω_0	improper torsion equilibrium
ϕ	electrostatic potential
π	number $\pi = 3.14\dots$
ρ	charge density
σ	decay factor
τ	temperature relaxation parameter
τ_p	pressure relaxation parameter
θ	angle
θ_0	angle bending: equilibrium
\tilde{v}	average velocity
\vec{n}	pulling direction
\vec{r}_{COM}	centre of mass
ξ	torsion
ζ	friction
A	acceptor
a	acceleration
b	bond length

b_0	bond length equilibrium
c_v	thermal capacity
D	donor
E	self-energy
e	charge of an electron
E_{CON}	constraining potential
E_{int}	interaction energy
E_{kin}	kinetic energy
E_{pot}	potential energy
F	force
f	partition function
H	Hamiltonian
I	ionic strength
k	multiplicity
k_ω	force constant: improper
k_θ	force constant: angle
k_ξ	force constant: torsions
k_B	Boltzmann constant $k_B = 1.3806503 \cdot 10^{-23} \text{ m}^2 \text{ kg s}^{-2} \text{ K}^{-1}$
k_b	force constant: bond
k_{CON}	force constant: constraints
M	total mass
m	mass
N	number of atoms
n	number of moles
N_A	Avogadro number $N_A = 6.02214129(27) \cdot 10^{23} \text{ mol}^{-1}$
N_{DF}	number of degrees of freedom
N_{up}	update interval for r_{res}
p	pressure
p_{ref}	reference pressure
p_x	momentum
Q	heat bath mass
q	partial charge
R	stochastic random term
r	coordinate
r_0	reference point
r_{cut}	cut-off radius
R_c	universal gas constant $R_c = 8.3144621(75) \text{ J mol}^{-1} \text{ K}^{-1}$
r_{res}	reservoir radius
$Rmin$	vdW equilibration distance
s	distance

T	temperature
t	time
T_{bath}	external bath temperature
T_{DA}	electronic coupling matrix
t_{tot}	total time
V	potential energy
v	velocity
V_{bend}	angle bending energy
V_{bonded}	bonded energy
V_{elect}	electrostatic energy
$V_{improper}$	improper energy
$V_{non-bonded}$	non-bonded energy
$V_{stretch}$	bond stretch energy
$V_{torsion}$	torsion energy
V_{vdW}	van der Waals energy
V_{com}	commando potential
V_m	cell potential
v_{SMD}	harmonic pulling speed

Contents

Abstract	iii
Zusammenfassung	v
Publications	vii
List of abbreviations	xi
List of symbols	xiii
Contents	xvii
1 Introduction	1
2 Surfaces and biological membranes	3
2.1 The plasma membrane	3
2.2 Bare surfaces	4
2.3 Functionalized metal surfaces	5
2.4 Limitations of surface models	7
3 Biological systems	9
3.1 Cytochrome <i>c</i>	9
3.2 Bone morphogenetic protein 2	9
3.3 Sulfite oxidase	11
3.4 [NiFe]-hydrogenase	14
3.4.1 Oxygen sensitive [NiFe] hydrogenase	15
3.4.2 Oxygen tolerant [NiFe] hydrogenase	15
3.4.3 Immobilization and application of [NiFe] hydrogenases	17
3.5 <i>Ciona intestinalis</i> voltage-sensing protein	18
4 Molecular Mechanics	21
4.1 Force fields	21
4.2 The potential energy function	21
4.2.1 Bond stretching	22
4.2.2 Angle bending	22
4.2.3 Bond torsions	23
4.2.4 Improper torsions	23
4.2.5 Van der Waals interactions	23
4.2.6 Electrostatic interactions	24

4.3	Boundary conditions	24
4.3.1	Open cell	25
4.3.2	Implicit solvent	25
4.3.3	Rigid boundary conditions	25
4.3.4	Stochastic boundary conditions	25
4.3.5	Periodic boundary conditions	25
4.4	Computational solutions for non-bonded long-ranged interactions	26
4.4.1	Cut-offs and neighbour lists	27
4.4.2	Particle mesh Ewald summation	28
5	Molecular dynamics simulations	29
5.1	Classical mechanics	29
5.2	Stochastic dynamics	30
5.3	Propagation over time	30
5.4	Ensemble theory	32
5.4.1	Temperature control	33
5.4.2	Pressure control	33
5.5	Restrained or steered molecular dynamics simulations	35
5.6	Typical protocol of a classical MD simulation	35
5.7	General output of classical MD simulations	38
6	Molecular Modelling	39
6.1	Homology Modelling	39
6.2	De Novo Modelling	39
7	Data analysis	41
7.1	Dipole moment	41
7.2	Electrostatic surface potential	42
7.3	Interaction energy	42
7.4	Root mean square deviation	43
7.5	Root mean square fluctuation	44
7.6	Radius of gyration	44
7.7	Electron transfer	44
8	Computational resources and tools	47
9	Supplemental experimental measurements and QM/MM calculations	49
9.1	Vibrational spectroscopy	49
9.2	Surface enhanced vibrational spectroscopy	50
9.3	Electrophysiological measurements	51
9.4	QM/MM calculations	52
10	Results	55
10.1	Molecular Dynamics Simulations of the Adsorption of Bone Morphogenetic Protein-2 on Surfaces with Medical Relevance	55
10.2	Three-Dimensional Structural Model of Chicken Liver Sulfite Oxidase in its Activated Form	67

10.3	Adsorption of Sulfite Oxidase on Self-Assembled Monolayers from Molecular Dynamics Simulations	75
10.4	Insights into the structure of the active site of the O ₂ tolerant membrane bound [NiFe] hydrogenase of <i>R. eutropha</i> H16 by molecular modelling	85
10.5	Effect of the protonation degree of a self-assembled monolayer on the immobilization dynamics of a standard [NiFe] hydrogenase.	91
10.6	An integral, rational strategy for immobilizing oxygen tolerant [NiFe] hydrogenases on electrode surface	103
10.7	The linker pivot in Ci-VSP: the key to unlock catalysis	109
11	Conclusions and Outlook	123
11.1	Cytochrome <i>c</i>	123
11.2	Bone morphogenetic protein-2	123
11.3	Sulfite oxidase	123
11.4	[NiFe] hydrogenases	124
11.5	<i>Ciona intestinalis</i> voltage sensing phosphatase	124
11.6	Outlook	124
12	Danksagung	125
	Bibliography	127

1 Introduction

The title of this work raises three questions:

- Why is the adsorption of biomolecules on organic or inorganic surfaces of interest?
- Why are molecular dynamics simulations an adequate tool for describing these adsorption dynamics?
- Which biomolecules and surface devices are investigated here and what is their technological relevance?

To give a general answer to the first issue, one has to include a wide field of research and applications. *Inter alia*, immobilization of biological macromolecules on different surface materials is important in biomedicine, regenerative energy development, biosensor application, biological catalysis, basic research, environmental science, material development, and space flight. In all these widely scattered sectors, optimization and regulation of surface-protein interfaces is desired and is, therefore, a hotspot for research [2]. In this work, these interaction and immobilization processes are evaluated by classical molecular dynamics simulations to obtain insights on the atomic level. The choice of the method leads to the second question, why molecular dynamics simulations are an appropriate technique for describing protein-surface systems.

Molecular dynamics (MD) simulations are an excellent tool to investigate the time dependent evolution of a molecular system. For processes of large proteins, classical MD simulations offer a suitable trade-off between accuracy and efficiency. They describe the dynamics of the particles by solving Newton's equations of motion referring to a potential energy function, the force field [3, 4]. Their practice in adsorption studies is justified by the limitations in experiments. Usually, experimental measurements grant a qualitative overview of the functionality of the treated system, but lack detailed information on the atomic level, which can be gained by atomistic MD simulations. However, these structural and dynamic details play a key role for rational optimization of the functionality of a system. Thus, this work provides the complementary part to many experimental studies and contributes its part to the complete picture of the immobilization processes.

The potential of classical MD simulations to describe adsorption and immobilization processes of biomolecules has been shown in a variety of studies, as reviewed recently [5–8]. Thereby, the surfaces are classified as hydrophobic or charged which strongly influences the interaction with biomolecules [2]. Additionally, these reviews show that theoretical studies get more and more important for modelling and predicting adsorption and immobilization processes. A meaningful factor for this development is the increasing power of today's computers that offers longer simulations and larger systems.

In this work, a couple of biological biomolecules and their interaction with various bare or modified surfaces have been studied. While the selection of the biosystems includes cytochrome *c*, bone morphogenetic protein-2 (BMP-2), sulfite oxidase (SO), [NiFe] hydrogenases and Ciona intestinalis voltage sensing protein (Ci-VSP), the surface devices are represented by bare graphite and titanium

dioxide slabs, organic double layer lipid membranes and hybrid systems of gold surfaces coated with different self-assembled monolayers (SAMs). The modification with SAMs is an excellent technique to functionalise electrodes, to change their properties and to use the benefits of both components, namely, the metal and the SAM [9].

The general goal of this work is to get deeper insights into the adsorption dynamics of the listed biomolecules and to understand their interaction with the corresponding surfaces. The wide range of the treated biomolecules and their different functionalities make them interesting candidates in different fields of research, as briefly explained in the following.

Cytochrome *c* is a small, very stable, and well-studied heme protein and is, therefore, the ideal test system for fundamental research in both, experimental and theoretical points of view. Here, cytochrome *c* is mainly analysed with respect to its electrostatic properties by simulating different mutants in solution and in the electric field of amino-terminated SAMs coating a gold electrode [10, 11] (section 3.1).

Furthermore, BMP-2, a homodimeric protein enhancing bone and cartilage formation, and its interaction with implant surfaces [12], namely, graphite and titanium dioxide, is a part of this work. The motivation behind this adsorption study is to get detailed insights into the interaction dynamics that contribute to optimize and to increase the biocompatibility of body implants that are under biomedical research (chapters 3.2 and 10.1).

Beside these relatively small proteins, SO and [NiFe] hydrogenases are multi-domain enzymes carrying several cofactors and are in the focus of biosensor technology and biofuel cell development, respectively. Thus, the dynamics of these proteins on bare or modified metal surfaces is of particular interest. The focus in terms of SO was put on the intramolecular-electron transfer (IET) properties that are essential for a proper functionality. It is elucidated how this electron flux is influenced by conformational restrictions upon contact with modified gold electrodes (chapters 3.3, 10.2 and 10.3). For [NiFe] hydrogenases much effort has been done to optimize surface properties and experimental conditions to accomplish a stable and strongly immobilized enzyme able to transfer electrons to and from the functionalized electrode surface (chapters 3.4, 10.4, 10.5 and 10.6).

In contrast to the immobilization on bare or functionalized inorganic materials, the voltage sensitive phosphatase Ci-VSP is embedded in the plasma membrane and has a crucial role in signal transduction and cancer genesis in cells. One meaningful step during the cascade is the recruitment of the enzyme towards the membrane aligning the phosphate domain for catalysis. Here, special attention is paid to the dynamics and interaction of a short linker region connecting the main domains, voltage sensor and phosphatase (chapters 3.5 and 10.7).

The majority of the atomistic MD simulations performed for the enumerated systems has been compared or combined with experiments. Here, it is noticeable that, in general, the two techniques agree very well with another and offer detailed insights into the investigated adsorption or interaction processes.

2 Surfaces and biological membranes

This chapter gives a short introduction into organic and inorganic **surfaces** used in the theoretical adsorption studies and associates these materials with the biological background.

The interest in bare and modified surfaces combined with biomolecules is motivated by a wide field of research. Here, three important sectors referring to inorganic, biological and hybrid surfaces of metal and monolayers are touched, namely, medical practice, alternative energies and development of biosensors. Besides biomembranes and bare surfaces mimicking medical implant surfaces, electrodes modified with self-assembled monolayers (SAMs) have been modelled in the context of regenerative energies and biosensor development.

2.1 The plasma membrane

Plasma- or biomembranes composed by a lipid bilayer are responsible for the essential cell compartmentation in living organisms. Thus, they play an major role in cell signalling and transport by interacting with many types of biomolecules. Beside proteins embedded in the plasma membrane, such as ion channels and pumps, other soluble substrates or enzymes are transported towards the double layer and are released again after the interaction. The understanding of these partially unknown or elusive processes is extremely important for the functionality of living systems and is, therefore, a target of many research groups.

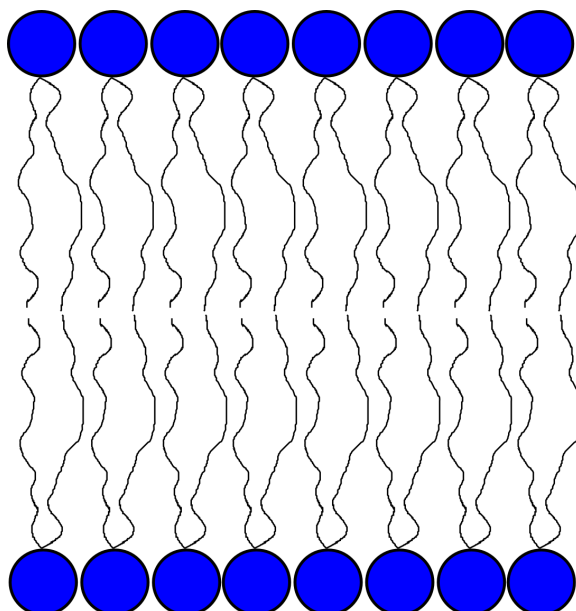


Figure 2.1: Schematic representation of a phospholipid membrane. The scheme shows a simplified plasma membrane consisting of phospholipids only. The black tails indicate the hydrophobic fatty acids and the blue spheres the various phosphate head groups which are differently modified.

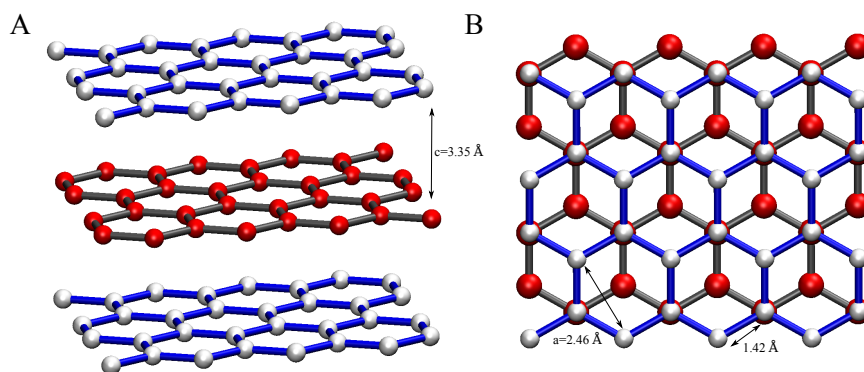


Figure 2.2: Graphite unit cell. Panel A shows the side-view of a three layer graphite surface. The lattice constant c describes the separation distance between two neighbouring slabs. The white and red spheres denote the carbon atoms. While the white-blue layers are symmetric to each other, the red-grey one is shifted. The same colour code is used in panel B showing the graphite from above to demonstrate the shift between two adjacent layers. Additionally, the nearest neighbour spacing and the lattice parameter a are indicated.

Plasma membranes are built up by different phospholipids whereupon the hydrophobic fatty acids form the interior of the bilayer and the phosphate head groups the outer part (figure 2.1). The various phospholipids are not equally, but asymmetrically distributed in the membrane [13]. The most common phospholipids at the outer leaflet of the membrane are sphingomyelin and phosphatidylcholine (PC), while negatively charged phosphatidylserine and phosphatidylethanolamine (PE) are mostly found at the cytosolic side of the bilayer. This asymmetry is not absolute, because the phospholipids are not covalently bound to each other and are, therefore, able to translocate within the bilayer. These spontaneous reorganizations are controlled and regulated by so-called flippases, which maintain the asymmetry of the membrane [14]. Other phospholipids, such as phosphatidyl inosides, are important signalling molecules, but exist in much lower concentrations [15–17].

2.2 Bare surfaces

The interaction of biomolecules with bare surfaces is, *inter alia*, of great interest in the biomedical sector, where unmodified surfaces are commonly used as implant devices. In this context, **graphite** and **titanium** implants are two examples for bare surface materials. Both lightweight devices exhibit a high biocompatibility and stability in living tissue [18, 19]. Nevertheless, molecular processes which enhance these properties are still elusive and under discussion, because detailed information of these interactions are partially lacking. In this current state-of-art, insights on the atomic level are of high demand to understand unpredictable processes leading to variations in the biocompatibility in different patients.

Graphite consists of multiple non-covalently bound flat carbon layers. Each layer is composed by hexagonally arranged carbon atoms and is shifted with respect to the above and subjacent carbon planes as shown in figure 2.2. The contact between the planar layers is stabilized by van der Waals (vdW) interactions. This configuration results in a strongly hydrophobic and unpolarized surface holding delocated electrons in the ring system, which give graphite a metallic character.

Titanium is oxidized immediately to **titanium dioxide** when it is exposed to atmospheric oxygen conditions. Thus, titanium implants are coated by a titanium oxide film, which gets in contact with

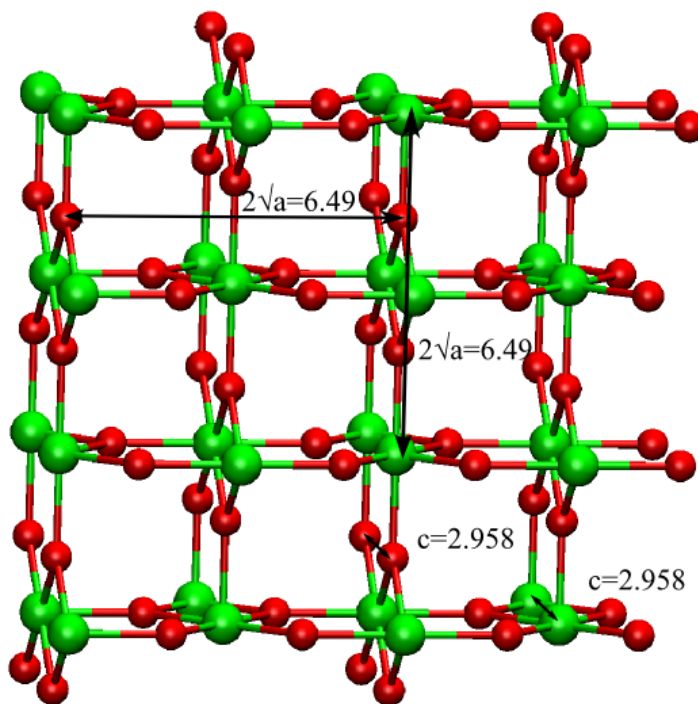


Figure 2.3: Extended titanium dioxide unit cell. The figure visualizes the organization of a titanium dioxide (110) surface. Titanium and oxygen atoms are coloured in green and red, respectively. Additionally, the unit cell parameters $a = b$ and c are indicated in the scheme. The nearest neighbour distances between titanium and oxygen are 1.95 and 1.98 Å for the out-of and in-plane distances, respectively.

the body and affects the interaction with surrounding biomolecules. Titanium dioxide occurs in three main forms: rutile, anatase and brookite [20]. Here, we address to the most common rutile whose extended unit cell is shown in figure 2.3. In contrast to graphite, titanium dioxide rutile is one coherent construct with a distinct charge distribution leading to positively charged six-fold coordinated titanium atoms and negatively charged oxygen anions [20, 21].

2.3 Functionalized metal surfaces

The functionalization of solid nanostructured materials with **self-assembled monolayers** (SAMs) offers a combination of both, bare metal or metal oxide surfaces and biological monolayers [9].

But why is the coating with monolayers needed?

The modification has two main reasons. Firstly, SAMs change the surface properties and adsorption can be controlled by the choice of the terminal group, and secondly, the direct contact between electrodes and biomolecule affecting protein stability is avoided. This combination of biological SAMs and metal electrodes offers the experimental insight into electron transfer processes by electrochemistry or conformational changes by spectroscopy, where the signal enhancement by the metal, here gold, is utilized (chapter 9).

The functionalization of the overlaying SAMs has to be considered carefully according to the properties of the treated biomolecule. In this work, oxidation resistant Au(111) surfaces coated with

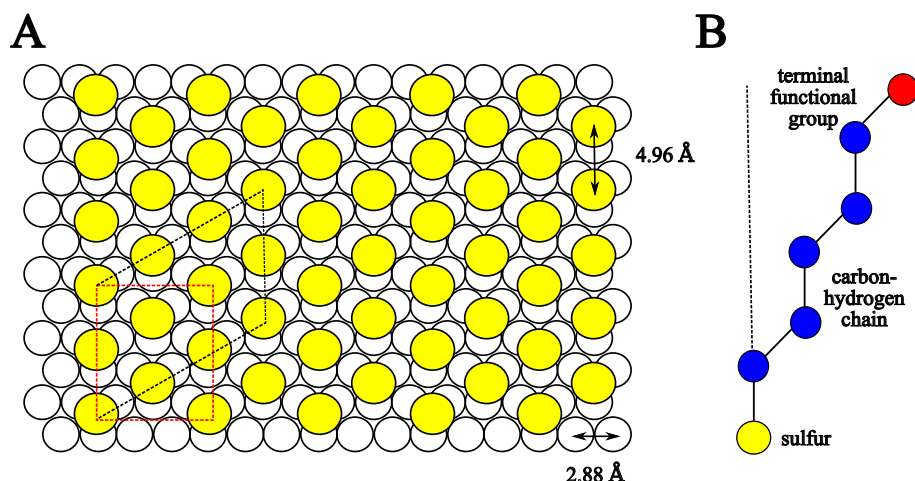


Figure 2.4: Schematic view of the coverage pattern of alkanethiol SAMs on Au(111). Panel A visualizes the coverage of alkanethiol SAMs on a Au(111) surface. The white and yellow spheres indicate the gold particles and the chemi-adsorbed sulphur atoms of the SAM, respectively. The lattice formed by the sulphur atoms with respect to the underlying gold film is described as a $(\sqrt{3} \times \sqrt{3})R30^\circ$ lattice (red dashed box), where the sulphur atoms are located in the three-fold hollow sites of the gold [22]. The $R30^\circ$ term is addressed to the rotation of the SAMs leading to a herringbone structure [22]. Taking these differing orientations of the SAMs into account, one obtains a $c(4 \times 2)$ super-lattice (black dashed) [23]. Figure B shows the scheme of a pentanethiol hydrochloride SAM, where the dashed line represents the surface normal. The red coloured terminal group is a wild card for small functional groups, such as listed in table 2.1. Blue and yellow balls indicate the carbon and sulphur atoms, respectively.

Name	Chain length	functional group	Chapter
5-carboxypentanethiol hydrochloride	5	$-\text{COO}^-$	10.6
5-carboxypentanethiol hydrochloride*	5	$-\text{COOH}$	10.6
6-mercaptohexanol	6	$-\text{OH}$	10.3
6-aminohexanethiol hydrochloride	6	$-\text{NH}_2$	10.5, 10.6
6-aminohexanethiol hydrochloride*	6	$-\text{NH}_3^+$	10.5, 10.6
8-aminoctanethiol hydrochloride	8	$-\text{NH}_2$	10.3
8-aminoctanethiol hydrochloride*	8	$-\text{NH}_3^+$	10.3

Table 2.1: Overview of the used alkanethiole SAMs. The asterisk marks the protonated species.

alkanethiols differing in chain length and termination were used. The homogeneous coverage pattern or super-lattice of these systems is shown in figure 2.4. The length of the alkanethiol chains determines the thickness of the monolayer and regulates the electronic conductivity, while the terminal group composition defines the surface properties [9]. Additional benefits of these tailored nanostructured SAMs are their good capability to mediate electron transfer between the biomolecule and the electrode and to mimic a natural biological environment.

Here, relatively short and differently modified alkanethiols were used as SAMs. The utilized SAMs are listed in table 2.1.

2.4 Limitations of surface models

The modelling and simulation of metal devices, such as gold, silver or titanium, is a challenging task. Mainly perfect and defect-free devices are used, which are not completely agreeing with experimental observations [24]. However, the assumption of perfect surfaces is justified by two points: a) the ratio between surface and adsorbate size and b) the limited simulation cell size.

With today's computer resources, systems are usually limited to a bare or modified surface, one biomolecule and the surrounding solution. In such a system, the surface is large compared to the adsorbate and is, therefore, assumed to be flat within the small interaction area. This adoption ignores small randomly distributed defects and irregularities of the surface that might be adsorption hotspots in some cases [25].

Another interesting point in this context is the coating of metals with SAMs [9]. The functionalization with SAMs, here alkanethiols, is done homogeneously and systematically and in agreement with the perfect metal slab. This results in a well-defined lattice of the sulphur atoms of the SAM as shown in figure 2.4 [26]. This coverage pattern also neglects defects from the model.

3 Biological systems

3.1 Cytochrome *c*

Cytochrome *c* is a small, thermostable and soluble mono-heme protein that is involved in many electron transfer processes, where it acts as electron carrier. For example, it plays a key role in the respiratory chain for ATP synthesis using the heme cofactor as redox-intermediate to transfer electrons between cytochrome *c* reductase and cytochrome *c* oxidase [27]. It is present in nearly all biological organisms and is active at the inner- and at the intra-mitochondrial membrane space [28]. Furthermore, cytochrome *c* is involved in apoptosis, programmed cell death, when released by the mitochondria into the cytoplasm upon nitration [29].

Because of its small size, its high stability, and good detectability by its red colour, cytochrome *c* is one of the best studied proteins. For theoretical calculations, it is an ideal model system, because many crystallographic structures have been resolved and stored in the protein database (PDB) [30] (<http://www.rcsb.org>) and, additionally, molecular dynamics calculations on such a small system are computational affordable.

Cytochrome *c* contains 104 amino acids, which are forming three α -helices (figure 3.1). The iron of the *c-type* heme, which is responsible for the red colour, is in most cases coordinated by a histidine and a methionine ligand that lie within a conserved CXXCH motif [31, 32]. For interaction with redox partners, such as the phospholipid membrane or surface devices, electrostatic properties of cytochrome *c* resulting in a strong dipole moment play a major role [33–35]. This electrostatic gradient or dipole moment shown in figure 3.1 is mainly dominated by surface exposed lysine residues leading to a positive overall charge of +8 e under physiological conditions. These residues are clustered in binding hot spots, which have been determined to interact with negatively charged surfaces [36].

Although cytochrome *c* is extensively studied, molecular processes are still under discussion and in the focus of many working groups. A very common approach is mutagenesis experiments, where single or a couple of amino acids are replaced by other residues or labelled probes [10, 11]. These experiments allow a deeper insight into the mechanisms by identifying functionally important single residues. However, many open questions in this area still exist. One question which is specifically addressed in this work is how the presence of a modified gold surface affects the dynamics of cytochrome *c* and the local electric field in different single mutants. This point is investigated by a combined approach of IR and SEIRA spectroscopy and molecular dynamics simulations and discussed in [10].

3.2 Bone morphogenetic protein 2

Bone morphogenetic protein 2 (BMP-2) is a member of the transforming growth factor β (TGF- β) family [38] and is, among other proteins, responsible for cartilage and bone formation in human embryonic development and adult tissue [39]. These properties make it a promising candidate for

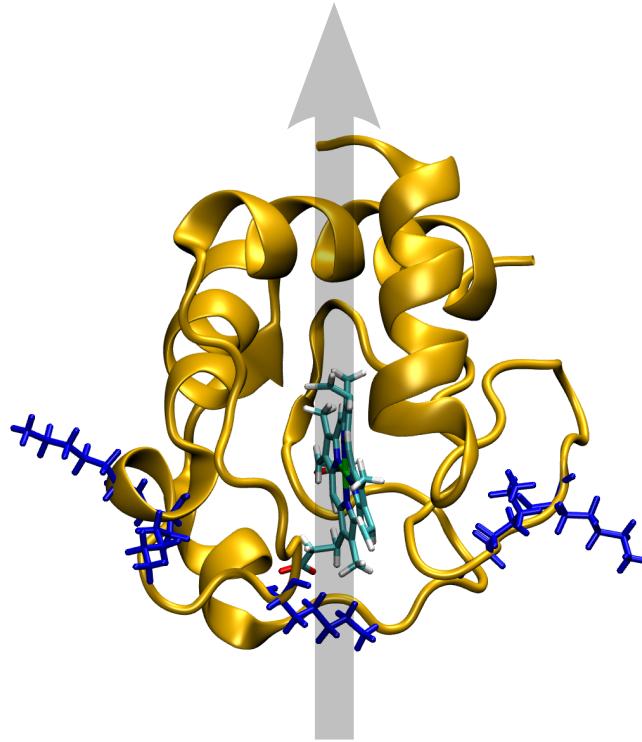


Figure 3.1: Crystallographic structure of yeast cytochrome *c* (PDB: 1YCC [37]). The protein backbone is coloured in orange and lysine residues involved in surface binding in blue. Additionally, the heme cofactor is depicted by the the atom colouring of VMD (cyan: carbon, red: oxygen, blue: nitrogen and white: hydrogen). The grey shaded arrow marks the dipole moment the protein including its heme cofactor.

medical applications. Particularly in the sector of implant development, BMP-2 is of great interest and first successful improvements in dental and orthopaedic practice to increase the biocompatibility of the implant device have been achieved recently [40–43].

In this context, the interaction of BMP-2 with **implant surfaces** and structural reorganization upon adsorption are of interest. In particular, the structural stability and effectiveness of BMP-2 upon immobilization play a crucial role.

BMP-2 functions locally, but induces bone formation ectopically. This means that osteoblast differentiation is activated in all tissues where BMP-2 occurs. To avoid this unlocalized bone formation, the spreading of BMP-2 has to be controlled by trapping it at the implant site, where it should trigger the signal cascade leading to bone growth.

Both, a couple of biochemical experiments and crystallographic structures showing BMP-2 as isolated enzyme or in complex with its receptors [44–49], revealed that BMP-2 is active as homo-dimer. Interaction with its type I and II receptors leads to a signal cascade inducing osteoblast differentiation [38, 44, 45, 47]. Beside the identification of the receptor I and II binding sites, the gained crystallographic structures indicate that seven disulphur bridges stabilize the structure. The similarity of the dimeric structure of BMP-2 allows comparing it to a human hand [48]. Thus, the receptor binding sites are nomenclatured as *wrist* and as *knuckle* epitopes according to their location on the “hand”. While the knuckle epitopes, the binding sites for the type II serine/ threonine receptor kinase, are settled on each single monomer, the wrist epitopes, which bind to the type IA receptor, are built by both monomers (figure 3.2), which indicates the importance of the dimerization [48, 49] (figure 3.2).

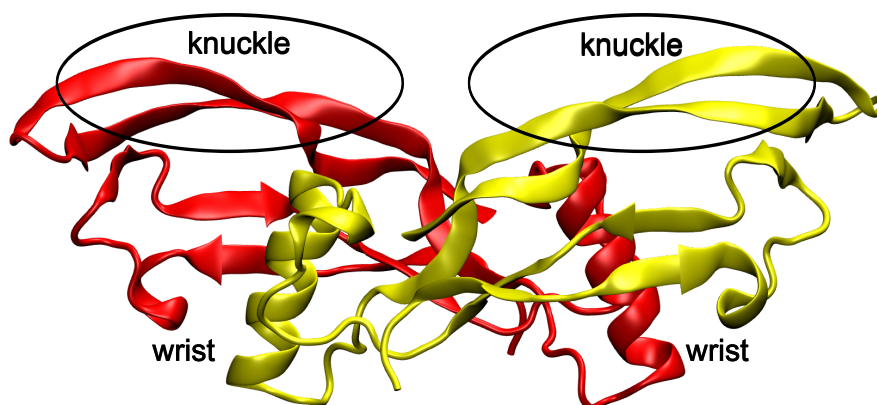


Figure 3.2: Crystallographic structure of BMP-2 (PDB: 1REW). The protein backbones of the two chains are indicated in red and blue. Additionally, the binding epitopes for the receptors are marked as knuckle and wrist epitopes.

Because BMP-2 is lacking regions with strong anodic or cathodic character, an electrostatically driven immobilization seems to be unlikely, but cannot be excluded. A more promising procedure is the immobilization by hydrophobic interactions, because the binding epitopes are characterized as hydrophobic pockets and regions. As mentioned above, these regions are meaningful for the receptor interaction. Therefore, an adsorption has to be performed carefully to avoid a total blockage of the receptor binding sites of BMP-2. Moreover, stronger unfolding or denaturation processes have to be avoided upon adsorption.

The point of protein stability upon hydrophobic surface contact has recently addressed by a couple of theoretical studies. For example, the strong interaction of BMP-2 and graphite in implicit solvent leads to severe structural changes in the protein [50]. Other theoretical studies dealing with the adsorption of unipolar proteins, such as fibronectin and lysozyme, on hydrophobic surfaces showed similar results [51–54]. In contrast to these observations, Dong et al. simulated the immobilization of structurally stable BMP-2 on a hydroxyapatite surface [55, 56]. Taken together, these results demonstrate the complexity of the immobilization process and the difficulty to predict the adsorption behaviour without computational demanding MD simulations.

This contradiction reveals that much work has to be done to establish and to improve the use of BMP-2 in medicine. In particular, information on the atomic level is needed for a proper understanding of the molecular processes and mechanisms. Therefore, the adsorption of BMP-2 on two implant surfaces with medical relevance, namely, titanium dioxide and graphite, has been investigated by atomistic MD simulations. Titanium dioxide and graphite were chosen, because they bear very different surface characteristics, but are both used as implants. The results and more information are given in chapter 10.1.

3.3 Sulfite oxidase

Sulfite oxidases (SO) constitute, besides xanthine oxidases and DMSO reductases, the family of molybdenum containing enzymes [57]. Among the sulfite oxidase family one distinguishes between

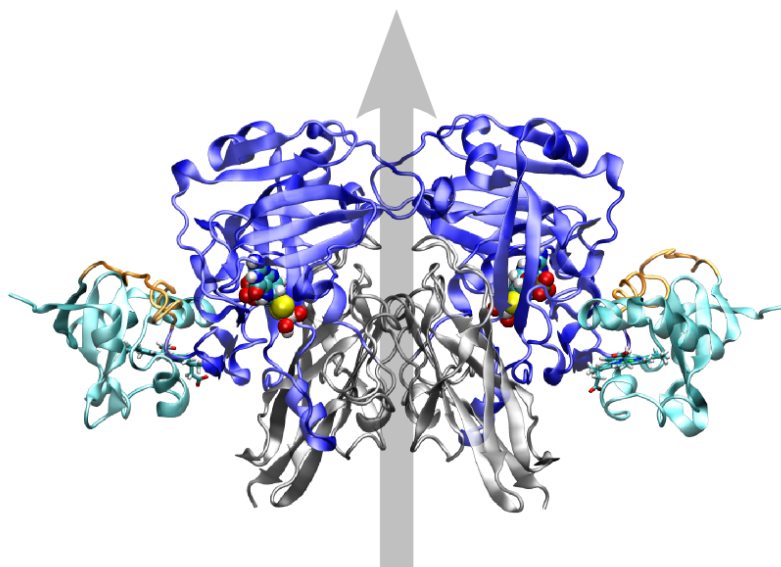
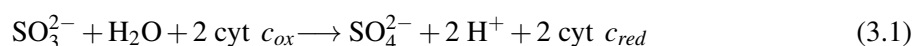


Figure 3.3: Three-dimensional structure of dimeric cSO (PDB: 1SOX). The structure shows the three domains of the cSO, namely, the cytochrome *b5* (cyan, residue 3–84), the molybdopterin containing (blue, residue 103–343) and the dimerization domains (grey, residue 344–466) of both monomers. The heme cofactors are indicated by sticks and the molybdopterin cofactor (Moco) is drawn by the van der Waals radii representation. Additional to these domains and cofactors, the flexible linker region (residue 85–102) connecting cytochrome *b5* and the Moco domain is represented in orange. The shaded arrow indicates the dipole moment of the enzyme.

sulfite oxidases and sulfite dehydrogenases according to their electron transfer mechanism to molecular oxygen. This work is addressed to sulfite oxidases, namely, to the chicken liver sulfite oxidase (cSO), which is highly homologous to human sulfite oxidase (hSO). Besides SO in animals, structurally different SO are present in plants [58, 59]. The structural and functional differences refer to the absence of a heme cofactor and the use of molecular oxygen as electron acceptor instead of cytochrome *c* in plant SO. Despite these discrepancies, the active site around the molybdopterin is highly conserved between these species.

cSO contains three domains, an **N-terminal cytochrome *b5*** unit, a central **Moco domain** and a **C-terminal dimerization domain**, which is stabilizing the dimeric structure of the enzyme (figure 3.3) [60]. SO is responsible for the metabolism of sulphur containing amino acids and enzyme defects could lead to SO deficiency, a severe neuronal disease resulting in early death [61]. During well functional catalysis, sulfite is oxidized to sulfate and two electrons are transferred to the active site of the SO [62]. Afterwards, they are stepwise transferred via the heme to the external electron acceptor ferricytochrome *c*.



Before releasing the electrons to ferricytochrome *c*, an **intra-molecular electron transfer** step from the active site to the heme, located in the cytochrome *b5* domain, is necessary and in the focus of many research groups. The concern of this step results from the spatial arrangement of the two redox partners with respect to each other. The crystallographic structure of cSO (PDB: 1SOX) shows the two metals of the cofactors in a separation distance of around 32 Å [60]. For electron transfer (ET) processes mediated by protein environment, this is a very huge distance leading to very slow

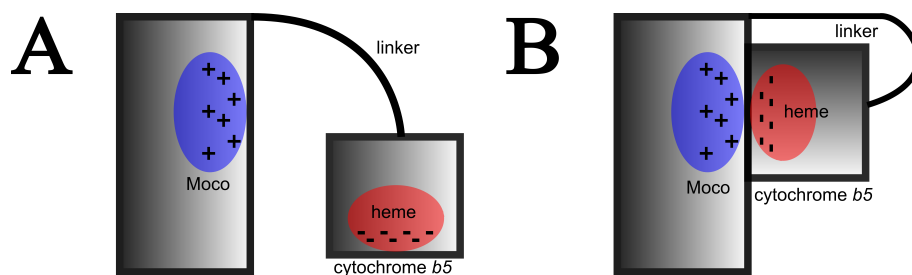


Figure 3.4: Proposed mechanism of domain motion in cSO [63]. The cartoon shows a SO monomer with its Moco/dimerization domain (large box) and its cytochrome *b5* unit (small box) in its relaxed (A) and activated (B) structure, where intra-molecular electron transfer occurs. Additionally, the opposite charged regions around the active site (blue) and the b-type heme (red) are indicated.

electron transfer rates. This fact stands in contradiction to ultra-fast intramolecular electron transfer (IET) rates obtained experimentally [63].

Therefore, a model for the intra-molecular electron transfer has been developed [63]. In the proposed mechanism, the negatively charged cytochrome *b5* unit undergoes a conformational change and docks to the binding pocket of the positively charged active site harbouring the molybdopterin (figure 3.4). The electrostatically driven rearrangement within the SO is thought to be enabled by the high flexibility of the linker region connecting the Moco with the cytochrome *b5* domain. This tether as well as amino acids of the active site have been targets in several mutagenesis studies and their importance for intra-molecular electron transfer and a well functional SO have been validated [64–67].

In order to get a detailed insight into the electron transfer properties and into the adsorption behaviour in general, immobilization studies on electrode surfaces are of great interest. The charge distribution within the enzyme reveals strongly negatively charged patches located at the cytochrome *b5* domain and at the C-terminal end of the dimerization domain which results in a **strong dipole moment** (figure 3.5) [68]. These areas are proposed to interact strongly with positively charged interaction partners, such as the electron acceptor cytochrome *c* or cationic electrode surfaces. Interaction with surface devices could interfere with the proposed domain motion mechanism [63] and block the **flexibility of the cytochrome *b5*** domain by strong immobilization, as illustrated in figure 3.6. Such an outcome has severe consequences on the functionality of the enzyme and strongly limits its application. Similar results have been obtained by increasing the viscosity of the solvent surrounding SO [66, 69]. An increased viscosity resulted in decreased electron transfer rates and seems to validate the model of domain motion events (figure 3.4). However, the atomic structure of an activated conformation has not been resolved by crystallographers, yet, but would offer a deeper insight into the functionality of the enzyme.

This work aims on two topics, namely, the **domain motion of the cytochrome *b* domain** towards the active site and on the **ionic strength dependent immobilization** process of the SO on positively charged amino-terminated monolayers. These two studies are summarized in chapters 10.2 and 10.3, respectively.

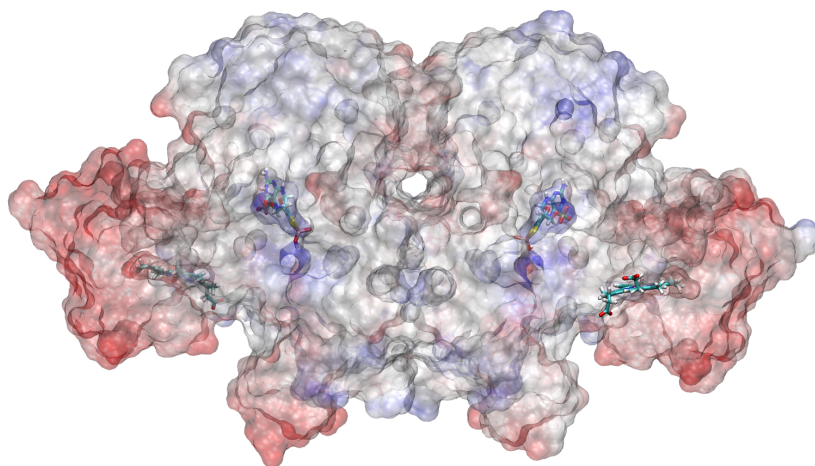


Figure 3.5: Electrostatic potential surface of cSO. The electrostatic potential surface of cSO calculated with the APBS tool [70] clearly indicates negatively charged regions (in red) at the cytochrome *b5* domain and at the C-terminal ends of each monomer. The orientation of SO is equivalent to figure 3.3.

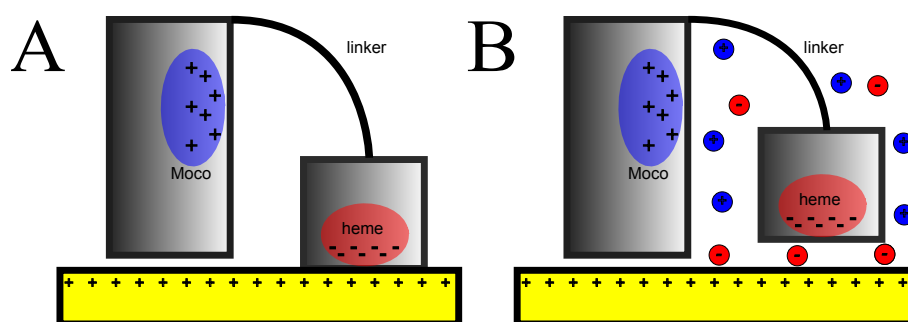


Figure 3.6: Proposed scheme of the ionic strength dependent immobilization of SO. The colouring of the scheme follows figure 3.4, but additionally it contains the yellow and positively charged surface and ions denoted as red (anions) and blue (cations) spheres. While panel A describes low ionic strength conditions, where the amount of ions is negligible and the cytochrome *b5* unit is able to adsorb on the surface, panel B shows the adsorption inhibiting effect of the ions under high ionic strength conditions.

3.4 [NiFe]-hydrogenase

Hydrogenases are enzymes that catalyse the reversible heterolytic cleavage of molecular hydrogen into protons and electrons.



This property makes them promising candidates for clean energy production. Particularly today, where the need of not renewable fossil fuels, such as coal, gases and mineral oil, is extremely increasing and their combustion leads to a threatening pollution of the atmosphere with carbon dioxides, the sector of alternative energy sources is getting more important.

Hydrogenases are classified by their metal content at the active site into [FeFe] hydrogenases, [NiFe]

hydrogenases and [Fe] hydrogenases [71, 72]. This work refers to [NiFe] hydrogenases. These enzymes are clustered into two groups: oxygen **sensitive** and oxygen **tolerant** [NiFe] hydrogenases. Oxygen intolerant, sensitive or standard hydrogenases are strongly inhibited by the presence of molecular oxygen and become inactive under small amounts of O₂ [73, 74]. Their long reactivation time reduces their direct industrial benefits [75]. In contrast to this behaviour, oxygen tolerant hydrogenases remain active under atmospheric conditions, which makes them much more suitable for technological applications [73, 74]. However, the three-dimensional structure and the functionality of standard hydrogenases are much better investigated which makes them interesting test systems because these properties were mostly unknown and elusive for oxygen tolerant [NiFe] hydrogenases in the beginning of this work. More details about these facts are given in the following sections 3.4.1 and 3.4.2.

One major research field for industrial application is the hydrogen driven biofuel cell [76]. Here, the hydrogenase enzymes get in contact with pure or modified electrode surfaces to function as effective catalysts. This is a crucial point, because surface interaction and adsorption could affect protein functionality or even lead to denaturation as reported earlier for other biomolecules [50–52, 54, 77–79]. In this field, the immobilization process of both, oxygen tolerant and intolerant hydrogenases, is of interest but details on the atomic level are largely unknown. A short overview of the current achievements of immobilizing [NiFe] hydrogenases is given in section 3.4.3.

3.4.1 Oxygen sensitive [NiFe] hydrogenase

Oxygen sensitive or standard [NiFe] hydrogenases, for which various three-dimensional structures are known for more than 15 years [80], are soluble heterodimeric enzymes. The first three-dimensional structure was solved for the bacterium *Desulfovibrio gigas* and consists of a small and a large subunit [80]. The large subunit harbours the conserved active site [72], a bimetallic Ni-Fe complex, and the small subunit incorporates three iron-sulphur (FeS) clusters mediating the electron transfer between the deeply buried catalytic site and the surface of the enzyme. The structure is shown in figure 3.7 in detail.

The bimetallic active site in standard [NiFe] hydrogenases is composed by a Ni and an Fe atom, which are connected by two bridging cysteines. Additionally, a third bridging position is occupied by exogenous ligands, such as H⁻, OH⁻ or O²⁻ [82–84]. This configuration depends on the redox state of the complex during the catalytic cycle [85, 86], which is still under discussion. Furthermore, the Ni atom is coordinated by two additional cysteines and the Fe by three inorganic ligands, namely, two CN⁻ and one CO. This ligation has been validated by spectroscopy [87], because induced scattering by the adjacent metals makes the determination by crystallography very hard.

As mentioned above, low amounts of oxygen deactivate standard [NiFe] hydrogenases [73, 74]. It is assumed that the active site changes into the inactive Ni-A state, whose recovery time for reactivation lies on time scales up to several hours. However, the mechanisms and the catalytic cycle are not fully understood and are still under discussion.

3.4.2 Oxygen tolerant [NiFe] hydrogenase

The oxygen tolerance is of outstanding interest in industrial application and hydrogenase science. Therefore, much effort has been made during the last years to identify its structural origin. Very important in this context are the first resolved crystallographic structures of these enzymes in a reduced state [88–90].

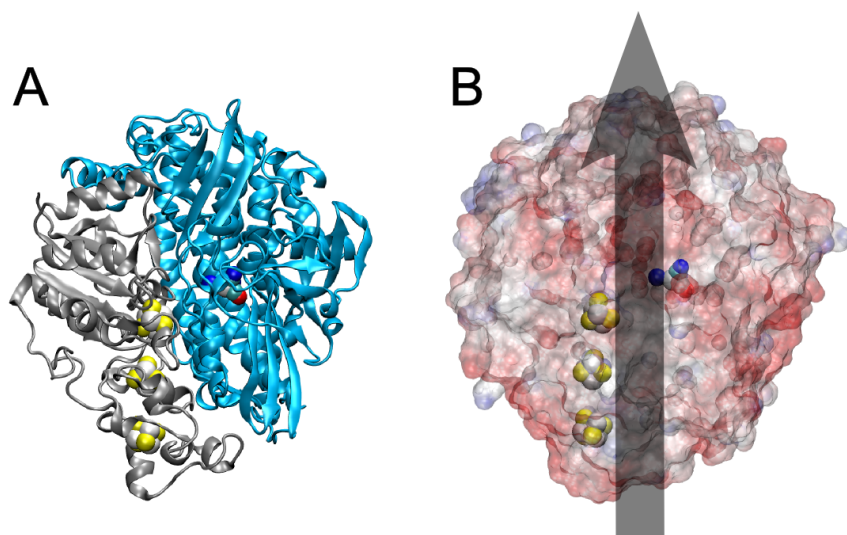


Figure 3.7: Crystallographic structure of the [NiFe] *D. gigas* (pdb: 2FRV) [80]. (A) shows the secondary structure of the enzyme. The small (264 residues) and large (536 residues) subunits are coloured in grey and blue, respectively. Additionally, the active site and FeS clusters are depicted as spheres. The black shaded arrow indicates the strong (>1100 Debye) total dipole moment of the enzyme [81]. (B) represents the electrostatic surface potential derived with the adaptive Poisson-Boltzmann solver (APBS) method [70]. Blue areas carry a positive and red regions a negative potential.

These first structures of oxygen tolerant hydrogenases have been published for the cytoplasmic **membrane bound hydrogenases (MBH)** of *Ralstonia eutropha* [88], *Hydrogenovibrio marinus* [89] and *Escherichia coli* [90]. Another remarkable feature of the MBH is the higher affinity to hydrogen compared to standard hydrogenases [91].

Beside the well-investigated MBH, other oxygen tolerant [NiFe] hydrogenases exist, namely, the soluble hydrogenase (SH) and the regulatory hydrogenase (RH). The bidirectional SH and RH are responsible for nicotinamide adenine dinucleotide (NAD⁺) reduction to NADH by hydrogen oxidation [92] and for measuring the hydrogen content in the cell [93, 94], respectively.

Biochemical mutagenesis experiments [91] and the resolved crystallographic structures revealed only small structural differences in the active site environment with respect to standard hydrogenases and predicted that the active site is not the origin of the oxygen tolerance. However, a larger structural anomaly in the MBH structures is observed at the proximal FeS cluster. Mutagenesis studies combined with electron paramagnetic resonance (EPR) showed that the **abnormal proximal FeS cluster** is a source for the oxygen tolerance (figure: 3.8) [95, 96]. This modified proximal FeS cluster exhibits two additional cysteine ligands compared to the standard species. Although these findings give new insights into the structure of [NiFe] hydrogenases, the mechanism for the oxygen tolerance is not completely understood.

Additional to these structural variations, the MBH holds a membrane **anchor at the C-terminus** of the small subunit and a **third subunit, a cytochrome *b* domain** that is also embedded in the membrane [97–101]. The three-dimensional structures of these additional building blocks in the MBH are not resolved, yet, and are, therefore, still unknown.

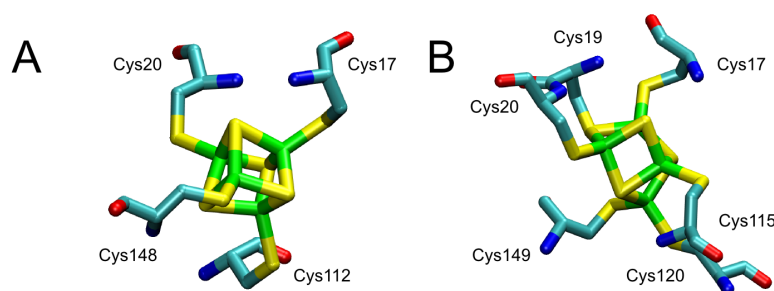


Figure 3.8: The reduced proximal FeS cluster in a standard hydrogenase and in the oxygen tolerant MBH. In the standard hydrogenase from *D. gigas* (pdb: 2FRV) [80] the proximal 4Fe4S cluster is coordinated by four cysteine ligands as shown in A. In the oxygen tolerant MBH of *R. eutropha* (pdb: 3RGW) [88], two additional cysteine residues contribute to the coordination of the abnormal 4Fe3S cluster and are identified as a source of the oxygen tolerance [96]. Sulphur atoms are coloured in yellow, Fe in green, carbons in cyan, oxygen in red and nitrogen atoms in blue. Hydrogen atoms have left out for clarity.

3.4.3 Immobilization and application of [NiFe] hydrogenases

First successful applications in hydrogen production were made in the last years by immobilizing [NiFe] hydrogenases on various electrode surfaces [73, 102–104]. The turnover rates and the amounts of produced hydrogen are very low. Nevertheless, the proof-of-principle for hydrogen production involving hydrogenases as catalysts has been shown.

Due to the overall negative charge and the strongly negatively charged patch at the distal FeS cluster in standard hydrogenases, a strong electrostatically driven adsorption on charged devices has been assumed [81, 105], but detailed information of the immobilization on the atomic level was still lacking in the beginning of this work. It was predicted that upon adsorption the electric communication between the active site and the electrode surface is enabled by a conductive wire formed by the FeS clusters [80].

To gain a deeper understanding in this field, the initial adsorption process of standard hydrogenases on modified electrode surfaces were theoretically investigated. Thus, molecular dynamics simulations (chapter 5) combined with dipole moment calculations were performed to discover optimal immobilization conditions on amino-terminated self-assembled monolayers (SAMs). The results of the combined approach of theory and surface enhanced infrared absorption (SEIRA) measurements are summarized in chapter 10.5.

In terms of the MBH, the immobilization procedure is much more complex. As stated in section 3.4.2 the MBH contains two additional building blocks, namely, the C-terminal membrane anchor and the third subunit. This increased protein complexity and the fact that the structures of these elements are still unknown make calculations to predict adsorption and immobilization very difficult. Therefore, a high fraction of experimental work has been carried out with the dimer instead of the trimer [106, 107]. Theoretical investigation, namely, molecular dynamics simulations of the adsorption behaviour, analyse beside the surface composition, the problem of incomplete structures and the importance of the C-terminal membrane anchor in chapter 10.6. In these calculations, a comparison of the immobilization of the MBH on differently coated gold electrodes was performed with and without the C-terminal anchor of the small subunit. Unfortunately, these calculations were still neglecting the third subunit, because of the lack of an adequate template.

3.5 *Ciona intestinalis* voltage-sensing protein

The *Ciona intestinalis* **voltage-sensing phosphatase** (Ci-VSP) is a voltage dependent protein consisting of two coupled modules, namely, the N-terminal **voltage sensory domain** (VSD) and the intracellular **catalytic domain** (CD).

The VSD is a putative four transmembrane helix construct which is changing its conformation in the membrane upon de- and repolarisation [108–110]. During this motion according to the electric field, charged amino acids are rearranged within the plasma membrane which results in a detectable charge flow. The VSD exhibits a high sequence similarity to voltage gated ion channels [111]. Its potential triggered motion within the membrane regulates the activity of the CD but the underlying mechanism of this coupling is still elusive.

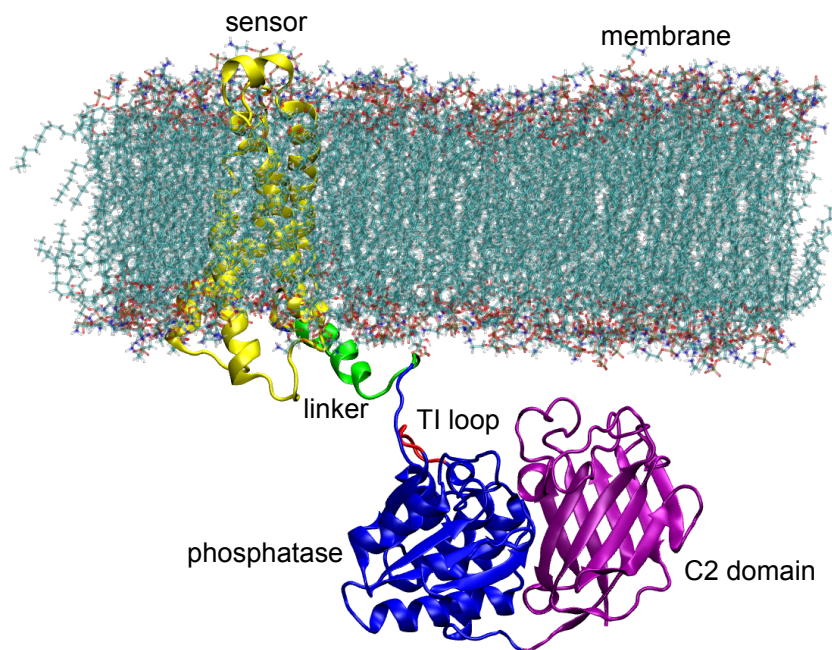


Figure 3.9: Structure of Ci-VSP embedded in the plasma membrane according to the homology model. The membrane and the protein backbone are represented in the sticks and cartoon representations, respectively. The domain structure of Ci-VSP is indicated by the following colour code (yellow: VSD, green: linker, blue: phosphatase, red: TI loop, violet: C2 domain). The model is based on the crystallographic structures 2R9R [112] from the voltage-dependent Shaker family K^+ ion channel and 3AWE [113] from the Ci-VSP phosphate/C2 complex.

The CD is composed of two domains, the **phosphatase** (PD) and the **C2 domain**. While the C2 domain is assumed to participate in the membrane interaction and recruitment [114], the PD harbours the active site of the enzyme responsible for dephosphorylation of the signal molecule phosphatidylinositol 4,5-bisphosphate (PIP2) [15, 115–119] located in the membrane. The active site in the phosphatase is composed by a HXC₅RT motif which is typical for protein tyrosine phosphatases that cleave phosphate from phospholipids and proteins [120].

The recently resolved crystallographic structure of the CD complex of Ci-VSP [113] confirmed the high similarity, which was postulated by the high sequence homology to other members of the protein

tyrosine phosphatase family, such as the tumour suppressor PTEN (phosphatase and tensin homologue) [114]. However, a complete three-dimensional structure of Ci-VSP is still missing which makes it difficult to identify the functionality and, in particular, the coupling mechanism between VSD and CD. Most likely, the positively charged linker connecting the two domains plays major role in the coupling between the two modules [108]. This assumption is based on several mutagenesis experiments that induced a decreased activity of Ci-VSP by deletions or mutations within the linker [121, 122].

The significance of the linker interactions is underlined by Hossain et al. [123], who predicted a bidirectional effect of the linker. They predicted that conformational changes in the CD result from motions of the VSD and *vice versa*. These interactions of the linker involve electrostatic interactions and a recruitment to the membrane, which might result in activation of the CD [121, 124, 125].

The investigations in this work are focussed on the structure, the dynamics, and the coupling character of the linker. Therefore, a homology model based on the crystallographic structures of Ci-VSP (CD) and a voltage-dependent Shaker family K⁺ ion channel (VSD) has been constructed (figure 3.9). Here, the initial linker geometry has been modelled in an α -helical conformation [126]. The results of the molecular dynamics simulations and the supplemental electrophysiology are represented in chapter 10.7.

4 Molecular Mechanics

The energetic characterization of biomolecules gives information about many properties, such as stable conformations, possible folding pathways or protein aggregations. One way to determine the potential energy of a large biological system is **Molecular Mechanics**.

Molecular Mechanics describes the potential energy by additive physical energy functions. In this approach, atoms are defined as charged mass points connected by springs representing the unbreakable bonds. Electrons are not modelled explicitly, but their contribution to the potential energy is included in the global energy function, called the **force field**. In the following, force fields are explained in more detail.

4.1 Force fields

The choice of the force field, which is the function for the potential energy calculation (section 4.2), has to be considered carefully. A force field consists of three parts, namely, the function, the atom types, and the parameter set.

Force fields are optimized and assembled for different systems and applications and strongly vary from each other. For example, the MM2 force field [127] is developed for small organic compounds in the gas phase, while the CHARMM force field is designed for larger biomolecules [128].

This fact biases the application of force fields. Not every force field is able to describe all elements in different molecular environments adequately. Therefore, each force field has its own definition of atom types. This means that each atom is not only defined by its element, but also by its environment. For example, a carbon atom can be located in very different environments, such as the diamond (sp^3 -hybridization) and a terminal carboxyl group (sp^2 -hybridization) which requires two different atom types characterized by their own parameters.

The parameter set contains all constants determining the interactions between the atom types. This comprises, *inter alia*, partial charges, van der Waals radii, spring constants and the corresponding energy minima for bonds, angles and torsions. These empirical constants have been derived by experiments and ab-initio calculations and are not transferable between different force fields [129].

In the following section 4.2, the potential energy calculation defined in the CHARMM force field [128, 130] is explained in more detail.

4.2 The potential energy function

In the CHARMM force field [128, 130], the potential energy $V(r = 0, \dots, N - 1)$ of a molecular system consisting of N atoms is a function of the positions r of all particles. The potential energy is constituted of two terms representing the bonded and the non-bonded interactions.

$$V = V_{\text{bonded}} + V_{\text{non-bonded}} \quad (4.1)$$

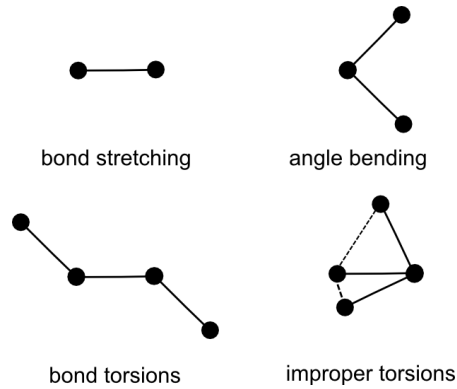


Figure 4.1: Scheme of internal motions. The figure shows the non-bonding interaction between two (bond stretching V_{stretch}), three (angle bending V_{bend}) and four particles (bond V_{torsion} and improper torsions V_{improper}).

The bonded energy V_{bonded} is the sum of the bond stretching V_{stretch} , the angle bending V_{bend} , the torsions around bonds V_{torsion} , and the improper torsions V_{improper} . The non-bonded term $V_{\text{non-bonded}}$ contains the van der Waals V_{vdW} and electrostatic V_{elect} energies.

$$V = V_{\text{bonded}} = V_{\text{stretch}} + V_{\text{bend}} + V_{\text{torsion}} + V_{\text{improper}} \quad (4.2)$$

$$V = V_{\text{non-bonded}} = V_{\text{vdW}} + V_{\text{elect}} \quad (4.3)$$

The energy contributions are discussed in more detail in the following.

4.2.1 Bond stretching

The bond stretching accounts for the interaction between pairs of bonded atoms according to Hooke's law. The energy is allegorised by a harmonic potential, which is dependent on the deviation of the bond length b to its equilibrium reference value b_0 . The shape of the harmonic potential well is defined by the force constant k_b .

$$V_{\text{stretch}} = \sum_{\text{bond}} k_b (b - b_0)^2 \quad (4.4)$$

4.2.2 Angle bending

The angle bending potential describes the interaction between three atoms in a valence angle. It is, as the bond stretching, modelled by a harmonic potential. Here, k_θ denotes the force constant and $\theta - \theta_0$ the difference between the angle θ to its equilibrium θ_0 .

$$V_{\text{bend}} = \sum_{\text{angle}} k_\theta (\theta - \theta_0)^2 \quad (4.5)$$

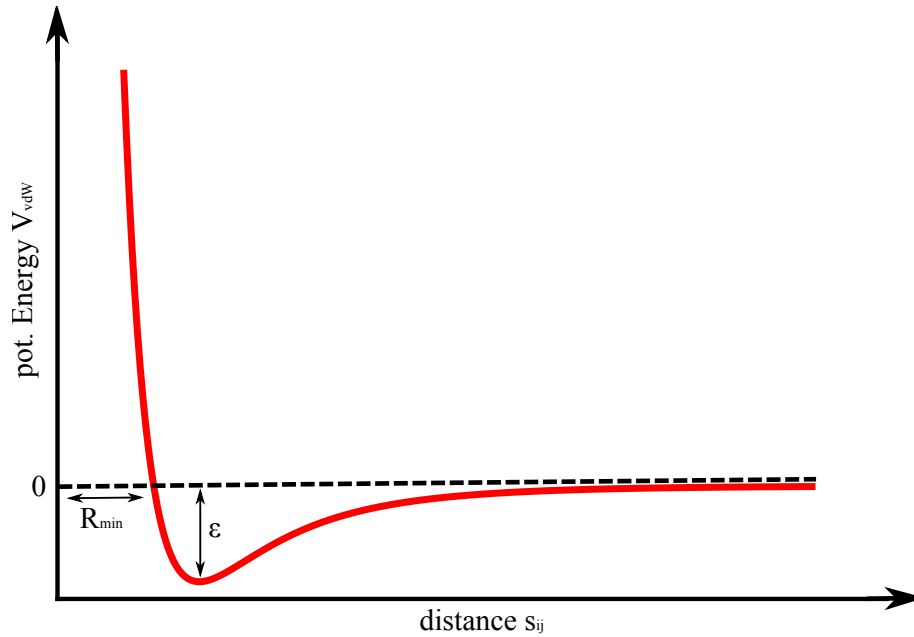


Figure 4.2: Scheme of the Lennard-Jones potential. The figure shows a typical Lennard-Jones potential describing the vdW energy between two particles. Here, R_{min} and ϵ denote for the equilibrium distance, where the force between the two atoms i and j is zero, and the depth of the energy well, respectively.

4.2.3 Bond torsions

The periodic potential specifying the bond torsions (also called dihedrals) comprises four covalently bound atoms (figure 4.1). It takes the force constant k_ξ , the torsion ξ , the phase shift γ and the multiplicity of the function k ($k=1,2,3,\dots$) into account.

$$V_{\text{torsion}} = \sum_{\text{torsion}} k_\xi [1 + \cos(k\xi - \gamma)] \quad (4.6)$$

4.2.4 Improper torsions

The improper dihedrals (or out of plane bendings) are represented by a harmonic potential, as described for the bond stretching and angle bending functions. The energy is increasing with the force constant k_ω and the deviation between ω and its equilibrium condition ω_0 . The improper dihedrals avoid prohibited transitions, such as 360° torsions in aromatic rings.

$$V_{\text{improper}} = \sum_{\text{improper}} k_\omega (\omega - \omega_0)^2 \quad (4.7)$$

4.2.5 Van der Waals interactions

The van der Waals (vdW) energy term between particles i and j , which are separated by a distance of more than three bonds, is described by the 12-6 Lennard-Jones potential (figure 4.2). It consists of an attractive $\left(\frac{R_{min_{ij}}}{s_{ij}}\right)^6$ term, which is derived from the London potential, and a repulsive $\left(\frac{R_{min_{ij}}}{s_{ij}}\right)^{12}$ part. $R_{min_{ij}}$ indicates the equilibration distance between atom i and j , where the particles do not

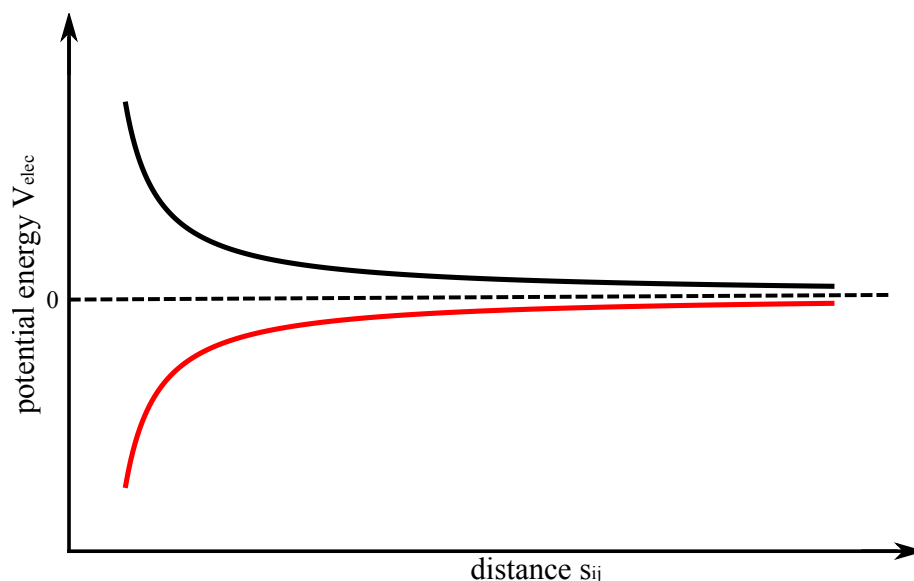


Figure 4.3: Scheme of the Coulomb potential. The black and red curves describe the Coulombic potential between two equally and contrary charged particles, respectively. While equally charged particles attract each other, opposite charges repel each other and result in positive Coulomb energies.

attract or repel each other, and ϵ defined the depth of the potential well. s_{ij} denotes the distance between the atoms i and j .

$$V_{vdW} = \sum_{vdW} \epsilon \left[\left(\frac{Rmin_{ij}}{s_{ij}} \right)^{12} - 2 \left(\frac{Rmin_{ij}}{s_{ij}} \right)^6 \right] \quad (4.8)$$

4.2.6 Electrostatic interactions

The electrostatic energy is simply calculated with the Coulombic law. The potential between two atoms i and j , which are separated by more than three bonds, is dependent on the partial charges q_i and q_j and the distance s_{ij} between the corresponding atoms. η accounts for the dielectric constant *in vacuo*. A typical Coulomb potential is shown in figure 4.3.

$$V_{elec} = \sum_{elec} \frac{q_i q_j}{4\pi\eta s_{ij}} \quad (4.9)$$

4.3 Boundary conditions

The high computational demand of MM based simulations strongly limits the cell volume of the simulation box. This limitation leads to a high fraction of atoms that interact with the artificial borders. These interactions have to be handled carefully, because they might induce artefacts in the potential energy and dynamics (chapter 5) of a system. Thus, the choice of the boundary conditions to minimize the artificial character is a relevant problem. Five main ideas to handle the box borders are briefly introduced.

4.3.1 Open cell

In an open cell, the particles are allowed to move in vacuum. This technique is only useful for the investigation of ultra fast processes but not for the treatment of biomolecules on surfaces. There are many examples in literature that the dynamics of biomolecules in vacuum strongly differs from the behaviour in solution [131–133].

4.3.2 Implicit solvent

The realization of a system using implicit solvent is similar to the open cell approach [134–136]. The molecule of interest is placed in an unlimited cell, but instead of a vacuum, a dielectric background medium accounting for the solvent interactions is used. This dielectricum mimics the solvent, but explicit atoms are lacking. The method is useful to save computational power by removing many atoms from the system. The disadvantage in the approach is the lack of explicit contacts between solute and solvent. The most common approaches to calculate the solvation free energy are based on the Poisson Boltzmann equation [135] and the computational efficient generalized Born theory [137].

4.3.3 Rigid boundary conditions

In rigid boundary conditions the system cell (or the reaction region) is simply limited by a (potential) wall. Since this border repels particles, it may lead to artificial and unwanted dynamics. Therefore, rigid boundary conditions are seldom used for the simulation of biomolecules.

4.3.4 Stochastic boundary conditions

The application of stochastic boundary conditions introduces a thermal reservoir or bath around the simulation cell and is, in particular, used for molecular dynamics discussed in the following (chapter 5). Each particle translating into this area is treated by an additional stochastic force term, which accelerates the translation back into the reaction region [138]. The additional stochastic term is realized by the general Langevin equation [139, 140].

$$m_i \frac{dv_i}{dt} = -m_i \zeta v_i + R_i - \frac{\delta U}{\delta r_i} \quad (4.10)$$

Here, $-m_i \zeta v_i$ is the friction, R_i a random gaussian distributed force and $\frac{\delta U}{\delta r_i}$ a term for balancing the temperature of the system, which is changed by the friction and random force. In these terms, ζ denotes the friction coefficient. This treatment of the box borders becomes useful, when the simulated system has a centre of interest around which a reaction region can be defined. The process is strongly related to the Langevin equation used in stochastic dynamics (section 5.2).

4.3.5 Periodic boundary conditions

Periodic boundary conditions (PBC) are a widespread technique in molecular mechanics and classical molecular dynamics simulations (chapter 5) to create more realistic conditions [3, 141]. To avoid or to minimize the artificial character of interactions with the box borders, PBC mimic mirror cells in all directions of the unit cell to obtain a periodic and infinite system (figure 4.4). Especially for liquids, crystals and infinite surface systems these conditions are of high relevance and generate bulk conditions close to nature. Furthermore, long-range electrostatics are much better represented

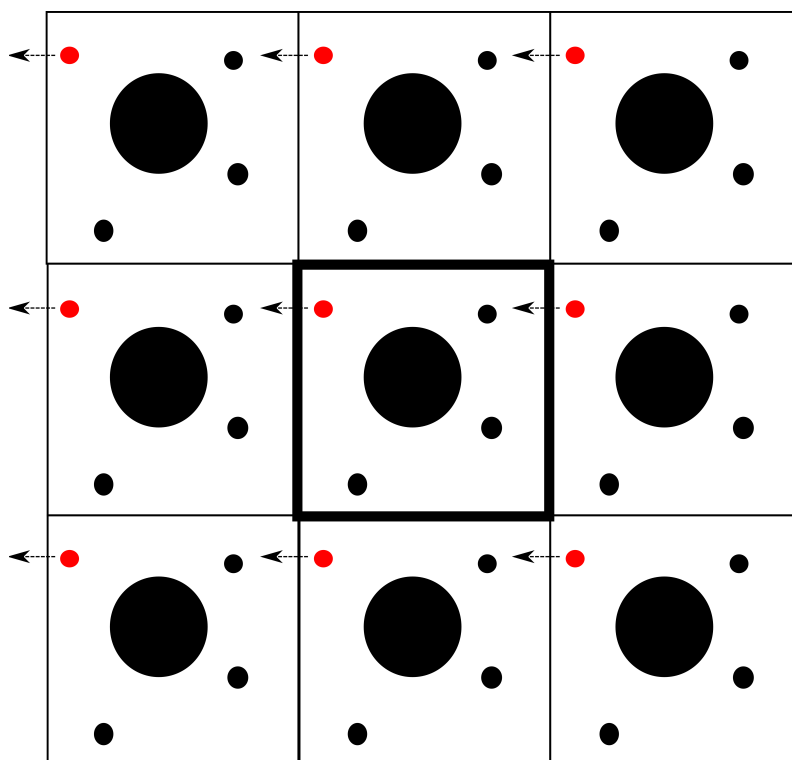


Figure 4.4: Scheme of periodic boundary conditions. The unit cell in the centre is surrounded by image cells in all directions. For clarity, the scheme is drawn in 2D. The arrow indicates the motion of the red marked atom into the neighbouring image cell.

by PBC than by cut-offs forced by the system borders (section 4.4). Replacing PBC by a larger system box requires a lot of extra computer power, which is not manageable with today's computers.

A rule for the minimal box size of a periodic system is the so-called **minimum image convention**. It states that the longest cut-off has to be smaller than the shortest edge of a simulation box. This is particularly important for smaller systems. Too small simulation boxes or too large cut-offs result in strong self-interaction effects, which artificially bias the motion of the particles. More information for computational efficient realizations is given in the following chapter.

4.4 Computational solutions for non-bonded long-ranged interactions

As shown in the previous section 4.2, the pairwise and additive force evaluation of non-bonded interactions is strongly distance dependent. Therefore, a computational effective way to determine long-ranged interactions between atoms, in particular under PBC, is required. A trivial approach summing over all atom pairs leads to a runtime of $O(N^2)$, where N is number of atoms in the cell. Because this summation is computational demanding and very slow for bigger systems, several methods, such as simple **cut-off procedures**, improved **Verlet neighbour lists** [141, 142] and **particle Mesh Ewald summations** [143] have been introduced.

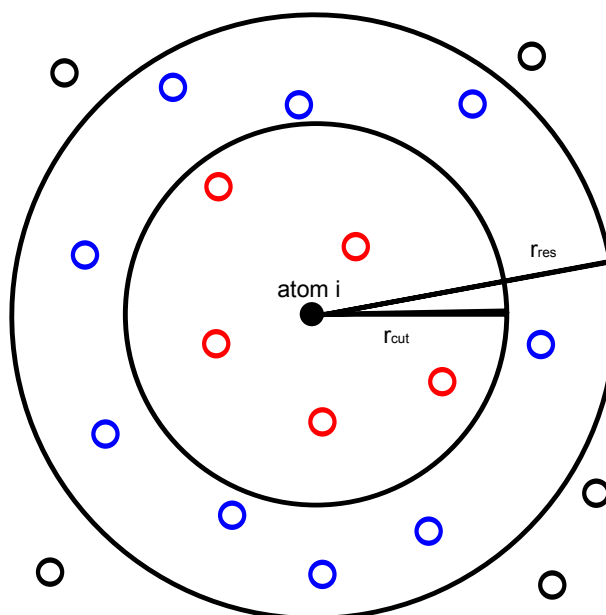


Figure 4.5: Scheme of the Verlet neighbour list algorithm. The atoms around a central atom i are divided into three groups: Atoms within the cut-off radius r_{cut} (red), atoms within the neighbour list r_{res} (blue) and particles in no list (black).

4.4.1 Cut-offs and neighbour lists

A very simple method for saving computational time is the use of **cut-offs**. Thereby, all interactions beyond a certain cut-off are truncated and their contribution to the potential energy is ignored. For vdW interaction this limitation is easily adaptable, because the interaction force between particles vanishes to zero within approximately 12 \AA (figure 4.2). In contrast to vdW interactions, long-ranged electrostatic forces have a non-negligible effect. This problem is often solved by using the **Particle mesh Ewald summation**, as briefly introduced in section 4.4.2.

Another computational demanding task in using cut-offs is the determination of the atoms that are within the cut-off range of the central atom i . An efficient way to generate these spheres is **Verlet neighbour lists** [142]. In this method, two radii, r_{cut} and r_{res} , around a central atom i are defined (figure 4.5). The sphere defined by r_{cut} includes all atoms within the cut-off range of atom i . Further, the reservoir region contains all atoms in a radius of r_{res} with respect to the central atom i which are not in r_{cut} . Typically, r_{res} is $2 - 4 \text{ \AA}$ larger than the cut-off r_{cut} for the vdW and short-ranged electrostatics. In molecular dynamics (chapter 5), it has to fulfil

$$r_{res} - r_{cut} > N_{up} \bar{v} \Delta t \quad (4.11)$$

where Δt is the time step, N_{up} the update interval for the reservoir list r_{res} and \bar{v} the average atom velocity.

The runtime of this methodology is strongly dependent on the update interval N_{up} of the neighbour lists. If the lists are not updated at every step Δt , because the displacement of all atoms in r_{res} is very small, the distance evaluation can be accelerated by one order to $O(N)$ and atoms outside of r_{res} can be excluded in the summation. Otherwise, when the displacement is very large, the update interval becomes very small and the gain in computational speed is minimal.

4.4.2 Particle mesh Ewald summation

Simple cut-off procedures neglect the long-ranged character of electrostatic interactions. To expand the potential energy function by taking these long-ranged electrostatics under PBC into account, the **particle mesh Ewald** (PME) summation [143, 144] is a computationally efficient way.

In this lattice sum method, the real space summation of long-ranged electrostatics is converted into the equivalent reciprocal Fourier space. In doing so, one maps the gaussian shaped charge densities of the point charges on a discrete lattice for fast Fourier transformations to obtain a fast converging sum for the long-range electrostatics.

For simulations using PME, the charge neutrality of the system is a stringent requirement to avoid converging problems and errors. In total, one gains two fast converging terms, namely, the real space short-ranged and the Fourier space long-ranged interactions. The computational time is reduced from $O(N^2)$ for the calculations using the realspace only to $O(N \cdot \log(N))$ by using the PME summation for long-ranged electrostatics.

5 Molecular dynamics simulations

Experimental analysis of ultra fast biological events on the atomic level is a costly and extremely difficult procedure. Therefore, theory is needed to obtain a deeper insight into these processes. One tool for the analysis of such processes is **molecular dynamics** (MD) simulations describing the time dependent evolution of a system. Such calculations can be executed on different levels of theory, namely, **quantum mechanical** (QM) calculations, **molecular mechanics** (MM) using all-atom empirical force fields (chapter 4), and **coarse-grained** methods. The choice depends on the goal of the corresponding study.

On the one hand, QM based ab-initio and semi-empirical methods describe the system by its electronic structure and provide a high level of accuracy by solving the time dependent Schrödinger equation by the laws of quantum chemistry. But, on the other hand, they are computational demanding, so that the treated system size and the simulations time are strongly limited to several hundreds of particles and a few picoseconds.

In contrast to these methods, classical MD simulations based on Molecular Mechanics (chapter 4) are a comparable crude method that does not take the distribution of the electrons into account. However, this exclusion allows the treatment of larger systems, such as biomolecules, and enables longer trajectories on the nanosecond time scale.

Beside quantum mechanics and classical dynamics, coarse-grained methods, such as MARTINI sampling, exist. These methods apply further restrictions or simplifications to the system and treat groups of atoms as single particles. These techniques considerably reduce the number of the degrees of freedom. By doing so, they allow longer trajectories and a better sampling of the conformational space [145–147]. Application of such techniques on membrane complexes has been reviewed for example by Ash and coworkers [148].

For this work dealing with the interaction of huge biomolecules with surfaces or biological devices, where the dynamics of single atoms is of interest, classical MD simulations are an excellent trade-off between accuracy and computational demands. With today's computers, adsorption simulations of several hundreds of nanoseconds (ns) up to milliseconds (ms) are possible. These calculations give insights into the molecular behaviour and stability of the complete enzymes by solving Newton's equations of motion for all atoms of the system.

5.1 Classical mechanics

Classical dynamics treats the evolution of an N -body problem over time.

In this procedure, the potential energy function (section 4.1) is applied in each time step to determine the force F_i acting on a mass particle i ($i = 1 \dots N$). By means of Newton's equation of motion, the new atom coordinates are reassigned

$$F_i = m_i a_i = m_i \frac{dv_i}{dt} = m_i \frac{d^2 r_i}{dt^2} \quad (5.1)$$

In this equation, the force F_i is the product of the mass m and acceleration a of particle i , which is denoted as the first and second derivative of the velocity v_i and the coordinates r_i over time t , respectively. Furthermore, F_i is defined as the negative gradient of the potential energy V calculated by the force field.

$$F_i = -\nabla_i V \quad (5.2)$$

Taken together, these two relations describe the derivative of the potential energy as a function of the coordinate changes over time.

$$-\frac{dV}{dr_i} = m_i \frac{d^2 r_i}{dt^2} \quad (5.3)$$

With this equation, the trajectory of a particle i can be determined by its initial coordinates r_i , its initial velocity v_i and its initial acceleration a_i . The coordinates r_i and the acceleration a_i can be obtained from a crystallographic structure for example and from the derivative of the potential energy of the system, respectively. The initial distribution of the velocities $p(v_i)$ has to be estimated. This estimation of $p(v_i)$ plays a crucial role, because the entire dynamics of the system is deterministic and, therefore, dependent on the initial condition. The initial random guess for the velocities along one coordinate is often performed by the Maxwell-Boltzmann distribution at a given temperature T .

$$p(v_i) = \sqrt{\frac{m_i}{2\pi k_B T}} \exp\left(-\frac{1}{2} \frac{m_i v_i^2}{k_B T}\right) \quad (5.4)$$

In this equation, k_B denotes the Boltzmann constant.

5.2 Stochastic dynamics

An extension to classical dynamics is stochastic dynamics. This **stochastic Langevin dynamics** adds two additional terms to the equations of motion (equation 5.3), namely, a **friction** ζ_i and a **stochastic random term** R_i (section 4.3.4).

$$\frac{d^2 r_i}{dt^2} = \frac{F_i}{m_i} + \frac{R_i}{m_i} - \zeta_i \frac{dr_i}{dt} \quad (5.5)$$

This addition does not interfere with the energy conservation of the system, because the stochastic force R_i adds and the friction ζ_i removes kinetic energy (E_{kin}) from the system. The energy conservation is enabled by coupling R_i to an external bath as described in section 5.4.1.

$$R_i^2 = 6m_i \zeta_i k_B T_{bath} \quad (5.6)$$

5.3 Propagation over time

For the integration over time of the potential energy, no analytical solution exists. This is an outcome of the complexity of this function, which is dependent on all $3N$ particle coordinates in space. Due to this fact, a numerical solution for this problem is needed. Such an algorithm has to fulfil a couple of requirements. It has to be computationally effective, it has to offer a high precision and stability, the momentum and the total energy have to be conserved, it has to be time reversible and symplectic,

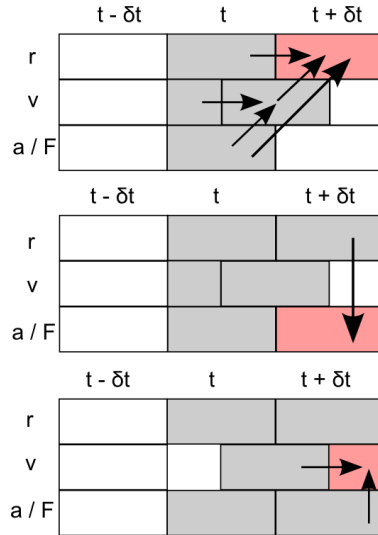


Figure 5.1: Scheme of the velocity verlet algorithms. The velocity scheme, as it is used in NAMD, is a three step procedure to solve the equations of motion.

which means it has to conserve the density of the phase space over time, and it has to grant a reasonable integration time step for application.

A couple of similar algorithms satisfying these criteria exists, e.g. the Verlet [142], the velocity Verlet [149], the Leap-frog [150], and the Beeman algorithms [151]. The calculations in this work were carried out with NAMD [152], which is supporting the **velocity Verlet** method [142, 149] for integration.

The velocity Verlet scheme is comparable to the other methods in terms of computational demands and provides a high level of accuracy, which is not granted in explicit Euler or semi-implicit Euler methods [153]. An advantage compared to the strongly related Leap-frog algorithms is that the velocities and coordinates are determined at the same time t . By taking the velocities explicitly into account (figure 5.1), it solves the first step problem, which is present in the normal Verlet scheme.

$$r(t + \delta t) = r(t) + v(t)\delta t + \frac{1}{2}a(t)\delta t^2 \quad (5.7)$$

$$v(t + \delta t) = v(t) + \frac{1}{2}[a(t) + a(t + \delta t)]\delta t \quad (5.8)$$

In each step, the acceleration is gained by the derivative of the potential energy by using $r(t + \delta t)$. The procedure is spanned by a three step scheme and not a four step scheme as it is used by the Leap-frog method [150].

1. Calculate $r(t + \delta t)$
2. Derive $a(t + \delta t)$ from potential energy using $r(t + \delta t)$
3. Determine $v(t + \delta t)$

The Beeman algorithms [151] is closely related to the velocity Verlet method, but it monitors a slight smaller error in the energy calculation which is connected with additional computational costs.

5.4 Ensemble theory

A typical simulation box of a macromolecular system contains more than 10^5 single particles with different microscopic states. Each microscopic state is assigned by its coordinates in the multidimensional phase space. In other words, the microscopic state of an atom is defined by its position r and its velocity v (or momentum $p_x = mv$). To obtain the thermodynamic state of a system, a set of macroscopic observables (e.g. temperature, internal energy, volume, or pressure) has to be determined. This data, which can be derived by experiments, is defined in terms of **ensemble averages** of N microscopic states. To gain the information of the multidimensional phase space, **statistical mechanics** is required. In statistical mechanics, the average of an observable is defined by ensemble averages [154].

$$\langle O \rangle_{ensemble} = \int \int dp_x^N dr^N O(p_x^N, r^N) P(p_x^N, r^N) \quad (5.9)$$

In equation 5.9, r denotes the atom position, p_x the atom momentum and $O(p_x^N, r^N)$ the observable of interest. The momentum p_x can be determined by the velocity v and the mass m of the particle $p_x \equiv mv$. $P(p_x^N, r^N)$ defines the probability density of the ensemble and is dependent on the Boltzmann constant k_B , the Hamiltonian H and a partition function f .

The procedure of calculating ensemble averages is computational expensive and, therefore, the axiom based **ergodic hypothesis** is used in MD simulation for the determination of averages. The ergodic hypothesis assumes that the ensemble average $\langle O \rangle_{ensemble}$ equals the time average of the observable $\langle O \rangle_{time}$.

$$\langle O \rangle_{ensemble} = \langle O \rangle_{time} \quad (5.10)$$

The fulfilment of this statement requires a large enough sampling of conformations to obtain a set of all possible states. The time average at time t is calculated over steps of Δt .

$$\langle O \rangle_{time} = \lim_{\Delta t \rightarrow \infty} \frac{1}{\Delta t} \int_{t=0}^{\Delta t} O(p^N(t), r^N(t)) dt \approx \frac{1}{n} \sum_{t=1}^n O(p^N, r^N) \quad (5.11)$$

Frequently used ensembles defined by all different microscopic states forming one thermodynamic state are the

- NVE ensemble - the microcanonical ensemble
- NVT ensemble - the canonical ensemble
- NPT ensemble - the isobaric isothermal ensemble
- ι VT ensemble - the grand canonical ensemble

where N is the number of particles, V the volume, E the energy, T the temperature and ι the chemical potential.

For atomistic MD simulations treating large biomolecules the grand canonical and the microcanonical ensembles are not very suitable. In the grand canonical ensemble, N varies during a simulation to maintain the defined chemical potential ι . This discontinuity in N is very difficult to manage in MD simulations, but can easier be realized in Monte Carlo simulations. The disadvantages of the microcanonical ensemble are its lacking external control mechanisms. Thus, fluctuations and drifts in the energy induced by numerical inaccuracies are observed in this ensemble.

More suitable for MD simulations are the NVT and NPT ensembles that reflect experimental conditions very well. One advantage of these ensembles is that T and p can be described independently. Methods for temperature and pressure control [155] are briefly outlined in sections 5.4.1 and 5.4.2.

5.4.1 Temperature control

System variables, such as the temperature T and the pressure p , can be maintained by different approaches.

The easiest way to control the temperature T of a system is to forbid fluctuations and **rescale the velocities** of all particles according to a fixed reference temperature. This method is not used in MD simulations, because it could lead to errors in the dynamics and does not agree with statistical ensemble theory. These observations result from the difference between the temperature used to solve the equations of motion and the fixed reference temperature.

Instead, the temperature is often scaled by coupling processes. The main idea in this temperature control process is to modify the equations of motion by a controllable first order temperature relaxation parameter τ that describes the weak-coupling to an external bath with the temperature T_{bath} . This technique is known as Berendsen thermostat [156].

$$\frac{dT(t)}{dt} = \frac{1}{\tau} (T_{bath} - T(t)) \quad (5.12)$$

The temperature T of a system is defined by the intrinsic kinetic energy E_{kin} , which is given by the equipartition theorem

$$E_{kin}(t) = \sum_{atoms} \frac{1}{2} m v(t)^2 = \frac{3}{2} N k_B T(t) \quad (5.13)$$

Here, m is the mass, v the velocity, N the number of degrees of freedom and k_B the Boltzmann constant. Scaling according to the desired temperature T_{bath} is achieved by rescaling the velocities v of all atoms in the system by a velocity rescaling factor λ_T that allows the calculation of ΔE_{kin} , the change in the kinetic energy.

$$\Delta E_{kin} = (\lambda_T^2 - 1) \frac{3}{2} N k_B T(t) \quad (5.14)$$

This change in E_{kin} leads to a temperature change ΔT , which is dependent on the change of the thermal capacity c_v per degree of freedom of the system. Possibly, c_v is not exactly determinable in the system. Nevertheless, this fact does not affect the dynamics, because the temperature relaxation factor τ is controllable.

$$\Delta T = \frac{1}{N c_v} \Delta E_{kin} \quad (5.15)$$

Combination of the equations 5.12– 5.15 leads finally to the velocity rescaling factor λ_T .

$$\lambda_T = \sqrt{1 + c_v \frac{2}{3 k_B} \frac{\Delta t}{\tau} \left(\frac{T_{bath}}{T(t)} - 1 \right)} \quad (5.16)$$

5.4.2 Pressure control

The pressure control in a many particle system can be handled analogous to the temperature control. Instead of adjusting the velocities v , as it is done in temperature coupling, the **coordinates of the**

particles r are modified in the pressure control procedure. In the weak-coupling routine [156, 157], the actual pressure is scaled by a parameter τ_p to a reference pressure p_{ref} .

$$\frac{dp(t)}{dt} = \frac{1}{\tau_p} (p_{ref} - p(t)) \quad (5.17)$$

Furthermore, the changes in the cell volume V are determined by a factor λ_p .

$$\Delta V = (\lambda_p^3 - 1) V \quad (5.18)$$

Taking the isothermic compressibility β of the system, which is given by

$$\beta = -\frac{1}{V} \left(\frac{\delta V}{\delta p} \right)_T \quad (5.19)$$

or

$$\Delta p = -\frac{\Delta V}{(\beta V)}, \quad (5.20)$$

and the equations 5.17 and 5.18, into account, the following term for λ_p , the rescaling factor for the cell volume V , is obtained.

$$\lambda_p = \sqrt[3]{1 - \beta \frac{\Delta t}{\tau_p} (p_{ref} - p)} \quad (5.21)$$

Changes in V indirectly affect the pressure p of the cell, as described by the ideal gas law $pV = nR_c T$, where R_c and n denote for the universal gas constant and the number of moles, respectively. With the factor λ_p it is possible to adjust p by scaling the coordinates r of the system in the virial theorem.

$$p = \frac{1}{V} \left(N_{DF} k_B T - \frac{1}{3} \sum_{i=1} \sum_{j=i+1} s_{ij} F_{ij} \right) \quad (5.22)$$

In this equation, N_{DF} denotes the number of degrees of freedom, k_B the Boltzmann constant, F_{ij} the force and s_{ij} the distance between atom i and j .

Beside the weak-coupling, other options for temperature and pressure control exist. In contrast to various coupling algorithms, the Nosé-Hoover thermostat adds an additional stochastic friction term to the equations of motions (equation 5.1) [158]. In this method, coupling of the system with the external heat bath is controlled by the Langevin dynamics (see equation 4.10) [159]. Therefore, the algorithm is called Nosé-Hoover Langevin piston method.

$$\frac{dp}{dt} = \sum_{i=1} \sum_{j=i+1} r_{ij} F_{ij} - \frac{\zeta}{Q} p(t) \quad (5.23)$$

In this equation, the heat-bath-mass Q is approximated as $Nk_B T$ and the friction coefficient ζ is given by.

$$\frac{\Delta \zeta}{dt} = \sum_i \frac{1}{2} m_i v_i^2 - \frac{3}{2} N k_B T \quad (5.24)$$

Equation 5.23 allows the rescaling of the equations of motion as it is done in NAMD [152].

5.5 Restrained or steered molecular dynamics simulations

The high demand of computational time required for MD simulations leads to a limited simulation time and an incomplete sampling of the phase space [160, 161]. For example, very rare transitions between different equilibria restricted by energy barriers cannot be simulated on these short time scales. Therefore, **steered molecular dynamics** (SMD) is a useful tool to enhance the sampling along a certain reaction coordinate [162, 163]. This includes large domain motions [164], docking of a ligand into a binding pocket [165] or folding and unfolding events [166, 167].

Another way to save computational time is restraining the system by applying artificial external forces to a subset of atoms. In the following, three methods, namely, fixed, restrained, and steered MD simulations are described in more detail.

By **fixing atoms** to their position, the corresponding degrees of freedom (rotation and translation) are just removed from the simulation. The disadvantage of this technique is the possible bias in the dynamics induced by reducing the number of degrees of freedom N_{DF} .

In **restrained simulations**, the motion of a particle is controlled by linking it to a reference point r_0 . The underlying constraining force is described by a harmonic potential E_{CON} defined by a force constant k_{CON} and the distance between current position r and reference point r_0 .

$$E_{CON} = \frac{1}{2}k_{CON}(r - r_0)^2 \quad (5.25)$$

In contrast to harmonic position constraints, **steered molecular dynamics** pull the centre of mass (COM) of a selection along a defined direction \vec{n} . The harmonic pulling speed v_{SMD} and direction \vec{n} for the dummy atom have to be given as input.

$$E_{SMD}(\vec{r}_1, \vec{r}_2 \dots t) = \frac{1}{2}k \left[v_{SMD}t - \left(\vec{r}_{COM}(t) - \vec{r}_{COM}(0) \right) \vec{n} \right]^2 \quad (5.26)$$

$\vec{r}_{COM}(0)$ and $\vec{r}(t)$ denote the initial and the current COM of the atom selection and t is defined as $t \equiv N_{ts}dt$, where N_{ts} labels the elapsed number of dt large time steps.

Another way to save computational time in classical MD simulations is freezing the bonds to **hydrogen atoms**. The X-H stretching is located between 1 and 2 fs and is limiting the applied time step to 1 fs. Freezing these bonds offers the possibility to enlarge the time step to 2 fs, which is saving a lot of computational resources. A couple of similar algorithms, such as the SHAKE [168], RATTLE [169] or SETTLE [170] algorithms, enable this bond fixing.

Additional to these restrictions, several **water models** have been developed to save additional computer time. For example, the TIP3P model [171] treats the water molecules as rigid bodies removing their internal coordinates from the system. This is drastically affecting the simulation time, because water constitutes a large fraction of a biological system.

5.6 Typical protocol of a classical MD simulation

The typical MD simulation protocol is shown in figure 5.2. The first step deals with the initial coordinates of a molecule. This starting state or geometry is often extracted from crystallographic structures deposited in the protein database [172]. If this structural information is lacking, models

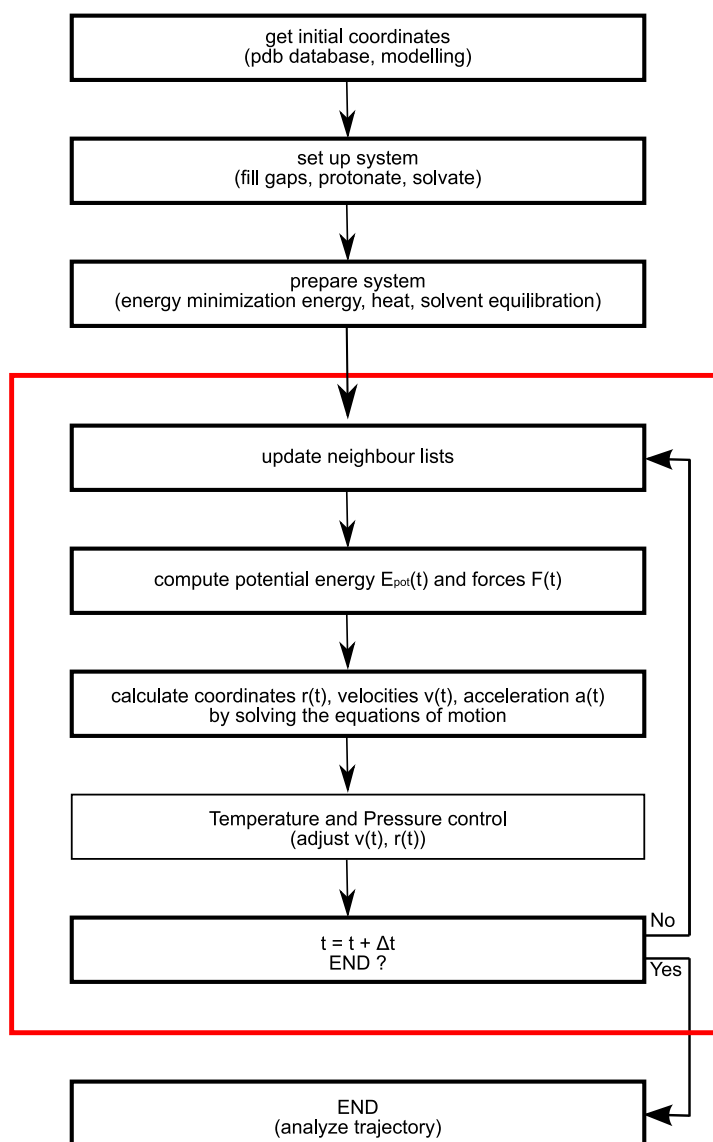


Figure 5.2: Schematic structure of an MD simulation.

have to be developed (chapter 6). After extracting the initial geometry, incomplete regions, such as possible gaps in the structure or missing atoms, have to be inserted. Structures resolved by X-ray often lack hydrogen atoms, because their detection is extremely difficult with this technique. Therefore, the structure has to be protonated. Often, conditions around pH 7.0 are chosen, where histidine residues exhibit changes in the protonation according to their environment. In this context, the pK_a value prediction tool PROPKA [173, 174] is very useful to determine the configuration of amino acids in the system.

Before starting the molecular dynamics run, also called production run, the solvated model has to be prepared carefully by an **energy minimization**. This step is necessary to clean possible steric instabilities in the structure. In particular, badly resolved or lacking regions might be affected by poorly defined coordinates. The minimization is performed at $T = 0$ K and searches a global minimum in the potential energy landscape. This sampling is a complex procedure and can be performed on different levels by various algorithms. The simplest method is called the *steepest decent* [175]

and follows the gradient of the potential energy. The integrator is very effective, but has problems to detect the global minimum. Another disadvantage of this first-order algorithm is the efficiency around a minimum, where the energy landscape is characterized by a very small gradient. An extension of the *steepest descend* algorithm is the *conjugate gradient* method [176], where additionally to the search along the energy landscape gradient another orthogonal component is used. By doing so, it is possible to jump over energy barriers, which is not feasible in the *steepest gradient* routine. After the energy minimization, the system has to be **heated** to the desired temperature. During this step, it is not unusual to add artificial restraining forces (section 5.5) to stabilize the protein structure, because the added thermal energy is significantly increasing the velocities of the particles. In the following **solvent equilibration**, the hydration of the biomolecule and other components in the simulation cell is performed.

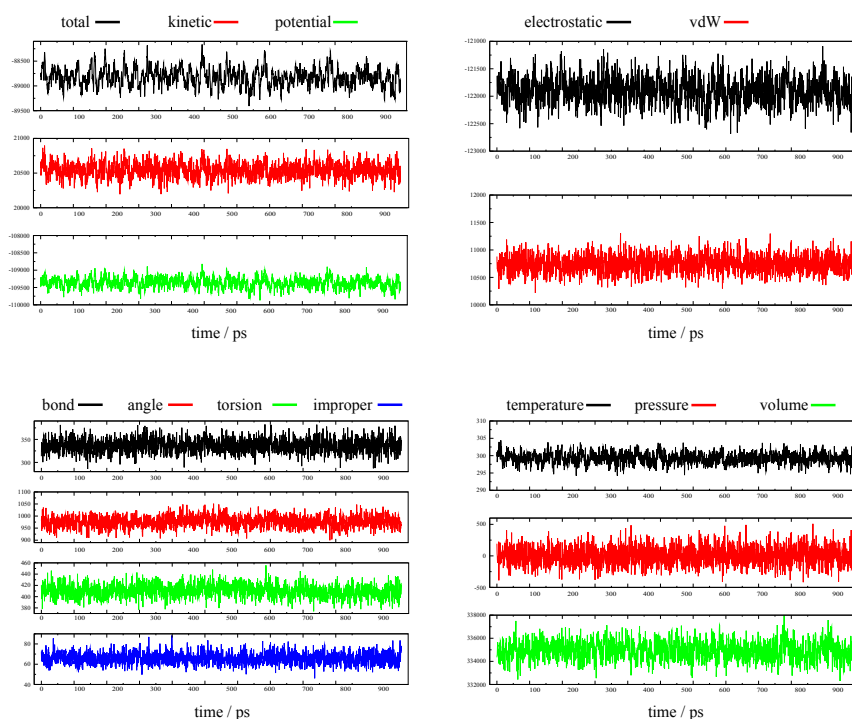


Figure 5.3: Typical evolution of selected observables during an atomistic MD simulation. The example on oxidized human cytochrome *c* [177] demonstrates the conservation of the energy, the temperature and the pressure in an NPT ensemble. The absolute energy values are not essential for this qualitative analysis.

After these preparation steps, the system is configured for the **production dynamics** as shown in figure 5.2 (red box). At first, the neighbour lists for the vdW and short-ranged electrostatics have to be updated (section 4.4.1). With this information, the computation of the potential energy and the forces at this time t follows as described in section 4.2. In the next two steps, the system is updated by applying the equation of motion (section 5.3) and the temperature (section 5.4.1) and pressure control (section 5.4.2). After deriving the new internal coordinates this procedure has to be resumed until the desired simulation time is reached by steps of Δt .

5.7 General output of classical MD simulations

The main output of classical MD simulations is the trajectory describing the time dependent evolution of all particles in the system. Besides these details about the dynamics, the evolution of macroscopic observables, such as energy, temperature, pressure and volume of the system are given in the output. A typical behaviour of these parameters is shown in figure 5.3.

Additionally to this standard output, details of the dynamics and the system can be obtained by post-processing of the gained coordinates in the trajectories. For example, distances, angles and interaction energies can be calculated and analysed by VMD scripting and plug-ins. More details are given in the following chapter 7.

The typical evolution over time shown in figure 5.3 is characterized by a high stability with a certain oscillation of the observables. This behaviour reflects the underlying algorithm adjusting the parameters to the desired values.

6 Molecular Modelling

6.1 Homology Modelling

Homology modelling is a concept for deriving a structural model for a *target*, a protein without known 3D structure, by knowledge of already resolved structures. In this method, a set of *templates*, strongly homologous experimentally determined 3D structures, and a sequence alignment between *templates* and *target* are the requirements for a successful modelling. Under the widely accepted assumption that sequence correlates with structure [178], a high sequence similarity between *template* and *targets* is the basis for a good and reasonable homology model for a biomolecule. Moreover, structures of homologous proteins are usually stronger conserved than their sequences during evolution [179–182], which underlines the qualification of this method.

The modelling procedure by homology is divided into three steps. At first, an adequate three-dimensional *template* structure or a set of *templates* structures with a preferably high sequence identity to the *target* have to be identified. The obtained sequence alignment constitutes the basis for the second step, the model construction, where critical and important regions have to be treated carefully and require special attention. For example, binding sites, active centres, and cofactors have to be structurally conserved and embedded reasonably in the protein environment. Often this is done by applying spatial restraints. In the last step, the obtained models have to be analysed, verified and, when necessary, optimized. Frequently, loop regions at the protein surface monitor discrepancies between model and *targets* and are, therefore, energy minimized by fixing the rest of the model. Additionally, the torsions of the protein backbone have to be checked by Ramachandran plot analysis [183, 184] or comparable techniques.

Here, the Modeller package (version 9.5) [185] has been used to construct the homology model of the MBH (chapter 10.4).

6.2 De Novo Modelling

Tertiary structure prediction of biomolecules by only knowing the amino acid sequence is a difficult and computational demanding task. Nevertheless, the so-called **de Novo design** or modelling of an unknown structure, called the *target*, is in many cases the only possibility to get a three-dimensional model. With this procedure, it is possible to derive 3D structures of totally unknown biomolecules or building blocks lacking a reasonable *template*.

Most methods for deriving a tertiary structure by its sequence are searching the global free energy minimum by sampling many possible structures. This approach is based on the assumption that the native protein structure is close to the global energy minimum [186]. The evaluation of the derived structures is performed by energy and statistical criteria, similar to those used in protein folding research.

Such calculations are extremely computational demanding and require an adequate potential for the

energy calculations, a fast algorithm for sampling the energy landscape, and a suitable scoring procedure [187]. One comparable fast routine is the Robetta program [188], which predicts the tertiary structure, when sequence comparison does not lead to a reasonable *template* for homology modelling. For the de Novo modelling process, secondary structure prediction tools, such as PsiPred [189] or SAM [190], give very useful information.

PsiPred is a computational effective three level prediction method using the primary structure as input. In a first step of the routine, position specific scoring matrices created by the very robust and fast PSI-Blast search algorithm [191] are used to identify similar sequences. Then in a second and third step, these results are filtered in a two layer neural network to predict the secondary structure of the *target*.

The SAM algorithm uses a different procedure to identify similar sequences and to predict the secondary structure. In this algorithm, homologous or similar sequences are searched and clustered in two data sets by Wu-BLASTP (W. Gish, 1996-2003 <http://blast.wustl.edu>). In the following, these sequence sets are multiple aligned and used to define and to train a Hidden Markov model (HMM). This HMM is then used in a second step for the database search and for the structure prediction.

7 Data analysis

The analysis of protein properties is helpful for the planning and evaluation of MD simulations. Often an efficient immobilization is dependent on the electrostatic interactions between adsorbant and surface. Thus, the determinations of the dipole moment (section 7.1) and the electrostatic surface potential (section 7.2) of biomolecules help finding a favourable initial placing on the surface. The interest in the initial conditions is based on the fact that large reorientations of biomolecules on surfaces exhaust the computational power and are, therefore, hardly affordable. Complementary to these calculations, an interaction energy (section 7.3) sampling between the biomolecule in different orientations and the corresponding surface could be performed. This approach takes, additionally to the electrostatics, van der Waals forces into account and provides information of energetically favourable initial scenarios. Such a sampling, however, requires specific knowledge of the surface and is computational more complex.

The evaluation of classical MD simulations takes the system and protein stabilities into account. System stability is probed by analysing the temporal evolution of conserved quantities, such as temperature and energy (figure 5.3). The overall protein stability is described by the evolution of the root mean square deviation (section 7.4) and the radius of gyration (section 7.6). The root-mean square fluctuation (section 7.5) offers details about the structural fluctuations of single residues within the biomolecule.

Additionally, structural post-MD analysis provides, *inter alia*, information about electron transfer pathways (section 7.7) and adsorption strength in terms of interaction energy (section 7.3).

7.1 Dipole moment

The overall dipole moment of a protein gives information of the separation of positive and negative charges. It is dependent on the distances r_i and partial charges q_i of the atoms. r_i is defined as the distance to a reference point and the partial charges are set according to the used force field. The reference point is assigned by the COM or the centre of geometry (COG) of the protein. Here, the centre of mass was utilized taking the mass m_i of atom i , the total mass of the protein M and the coordinates r_i of particle i into account.

$$r_{COM} = \frac{1}{M} \sum_{atoms} m_i r_i \quad (7.1)$$

With this definition, the dipole moment μ can be calculated as follows.

$$\mu = \sum_i q_i (r_i - r_{COM}) \quad (7.2)$$

7.2 Electrostatic surface potential

Electrostatic properties are important factors for describing molecular interactions. Particularly, enzyme-surface interactions or docking procedures are often driven by electrostatic attraction. In surface science, surface modifications are frequently used to enable the desired interaction. A well established approach to calculate electrostatic properties of biomolecules is based on the Poisson or Poisson-Boltzmann equation. In the continuum model APBS [70], the macromolecule is modelled by a low dielectric constant, while the solvent is described with a high dielectric. In the Poisson equation, the electrostatic potential ϕ is dependent on the charge density ρ and the dielectric constant η .

$$\nabla \cdot \eta(r) \nabla \phi(r) = -4\pi\rho(r) \quad (7.3)$$

where ∇ abbreviates for $(\frac{\delta}{\delta x} + \frac{\delta}{\delta y} + \frac{\delta}{\delta z})$. This relationship can easily be reduced to the Coulombic Law by assuming simple point charges and a constant dielectric instead of a position dependent dielectricum. The insertion of mobile ions into the electric field of the biomolecule requires an additional term for characterizing the distribution of the ions. Due to this incorporation of a Boltzmann distributed ion environment one obtains the Poisson-Boltzmann equation.

$$\nabla \cdot \eta(r) \nabla \phi(r) - \kappa'(r) = -4\pi\rho(r) \quad (7.4)$$

The Boltzmann term κ' is defined as

$$\frac{\kappa'^2}{\epsilon} = \frac{8\pi N_A e^2 I}{10^3 \eta k_B T} \quad (7.5)$$

where N_A , e , η and I denote for the Avogadro number, the charge of an electron, the dielectric constant and ionic strength, respectively.

In the APBS program, the Poisson-Boltzmann equation is solved by the `finite element toolkit` (FEtk) [192, 193].

7.3 Interaction energy

The interaction energy E_{int} between two interaction partners A and B is a good indicator whether these two substances attract or repel each other. In this work, the interaction energy between inorganic surfaces or biological devices and the adsorbates of interest, e.g. biomolecules, is analysed. The calculation is performed by evaluation of the self-energies E_A and E_B of the two interacting partners A and B, which are subtracted from the overall self-energy E_{AB} .

$$E_{int} = E_{AB} - E_A - E_B \quad (7.6)$$

Moreover, one has to note that the interaction energy between surface and adsorbing biomolecule is composed of non-binding terms only, because breaking and formation of covalent bonds is not allowed in MD simulation. The self-energies are determined according to the used force field (here: the CHARMM force field). For this purpose, the VMD plug-in NAMDEnergy has been used.

The calculation of interaction energies is helpful for planning and analysing MD simulations. They

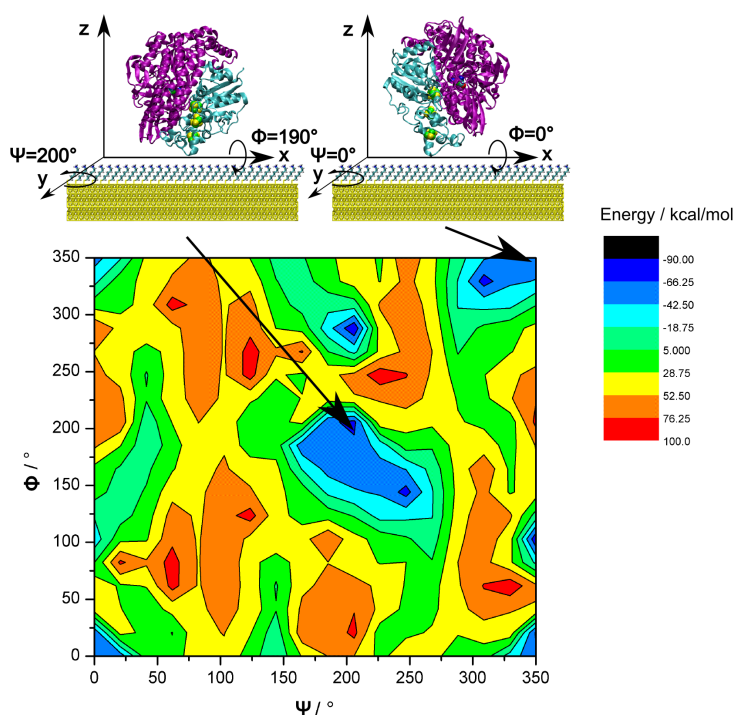


Figure 7.1: Example of an interaction energy sampling between adsorbate and surface. The figure shows the energy landscape between an amino-terminated SAM coating a gold electrode and the standard hydrogenase of *D. gigas* [80] in different orientation. The figure is reprinted from the Langmuir publication discussed in section 10.5 [194]. Additionally, the energetically most favourable orientations are visualized above the diagram. (Reprinted with permission from *Langmuir* (2013), 29 (2): 673–682. Copyright 2013 American Chemical Society.)

are suitable to describe the interaction strength between two partners, but can also be used for sampling of the energy landscape. This sampling procedure is performed to identify most favourable initial orientations of the adsorbates with respect to the surface. For all conformations that are obtained by rotating the enzyme systematically along the surface dimensions, the interaction energy is evaluated and energetically most favourable regions in the energy landscape are identified (chapters 10.5 and 10.6). An example is shown in figure 7.1.

7.4 Root mean square deviation

The root mean square deviation (*rmsd*) is a measure for protein stability. It compares two conformations of n atoms at different times of the trajectory. Usually, the initial structure is aligned to the coordinates of conformations obtained during the simulation.

$$rmsd = \sqrt{\frac{1}{N} \sum_i (r_{k,i} - r_{l,i})^2} \quad (7.7)$$

The difference between two frames k and l of the trajectory is the square root of the sum of the squared displacements of all atoms i , which are normalized by the total number of atoms N . This average value increases with decreasing stability. While the *rmsd* of all atoms displays the motion of

the protein side chains, the *rmsd* of the backbone atoms is a useful measure to investigate the stability of secondary structure elements.

7.5 Root mean square fluctuation

The root mean square fluctuation (*rmsf*) monitors, in contrast to the *rmsd*, the fluctuation of a single atom over time. At each time frame i the position difference between the current position r and the reference value r_{ref} is evaluated and averaged over the total time t_{tot} . The *rmsf* displays the mobility of an atom of interest and a screening over the entire protein indicates flexible regions within the protein. As reference value for the determination of the *rmsf* the average position or the starting position are used. In order to obtain the fluctuation strength and to discard protein translation and rotation an averaged value gives the best results.

$$rmsf = \frac{1}{t_{tot}} \sqrt{\sum_i (r(i) - r_{ref})^2} \quad (7.8)$$

7.6 Radius of gyration

The radius of gyration *radgyr* is a measure for the shape of a protein.

$$radgyr = \sqrt{\frac{1}{N} \sum_i (r(i) - r_{ref})^2} \quad (7.9)$$

Here, N , r and r_{ref} are the number of particles, the coordinates and a reference coordinate, respectively. Often the centre of geometry or the centre of mass are taken as reference points.

7.7 Electron transfer

Non-adiabatic ET processes mediated by the protein environment bear a very weak coupling and the corresponding ET rates (k_{ET}) can be evaluated by Marcus theory [195].

$$k_{ET} = \varepsilon = \frac{2\pi}{\hbar} FC |T_{DA}|^2 = \frac{2\pi}{\hbar} \frac{\exp\left(-(\Delta G + \lambda)^2 / 4\lambda_r k_B T\right)}{\sqrt{4\pi\lambda k_B T}} |T_{DA}|^2 \quad (7.10)$$

In equation 7.10, FC and T_{DA} abbreviate the Franck-Condon factor and the electronic coupling or tunnelling matrix between the donor D and the acceptor A , respectively. Furthermore, ΔG stands for the driving force and λ_r for the reorganization energy. The terms \hbar , k_B and T denote for the Planck constant, the Boltzmann constant and the temperature, respectively.

In this work, the most favourable electron pathways have been determined by estimating the electronic coupling matrix T_{DA} with the PATHWAYS program developed by Beratan et al. [196, 197]. This model takes only structural properties of given biological geometries into account. It uses the structural information to find the strongest coupling pathway by an effective graph search algorithm [196]. Hereby, three different tunnelling modes are possible, namely, the tunnelling along a covalent bond (CB), a jump mediated by a hydrogen bond (HB) and a through space jump (TS). These three modes are characterized by different penalties and their product is proportional to T_{DA} .

$$T_{DA} \approx \prod_i \sigma_i^{CB} \prod_j \sigma_j^{HB} \prod_h \sigma_h^{TS} \quad (7.11)$$

The decay factors along a covalent bond σ^{CB} , a hydrogen bond σ^{HB} and a through-space jump σ^{TS} are defined as following.

$$\sigma^{CB} = \sigma_i^{CB} = 0.6 \quad (7.12)$$

$$\sigma^{HB} = \sigma_j^{CB} = (\sigma^{CB})^2 \exp(-1.7(s - 2.8)) \quad (7.13)$$

$$\sigma^{TS} = \sigma_h^{TS} = \sigma^{CB} \exp(-1.7(s - 1.4)) \quad (7.14)$$

The included distance s between the corresponding donor and acceptor describes the distance dependence for these tunnelling modes along a hydrogen bond and through space. In this model, the coupling between donor and acceptor and the first and last bonds are neglected.

The computation of T_{DA} allows the approximation of maximal electron transfer rates K_{ET}

$$k_{ET} \approx B |T_{DA}| \quad (7.15)$$

where B denotes a constant pre-factor and can be estimated to be 10^{14} s^{-1} . This value results from assuming that the strongest electronic coupling between a donor and acceptor separated by 3 Å or two covalent bond steps is 10^{13} s^{-1} [198].

8 Computational resources and tools

The computational demanding MD calculations were carried out on the supercomputer cluster of the 'Hoch- und Höchstleistungsrechnen Norddeutschland' (HLRN). A small insight into the supercomputer architecture is shown in figure 8.1.

The use of such a supercomputer is justified by the high computational demand. A typical system including a biomolecule, a surface, and explicit solution contains more than 150.000 atoms. To simulate such a system with 128 CPUs (16 nodes with 8 tasks) in parallel, approximately 0.3 days per nanosecond of simulated time are required. This results in more than two weeks for simulating a 50 ns long trajectory. Additionally to the pure calculation time, waiting times in the queue prolong the simulation procedure. Nevertheless, on single or even multi core CPUs such calculations are not affordable. Besides the required hardware on a supercomputer cluster, a software with excellent parallelization is the basis for using the resources efficiently. **NAMD** in the versions 2.6 and 2.7 was used [152], which fulfilled these requirements.

In the future, two different approaches to speed up MD simulations are coming up. First, the improvement of the NAMD code offers the opportunity to use the computer resources more efficiently. The latest update has been released recently in September 2012. Second, the development of the CUDA technology grants a new perspective to use graphic card processors (GPUs) to run MD simulations. This technique is getting more and more important, because it has the potential to replace the very expensive supercomputer architecture by small and comparable cheap graphic cards.

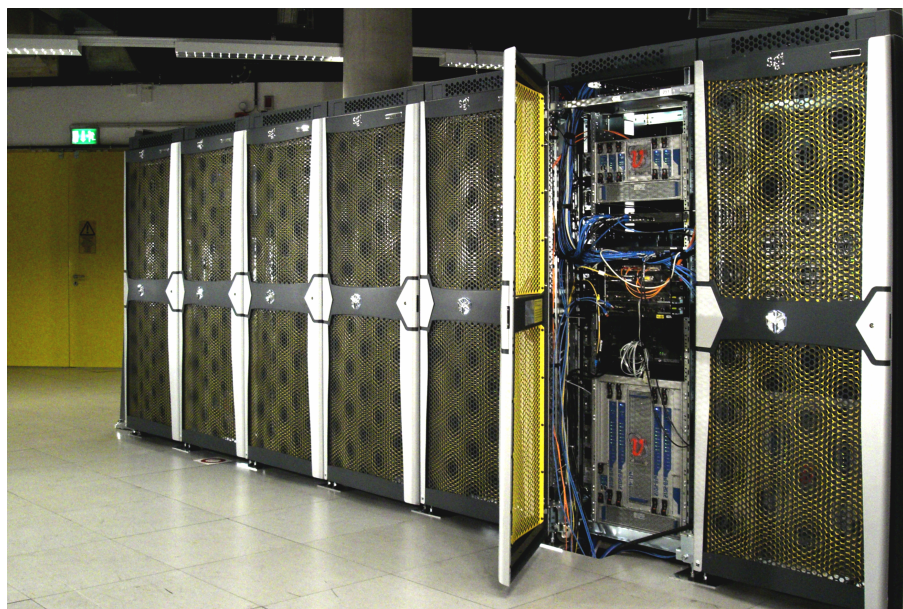


Figure 8.1: Insight into the HLRN supercomputer architecture taken in 2008. The photo has been copied from the HLRN website (www.hlrn.de) and shows a small part of the computer cluster at the Berlin Complex at the Conrad Zuse Institute (ZIB).

9 Supplemental experimental measurements and QM/MM calculations

This chapter briefly describes the experimental work and the calculations done in cooperation. The SEIRA spectroscopy experiments have been performed by Ingo Zebger, Diego Millo and Nina Heidary under the supervision of Peter Hildebrandt and Anna Fischer. The Surface Enhanced Resonance Raman Spectroscopy (SERRS) measurements have been carried out by Murat Sezer and Inez Weidiger in the group of Peter Hildebrandt and the electrophysiology has been done by Kirstin Hobiger in the group of Thomas Friedrich. The QM/MM calculations have been performed by Yvonne Rippers in the group of Maria Andrea Mroginiski.

All these measurements are a complementary counterpart to the theoretical MD simulations and useful to validate the calculated results. On the one hand, information on the atomic level is difficult to obtain by these experimental techniques and has to be allured by theory, but on the other hand, they provide a detailed insight into the macroscopic behaviour of the treated biomolecules, which is limited by the system size in MD simulations. So a combination of both methods offers a complete picture of the system.

The QM/MM calculations describe a system on a higher level of theory and are, therefore, a powerful technique to gain electronic properties and spectra out of snapshots extracted from classical MD simulations. In particular, they are very helpful when modelling metal cofactors.

9.1 Vibrational spectroscopy

Vibrational spectroscopy comprises two complementary techniques, infrared (IR) absorption and Raman spectroscopy [199]. Both methods offer qualitative and quantitative information about the investigated sample structure that can be extracted out of the spectra reflecting the transitions in the molecule.

In **IR spectroscopy**, characteristic molecular vibrations are excited by the absorption of photons. For this purpose, the sample is irradiated with polychromatic light. Photons with an energy required for the transition ($\hbar\nu_k$) from the ground state ($\hbar\nu_f$) to an excited vibrational level ($\hbar\nu_i$) are absorbed and induce the transition. Here, \hbar and ν denote for the Planck constant and the frequency, respectively.

$$\hbar\nu_k = \hbar\nu_f - \hbar\nu_i \quad (9.1)$$

These energies required to induce the transitions are located in the IR regime and, therefore, the absorption of light quanta is named IR spectroscopy. A vibration is IR active if its dipole moment changes during the vibration.

In contrast to IR absorption, **Raman spectroscopy** is based on the weak inelastic scattering of monochromatic light on a sample, called the Raman Effect. Irradiation of a molecule with a laser beam leads to inelastic scattering of photons and results in an energetic change between incident

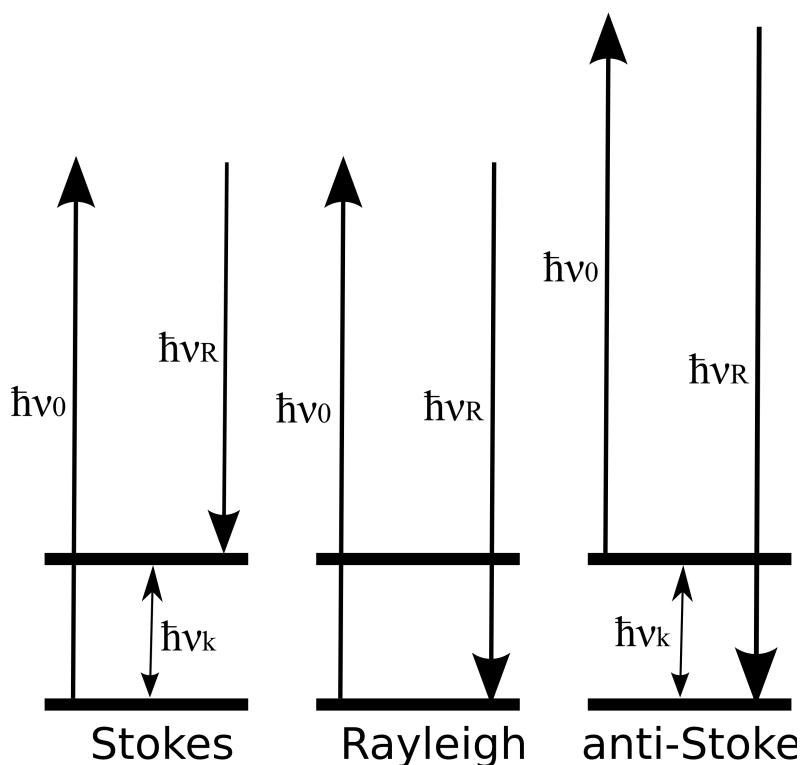


Figure 9.1: Scheme of the energetic transitions in Raman scattering.

($\hbar\nu_0$) and scattered photons ($\hbar\nu_R$). This energy difference corresponds to the energy required for the transition from the ground to an excited state in the molecule.

$$\hbar\nu_0 - \hbar\nu_R = \hbar\nu_f - \hbar\nu_i \quad (9.2)$$

These energy changes with respect to the incident light are named Stokes and anti-Stokes scattering. The elastically scattered light is called Rayleigh scattering (figure 9.1). A vibration is Raman active if it leads to a change in the polarisability during the vibration.

9.2 Surface enhanced vibrational spectroscopy

The discovery of the strong enhancement of several orders of magnitude of the Raman scattering of molecules adsorbed on a rough metal surface was the basis for surface enhanced vibrational spectroscopy. To describe the effect classical electromagnetic theory is applied [200–202]. It states that the coupling between the incident electric field of the light and the plasmons of the metal induces an additional strong electric field normal to the surface (figure 9.2). This field additionally induces and enhances Raman scattering in the near-field. This effect is called **surface enhanced Raman** (SER) effect. The increased sensitivity can further be enhanced when the excitation energy (or frequency) is in resonance with both the surface plasmons and the transitions in the sample. In this way, two phenomena, the resonance Raman Effect and the surface enhancement, are combined. The technique is called **surface enhanced resonance Raman** (SERR) spectroscopy.

The enhancement in **surface enhancement IR absorption** (SEIRA) is much weaker compared to the SERS, but its underlying background is also the classical electromagnetic theory. The incident

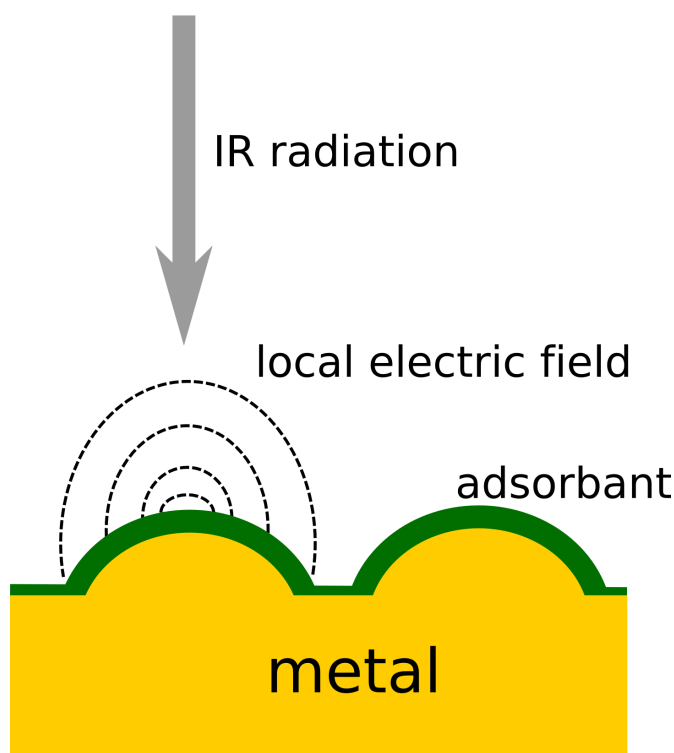


Figure 9.2: Schematic representation of the surface enhancement. The incident light (here: IR radiation) induces a dipole in the metal particles (islands) which then leads to an enhanced oscillating electric field of the same frequency as the excitation. This local electric field in turn induces the transitions in sample which are perpendicular to the rough surface.

polychromatic light induces an oscillating dipole in plasmons of the metal, which strongly increases the electric near-field perpendicular to the surface (figure 9.2). This field enhances the transitions of the modes of the sample that are normal to the surface. The enhancement decreases distance d dependent with $\sim \frac{1}{d^6}$.

Both techniques show the strongest enhancement on nanostructured Ag or Au surfaces. These surfaces are often coated with biological spacers, such as SAMs, to avoid the degradation or denaturation of the biological sample upon contact with the metal surface. This modification weakens the distant dependent enhancement, but is sufficient in a range up to 10 nm of the metals.

9.3 Electrophysiological measurements

Electrophysiology comprises the analysis of electric signals in biological cells. This includes voltage and current flow measurements across biological membranes.

A widely used and well established method is the *Two Electrode Voltage Clamp* technique (TEVC) which enables the recording of electric currents across the plasma membrane at a given potential [203]. The measuring principle of the TEVC is based on the usage of two different electrode pairs. One of these pairs measures the actual membrane potential of the cell (V_m) and compares this one continuously with a desired commando potential (V_{com}). In case V_m and V_{com} are unequal, an electric current is actively injected into the cell over the second electrode pair until V_m is the same as

V_{com} . The current being required to keep V_m at V_{com} is the signal of the TEVC and contains information about the electric conductivity or capacitance of the cell membrane.

In summary, the procedure of the TEVC is suitable to investigate voltage-dependent membrane proteins, such as ion channels or voltage-activated enzymes.

9.4 QM/MM calculations

Hybrid QM/MM calculations are a combination of two methods, accurate quantum-mechanics (QM) and fast molecular mechanics (MM) [204, 205]. In this method, the region of interest, e.g. the active site or reaction centre, is treated at the QM level, while the surrounding sphere is handled with a comparable fast, but crude classical MM force field (figure 9.3). This approach allows an accurate description of the small QM region that is embedded in the charge cloud of the MM area.

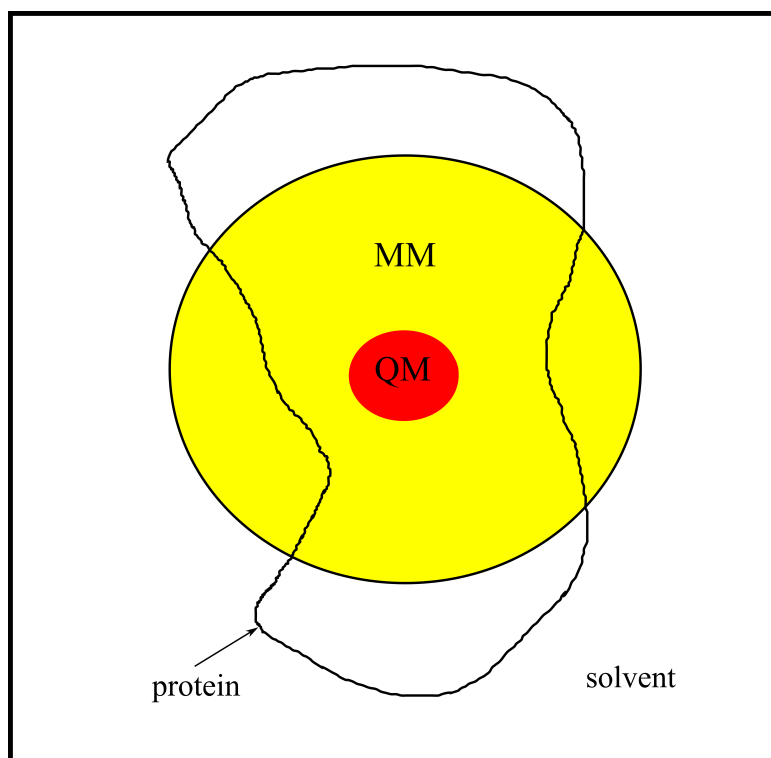


Figure 9.3: Schematic representation of a QM/MM system. The red part indicates the QM region containing the site of interest. This QM sphere is surrounded by a MM treated region. Typically, the QM part contains the active site and important adjacent residues, while the comparable large MM regions includes the large parts of the protein and solvent.

A challenging issue in this context is the coupling between the QM and the MM regions and, in particular, the treatment of covalent bonds between QM- and MM-atoms [205]. Simple addition of the energy terms of the two parts biases the system, because the two regions are strongly coupled with each other. To overcome this problem, different approaches have been developed [206].

A common approach to treat covalent bonds between the QM and MM parts is the insertion of dummy linker atoms [206]. Usually, a hydrogen atom is inserted to fulfil the valence criteria and the bonded terms in the QM and the MM regions, respectively. This atom does not belong to the real system.

Another proceeding is boundary schemes [207, 208]. Here, the MM atom is modified and included in both parts. In the MM region it behaves unchanged, but in the QM sphere it mimics the properties of a residue environment.

A third method is the use of frozen hybrid orbitals to fill the truncated bonds in the QM region [204]. Although further optimization of QM/MM methods is possible, they are a powerful tool to describe a reactive centre with a high accuracy and in a very realistic way.

10 Results

10.1 Molecular Dynamics Simulations of the Adsorption of Bone Morphogenetic Protein-2 on Surfaces with Medical Relevance

Tillmann Utesch, Grazia Daminelli, and Maria Andrea Mroginski

Reprinted with permission from *Langmuir* (2011), 27, 13144-13153

Copyright 2011 American Chemical Society.

Overview

In this study, the adsorption dynamics of BMP-2 on medically relevant graphite and titanium dioxide surfaces was simulated by two approaches. On the one hand, the interaction was modelled by classical MD simulations only. On the other hand, a hybrid approach of SMD and subsequent MD simulations was used to accelerate the adsorption by applying artificial forces. In both scenarios, BMP-2 was initially placed in different orientations on the surface materials to avoid computationally demanding reorientations.

MD and hybrid simulations led to comparable results.

Structurally stable BMP-2 adsorbed weakly and unspecifically on graphite and exhibited a high degree of mobility on the surface. As expected, BMP-2 showed the most favourable interaction energy and the strongest adsorption when hydrophobic regions of the protein got in contact with the graphite surface.

In contrast to these findings, BMP-2 desorbed from the non-passivated titanium dioxide surface. The desorption process was not directly initiated by the surface, but by the water layer formed on the titanium dioxide. This well-ordered water adlayer or hydration shell stands in strong competition with BMP-2 in adsorbing on the surface and avoided direct contact of BMP-2 with the implant device. This observation demonstrated the importance of explicit water molecules, which were responsible for the adsorption dynamics disagreeing with the initial expectation and *in vacuo* interaction energy calculations.

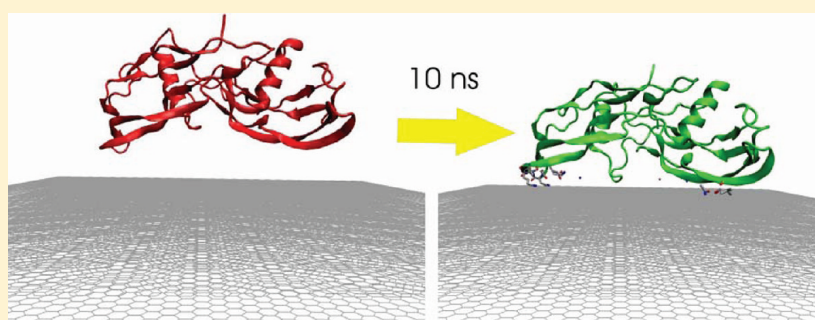
Molecular Dynamics Simulations of the Adsorption of Bone Morphogenetic Protein-2 on Surfaces with Medical Relevance

Tillmann Utesch, Grazia Daminelli, and Maria Andrea Mroginski*

Institut für Chemie, Technische Universität Berlin, Sekr. PC 14, 10623 Berlin, Germany

S Supporting Information

ABSTRACT:



Bone morphogenetic protein-2 (BMP-2) plays a crucial role in osteoblast differentiation and proliferation. Its effective therapeutic use for ectopic bone and cartilage regeneration depends, among other factors, on the interaction with the carrier at the implant site. In this study, we used classical molecular dynamics (MD) and a hybrid approach of steered molecular dynamics (SMD) combined with MD simulations to investigate the initial stages of the adsorption of BMP-2 when approaching two implant surfaces, hydrophobic graphite and hydrophilic titanium dioxide rutile. Surface adsorption was evaluated for six different orientations of the protein, two end-on and four side-on, in explicit water environment. On graphite, we observed a weak but stable adsorption. Depending on the initial orientation, hydrophobic patches as well as flexible loops of the protein were involved in the interaction with graphite. On the contrary, BMP-2 adsorbed only loosely to hydrophilic titanium dioxide. Despite a favorable interaction energy between protein and the TiO_2 surface, the rapid formation of a two-layer water structure prevented the direct interaction between protein and titanium dioxide. The first water adlayer had a strong repulsive effect on the protein, while the second attracted the protein toward the surface. For both surfaces, hydrophobic graphite and hydrophilic titanium dioxide, denaturation of BMP-2 induced by adsorption was not observed on the nanosecond time scale.

INTRODUCTION

Adsorption of proteins onto inorganic materials is a key topic in a wide range of fields, such as biomaterials, biochemistry, biophysics, and biomedicine.^{1,2} The specific properties of the surface govern the final conformation and activity of the adsorbed protein. If the biological response of the protein can be preserved, the surface may acquire new functionalities, as aimed in regenerative medicine and tissue engineering, where, for example, orthopedic and dental implants are treated with bone morphogenetic proteins to improve osteointegration.^{3–10}

One promising osteoinductive protein is bone morphogenetic protein-2 (BMP-2), a dimeric cysteine knot protein, which plays an important role in bone and cartilage formation in embryonic development and adult tissue in human¹¹ and in increasing the biocompatibility of implants.⁷ BMP-2 acts locally, inducing osteoblast formation ectopically. Therefore, a stable adsorption of BMP-2 onto implant surfaces is required to induce bone growth at the implant site, but not in other organs. At the same time, the protein

must be able to interact with its receptors, thus triggering the signal cascade which induces proliferation of osteoblasts. A too strong binding to the inorganic surface may lead to partial denaturation, affecting the activity of the protein. In the functionalization of implant surfaces by BMP-2 adsorption, a trade-off needs to be found between stable adsorption and maintenance of the protein activity.

In the case of BMP-2, the signaling cascade which leads to osteoblast differentiation is triggered by binding of the protein to its type I and type II receptors.^{12–15} BMP-2 binding regions have been characterized by Nickel et al.^{16,17} The binding site of type IA receptor, called wrist epitope, is highly discontinuous and comprises the prehelix loop and helix $\alpha 1$ of one monomer and $\beta 8$ strand with inner loop 1 of the other monomer.^{12,17} The binding site of

Received: July 1, 2011

Revised: August 17, 2011

Published: September 29, 2011

type II serine/threonine receptor kinase, on the other hand, named the knuckle epitope, is settled at each monomer and involves the Asp34 and His39 in the $\beta 3$ and $\beta 4$ strands, respectively, as well as the Ser88 and Leu90 in $\beta 7$ and Leu100 in $\beta 8$.¹⁸

A detailed knowledge of the part of the protein involved in the adsorption to a surface and the understanding of the nature of the protein/surface interaction is crucial for the development of effective BMP-2-functionalized devices. Protein adsorption on a nanosecond to microsecond time scale can be studied at the atomic level using molecular dynamics (MD) simulations. For example, Raffaini et al. simulated the sequential adsorption of proteins and the adsorption of a fibronectin module on hydrophobic graphite and demonstrated the strong interaction with the surface leading to larger structural rearrangements in the protein.^{19,20} Monti et al. studied the adsorption of small peptide building blocks of EAK16 on a titanium dioxide surface with MD simulations and identified the most probable conformations on the small dipeptides.²¹ The initial stages of the adsorption of a hexapeptide onto TiO₂ in aqueous environment were investigated by Skelton et al., who showed how the interaction with the surface was mediated by a water layer at the interface.²² Adsorption/desorption processes of large biomolecular systems are generally too long to be observed within pure MD simulations. Steered molecular dynamics (SMD) simulations were found to improve this limitation. Here, artificial forces are used to pull the system in a specific direction, accelerating the adsorption/desorption process. One special SMD technique is based on constant velocity pulling, where a dummy atom connected via a virtual spring to the SMD atoms is pulled with a constant velocity in the direction of interest. With these external forces, simulations of processes such as the unfolding of proteins,²³ the undocking of ligands out of binding pockets,²⁴ the domain motion in sulfite oxidase,²⁵ or the adsorption of a single chain of BMP-2 on a hydroxyapatite (001) surface²⁶ became possible on computationally accessible time scales.

In our study, we used classical MD simulations and a hybrid approach of SMD combined with MD to investigate the initial stages of the adsorption behavior of BMP-2 on two different surfaces: hydrophobic graphite and hydrophilic titanium dioxide. We chose these two materials, because of their appropriate biomedical properties, their high biocompatibility, and their common application as orthopedic and dental implants.^{27,28} As the surface of titanium quickly passivates when exposed to air,²⁹ we used titanium dioxide instead of titanium as surface material.

Very recently, a couple of papers dealing with MD simulations of BMP-2 were published. Oliveira and co-workers compared the stability of the monomeric and dimeric form of the BMP-2 protein, both in vacuum and in water environment.³⁰ This study showed that the most important factor for stabilizing secondary and tertiary structures of BMP-2 is not dimerization of the protein but the aqueous environment. In addition, they investigated the adsorption of BMP-2 on a surface coated with hydrophobic spacer molecules.³¹ Here they found that the conformation of the protein in both its monomeric and dimeric forms was preserved. Adsorption of the dimer occurred only at one site, leaving most of the BMP-2 surface free to interact with possible cell receptors. Opposite conclusions were arrived at by a MD study of BMP-2 on graphite, which used implicit inviscid (i.e., without Langevin dynamics) water to model the solvent environment.³² The authors of this study observed strong denaturation of the protein upon adsorption of the monomeric form of BMP-2, concluding that interactions with cell receptors might be unlikely.

Our work dealing with the bioactive (dimeric) form of BMP-2, using explicit water to model the environment, and comparing the adsorption patterns of BMP-2 upon approaching hydrophobic and hydrophilic surfaces with different initial conformations extends the range of these studies and contributes to the understanding at the atomic level of the initial stages (nanosecond time frame) of the adsorption process of BMP-2.

MATERIALS AND METHODS

1. Computational Setup. The atomistic MD simulations were performed with NAMD 2.6.³³ All calculations were carried out under periodic boundary conditions in explicit TIP3P water³⁴ with a cutoff distance of 12 Å for van der Waals (vdW) and real space electrostatic interactions. Long-range electrostatics was computed with the particle mesh Ewald summation (PME).³⁵ Rigid bonds to all hydrogen atoms enabled by the SHAKE algorithm allowed a 2 fs time step.³⁶

2. Protein. The initial configuration of the protein was taken from the 1.86 Å resolution X-ray structure 1REW of the PDB database, which contains the complex of BMP-2 with its type IA receptor.³⁷ We extracted the coordinates of the two chains of the BMP-2 homodimer and all crystallographic water molecules, while the receptor molecule was discarded. Coordinates of the first 12 residues of each monomer, corresponding to the N-terminus, are missing. Therefore, our starting protein model consisted in two sequences of 103 residues and 133 crystallographic waters. The system was protonated at pH 7 with the HBUILD routine³⁸ implemented in the CHARMM code.³⁹ Histidine residues were protonated on their $\delta 1$ nitrogen, in accordance with the configuration of their specific environments. Disulfide bonds involved in the three intrachain sulfur bridges on each monomer and one sulfur bridge between Cys78 of the two monomers were defined according to the indications given in the pdb file.³⁷ Finally the whole system was solvated in a 122³ Å³ cubic box of pre-equilibrated TIP3P water.³⁴ The resulting homodimer structure had a total charge of $-8 e$, which was neutralized by adding 24 Na⁺ and 16 Cl⁻. These ions were inserted close to all charged side chains, replacing noncrystallographic water molecules, in order to approximate physiological conditions. The BMP-2 molecule was described using the all-atoms CHARMM27 force field.⁴⁰

The protein was pre-equilibrated in a water box by performing first 10⁴ steps of energy minimization with decreasing restraints—from 50 to 5 kcal/(mol Å²)—on heavy protein atoms. Subsequently, the system was heated for 50 ps with weak restraints [5 kcal/(mol Å²)] on the protein backbone, followed by a 100 ps MD simulation, where the restraints on the protein were released. Finally, the free BMP-2 in water solution was equilibrated for 5 ns. The final equilibrated BMP-2 structure was employed for the later adsorption simulations.

3. Surfaces. We constructed the graphite and the perfect TiO₂ (001) rutile surfaces by duplication of small unit cells, using the lattice parameters $a = 2.4612$ Å and $c = 6.7079$ Å of a hexagonal cell⁴¹ and $a = 4.5936$ Å and $c = 2.9587$ Å of a tetragonal cell,^{41,42} respectively. The graphite unit was built without charge separation. For titanium dioxide, we used partial charges of 2.196 e for 6-fold coordinated titanium and $-1.098 e$ for oxygen surface atoms, according to results of ab initio calculations for bulk atoms of the surface.⁴³ For graphite, we took the nonbinding parameters of benzene included in the CHARMM27 force field⁴⁰ as done previously by Connolly et al.⁴⁴ Whereas for titanium dioxide, the parameter set was obtained by combining average CHARMM27 parameters⁴⁰ for the oxygen atom and force field parameters optimized by Borodin et al.⁴⁵ for the Ti–O pair interaction. The following Lennard-Jones parameters were employed for the calculations: $r_{\min}/2(O) = 1.7$ Å, $r_{\min}/2(Ti) = 2.2$ Å, $\epsilon(O) = -0.12$ kcal/mol, and $\epsilon(Ti) = -0.041$ kcal/mol.

The total size of the four-layer graphite and tetragonal titanium dioxide surfaces were 116.7 Å × 117.7 Å × 17.5 Å and 114 Å × 114 Å × 14.5 Å in the x , y , z direction, respectively, which is sufficiently large

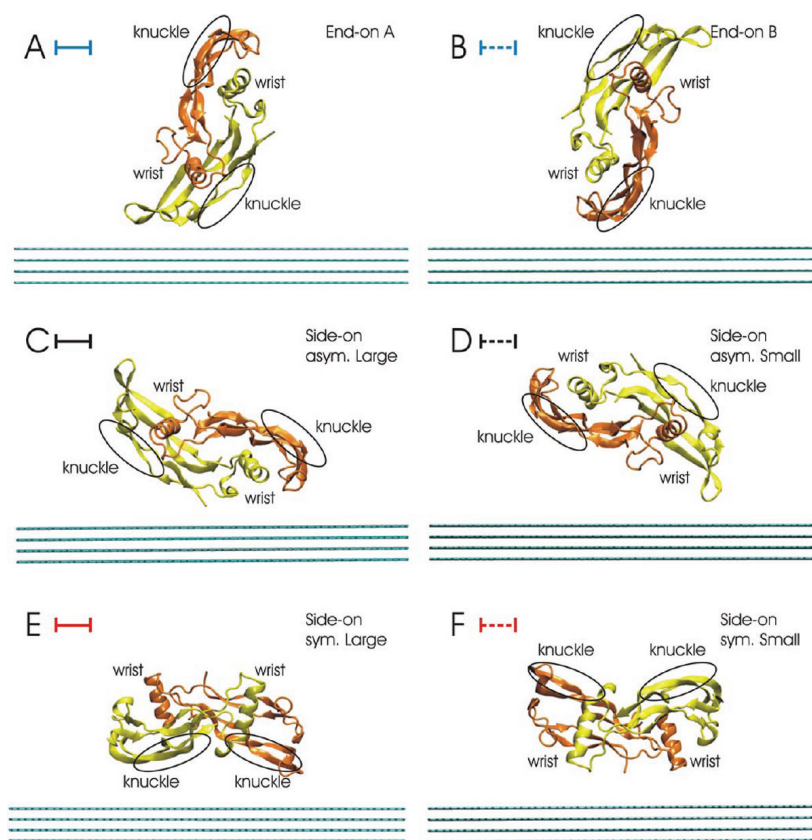


Figure 1. Initial orientations of BMP-2 homodimer on graphite (titanium dioxide analogue). The single monomers are given in yellow and orange colors. Wrist and knuckle descriptors indicate for each monomer the binding epitope for type IA and type IIA receptors. Panels A and B show the end-on and panels C–F the side-on conformations. Panels C and D are the asymmetric cases with large and small interaction interface, respectively. The symmetric conformations are shown in panels E and F for the large and the small interface, respectively.

enough to guarantee a minimum separation distance of 30 Å between the protein and its image and the surface image.

4. Preparation of Protein–Surface Systems. Given the size of the protein/surface system, consisting in ca. 17×10^4 atoms, advanced approaches to sample the entire conformational space, such as replica exchange⁴⁶ and simulated tempering,⁴⁷ are computationally demanding and, therefore, for our simulation system, not applicable. Instead of performing a complete conformational sampling, we considered six initial scenarios with BMP-2 lying in different orientations with respect to the surfaces, two end-on and four side-on orientations, as shown in Figure 1. The starting geometries were constructed by setting the surface slabs parallel to each face of the box containing the solvated and pre-equilibrated BMP-2 molecule. In the following, side-on orientations, where both chains of the homodimer are similarly orientated to the surface, are called symmetric and orientations with primarily one chain facing the surface are indicated as asymmetric. In addition, we differentiate between structures tilted by 180° to each other according to the area of the protein in the vicinity of the surface, which can be large or small. The large and small descriptors are defined only qualitatively and refer to the initial configurations. In total, we obtain two end-on orientations (end-on A and end-on B) with similar interaction interfaces of different chains and four side-on orientations (symmetric-large, symmetric-small, asymmetric-large, asymmetric-small). Residues belonging to the second monomer are indicated by an asterisk.

In all 12 constructed systems (six graphite, six titanium dioxide), we set the initial separation distance between BMP-2 and the surface to 5 Å to avoid long MD simulation trajectories.²⁰ Water molecules and ions very close to the borders of the cell, the protein, or the surface were deleted in order to avoid steric clashes between images and allow water molecules and ions to accommodate freely in the vicinity of the protein and surfaces. Deleted ions were reintroduced randomly, replacing water molecules in order to keep the systems neutral.

5. Computer Simulations. The computer simulations were performed using as starting geometries the BMP-2/graphite and BMP-2/TiO₂ systems described in the previous section. Following the energy minimization with the conjugated gradient and heating to 300 K, we equilibrated each system for 200 ps with stepwise decreasing of the position restraints on the protein backbones of 5 kcal/(mol Å²). After this short thermal equilibration, the total energy of all protein–surface systems remained stable, as show in Figure S1 (Supporting Information). Subsequently, we carried out a 10 ns adsorption dynamics of free BMP-2 on the fixed surface under constant pressure of 1 atm and temperature of 300 K facilitated by Langevin piston dynamics.⁴⁸

In the first step of the hybrid approach combining SMD and MD simulations, artificial forces were applied to the protein backbone, dragging it toward the surface with constant velocity of 0.025 Å/ps, thus accelerating the adsorption process. The spring constant connecting the pulling dummy atom with the protein backbone of BMP-2 was set to 1 kcal/(mol Å²)

[or 69.479 pN/Å²] in all 500 ps long SMD simulations. The root mean square deviation curves for the heavy atoms on the backbones remain steady at a value of ca. 2 Å (Figure S2, Supporting Information), indicating that the protein backbone is practically not affected by the artificial forces during the SMD procedure. In a second step, BMP-2 was relaxed on the surface in a 2.5 ns MD simulation in order to establish the most important contacts between the interaction partners. Extension of the simulation to 5 ns proved to be unnecessary, as no additional protein/surface interactions could be observed. In the last part, the protein was pulled away from the surface to speed up desorption. In this SMD, the spring constant and the pulling velocity were increased to 50 kcal/(mol Å²) and to 0.25 Å/ps, respectively. The pulling direction was changed by 180° to break the interaction between BMP-2 and surface and to accelerate desorption. During this process, the most important interacting amino acids were identified by their short separation distance to the surface. In all steered molecular dynamics simulation, spring constant and velocity of the pulling atom were carefully chosen to accelerate adsorption or desorption processes while avoiding the artificial denaturation of the protein.

Interaction energies between the protein and the surfaces during the MD and SMD simulations were computed using the NAMD energy plugin in the VMD package,⁴⁹ whereas the forces acting on the pulling atom during the simulated adsorption/desorption process were computed with the NAMD2.6 code.³⁵

RESULTS AND DISCUSSION

1. Adsorption on the Graphite Surface. On the nanosecond time frame, molecular dynamics simulations of BMP-2 on graphite show some adsorption features that are common to all considered orientations: first of all, the protein does interact with the surface and this interaction is stable in time. The observed stability does not imply immobilization of the protein, it is rather a dynamical process that involves various residues sequentially. This results in the protein rocking on the surface back and forth as well as partially rotating perpendicular to the surface. After the initial nearing of the protein to graphite, no large movements are observed along this direction. The interaction with the surface is neither affecting the overall structure of the protein nor destroying important structural elements of BMP-2. These observations are underlined by the low root mean square deviation (rmsd) of the protein backbone fluctuating around 2 Å and the nearly unchanged radius of gyration.

As expected for a system with a large amount of solvent, adsorption of the protein onto the surface is not mirrored in a change of the potential energy curve of the whole system. Total, potential, and kinetics energy stabilize within 200 ps, showing stationary fluctuations thereafter (see Figure S1, Supporting Information). For each orientation, adsorption of the protein to the surface is measured by the number of contacts, defined as the number of protein atoms within 5 Å from the surface, by the minimal distance between protein and surface, and by their interaction energy. The time-dependent traces of these quantities are given in Figures 2 and 3 for MD and SMD/MD simulations, respectively. Due to the absence of partial charges in the graphite, the interaction energy between protein and surface is composed of the van der Waals (vdW) part only, and electrostatic interaction energies are lacking. This explains the very good correlation observed between interaction energy and number of contacts, as listed in Table 1.

In the two end-on configurations (structures A and B in Figure 1), side chains of Val33, Pro36, and Val98 in structure A and Val33*, Pro36*, and Leu90* in structure B point directly to

the graphite, while the hydrophobic part of the receptor binding knuckle epitope (Ala34, Leu90, and Leu100) lies in the vicinity of the surface. Bordering the hydrophobic patch and also facing the graphite are two flexible loops containing a couple of polar or charged residues (Ser24, Asn29 on one side and Glu96 and Lys97 on the other side). During the end-on A MD simulation, residues of these loops readily come close to the surface, but the interaction is transient. Only after about 3 ns, the interaction with Ser24 and Asn29 of one loop stabilizes, bringing the protein within 3 Å from the surface (Figure 2b, blue continuous line). A longer lapse of time is needed for the hydrophobic patch to initiate a stable contact with the surface. This starts after about 7 ns with Pro36 and is readily stabilized by the additional interaction with Val33. The two residues act as a pivot point, and their adsorption induces a slight rotation of the protein, which aligns the hydrophobic patch parallel to the surface. As a consequence, interaction with the flexible loop containing Ser24 and Asn29 is broken, while Ala34, Leu90, and Val98 adsorb to the surface. At this point the number of contacts fluctuates around 40 atoms, while the interaction energy stabilizes at about -40 kcal/mol. The use of artificial forces pulling the protein toward the surface induces the same adsorption pattern (Figure S3, Supporting Information). Due to the additional adsorption of Leu100 of the knuckle epitope, the number of contacts increases and the interaction energy goes to -46 kcal/mol (Figure 3c, blue continuous line).

MD simulation of the end-on B configuration shows a much weaker adsorption of BMP-2 on graphite, which is reflected in higher minimal separation distances and lower interaction energies (Figure 2b,c, blue dashed lines). After about 8.5 ns, short lasting contacts involving the charged residue Glu96* and more sporadically hydrophobic Val33* and Val98* establish only a weak interaction. The structural discrepancies between the two starting end-on models are minimal; therefore, a completely different adsorption pattern is unlikely. Results obtained using the hybrid SMD/MD approach, where BMP-2 was first forced to come closer to the surface, clearly indicate that the adsorption patterns for the two orientations are indeed similar: in both cases, hydrophobic patches including the knuckle epitope lead to a stable adsorption on graphite. Charged or polar residues of the two flexible loops are also interacting with graphite, but their adsorption is normally less stable in time (Figure S3, Supporting Information). In the case of the end-on B configuration, a further stabilization of the adsorption process is detected after artificial steering of the protein toward the surface and 1 ns of MD, increasing the number of contact of about 20 atoms and the interaction energy to -65 kcal/mol (Figure 3a,c, blue dashed line). The residues responsible for this are Lys97* and its neighbor Glu96*. Their location in a flexible loop region allows the alignment of their long and flexible side chains parallel to the surface, thus maximizing the hydrophobic interaction with graphite. Desorption curves of selected residues (Figure S5, Supporting Information) highlight the importance of the hydrophobic groups Val98, Leu90, Leu100, Ala34, Val33, and Pro36 for both end-on configurations and the particular stability of the interaction between graphite and Lys97* in the end-on B orientation.

While the two end-on models are very similar, the four side-on orientations differ from each other substantially.

In the asymmetric-large system (structure C in Figure 1), three distinct portions of the protein are directly facing the surface: the hydrophobic patch corresponding to the wrist epitope and comprising residues Phe49 to Asp53; the area adjacent the N-terminus, a

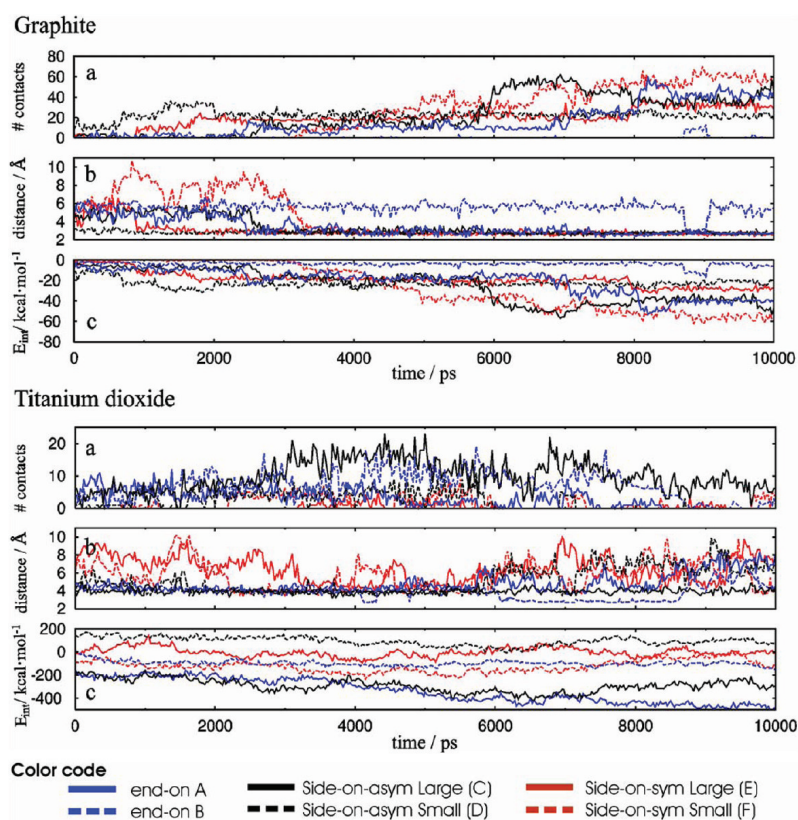


Figure 2. Interaction of BMP-2 with graphite and titanium dioxide during MD simulations: (a) number of contacts, (b) minimal separation distance and (c) interaction energy between BMP-2 and the surface.

very flexible segment consisting of Ser12, Ser13, and Lys15; and the hydrophilic and flexible loop formed by Glu94*, Asn95*, Glu96*, and Lys97*. The first contacts of the protein with the surface, established by the flexible segments involving the polar/charged terminations of the residues (Ser12–Lys15 and Glu94*–Lys97*) are rather unsteady. They stabilize only when the side chains are able to orientate parallel to the surface, thus maximizing the hydrophobic interaction with graphite. As the overall conformation of the protein is preserved, long-lasting alignments of these segments parallel to the surface are mutually excluding: they occur either at the terminus Ser12–Lys15 (MD trajectory) or at the charged loop Glu94*–Lys97* (SMD trajectory).

On the contrary, the hydrophobic patch facing the surface constitutes a spot for interaction with graphite. After about 2.5 ns, Pro50 of the wrist epitope establishes a stable contact to the surface. This residue has an anchor effect and leads to the nearing of the wrist epitope to graphite and the frequent arrangement of the amino acid side chains parallel to the surface. The interaction energy found in MD simulations is around -40 kcal/mol (Figure 2c, black continuous line), comparable with the end-on A adsorption, where interaction occurs through the other hydrophobic patch, the knuckle epitope. A slightly more negative value is found for the SMD trajectory (Figure 3c, black continuous line), where the docking of the protein guided by Pro50 causes a very advantageous alignment of His54, with the aromatic ring lying almost permanently parallel to graphite (Figure S3, Supporting

Information). Probably due to the strength of the interaction with the adjacent Pro50, Phe49 has not the flexibility to set its aromatic ring parallel to graphite; therefore, its adsorption is weaker. These observations explain the desorption curves of Phe49, Pro50, and His54 given in Figure S6 (Supporting Information).

The asymmetric-small arrangement (structure D in Figure 1) differs from the asymmetric-large equivalent in that only one monomer faces the surface through the Glu94*–Lys97* loop. The protuberant nature of this segment prevents the wrist epitope on the second monomer to get closer to the surface, so that attraction between hydrophobic patches of the protein and the graphite does not occur. Indeed, in both MD and SMD simulations, Asn95* and Glu96* and, more sporadically, Glu94* and Lys97* establish contacts to graphite. The favorable alignment of their long side chains leads to adsorption of the protein to graphite. The adsorption is rather stable in time, although being weak (about -20 kcal/mol, Figure 2c, black dashed line).

In the symmetric-large configuration (structure E in Figure 1) the knuckle epitopes of both monomers lie in the vicinity of the surface. Between the two β -strands containing Leu90 and Leu100 of the epitope we find the flexible turn of Glu94–Glu96 with the adjacent Lys97 pointing directly toward the surface. In the first nanosecond of MD, Leu100 and Lys97* interact intermittently with the surface. Thereafter, the interaction with the flexible loop on the second monomer prevails. A slight rotation of the protein brings the epitope in an end-on orientation with respect to graphite

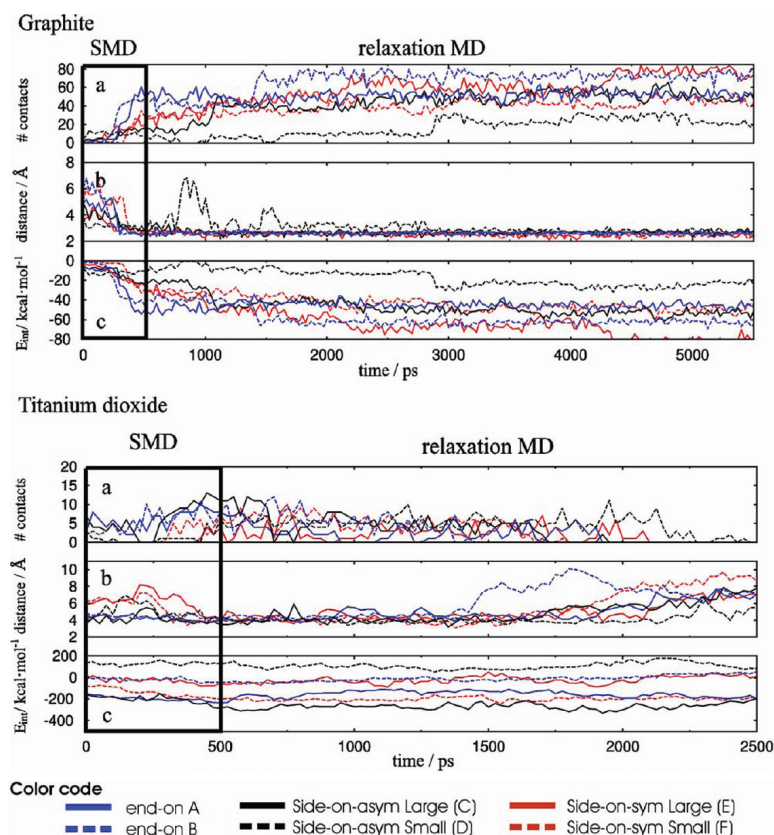


Figure 3. Interaction of BMP-2 with graphite and titanium dioxide during SMD (500 ps) and MD (5/2.5 ns) simulations: (a) number of contacts, (b) minimal separation distance and (c) interaction energy between BMP-2 and the surface.

Table 1. Interaction of BMP-2 with Graphite at the End of the SMD/MD Simulation

	conformation ^a	$E_{int}/\text{kcal mol}^{-1b}$	number of contacts ^b	main interacting residues ^c
A	end-on A	-46 ± 2	52 ± 4	Val33, Ala34, Pro36, Leu90, Val98, Leu100
B	end-on B	-63 ± 3	73 ± 5	Val33, Ala 34, Pro36, Leu90, Leu100 Lys97
C	side-on asym large	-53 ± 2	49 ± 4	Phe49, Pro50, His54 Glu94*, Asn95*
D	side-on asym small	-23 ± 2	21 ± 2	Asn95, Glu96
E	side-on sym large	-83 ± 5	77 ± 5	Ser88, Leu90, Val98, Leu100, Asn102 His54, Asn56 Asn95*, Lys97*
F	side-on sym small	-50 ± 4	45 ± 4	Asn71, Ser72, Lys73 Ser72*, Lys73*

^a Final structures are shown in Figure 4 and Figures S3 and S4 of the Supporting Information. ^b Average over the last 500 ps. ^c Residues with at least two atoms within 5 Å from the graphite surface.

and prevents any further contact of the first monomer to graphite. The interaction energy is low, about -25 kcal/mol (see Figure 2c, red continuous line).

The artificial pulling of the protein toward the graphite stabilizes the interactions of Lys97* and Leu100, favoring the adsorption of both chains. The additional participation of Asn95* on one side and of Ser88 and Asn102 on the other side locks BMP-2 at two points and lets the protein come closer to the surface in a symmetric manner. As a consequence, a third interaction spot appears between these two anchors. After about 2 ns, prehelix His54 and Asn56 start interacting extensively with the surface. In particular, His54, aligning its aromatic ring parallel to the surface, achieves a

very stable contact to graphite. The number of contacts increases again after 4.5 ns, due to the nearing of Leu90 and Val98, bringing the interaction energy to -80 kcal/mol (see Figures 4 and 3c, red continuous line).

In the symmetric-small configuration (structure F in Figure 1) the post helix turns of both monomers are facing the graphite with the hydrophilic groups Ser72 and Lys73 showing the smallest distances to the surface. A continuous interaction between the turn of one monomer and graphite occurs after about 3 ns and stabilizes when the long side chain of Lys73 sets parallel to the surface. After 5 ns the occasional interaction with the second monomer becomes steady and the protein, anchored at two points,

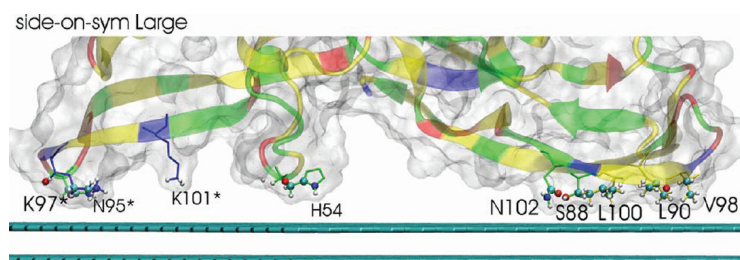


Figure 4. Final structure of BMP-2 with side-on symmetric-large orientation adsorbed on graphite, resulting from the SMD simulation. Residues interacting with the surface are plotted as sticks. Bond colors indicate the residue type: blue for positively charged, green for polar, and yellow for nonpolar. Only protein atoms within 5 Å away from the surface are represented by balls. The structures obtained for the remaining orientations are given as Supporting Information (Figures S3 and S4).

comes closer to the surface. Various segments of the protein situated between these two points show enough flexibility to interact intermittently with the surface, in particular, Asn71, Lys76, and the N-termini Ser12 of both monomers. The interaction energy, of about -60 kcal/mol, involves exclusively charged or polar residues. A similar trajectory follows the artificial acceleration of the protein toward the graphite. The weaker interaction energy and lower number of contacts observed in SMD/MD is related to a certain loss of dynamics in the flexible region between the two adsorption spots, induced by the very stable alignment of Lys73 and Ser72*.

The analysis of the adsorption patterns observed for structures A–E showed that BMP-2 adsorbs to graphite in all orientations, without denaturing. However, the time frame of these simulations is not sufficiently long to equilibrate the behavior of these systems, and orders-of-magnitude longer simulations are necessary to properly represent the final structure of BMP-2 on graphite. The interaction energies, having no Coulombic component, are weak compared to values reported by Dong et al.,²⁶ who simulated the interaction of BMP-2 on hydroxyapatite.

As shown in Table 1, the interaction observed in the present work at an early stage of BMP-2 adsorption involves hydrophobic patches as well as polar/charged residues situated in flexible loops of the protein. A quantitative comparison of the interaction energies involving hydrophobic and hydrophilic groups is beyond the possibility of the present study, which, using a fixed-charge-distribution model, cannot account for polarizing effects on the protein and on the graphite. Nevertheless, compared to the hydrophilic ones, hydrophobic interactions seems to be energetically more favorable and more stable in time, although they require longer time to be established.

The hydrophobic residues adsorbing to graphite correspond to the epitopes regions of BMP-2 or are located in their immediate vicinity. Interactions involving the wrist epitope, binding type I receptors, or the knuckle epitope, binding type II receptors, are energetically similar. Adsorption involving the wrist epitope is observed for the side-on-large orientations (C and E in Figure 1), while accessibility of the wrist may be slightly hindered in the asymmetric-small model (D in Figure 1), where the patch faces the surface. Direct interaction of the knuckle epitope is observed in the end-on orientations and in the side-on symmetric-large model (A, B, and E in Figure 1).

It was reported that in the wrist epitope only Leu51 and Asp53 represent a hot spot of binding to BMP-2 receptor IA, while Phe49 and Pro50 are required to optimize the hydrogen-bonding network.³⁷ In all simulations, Leu51 and Asp53 are not directly participating in the adsorption, except for in the large models (C and

E in Figure 1), where Asp53 is sporadically in contact with the surface. While Phe49 and Pro50 stay relatively far from the surface in the symmetric-large model E, they adsorb stably to graphite in the asymmetric-large model C, so that the building of the hydrogen-bonding network may be impossible.

Flexible loops containing charged or polar residues play also an important role in BMP-2 adsorption to graphite. Their flexibility allows a swift interaction with the surface, which is however less stable in time. This can be attributed to the competitive interaction with water, whose solvation effect can break the contact to the surface. Nevertheless, residues with long side chains (like lysine) may be able to align their chain parallel to the graphite, maximizing the interaction with the surface, which then becomes very stable and difficult to break.

2. Adsorption on the Titanium Dioxide Surface. The 10-ns-long molecular dynamics simulations of BMP-2 on titanium dioxide show for all orientations a very loose and unstable initial adsorption of the protein onto the surface. The result is astonishing, particularly if we consider the interaction energies between protein and TiO_2 , which are much larger than in the graphite systems and, for some orientations, clearly favor adsorption (Figure 2c). A visual inspection of MD and SMD/MD trajectories reveals that the loose adsorption of BMP-2 is related to water molecules. In the vicinity of TiO_2 , we observe a highly ordered layer of water, in which one O–H bond aligns almost perpendicularly to the surface (Figure 5). Hydrogen atoms of the water molecules point to negatively charged oxygen atoms of the TiO_2 surface, building within 25 ps a stable hydrogen-bond network. The rapid reorientation of the solvent maximizes the interaction of water with the hydrophilic TiO_2 surface, preventing the protein from interacting directly with the surface. A similar effect was reported in Car–Parrinello molecular dynamics studies on anatase and rutile surfaces, where water units competed with small organic molecules for adsorption onto TiO_2 surfaces.⁵⁰ Figure 5 shows also the density of water oxygen atoms in dependence of the distance to the surface. A two-layer water structure is evidenced. The prominent peak observed at 2.5 Å from the TiO_2 surface corresponds to the oxygen atoms of the first water adlayer. A second, smaller peak lies at 4.5 Å, giving the position of the second adlayer. At larger distances from the surface, no preferential orientation of water molecules is found. Similar density profiles of water oxygen atoms were found in MD simulations reported by Skelton et al.,²² who studied the adsorption of a hexapeptide onto the rutile (110) surface. They reported the formation of at least four water layers, of which the first two were most significant for the indirect binding of the hexapeptide.

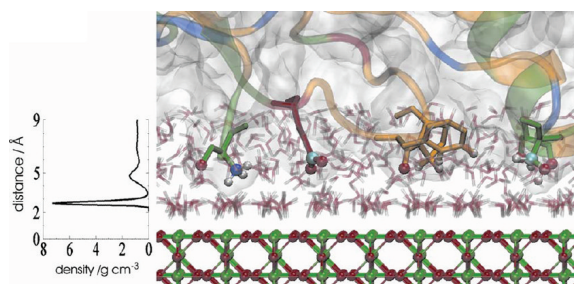


Figure 5. (Left) Distribution of water oxygen atoms as a function of the distance to the TiO_2 surface. A first density maximum at around 2.5 Å away from the titanium dioxide surface denotes the first water adlayer, followed by a minimum at 3–3.5 Å. A smaller peak represents the second hydration layer, located at 4.5 Å from the surface. The water oxygen density in this layer is increased compared to bulk water, but much smaller than in the first adlayer. (Right) BMP-2 on TiO_2 during the MD simulation. Depicted water molecules are within 9 Å from the TiO_2 surface. Protein atoms within 5 Å from the surface are given in ball-and-stick representation. The snapshot was taken during the MD simulation of the asymmetric-large orientation, structure C in Figure 1.

Table 2. Forces Exerted by Water Layers on the Protein

	F_{1-3} / pN^a	F_{3-5} / pN^a	F_{5-7} / pN^a	F_{7-9} / pN^a
(A) end-on A	170	-114	-26	-5
(B) end-on B	128	-75	-40	-4
(C) asym-large	218	-136	-54	-7
(D) asym-small	162	-104	-47	-4
(E) sym-large	231	-157	-64	6
(F) sym-small	176	-118	-43	4
average	181	-117	-46	-2

^a Forces of water layers acting on BMP-2 in the direction of the surface normal averaged over the 10 ns long MD simulations. Positive and negative values denote repulsive and attracting forces, respectively. The water layers are separated into 2 Å wide slabs. Thus, F_{1-3} , F_{3-5} , F_{5-7} , and F_{7-9} represent the forces on the BMP-2 due to water layers located within 1 and 3 Å (first water adlayer), 3 and 5 Å (second water adlayer), 5 and 7 Å, and 7 and 9 Å, respectively, with respect to the TiO_2 surface.

Interaction energies between TiO_2 and the first water adlayer are about 3 orders of magnitude larger than between TiO_2 and BMP-2. The analysis of the interaction forces gives a deeper insight in the role played by water. The first water adlayer is pulled toward the surface by forces of more than 7000 kcal/(mol Å), while BMP-2 is attracted by TiO_2 with forces of around 20 kcal/(mol Å), which are much weaker. The considerable difference between forces acting on water and on BMP-2 explains why the protein is not able to break the water layer formation. In addition, the first water adlayer has a repulsive effect on BMP-2, which is 1 order of magnitude higher than the attraction force of the surface on BMP-2 (Table 2). Nevertheless, BMP-2 is not totally desorbing from the TiO_2 , because the second water adlayer has an attractive effect on BMP-2 and is involving BMP-2 in the hydrogen-bond network. This effect is decreasing when moving away from the surface, where water molecules do not attract or repel BMP-2. The repulsive effect of adsorbed water layers was already described in earlier theoretical studies, reporting the formation of a highly

ordered water layer repelling organic molecules away from a hydrophilic surface.^{51–53} On the contrary, Skelton et al.²² showed that the formation of layers of structured water at the interface with rutile (110) was not detrimental to the stable binding of an hexapeptide. Therefore, the formation of water adlayers is not per se a reason for hindering protein adsorption.

The presence of a strongly adsorbed water layer, which covers the surface and allows only an indirect interaction with the protein, explains the low number of contacts between BMP-2 and the surface (less than 20 atoms) and minimal distances of more than 4 Å, definitely larger than in the graphite systems (Figure 2). During the simulation, protein penetration of the first water adlayer coating the titanium dioxide, resulting in a minimal distance between BMP-2 and the surface of less than 3 Å, is a very rare and unstable state. However, integration of hydrophilic and charged protein side chains into the second adlayer is much more common and of much higher stability in the first part of the simulation. In the second 5 ns of the MD simulation, BMP-2 is desorbing behind the second water adlayer in nearly all configurations, which leads to minimal separation distances of more than 5 Å. Although, the protein/surface interaction can be influenced by the specific texture of the surface, as shown in the MD simulations on BMP-7 adsorbing onto various hydroxyapatite (HAP) surfaces,⁵⁴ analogous results (i.e., loose adsorption of the protein followed by desorption) were also observed when considering the (110) cut of rutile. Thus, the observed desorption is not in agreement with the work of Skelton et al.,²² showing the stable binding of an hexapeptide to the first two water layers covering a (110) rutile surface. However, a direct extrapolation of the adsorption pattern observed in a small peptide sequence to the behavior of a folded protein may be misleading.

Pulling BMP-2 toward the TiO_2 slab by applying artificial forces (SMD simulations) leads to a penetration of the second water adlayer, but not of the first layer, as indicated in minimal separation distances of about 4 Å (Figure 3). Applying higher artificial pulling forces does not result in breaking the first water adlayer, but in undesired structural rearrangement of the protein. Therefore, stronger pulling forces in SMD simulations were rejected. During the second part of the relaxation period following the SMD, BMP-2 is drifting away from the surface. This desorption is mostly induced by strong water/surface interactions and water/BMP-2 repulsion. Since the protein had already desorbed from the surface, SMD desorption studies were not carried out.

CONCLUSIONS

We performed MD and hybrid SMD/MD simulations to investigate the initial steps of the adsorption of BMP-2 homodimer on two different implant surfaces, hydrophobic graphite and hydrophilic titanium dioxide. We showed that the adsorption of the protein in the nanosecond time window is strongly influenced by the character of the surface and, in the case of titanium dioxide, by the presence of water. Van der Waals interactions between BMP-2 and graphite led to a stable although weak adsorption of the protein, involving hydrophobic patches as well as flexible loops of BMP-2, depending on the initial orientation of the protein. This weak adsorption of BMP-2 on the graphite surface may be biased by the molecular mechanics force field. Although the dynamics of hexane deposited onto graphite, as simulated by Connolly et al.⁴⁴ using the CHARMM force field, was found to agree well with experimental evidence, the computation of free energy of adsorption from MD simulations of peptide adsorption

on various functionalized alkanethiol self-assembled monolayers showed by comparison with experimental values that the CHARMM force field underestimates the strength of adsorption involving hydrophobic and positively charged amine surface groups.⁵⁵

In addition, we monitored only a very loose adsorption of BMP-2 to titanium dioxide, followed by desorption. This weak contact is an outcome of strong water–titanium dioxide interactions, which stand in competition with BMP-2 adsorption. We showed the formation of two adlayers of water, which have opposite influence on the protein. The first, highly ordered water adlayer has a strong repulsive effect on BMP-2, while the second one attracts the protein toward the surface, probably due to the formation of a hydrogen-bond network which involves the first adlayer on one side and the protein on the other side. The water-mediated attraction to the surface was nevertheless only temporary, as BMP-2 was finally desorbing from it.

The very loose interaction of BMP-2 with titanium dioxide contrasts with MD simulations on hydrophilic hydroxyapatite.²⁶ This may be related to the specific texture of the two surfaces: while the outermost layer of TiO₂(001) sees the alternation of positively charged Ti atoms and negatively charged O atoms, with a zero net charge, in HAP(001) this layer is constituted solely by calcium cations, resulting in a positively charged interface to water.

In our simulations, we used perfect surfaces without defects. Simulations of small molecules on titanium dioxide surfaces with different levels of hydroxylation showed that protein and solvent interact very strongly with surface regions containing defects.⁵⁰ By using perfect surfaces, we cannot exclude that the observed adsorption pattern may be somehow artificially biased. Especially in the case of titanium dioxide, surface defects by adding hydroxyl groups may alter the adsorption properties of water, resulting in a destabilized adlayer. By destroying the high order of the water, BMP-2 may be able to break the water adlayer establishing direct contacts with the titanium dioxide, which may result in a changed adsorption behavior compared with the perfect surface without defects.

In all our simulations, BMP-2 showed a high degree of stability, which may be biased by the choice of the CHARMM27 force field and the relatively short time window of only 10 ns considered for the MD simulations. Under these simulation conditions, the protein did not undergo major structural changes when interacting with the surface. This is in agreement with the findings of Dong et al., investigating the adsorption of BMP-2 on hydroxyapatite surfaces,²⁶ and results reported by Oliveira et al.,³¹ who studied the adsorption of BMP-2 to hydrophobic surfaces, but in clear contrast to the observations of Mücksch and Urbassek, who examined the adsorption of BMP-2 on graphite.³² Their study differs from ours in three aspects: the form of BMP-2 (monomer vs dimer), the force field (OPLS-AA vs CHARMM), and the water model used to simulate the aqueous environment (implicit inviscid water vs explicit water). According to Oliveira et al.,³¹ the secondary and tertiary structures of BMP-2 are stabilized by the water environment more than by dimerization. It may be possible that an implicit model of the solvent, which was shown to be an efficient way to speed up the adsorption of lysozyme on graphite,⁵⁶ is inadequate to describe the adsorption of BMP-2.

■ ASSOCIATED CONTENT

S **Supporting Information.** This material is available free of charge via the Internet at <http://pubs.acs.org>.

■ AUTHOR INFORMATION

Corresponding Author

*E-mail: andrea.mroginski@tu-berlin.de.

■ ACKNOWLEDGMENT

Computational resources from the Norddeutscher Verbund für Hoch- und Höchstleistungsrechnen (HLRN) are acknowledged. We also thank the DFG Cluster of Excellence “UniCat” for the financial support.

■ REFERENCES

- (1) Gray, J. *Curr. Opin. Struct. Biol.* **2004**, *14*, 110–115.
- (2) Hlady, V.; Buijs, J. *Curr. Opin. Biotechnol.* **1996**, *7*, 72–77.
- (3) Haidar, Z.; Hamdy, R.; Tabrizian, M. *Biotechnol. Lett.* **2009**, *31*, 1817–1824.
- (4) Haidar, Z.; Hamdy, R.; Tabrizian, M. *Biotechnol. Lett.* **2009**, *31*, 1825–1835.
- (5) Bessa, P. C.; Casal, M.; Reis, R. L. *J. Tissue Eng. Regen. Med.* **2008**, *2*, 81–96.
- (6) Granjeiro, J. M.; Oliveira, R. C.; Bustos-Valenzuela, J. C.; Sogayar, M. C.; Taga, R. *Braz. J. Med. Biol. Res.* **2005**, *38*, 1463–1473.
- (7) Slobodan, Vukicevic; Kubicki, J. D. (Eds.) *Bone Morphogenetic Proteins: Regeneration of Bone and Beyond*; Birkhäuser Verlag: Basel, 2004.
- (8) Bessho, K.; Carnes, D. L.; Cavin, R.; Chen, H. y.; Ong, J. L. *Clin. Oral Implant Res.* **1999**, *10*, 212–218.
- (9) Shah, A. K.; Lazatin, J.; Sinha, R. K.; Lennox, T.; Hickok, N. J.; Tuan, R. S. *Biol. Cell* **1999**, *91*, 131–142.
- (10) Wozney, J. M.; Rosen, V.; Celeste, A. J.; Mitsock, L. M.; Whitters, M. J.; Kriz, R. W.; Hewick, R. M.; Wang, E. A. *Science* **1988**, *242*, 1528–1534.
- (11) Hogan, B. L. *Curr. Opin. Genet. Dev.* **1996**, *6*, 432–438.
- (12) Kirsch, T.; Sebald, W.; Dreyer, M. K. *Nat. Struct. Mol. Biol.* **2000**, *7*, 492–496.
- (13) Massagué, J.; Attisano, L.; Wrana, J. L. *Trends Cell Biol.* **1994**, *4*, 172–178.
- (14) Namiki, M.; Akiyama, S.; Katagiri, T.; Suzuki, A.; Ueno, N.; Yamaji, N.; Rosen, V.; Wozney, J. M.; Suda, T. *J. Biol. Chem.* **1997**, *272*, 22046–22052.
- (15) Chaloux, E.; Lopez-Rovira, T.; Rosa, J. L.; Bartrons, R.; Ventura, F. *J. Biol. Chem.* **1998**, *273*, 537–543.
- (16) Nickel, J.; Dreyer, M. K.; Kirsch, T.; Sebald, W. *J. Bone Joint Surg. Am.* **2001**, *83*, S7–14.
- (17) Sebald, W.; Nickel, J.; Zhang, J. L.; Mueller, T. D. *Biol. Chem.* **2004**, *385*, 697–710.
- (18) Kirsch, T.; Nickel, J.; Sebald, W. *EMBO J.* **2000**, *19*, 3314–3324.
- (19) Raffaini, G.; Ganazzoli, F. *J. Mater. Sci.: Mater. Med.* **2007**, *18*, 309–316.
- (20) Raffaini, G.; Ganazzoli, F. *Langmuir* **2004**, *20*, 3371–3378.
- (21) Monti, S.; Carravetta, V.; Battocchio, C.; Iucci, G.; Polzonetti, G. *Langmuir* **2008**, *24*, 3205–3214.
- (22) Skelton, A. A.; Liang, T.; Walsh, T. R. *Appl. Mater. Interfaces* **2009**, *1*, 1482–1491.
- (23) Marszalek, P. E.; Lu, H.; Li, H.; Carrion-Vazquez, M.; Oberhauser, A. F.; Schulten, K.; Fernandez, J. M. *Nature* **1999**, *402*, 100–103.
- (24) Izrailev, S.; Stepaniants, S.; Balsara, M.; Oono, Y.; Schulten, K. *Biophys. J.* **1997**, *72*, 1568–1581.
- (25) Utesch, T.; Mroginski, M. A. *J. Phys. Chem. Lett.* **2010**, *1*, 2159–2164.
- (26) Dong, X.; Wang, Q.; Wu, T.; Pan, H. *Biophys. J.* **2007**, *93*, 750–759.
- (27) Eriksson, C.; Nygren, H. Å. *J. Biomed. Mater. Res.* **1997**, *37*, 130–136.
- (28) Albrektsson, T.; Jacobsson, M. *J. Prosthet. Dent.* **1987**, *57*, 597–607.

- (29) Ong, J. L.; Lucas, L. C.; Raikar, G.; Connatser, R.; Gregory, J. C. *J. Mater. Sci.: Mater. Med.* **1995**, *6*, 113–119.
- (30) Oliveira, A. F.; Gemming, S.; Seifert, G. *J. Phys. Chem. B* **2010**, *115*, 1122–1130.
- (31) Oliveira, A. F.; Gemming, S.; Seifert, G. *Materialwiss. Werkstofftech.* **2010**, *41*, 1048–1053.
- (32) Mücksch, C.; Urbassek, H. M. *Chem. Phys. Lett.* **2011**, *510*, 252–256.
- (33) Phillips, J. C.; Braun, R.; Wang, W.; Gumbart, J.; Tajkhorshid, E.; Villa, E.; Chipot, C.; Skeel, R. D.; Kalac, L.; Schulten, K. *J. Comput. Chem.* **2005**, *26*, 1781–1802.
- (34) Jorgensen, W. L.; Chandrasekhar, J.; Madura, J. D.; Impey, R. W.; Klein, M. L. *J. Chem. Phys.* **1983**, *79*, 926–935.
- (35) Darden, T.; York, D.; Pedersen, L. *J. Chem. Phys.* **1993**, *98*, 10089–10092.
- (36) Ryckaert, J. P.; Ciccotti, G.; Berendsen, H. J. C. *J. Comput. Phys.* **1977**, *23*, 327–34.
- (37) Keller, S.; Nickel, J.; Zhang, J. L.; Sebald, W.; Mueller, T. D. *Nat. Struct. Mol. Biol.* **2004**, *11*, 481–488.
- (38) Brünger, J.; Karplus, M. *Proteins* **1988**, *4*, 148–156.
- (39) Brooks, B.; Brucoleri, R.; Olafson, B.; States, D.; Swaminathan, S.; Karplus, M. *J. Comput. Chem.* **1983**, *4*, 187–217.
- (40) MacKerell, A. D.; Bashford, D.; Bellott, R. L.; Evanseck, J. D.; Field, M. J.; Fischer, S.; Gao, J.; Guo, H.; Ha, S.; Joseph-McCarthy, D.; Kuchnir, L.; Kuczera, K.; Lau, F. T. K.; Mattos, C.; Michnick, S.; Ngo, T.; Nguyen, D. T.; Prodhom, B.; Reiher, W. E.; Roux, B.; Schlenkrich, M.; Smith, J. C.; Stote, R.; Straub, J.; Watanabe, M.; Wiorkiewicz-Kuczera, J.; Yin, D.; Karplus, M. *J. Phys. Chem. B* **1998**, *102*, 3586–3616.
- (41) Wyckoff, R. W. G. *Crystal Structure*, 2nd ed.; John Wiley & Sons: London, 1963.
- (42) Naicker, P. K.; Cummings, P. T.; Zhang, H.; Banfield, J. F. *J. Phys. Chem. B* **2005**, *109*, 15243–15249.
- (43) Bandura, A. V.; Kubicki, J. D. *J. Phys. Chem. B* **2003**, *107*, 11072–11081.
- (44) Connolly, A. J.; Roth, M. W.; Gray, P. A.; Wexler, C. *Langmuir* **2008**, *24*, 3228–323.
- (45) Borodin, O.; Smith, G. D.; Bandyopadhyaya, R.; Bytner, O. *Macromolecules* **2003**, *36*, 7873–7883.
- (46) Marinari, E.; Parisi, G. *Europhys. Lett.* **1992**, *19*, 451–458.
- (47) Affentranger, R.; Tavernelli, I.; Di Iorio, E. E. *J. Chem. Theor. Comput.* **2006**, *2*, 217–228.
- (48) Feller, S. E.; Zhang, Y.; Pastor, R. W.; Brooks, B. R. *J. Chem. Phys.* **1995**, *103*, 4613–4621.
- (49) Humphrey, W.; Dalke, A.; Schulten, K. *J. Mol. Graphics* **1996**, *14*, 33–38.
- (50) Koppen, S.; Langel, W. *Phys. Chem. Chem. Phys.* **2008**, *10*, 1907–1915.
- (51) Hower, J. C.; He, Y.; Jiang, S. *J. Chem. Phys.* **2008**, *129*, 215101–215107.
- (52) Yang, A. C.; Weng, C. I. *J. Chem. Phys.* **2008**, *129*, 154710–154719.
- (53) Zheng, J.; Li, L.; Tsao, H. K.; Sheng, Y. J.; Chen, S.; Jiang, S. *Biophys. J.* **2005**, *89*, 158–166.
- (54) Dong, X. L.; Zhou, H. L.; Wu, T.; Wang, Q. *J. Phys. Chem. B* **2008**, *112*, 4751–4759.
- (55) Vellore, N. A.; Yancey, J. A.; Collier, G.; Latour, R. A.; Stuart, S. J. *Langmuir* **2010**, *26*, 7396–7404.
- (56) Raffaini, G.; Ganazzoli, F. *Langmuir* **2009**, *26*, 5679–5689.

10.2 Three-Dimensional Structural Model of Chicken Liver Sulfite Oxidase in its Activated Form

Tillmann Utesch and Maria Andrea Mroginski

Reprinted with permission from *J. Phys. Chem. Lett.* (2010), 1, 2159-2164

Copyright 2010 American Chemical Society.

Overview

The aim of this project was to shed light into the proposed domain motion mechanism in SO [63]. Therefore, hybrid SMD/MD simulations were carried out to obtain a conformation showing the two redox centres, namely, the Moco and heme, in a short separation distance to each other. In a first step, the domain motion of the flexible cytochrome *b5* unit towards the active site was forced by SMD simulations. Afterwards, the stability of the gained conformation was probed and validated in a subsequent equilibration performed by classical MD simulations.

Additionally, intra molecular electron transfer rates were analysed by the PATHWAYS tool [197] to further characterize the conformation. In doing so, we showed that IET in the derived model structure was settled on the same order of magnitude as experimentally determined rates. This was not the case for the initial model, the X-ray structure [60], where IET was much too slow.

Furthermore, residues involved in IET were identified. Beside the conserved arginine residue at the active site, the importance of interfacial water molecules forming a hydrogen bond network between the Moco and cytochrome *b5* was shown.

As proposed earlier [63], the activated conformation is stabilized by electrostatic interactions represented by salt-bridges between the positively charged active site pocket and the anionic cytochrome *b5* domain.

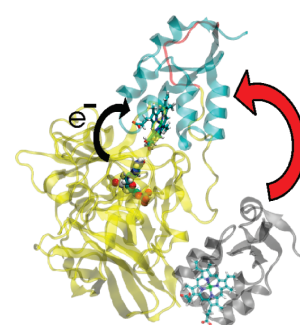
Three-Dimensional Structural Model of Chicken Liver Sulfite Oxidase in its Activated Form

Tillmann Utesch and Maria Andrea Mroginski*

Technische Universität Berlin, Institut für Chemie, Max-Volmer- Laboratorium, Sekr. PC14, Strasse des 17. Juni 135, D-10623 Berlin, Germany

ABSTRACT Sulfite oxidase (SO) catalyzes the conversion of sulfite to sulfate in almost all living organisms. In vertebrates, the catalytic process involves a rapid intramolecular electron transfer (IET) step between the molybdenum cofactor in the central domain and the heme in the cytochrome *b5* domain. The large distance between redox centers observed in the crystal structure disagrees with the fast IET rates measured experimentally. This conflict was explained by postulating a major rearrangement of the cytochrome *b5* domain toward the molybdopterin cofactor. Using steered molecular dynamics and molecular dynamics simulations, we generated a stable 3D structural model for chicken liver SO (CSO) in the activated form characterized by a short electron donor–acceptor distance consistent with the enzymes' experimentally obtained electron transfer properties. IET rates for the active complex were estimated with the Pathway model. The good agreement between calculated and experimental IET rates supports our structural model for the active CSO.

SECTION Molecular Structure, Quantum Chemistry, General Theory



Sulfite-oxidizing enzymes are found in prokaryotic and eukaryotic organisms.¹ Vertebrate sulfite oxidase (SO) is a homodimeric enzyme that catalyzes the final step in the degradation of sulfur-containing amino acids by oxidation of sulfite to sulfate with 2 equiv of ferricytochrome *c* (cyt *c*) as the terminal electron acceptor.^{1,2}



During catalysis, the oxidized molybdenum cofactor (Moco) located in the central domain takes up two electrons, and the Mo(VI) is reduced to the Mo(IV) state. The received electrons are sequentially transferred from the Mo to the oxidized Fe of the heme group located in the N-terminal cytochrome *b5* domain. In animals, the two domains are connected via a very flexible loop of 10 amino acids shown in the crystallographic structure of chicken liver sulfite oxidase (CSO)³ (Figure 1). This flexible loop is assumed to play an important role in the intramolecular electron transfer (IET) process because it facilitates the reorientation of the cytochrome *b5* domain toward the Moco harboring domain.^{3,4} After reduction of the heme, the electrons are transferred further to the external electron acceptor ferricytochrome *c*.

To date, the IET process is not completely understood. One of the most challenging questions is the discrepancy between high electron transfer (ET) rates measured in experiments⁵ and the large distance between the two redox centers, of ca. 32 Å, observed in the crystallographic structure of CSO.³ CSO has a high sequence similarity to human SO and is a typical representative for sulfite oxidases of higher vertebrates.

Pacheco and coworkers were able to explain the high IET rates in SO despite the large Moco-to-heme distance by introducing the idea of a very flexible cytochrome *b5* domain.⁴ In their model, they proposed the motion of the negatively charged cytochrome *b5* domain toward the cationic substrate-binding pocket to reduce the Mo–Fe distance and achieve fast IET rates obtained experimentally. In the proposed scheme, the flexible linker region connecting the two domains acts as a hinge and enables this rearrangement of the anionic cytochrome *b5* domain toward the active site. This hypothesis was supported by the observation made from laser flash photolysis experiments of a decreased IET with increasing viscosity of the solution.⁶ Additionally, molecular dynamics (MD) simulations of CSO monomer performed by Pushie et al.⁷ support the idea of a mobile cytochrome *b5* domain. In their work, they observed a highly mobile heme domain and estimated separation distances between the two redox centers varying from 27.4 to 56.9 Å. The effect of the tether flexibility on the IET reaction kinetics was investigated by Kawatsu and Beratan⁸ using a computational approach and very recently by Enemark and coworkers through laser flash photolysis and steady-state kinetics experiments.⁹ Despite the several experimental and theoretical attempts accomplished to unravel the structural properties of the SO in a catalytically active form characterized by a high IET rate and a

Received Date: May 7, 2010

Accepted Date: June 25, 2010

Published on Web Date: July 01, 2010

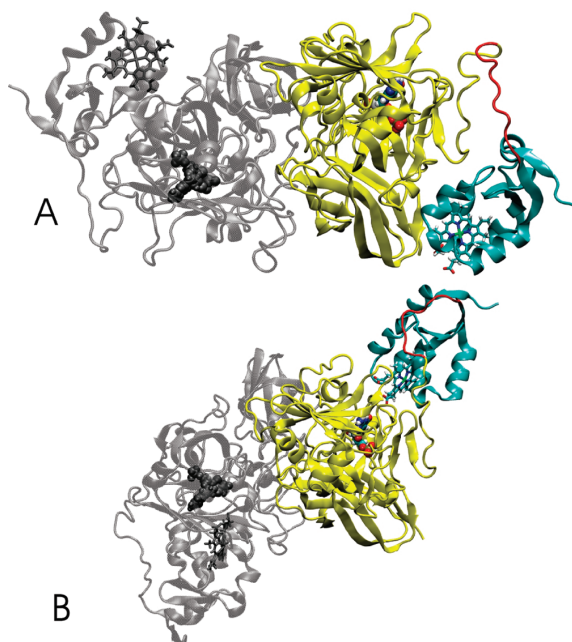


Figure 1. (A) Crystal structure of chicken liver sulfite oxidase (1SOX) and (B) 3D structural model of a CSO in the active form showing the cytochrome *b5* domain (cyan), the central domain (yellow), and the connecting loop (red) of subunit A. The B subunit is colored gray.

short Mo–Fe distance, there is still no precise 3D structure of such a complex available.

In this Letter, we describe a theoretical approach combining steered molecular dynamics (SMD) and MD all-atom simulations to obtain a stable 3D structural model of CSO in a “docked” form with a relatively short electron donor–acceptor distance consistent with the experimentally measured rapid IET rates. This study was complemented with the computation of IET rates using the Pathway model.¹⁰

Under the assumption that the sulfate leaves the Moco active site before the reoxidation of the Mo center, the structural model for the docked CSO was built in the absence of sulfate anion. This assumption is supported by experimental data showing the significant decrease in IET rate in CSO upon anion binding to the enzyme.⁵

In SMD, time-dependent external forces were applied to the cytochrome *b5* domain, pulling it sequentially and with constant velocity toward the substrate-binding pocket containing the Moco. The distance between the metals of the two redox centers decreased from 32 Å, as measured in the crystallographic structure, to <20 Å in the proposed “active” structure (Figure 2a). The structural integrity of the cytochrome *b5* domain is conserved along the entire SMD simulation, as reflected by the relatively low root-mean-square deviations (rmsd’s) of the corresponding protein backbone (Figure 2b). During the first 730 ps, the rmsd fluctuates around 1.2 Å until contact with the binding pocket of the Moco domain is achieved. At this point, induced by the interaction

with the Moco and dimerization domains, the rmsd of the cytochrome *b5* suddenly increases to ~2.0 Å.

After removing the external forces from the system, we observed a quick reorganization of the cytochrome *b5* domain, resulting in an increase in the Mo–Fe distance from ~17.5 to >20 Å (Figure 2a). In the relaxation and equilibration periods, the rmsd of the cytochrome *b5* domain remained steady around 1.85 Å, indicating a stable conformation without large structural changes (Figure 2b). Moreover, during the 14 ns simulation, the distance between the two redox partners fluctuated between 17 and 20 Å without increasing. This indicates that there is no repulsion between the cytochrome *b5* and Moco domains.

The root-mean-square fluctuations (rmsf’s) calculated from the MD simulation for all C_α of the SO monomer show a prominent peak in the linker region connecting the cytochrome *b5* domain to the Moco domain. The fluctuations in the loop are nearly twice as large as those in the cytochrome *b5* domain, where the rmsf lies between 1.0 and 2.0 Å (Figure 3). Strong fluctuations of up to 3.0 Å were predicted only in the N-terminal region of the cytochrome *b5* domain. The Moco and dimerization domains undergo only minor fluctuations of <2.0 Å.

In the stable conformation, which appeared right after SMD, the heme cofactor of the cytochrome *b5* is oriented in such a way that its propionate chains point toward the substrate binding pocket close to the Moco cofactor in a similar way as that observed in bacterial sulfite dehydrogenase (SDH).¹¹ In addition, the carboxyl groups of the heme are involved in the hydrogen bond network in the binding pocket and form salt bridges with the positively charged Lys-200 and Arg-450 residues that were originally exposed to the solvent. These salt bridges remained stable during the entire 14 ns MD simulation run and seem to be essential for stabilizing the docked conformation.

The amino acids of the Moco active site, Arg-138 and Tyr-322 as well as water molecules, which were not pushed away during the docking of the cytochrome *b5*, form the interface between the two redox cofactors. The water molecules are located in the narrow part of the cavity, where the cytochrome *b5* domain is not able to enter, because of steric hindrance. Arg-138 and Tyr-322 stayed stable during the entire simulation. In particular, because Tyr-322 is stabilized in the “active” SO conformation by interactions with His-140 and with bound water molecules, we did not observe any gating movement of Tyr-322, as reported by Pushie et al.⁷

Pathway decay factors ϵ and IET reaction rates were computed using the Pathway model¹⁰ described in the Computational Methods section and in the Supporting Information. The decay factors calculated every 10 ps of the MD trajectory are plotted in Figure 2c. From these decay factors, an average IET reaction rate (k_{ET}) of $5 \times 10^4 \text{ s}^{-1}$ could be derived. This result is 1 order of magnitude higher than the experimental values of $\sim 10^3 \text{ s}^{-1}$.^{4,5} This discrepancy lies, however, within the expected error of the Pathways model approach for computing ET rates, which strongly depends on the definition of the electron donor and acceptor groups and on the value of the prefactor relating the electronic coupling matrix and the ET rate.¹²

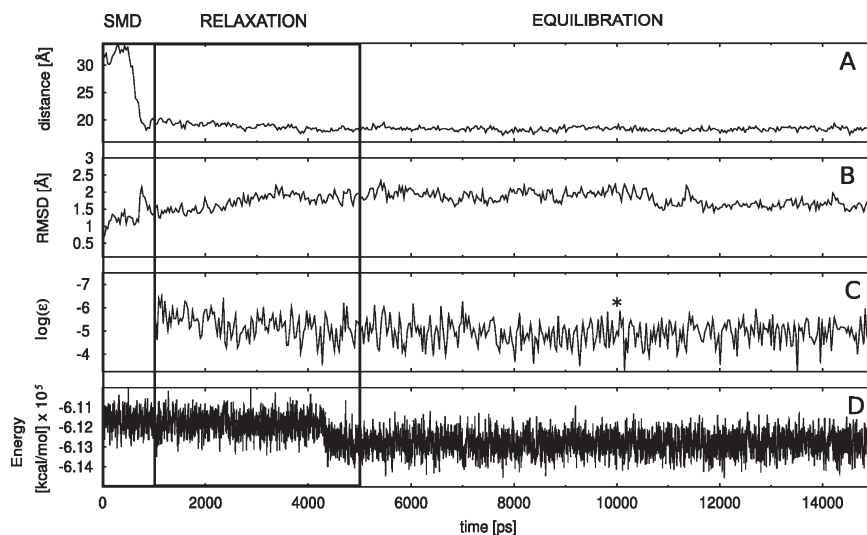


Figure 2. Results from the SMD (1 ns) and MD simulations (14 ns). (A) Distance plot between the Mo and Fe atoms of the redox centers, (B) rmsd of the protein backbone C_{α} atoms of the cytochrome *b5* domain, (C) ET pathways decay factors between the Mo and the Fe atoms as a function of simulation time, and (D) total energy of the whole protein. The asterisk in part C indicates the representative snapshot used in Figure 4.

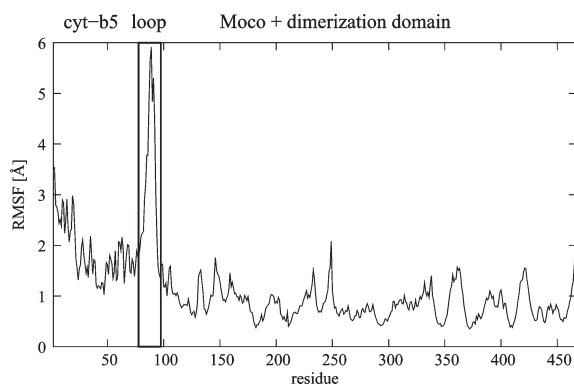


Figure 3. rmsf of the C_{α} atoms during the MD simulation. The marked peak indicates the high rmsf in the flexible loop connecting the cytochrome *b5* and the Moco domains.

We observed the highest electronic coupling rates when the electron tunnels along a hydrogen network involved two or three water molecules only (Table 1). These water-only mediated pathways occurred in 20% of all pathways calculated during the simulation. The importance for ET tunneling of structured water molecules at protein–protein interfaces has been previously discussed in the literature.¹⁵

The most frequent electron tunneling pathway, with 46.2% occurrence defined along Arg-138 and one bridging water molecule, lies on average within the same order of magnitude. Here it is important to note that these coupling rates are highly sensitive to small conformational changes, as reflected by the large fluctuations of up to two orders of magnitude of the electronic coupling rates sampled during the MD simulation (Figure 2c). For example, the loss of one

Table 1. Overview of the Fastest ET Pathways from Moco to Heme during MD Simulation According to Pathways Model

bridging residues	average T_{DA}	steps ^a	occurrence %
H ₂ O H ₂ O H ₂ O	5.65×10^{-5}	8 + 3 + 1	7.1
H ₂ O H ₂ O	2.39×10^{-5}	8 + 2 + 1	13.1
R138 H ₂ O	2.18×10^{-5}	10 + 2 + 1 8 + 1 + 2	46.2
Y322 H ₂ O H ₂ O	2.07×10^{-5}	8 + 3 + 1	7.3
R138 H ₂ O H ₂ O	9.55×10^{-6}	10 + 3 + 1	6.1
Y322 H ₂ O D321 R450	9.35×10^{-6}	8 + 4 + 1 10 + 4 + 1 11 + 4 + 1	3.9

^aThe steps of electron tunneling are defined according to the PATHWAYS algorithm: covalent bond, hydrogen bridge, and through-space-mediated steps.

hydrogen bond changes the residues participating in an electron tunneling pathway and the corresponding coupling rate by one order of magnitude. (See Table 1.) As a result of thermal protein fluctuations, electron tunneling pathways along Tyr-322, Asp-321, Arg-450, and water may also occur (Table 1).

According to our predictions, Arg-138, His-140, Asp-321, Tyr-322, and Arg-450 are the most important amino acids in the ET pathway in CSO (Figure 4). This observation is not totally in agreement with experimental results done on bacterial SDH, where the conserved Arg-138 residue is believed to play an indirect role in the IET process.¹¹ In contrast with CSO, no docking is required in SDH because the two domains harboring the different cofactors are tightly associated, resulting in a distance of 16.6 Å between the two metal centers.¹⁴ Therefore, Emesh et al. assumed that the cationic Arg-138 is more important for interaction and docking of the

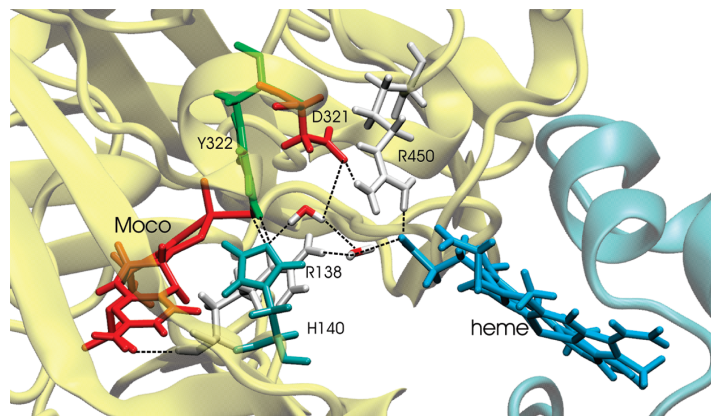


Figure 4. Representative snapshot (asterisk in Figure 2) of the interface area between heme and Moco cofactors. Hydrogen bonds and salt bridges are denoted as dotted lines.

heme domain rather than for IET. In our simulations, Arg-138 is located in the narrow region of the substrate-binding cavity and is not in direct contact with residues of the heme domain. This residue, however, plays an important role in stabilizing the H-bond network in the cavity and constitutes a fundamental link in the IET process in CSO. This observation derived from the theoretical model supports previous experimental results obtained from laser flash photolysis investigations on the R160Q and R160K mutants of human sulfite oxidase. (Arg-160 is the equivalent for Arg-138 in human sulfite oxidase.)¹⁵

In conclusion, by combining the SMD and MD simulations, we were able to generate a sound 3D structural model for the catalytically active “docked” form of CSO characterized by a short (~ 19 Å) Mo–Fe distance as compared with the original crystal structure. The good agreement between computed IET rates and the corresponding experimental values supports the reliability of the proposed structural model.

IET pathways from the Moco to the heme cofactor were identified. The IET between the two redox cofactors is dominated by the pathway involving the Arg138 residue and a single water molecule. Slightly faster, but much less frequent, are the pathways defined by two-to-three water molecules only. Because of the thermal motion of the protein and cofactor atoms, the ET rates fluctuate within two orders of magnitude around an average of $5 \times 10^4 \text{ s}^{-1}$, which is nevertheless in good agreement with the experimental value.⁵

COMPUTATIONAL METHODS

The initial structure of CSO was obtained from the Protein Data Bank (entry code 1SOX).³ Only the homodimeric enzyme including its Mo and heme cofactors and all crystallographic water molecules were extracted out of the crystal structure (1.8 Å resolution). Other fragments were ignored, and simulations were performed in the substrate unbound-state. Each monomer consists of 463 amino acids, one Moco, and one heme cofactor. Missing heavy atoms in the badly

resolved loop region (residues 85–95) and all hydrogens were added with the CHARMM package.¹⁶ Amino acid side chains and histidine residues were protonated according to pH 7 in their environment. In particular, the heme-coordinating histidines were protonated at the δ -nitrogen atoms following the model proposed by Leu et al.¹⁷ This procedure gives a strongly negatively charged protein model with a net charge of -36 e. Afterward, the system was solvated in a rectangular box ($174 \times 119 \times 120.5$ Å³) with explicit TIP3P water molecules¹⁸ and neutralized by the addition of sodium ions with VMD1.8.6.¹⁹ The all-atom simulations were performed with NAMD2.6²⁰ using the CHARMM32b force field.²¹ For the oxidized heme cofactors and the two ligating histidines, we used the parameter set and the partial charges derived by Leu et al.¹⁷ The molybdopterin including the Mo atom was treated as a rigid body using free energy calculations to restrain all internal coordinates. Nonbonding parameters for the Moco, derived by Metz et al. with DFT methods, were applied.²² After energy minimization, heating, and equilibration of the system of $\sim 236,000$ atoms, an SMD was performed for 1 ns, pulling the cytochrome *b5* domain of chain A sequentially toward the Moco cavity. For monomer B, no SMD was applied, but we involved it in the MD simulations to maintain the interaction area between the two monomers. To retain the secondary structure of the cytochrome *b5* domain during the presence of artificial pulling forces, we applied light restraints on its backbone torsions. Additionally, all backbone atoms located outside a 10 Å sphere from the heme iron were restrained to their positions by weak forces of $0.01 \text{ kcal/mol} \cdot \text{Å}^2$. To check for the stability of the gained conformation, a 14 ns long MD relaxation and equilibration phase followed the SMD. All calculations were carried out in an NPT ensemble at 300 K and atmosphere pressure using the Langevin piston method²³ with a time step of 2 fs enabled by rigid bonds applied to all hydrogens.²⁴ The simulations were performed with periodic boundary conditions in all directions, the particle-mesh-Ewald summation for electrostatic interactions,²⁵ and a simple cutoff of 12 Å for van der Waals interactions.

ET reactions over large distances mediated by the protein environment show a very weak coupling. These nonadiabatic ET rates can be described by Marcus theory²⁶

$$k_{\text{ET}} = \frac{2\pi}{\hbar} \frac{\exp[-(\Delta G + \lambda)^2 / 4\lambda k_{\text{B}}T]}{\sqrt{4\pi\lambda k_{\text{B}}T}} |T_{\text{DA}}|^2 \quad (1)$$

where ΔG is the driving force and λ is the reorganization energy. The electronic coupling matrix T_{DA} was approximated with the PATHWAY program,¹⁰ which calculates the electronic coupling matrix T_{DA} between a donor (D) and acceptor (A) for possible electron pathways as follows

$$T_{\text{DA}} \propto \epsilon \prod_i \epsilon_i^{\text{C}} \prod_j \epsilon_j^{\text{HB}} \prod_k \epsilon_k^{\text{TS}} \quad (2)$$

The coupling matrix T_{DA} depends on three possible tunneling modes of the electron. The electron can move along a covalent bond or a hydrogen bond or jump through space. The decay factor for electrons moving along covalent bonds is set to $\epsilon_i^{\text{C}} = \epsilon^{\text{C}} = 0.6$. The decay factors along hydrogen bonds and through-space jumps are distant R -dependent and described as $\epsilon_j^{\text{HB}} = (\epsilon^{\text{C}})^2 \exp(-1.7(R - 2.8))$ and $\epsilon_k^{\text{TS}} = \epsilon^{\text{C}} \exp(-1.7(R - 1.4))$, respectively. In the Pathways calculations, the interaction between the donor or acceptor and the first or the last bond of the tunneling pathway is not taken into account. The computation of the maximum ET reaction rate from the total decay factor, ϵ , is achieved using the following approximation

$$k_{\text{ET}} \approx A|\epsilon|^2 \quad (3)$$

In the same way as that done by Onuchic et al.,¹² we approximated the prefactor A to be 10^{14} s^{-1} by assuming that the maximum rate is 10^{13} s^{-1} at donor-to-acceptor separation of 3 Å (two covalent bond steps).²⁷

The ET pathways in CSO were defined, setting the molybdenum atom as electron donor and the iron atom on the heme as the electron acceptor. The strongest electronic coupling (T_{DA}) and the corresponding tunneling pathways were evaluated every 10 ps during the MD simulation.

SUPPORTING INFORMATION AVAILABLE Coordinates for the active SO monomer and details regarding the SMD and MD calculations as well as the estimation of IET rates. This material is available free of charge via the Internet at <http://pubs.acs.org>.

AUTHOR INFORMATION

Corresponding Author:

*To whom correspondence should be addressed. E-mail: andrea.mroginski@tu-berlin.de.

ACKNOWLEDGMENT We thank D. N. Beratan and I. Balabin for sharing the Pathway program with us and the Norddeutscher Verbund für Hoch und Höchstleistungsrechnen for providing computational resources. Financial support by the DFG Cluster of Excellence "UniCat" is acknowledged. We thank I. Weidinger and M. Sezer for helpful discussions.

REFERENCES

- Hille, R. The Mononuclear Molybdenum Enzymes. *Chem. Rev.* **1996**, *96*, 2757–2816.
- Macleod, R. M.; Handler, P.; Fridovich, I.; Farkas, W. Purification and Properties of Hepatic Sulfite Oxidase. *J. Biol. Chem.* **1961**, *236*, 1841–1846.
- Kisker, C.; Schindelin, H.; Rees, D. C. Molybdenum-Cofactor-Containing Enzymes: Structure and Mechanism. *Annu. Rev. Biochem.* **1997**, *66*, 233–267.
- Pacheco, A.; Hazzard, J. T.; Tollin, G.; Enemark, J. H. The pH Dependence of Intramolecular Electron Transfer Rates in Sulfite Oxidase at High and Low Anion Concentrations. *J. Biol. Inorg. Chem.* **1999**, *4*, 390–401.
- Sullivan, E. P.; Hazzard, J. T.; Tollin, G.; Enemark, J. H. Electron-Transfer in Sulfite Oxidase: Effects of pH and Anions on Transient Kinetics. *Biochemistry* **1993**, *32*, 12465–12470.
- Feng, C. J.; Kedia, R. V.; Hazzard, J. T.; Hurley, J. K.; Tollin, G.; Enemark, J. H. Effect of Solution Viscosity on Intramolecular Electron Transfer in Sulfite Oxidase. *Biochemistry* **2002**, *41*, 5816–5821.
- Pushie, M. J.; George, G. N. Active-Site Dynamics and Large-Scale Domain Motions of Sulfite Oxidase: A Molecular Dynamics Study. *J. Phys. Chem. B* **2010**, *114*, 3266–3275.
- Kawatsu, T.; Beratan, D. N. Electron Transfer Between Cofactors in Protein Domains Linked by a Flexible Tether. *Chem. Phys.* **2006**, *326*, 259–269.
- Johnson-Winters, K.; Nordstrom, A. R.; Emesh, S.; Astashkin, A. V.; Rajapakshe, A.; Berry, R. E.; Tollin, G.; Enemark, J. H. Effects of Interdomain Tether Length and Flexibility on the Kinetics of Intramolecular Electron Transfer in Human Sulfite Oxidase. *Biochem.* **2010**, *49*, 1290–1296.
- Beratan, D. N.; Betts, J. N.; Onuchic, J. N. Protein Electron-Transfer Rates Set by the Bridging Secondary and Tertiary Structure. *Science* **1991**, *252*, 1285–1288.
- Emesh, S.; Rapson, T. D.; Rajapakshe, A.; Kappler, U.; Bernhardt, P. V.; Tollin, G.; Enemark, J. H. Intramolecular Electron Transfer in Sulfite-Oxidizing Enzymes: Elucidating the Role of a Conserved Active Site Arginine. *Biochemistry* **2009**, *48*, 2156–2163.
- Tan, M. L.; Balabin, I.; Onuchic, J. N. Dynamics of Electron Transfer Pathways in Cytochrome *c* Oxidase. *Biophys. J.* **2004**, *86*, 1813–1819.
- Lin, J. P.; Balabin, I. A.; Beratan, D. N. The Nature of Aqueous Tunneling Pathways Between Electron-Transfer Proteins. *Science* **2005**, *310*, 1311–1315.
- Kappler, U.; Bailey, S. Molecular Basis of Intramolecular Electron Transfer in Sulfite-Oxidizing Enzymes is Revealed by High Resolution Structure of a Heterodimeric Complex of the Catalytic Molybdopterin Subunit and a *c*-Type Cytochrome Subunit. *J. Biol. Chem.* **2005**, *280*, 24999–25007.
- Feng, C. J.; Wilson, H. L.; Hurley, J. K.; Hazzard, J. T.; Tollin, G.; Rajagopalan, K. V.; Enemark, J. H. Essential Role of Conserved Arginine 160 in Intramolecular Electron Transfer in Human Sulfite Oxidase. *Biochemistry* **2003**, *42*, 12235–12242.
- Brooks, B. R.; Brucoleri, R. E.; Olafson, B. D.; States, D. J.; Swaminathan, S.; Karplus, M. CHARMM: A Program for Macromolecular Energy, Minimization, and Dynamics Calculations. *J. Comput. Chem.* **1983**, *4*, 187–217.
- Leu, B. M.; Zhang, Y.; Bu, L. T.; Straub, J. E.; Zhao, J. Y.; Sturhahn, W.; Alp, E. E.; Sage, J. T. Resilience of the Iron Environment in Heme Proteins. *Biophys. J.* **2008**, *95*, 5874–5889.
- Jorgensen, W. L.; Chandrasekhar, J.; Madura, J. D.; Impey, R. W.; Klein, M. L. Comparison of Simple Potential Functions for Simulating Liquid Water. *J. Chem. Phys.* **1983**, *79*, 926–935.
- Humphrey, W.; Dalke, A.; Schulten, K. VMD: Visual Molecular Dynamics. *J. Mol. Graphics* **1996**, *14*, 33–38.

- (20) Phillips, J. C.; Braun, R.; Wang, W.; Gumbart, J.; Tajkhorshid, E.; Villa, E.; Chipot, C.; Skeel, R. D.; Kale, L.; Schulten, K. Scalable Molecular Dynamics with NAMD. *J. Comput. Chem.* **2005**, *26*, 1781–1802.
- (21) MacKerell, A. D., Jr.; Bashford, D.; Bellott, M.; Dunbrack, R. L., Jr.; Evanseck, J. D.; Field, M. J.; Fischer, S.; Gao, J.; Guo, H.; Ha, S.; et al. All-Atom Empirical Potential for Molecular Modeling and Dynamics Studies of Proteins. *J. Phys. Chem. B* **1998**, *102*, 3586–3616.
- (22) Metz, S.; Thiel, W. A Combined QM/MM Study on the Reductive Half-Reaction of Xanthine Oxidase: Substrate Orientation and Mechanism. *J. Am. Chem. Soc.* **2009**, *131*, 14885–14902.
- (23) Feller, S. E.; Zhang, Y. H.; Pastor, R. W.; Brooks, B. R. Constant Pressure Molecular Dynamics Simulation: The Langevin Piston Method. *J. Chem. Phys.* **1995**, *103*, 4613–4621.
- (24) van Gunsteren, W. F.; Berendsen, H. J. C. Algorithms for Macromolecular Dynamics and Constraint Dynamics. *Mol. Phys.* **1977**, *34*, 1311–1327.
- (25) Darden, T.; York, D.; Pedersen, L. Particle Mesh Ewald: An $N \cdot \log(N)$ Method for Ewald Sums in Large Systems. *J. Chem. Phys.* **1993**, *98*, 10089–10092.
- (26) Marcus, R. A.; Sutin, N. Electron Transfers in Chemistry and Biology. *Biochim. Biophys. Acta* **1985**, *811*, 265–322.
- (27) Gray, H. B.; Winkler, J. R. Long-Range Electron Transfer. *Proc. Natl. Acad. Sci. U.S.A.* **2005**, *102*, 3534–3539.

10.3 Adsorption of Sulfite Oxidase on Self-Assembled Monolayers from Molecular Dynamics Simulations

Tillmann Utesch, Murat Sezer, Inez M. Weidiger, and Maria Andrea Mroginski

Reprinted with permission from *Langmuir* (2012), 28, 5761-5769

Copyright 2012 American Chemical Society.

Overview

To investigate the influence of a gold surface coated with amino-terminated SAMs on the flexibility of SO, classical MD simulations of the enzyme's adsorption were performed under different ionic strength conditions. To avoid long reorientations, the SO homodimer was positioned on the SAM with its dipole normal to the surface. It was demonstrated that the ionic strength had a high bearing on the adsorption behaviour of the SO homodimer, as it had been proposed earlier [68]. While the C-terminus and the cytochrome *b5* domains adsorbed strongly on positively charged SAMs under low ionic strength conditions, only sporadic contacts between the cytochrome *b5* unit and the monolayer were identified under high ionic strength of 750 mM. These results were induced by the repulsive anion layer formed on the SAM. This adlayer was much more pronounced at 750 mM ionic strength. The stable formation repelled the negatively charged cytochrome *b5* domains and avoided their immobilization on the SAM.

These variations in adsorption strength had a strong implication on the ET properties. As stated in chapter 10.2, a high flexibility of the cytochrome *b5* units is required for the formation of an activated conformation and for fast IET. However, the required domain motion was interrupted at low ionic strength conditions by the stable immobilization, but was still granted at higher ionic strength where the adsorption was inhibited by the ion adlayer. These results agree very well with the spectro-electrochemical measurements obtained by Sezer et. [68].

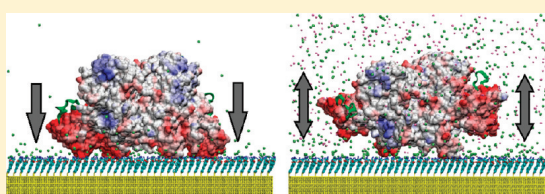
Adsorption of Sulfite Oxidase on Self-Assembled Monolayers from Molecular Dynamics Simulations

Tillmann Utesch,[†] Murat Sezer,[‡] Inez M. Weidinger,[†] and Maria Andrea Mroginski^{*,†}

[†]Technische Universität Berlin, Institut für Chemie, Sekr. PC 14, 10623 Berlin, Germany

[‡]ITQB-UNL, Av. da República, Estação Agronómica Nacional, 2780-157 Oeiras, Portugal

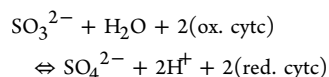
ABSTRACT: Sulfite oxidase (SO) is an enzyme catalyzing the terminal step of the metabolism of sulfur-containing amino acids that is essential for almost all living organisms. The catalytic activity of SO in vertebrates strongly depends on the efficiency of the intramolecular electron transfer (IET) between the catalytic Moco domain and the cytochrome *b5* (cyt *b5*) domain. The IET process is assumed to be mediated by large domain motions of the cyt *b5* domains within the enzyme. Thus, the interaction of SO with charged surfaces may affect the mobility of the cyt *b5* domain required for IET and consequently hinder SO activation. In this study, we present a molecular dynamics approach to investigating the ionic strength dependence of the initial surface adsorption of SO in two different conformations—the crystallographic structure and the model structure for an activated SO—onto mixed amino- and hydroxyl-terminated SAMs. The results show for both conformations at low ionic strengths a strong adsorption of the cyt *b5* units onto the SAM, which inhibits the domain motion event required for IET. Under higher ion concentrations, however, the interaction with the surface is weakened by the negatively charged ions acting as a buffer and competing in adsorption with the cathodic cyt *b5* domains. This competition prevents the immobilization of the cytochrome *b5* units onto the surface, allowing the intramolecular domain motions favoring IET. Our predictions support the interpretation of recent experimental spectroelectrochemical studies on SO.



1. INTRODUCTION

Sulfite oxidation catalyzed by enzymes is present in prokaryotic and eukaryotic organisms.^{1–3} The sulfite oxidase (SO) of vertebrates is a homodimeric protein holding a molybdenum (Mo) atom that is responsible for the final step in the degradation of sulfur-containing amino acids that is, *inter alia*, essential in humans. Inherited SO deficiency leads to severe neurological defects and subsequently to early death.⁴ Although the first therapeutic success in a clinical case study has been made recently,⁵ many questions, in particular, those concerning the SO functionality, are still open.

During the catalytic process, sulfite is oxidized to sulfate and two electrons are transferred sequentially from the active site, the molybdenum cofactor (Moco), via the N-terminal *b*-type-heme located in the small cyt *b5* domain to 2 equiv of ferricytochrome *c*.¹



Although a lot of effort has been expended in investigating the intramolecular and intermolecular electron transfer mechanisms, they are still not completely understood. Deeper insight into the molecular structure was granted by resolving the crystallographic structure of the chicken liver SO,⁶ which is a typical representation for a vertebrate SO. The structure shows the two redox centers—the Moco and heme cofactors—with a large separation distance of ~ 32 Å. Unfortunately, this

structural observation and the experimentally determined ultrafast intramolecular electron transfer (IET) rates are in conflict with each other.^{6,7} Therefore, Pacheco et al. proposed a scheme explaining the high IET rates.⁸ In their model, they postulated a reorientation of the cyt *b5* domains with respect to the active site. The suggested domain motion is based on two facts. On the one hand, the electrostatic attraction between the negatively charged cyt *b5* domain and the positively charged region of the active site drives and stabilizes the activated conformation. On the other hand, the very flexible tether connecting the cyt *b5* unit with the large Moco/dimerization domain enables the reorientation process by providing the needed mobility of the cyt *b5* domains. The importance of these two major features has been reinforced by mutagenesis experiments where selected amino acids of the active site and the linker were replaced.^{9–11} In addition to these measurements, studies changing the viscosity and the pH of the solution strongly strengthened the hypothesis of domain motion by showing viscosity-dependent IET rates.¹² Furthermore, theoretical investigations based on molecular dynamics (MD) simulations showed the high mobility of the cytochrome *b5* domains enabled by the flexible tether region.¹³ In these studies, the high mobility was proven, but the transition to a catalytically active structure of SO was lacking. The so-called activated conformation of SO, characterized by a

Received: December 21, 2011

Revised: February 28, 2012

Published: March 2, 2012

short Moco–heme distance, was derived by pulling the cytochrome *b5* domain with artificial forces toward the active site using the steered molecular dynamics simulations approach.¹⁴ The resulting conformation exhibited a high stability at least on the nanosecond timescale. In addition, the estimated IET rates were in good agreement and of the same order of magnitude as measured experimentally.⁷

To exploit the catalytic properties of SO for technological applications, (i.e., as a sulfite biosensor¹⁵), the enzyme has to be immobilized on a conducting support. First measurements of SO bound to amino-functionalized electrodes lead to a drastic decrease in the catalytic turnover rate.¹⁶ This result was rationalized by the strong interaction of the anionic *cyt b5* domain with the positively charged electrode interface, which prevented the formation of the activated Moco–heme complex necessary for fast IET.

Recent spectroelectrochemical investigations furthermore revealed a strong dependence of the IET and catalytic properties on the ionic strength of the buffer solution.^{17–19} In their work, Sezer and co-workers observed for high ionic strength conditions a drastic increase in the IET and apparent turnover rates.¹⁹ In agreement with dipole moment calculations, it was suggested that the SO dimer preferentially binds via its dimerization unit to the amino-terminated SAM with the *cyt b5* unit attached either to the Moco binding domain or to the SAM interface. The increase in ionic strength is then primarily related to the increased mobility of *cyt b5* and thus to its ability to switch between these two conformations. Thus, these results support the idea that uninhibited IET in SOs is possible only by conserving the high flexibility of the small *cyt b5* units.

To review this hypothesis and to gain more detailed insight into the complex surface–enzyme–solution system and its intermolecular interactions, we addressed the problem, namely, the immobilization of SO onto functionalized surfaces, from a theoretical point of view. For this purpose, we employed a classical all-atom MD simulation approach. The evaluation of proteins adsorbing on surfaces with MD simulations is a widely used and established technique.^{20–22} Within today's computational methods, MD simulations provide a suitable trade-off between accuracy and computational time for systems containing several hundred thousand atoms. They also allow a detailed view at the atomic level of processes on the nanosecond timescale involving complex macromolecular systems.²¹ This theoretical technique has been applied, for example, to sample initial orientation of proteins on surfaces and to the identification of important interaction hot spots.²² Processes such as the equilibration of proteins on surfaces or large reorganization events such as domain motions or protein folding can only be inferred because they take place on timescales of minutes or even hours.

In this work, we present the outcome collected from a series of MD simulation of the dimeric SO enzyme adsorbed on mixed amino- and hydroxyl-terminated SAMs at different ionic strengths. Our theoretical results support the idea that the ionic strength of the buffer solution affects the initial adsorption properties of the enzyme and in turn its catalytic activity.

2. MATERIALS AND METHODS

2.1. Protein, Sulfite Oxidase. The MD simulations reported in this work were performed using two conformations of the sulfite oxidase (SO) homodimer, which mainly differ from each other in the arrangement of the *cyt b5* subunit relative to the molybdenum binding domain (Figure 1). The initial coordinates for the first conformation

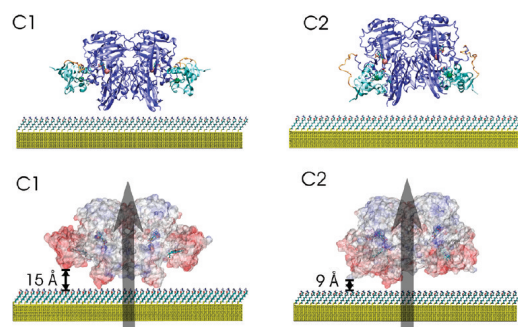


Figure 1. Initial orientations of SO on the SAM-coated gold surface in the C1 (left) and C2 (right) conformations. (Top) Domain structure of the SO: the Moco/dimerization domains of both monomers (dark blue), the *cyt b5* units (cyan), and the flexible linker regions (orange). The green and orange spheres depict the Fe and the Mo metal centers. (Bottom) Electrostatic potential surface of the enzyme on the surface. The red and blue parts describe negatively and positively charged surface regions, respectively. The gray arrow shows the direction of the total dipole moment of SO.

(conformation 1) were taken from the high-resolution (1.8 Å) crystallographic structure of chicken liver SO (1sox), characterized by a long separation distance between the two redox centers of about 32 Å.⁶ The atoms of the badly resolved tether region (amino acids 85–95) were incorporated into the CHARMM package²³ to obtain a well-connected protein structure. The second conformation (conformation 2) represents a model for the catalytically active form of SO where the molybdenum and the *cyt b5* subunits are tightly associated with each other as reflected by the shorter Mo–Fe distance of ca. 19 Å. The initial coordinates for conformation 2 were extracted from a theoretical model obtained by a steered MD approach combined with MD simulations and described in detail in a previous publication.¹⁴ In both conformations and without a loss of generality, we ignored the presence of the sulfite/sulfate substrate by assuming that it had already left the active site after rapidly transferring two electrons to the Mo center.

In all simulations, the apoprotein was described with the CHARMM32 force field.²⁴ For the heme cofactor and the two ligating histidines, we used the parameter set derived by Leu and co-workers.²⁵ The molybdopterin, including the Mo atom, was treated as a rigid body by applying hard restraints to all internal coordinates. This Mo cofactor was described using the nonbonding parameters derived by Metz et al.²⁶

Hydrogen atoms were inserted into the CHARMM package.²³ The protonation state of the amino acid side chains was set according to pH 7.0. Histidine protonation was manually adjusted to their environment, resulting in a protonation on the δ nitrogen for the heme-coordinating histidines, which is in agreement with the model of Leu et al.²⁵

2.2. Surface, SAM-Coated Gold. The surface employed for the adsorption simulations consisted of a pure defect-free Au(111) support surface functionalized in a 4/1/1 ratio of 6-mercaptohexanol ($S-(CH_2)_6-OH$), uncharged 8-aminooctanethiol hydrochloride ($S-(CH_2)_8-NH_2$), and protonated 8-aminooctanethiol hydrochloride ($S-(CH_2)_8-NH_3^+$) self-assembled monolayers (SAMs).

The protonation level of the amino-terminated SAMs was set to 50% as a crude estimation of the conditions that may be found at pH 7.0. The result obtained by Fears et al.²⁷ for pure amino-terminated SAMs was considered to be a reference point. All alkanethiol SAMs were covalently bound via their sulfur atoms to the gold slab, leading to a $(\sqrt{3} \times \sqrt{3})R30^\circ$ lattice of SAMs initially tilted by 30° on the gold electrode. The resulting nearest-neighbor spacing between the sulfur atoms in the lattice was 4.98 Å, as described earlier in the literature.²⁸ The SAMs were described with the CHARMM32 force field for

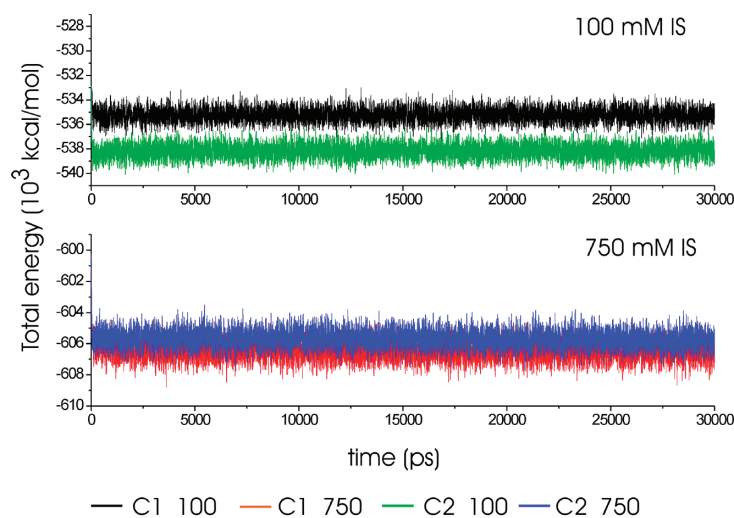


Figure 2. Convergence of the total energy (kcal/mol) for the C1_100 (black), C1_750 (red), C2_100 (green), and C2_750 (blue) models.

lipids.²⁴ With these settings, we obtained a total charge of +160 e^- for the SAM surface.

The perfect Au(111) was constructed by the replication of a small unit cell. The gold slab was simulated as uncharged and with the van der Waals (vdW) parameters described by Bizzarri et al.²⁹

2.3. System Setup. The two conformations of SO were placed adjacent to the SAM covering the gold surface and were solvated in explicit TIP3P water.³⁰ The dimensions of the rectangular system boxes were ca. $173 \times 120 \times 128 \text{ \AA}^3$ and contained more than 246 000 atoms for both conformations. By analogy to Sezer's experiments,¹⁹ we performed the simulations under 100 and 750 mM ionic strength (IS) buffer solutions containing sodium and chloride ions.

We prepared a total of four simulation systems: conformation 1 with 100 mM IS (C1_100) and 750 mM IS (C1_750) and conformation 2 with 100 mM IS (C2_100) and 750 mM IS (C2_750). In all four constructed systems, the initial separation distance between the surface, including the SAM and the SO, was set to ca. 5 \AA in order to avoid long preadsorption times. The orientation of the SO with respect to the surface was defined according to the dipole moment of the enzyme, which was computed by taking the center of mass as the reference. In all systems, the dipole moment was arranged normal to the gold plane reflecting the most probable orientation (Figure 1).³¹

2.4. Molecular Dynamics Simulations. In the first step, the four simulation systems were subjected to 30 000 energy minimization steps with the conjugated gradient algorithm. During this procedure, all heavy atoms were constrained to their positions. Initially, we applied a constraining force of $50 \text{ kcal}\cdot\text{mol}^{-1}\cdot\text{\AA}^{-1}$, which we stepwise decreased to $0.5 \text{ kcal}\cdot\text{mol}^{-1}\cdot\text{\AA}^{-1}$ at the end of the minimization. Each system was then heated to 300 K while weakly constraining the heavy atoms to their positions with a force of $0.5 \text{ kcal}\cdot\text{mol}^{-1}\cdot\text{\AA}^{-1}$. Afterward, a 60-ps-long solvent equilibration run was performed in order to hydrate the enzyme and the SAM surface properly. During the first half (30 ps) of this water equilibration step, the position of the heavy atoms of the SO and the SAM were kept weakly constrained as in the previous steps, with a force of $0.5 \text{ kcal}\cdot\text{mol}^{-1}\cdot\text{\AA}^{-1}$. These constraints were then removed from the systems, and all atoms were allowed to move freely in space during the remaining 30 ps. To maintain the integrity of the gold support and ensure a stable coverage with SAMs, we fixed all gold and sulfur atoms to their positions during all simulations.

The production run consisted of a 30 ns all-atom MD simulation where all atoms, except for the gold and sulfur atoms of the SAMs, were allowed to move freely. These simulations were carried out with the NAMD2.7 package³² by keeping the pressure (1 atm),

temperature (300 K), and cell size along the surface area constant. This NPAT ensemble was modeled with the Langevin piston method.³³ In doing so, we obtained an infinite surface in the x and y directions. A time step of 2 fs was possible via the RATTLE algorithm, which treats all bonds containing hydrogen atoms as rigid.³⁴ The vdW interactions and short-range electrostatics were handled with a simple cutoff of 12 \AA , and long-range electrostatics in the periodic system were calculated with the particle mesh Ewald (PME) summation.³⁵

The evolution of the adsorption course was monitored by evaluating the interaction energies and the number of contacts between the SO and the SAM. The number of contacts between the SO and the SAM is simply defined as the number of protein atoms within 5 \AA of the SAM surface. Average interaction energies between the protein and the surfaces during the last 10 ns of the MD simulations were computed using the NAMD energy plug-in in the VMD package.^{31,36}

3. RESULTS AND DISCUSSION

3.1. Protein Stability. The total energy plots shown in Figure 2 clearly reflect the stability of the four systems along the 30 ns MD simulation at 300 K. In all four cases, the total energy remains stable at around the corresponding average value (-6.07×10^5 , -6.06×10^5 , -5.38×10^5 , and -5.35×10^5 kcal/mol for C1_750, C2_750, C2_100, and C1_100, respectively), with standard deviations of only 500 kcal/mol. In particular, according to our calculations, the systems that were modeled at high ionic strength exhibit the lowest total energy values whereas those modeled at lower ionic strength are predicted to have ca. 12% higher energy.

The structural stability of the SO on the SAM-coated gold surface was further analyzed by calculating the root-mean-square deviation (rmsd) of the backbone atoms. The rmsd values were computed for each single domain (the Moco/dimerization domain and the cyt *b5* unit of both monomers) separately in order to exclude the overall structural reorientation caused by possible domain motion within the enzyme and the high flexibility of the linker region (Figure 3). For all models, the Moco/dimerization domain and the two cyt *b5* units showed high structural stability as reflected by the relatively low rmsd values of less than 2 \AA computed during the entire

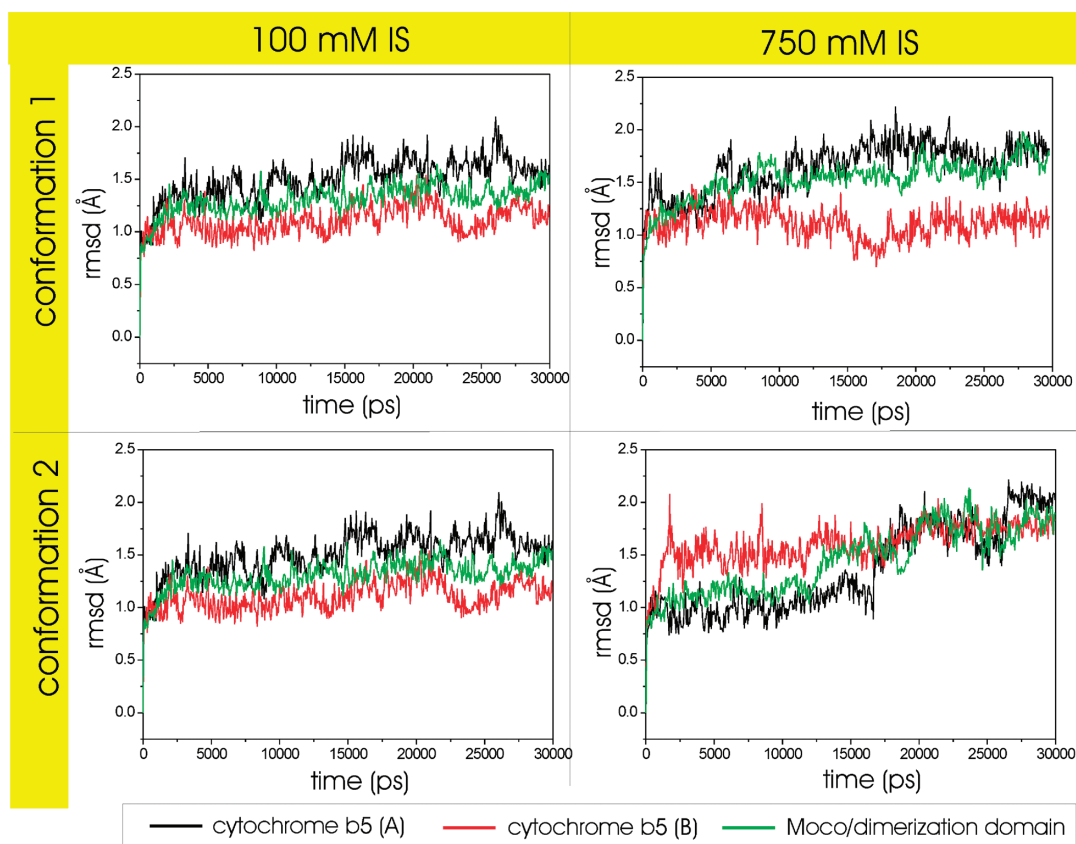


Figure 3. Root-mean-square deviations (rmsd) for the Moco/dimerization domain (green) and cyt *b5* domains of monomer A (black) and monomer B (red) as a function of time.

simulations. This indicates that the initial interaction with the surface does not alter the main backbone conformation of the individual domains but initially leads to a strong reorientation of the protein side chains in the vicinity of the SAM surface. The only regions showing high rmsd values (between 4 and 5 Å) were, as expected, the linker regions between the cyt *b5* units and the Moco/dimerization domain (plot not shown).

The reorientation of the amino acid side chains of the SO according to the electric field of the SAM is mirrored in the evolution of the protein dipole moment (Figure 4). In particular, we observe that within the first nanoseconds the dipole moment of the SO under low ionic strength conditions drastically increases from its initial values of ca. 1200 and 1800 D to more than 2000 and 2300 D for conformations C1 and C2, respectively. During the MD simulations, these values slightly increase, reaching final stable average values of 2300 and 2500 D, respectively, for each conformation. This high reorganization effect of the protein side chains under low ionic strength is weakened under high ionic strength conditions where the dipole moment displayed only small increases of 100 D for C1 and 250 D for C2. In these systems, the electric field of the SAM is buffered by the large number of Cl⁻ ions adsorbing to the surface.

3.2. Adsorption Behavior. Despite the high structural stability of the SO shown during all simulations, the adsorption behavior on the nanosecond timescale, differed depending on

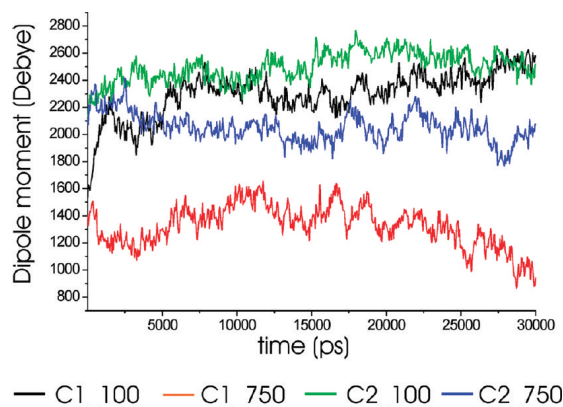


Figure 4. Total dipole moments (debye) of the C1_100 (black), C1_750 (red), C2_100 (green), and C2_750 (blue) models as a function of time.

the ionic strength of the system and the initial conformation of the enzyme. In particular, the different arrangements of the cyt *b5* domains within the SO protein that characterize the C1 and C2 conformations led to two distinct initial structures with unequal separation distances between the cyt *b5* domains and the SAM. For C1, we compute a minimum separation distance

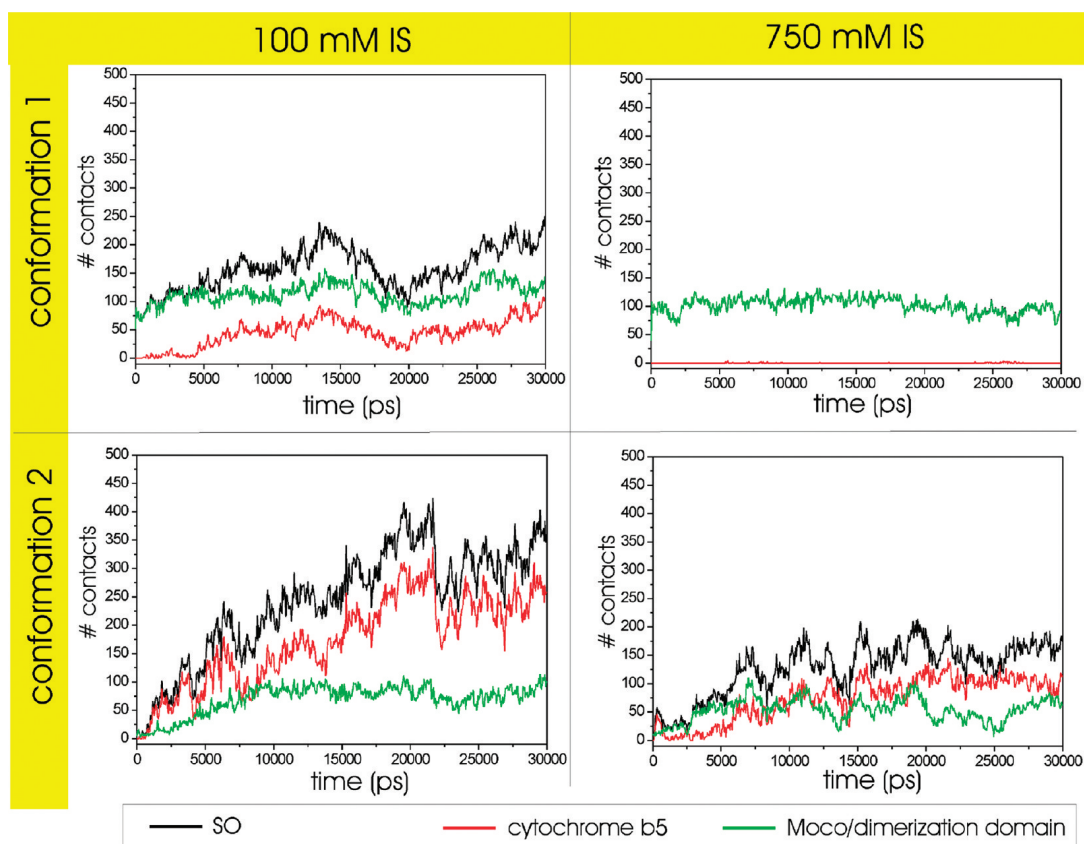


Figure 5. Number of contacts between the surface and the Moco/dimerization domain (green), cyt *b5* domains (red), and the entire SO enzyme (black) as a function of time.

of ~ 15 Å, which decreases to ~ 9 Å for the C2 conformation (Figure 1). This structural difference between the two equilibrated conformations influences the early steps of the protein adsorption process.

In addition, the structural analysis of the starting conformations and their electronic potential energy surfaces suggest that two main adsorption hot spots of the SO facing the functionalized gold surface exist, namely, the C termini of both SO monomers and the cyt *b5* domains (Figure 1). In the first case, the two flexible, negatively charged C termini not only exhibit the shortest initial separation distances but also are clearly exposed, in both conformations, to the SAM. Thus, we expected them to interact electrostatically with the positively charged $-\text{NH}_3^+$ headgroups of the monolayer and act as anchors in initializing the adsorption and enabling the approximation of further neighboring amino acids toward the surface. In the second case, the cyt *b5* domains with their strong anionic character facing the positively charge SAM surface are expected to move toward the surface and establish Coulomb contacts with the monolayer.

The structural asymmetry and electrostatic difference between the monomers in the C2 form, resulting from the high flexibility of the linker during the modeling procedure,¹⁴ induce a slight change in the direction of the total dipole moment compared to that of C1 and, consequently, a different

orientation of the two cyt *b5* domains with respect to the surface.

3.2.1. C1 Conformation. As expected, the C-terminal region of the C1 conformer of SO established strong contacts with the adjacently located SAM headgroups during the short pre-equilibration run. This quick reorientation of the side chains toward the surface appeared under both high and low ion concentrations, as reflected by the rapid change in the enzyme's dipole moment. Within the short pre-equilibration period of 60 ps, two C-terminal hot spots—the C-terminal end (Asp466, Gln465, Val464 and Ser 463) on the one hand and a strongly anionic loop region (Glu420, Ala421, Thr423, and Glu424) on the other hand—adsorbed on the SAM by fast reorientations of the protein side chains according to the electric field of the surface. The number of contacts that aggregate rapidly within a couple of picoseconds is approximately 100, which further supports the favorable role of this initial adsorption configuration. These mainly electrostatically driven interactions between the positively charged SAM headgroups and the anionic loops were slightly weakened under 750 mM IS. Glu420 seems to be responsible for this and loses contact with the surface.

In the first 5 ns of the simulation, residues of the Moco/dimerization domain still dominate the adsorption on the SAM under both ion concentrations. On average, the Moco/dimerization domain establishes 113.1 ± 18.3 and 101.6 ± 13.7 contacts in 100 and 750 mM IS, respectively (Figure 5).

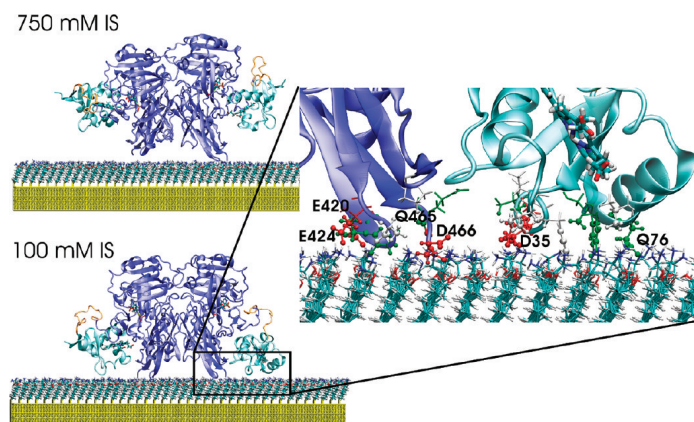


Figure 6. Orientation of SO after 30-ns-long MD simulations for the C1 conformation under 100 mM (top) and 750 mM (bottom) IS conditions. On the right, the adsorption interface between one monomer of the SO and the surface is shown. In this representation, all protein atoms within 5 Å of the surface are indicated (ball and sticks) and the corresponding amino acids are marked as sticks.

Besides the stable adsorption of the two in the C-terminal hotspots region, sporadic contacts between other regions of the Moco/dimerization domain and the surface are also observed. These contacts, involving, for example, Pro362 and Arg390, had short lifetimes of less than 100 ps and were therefore considered to be thermal fluctuations.

In contrast to the nearly ionic-strength-independent adsorption of the Moco/dimerization domain, the adsorption behavior of the anionic cyt *b5* units, initially settled more than 15 Å away from the SAM, showed a high dependency on the ion concentration. Although the cytochrome *b5* domains at a low ionic strength of 100 mM translated toward the surface and adsorbed after ~4 ns, the high ionic strength of the 750 mM Na⁺Cl⁻ buffer solution inhibited the entire domain motion, at least during the 30-ns-long MD simulation. Nevertheless, even under high ionic strength conditions, the presence of the charged SAM surface led to the reorganization of side chains in the cytochrome *b5* domains. In this case, however, only sporadic direct contacts between the cyt *b5* domains and the SAM were monitored (Figure 5).

At 100 mM IS, the most important residues involved in the adsorption of cyt *b5* are the negatively charged regions spanned by glutamic and aspartic acids (Glu11, Glu19, Glu20, Asp35, Glu38, and Glu72). These interactions arise after ca. 4 ns and accumulate during the remaining MD simulation. The sudden decrease in the number of contacts at about 20 ns is related to the change in orientation of the cyt *b5* domain of monomer A with respect to the SAM. At this point, the direct contacts of Glu19 and Glu20 with the surface are replaced by interactions involving the hydrophobic helix containing Glu72. This rotation or rolling of SO on the surface leads to the tilting of the heme cofactor with respect to the SAM from an initially parallel orientation to a 45° tilted conformation. Under the 750 mM IS condition, however, the orientation of both heme cofactors with respect to the surface remained unchanged within the 30 ns simulation (Figure 6).

3.2.2. C2 Conformation. The C2 conformation of SO displayed a similar adsorption behavior in terms of the C-terminal regions as observed for the C1 conformation, but with a certain delay. This lag time probably resulted from the initial placing of the SO on the highly ordered SAM. Sporadic initial contacts have already been established during the pre-equilibration run,

but approximately 2.5 ns is required to achieve stable adsorption involving at least 50 atoms of the enzyme. Interestingly, the number of contacts involving residues on the Moco/dimerization domain increases only slightly during the first 10 ns of the MD simulation until an average value of about 81 contacts is reached. Under low ionic strength conditions, the average number of contacts remains relatively steady with a standard deviation of only 13 contacts, but under high ionic strength condition, the number of adsorbed atoms of the Moco/dimerization domain strongly oscillates around 56 ± 19 contacts (Figure 5). The decreased number of contacts plus its high fluctuation is a strong indicator of the looser interaction between the Moco/dimerization domain and the SAM surface at high ionic strength. As observed for the C1 conformation, the initial contact of the C-terminal region was arranged by Asp466, which adsorbed stably even under high ion concentrations. Besides this initial anchor, the neighboring amino acids (Gln465, Val464, and Ser463) adsorbed sporadically at both ionic strengths.

After the first stable anchor point through Asp466 was established, the loop region involving Glu420, Ala421, Gly422, Thr423, and Glu424 interacted quickly within several hundred picoseconds with the SAM. Under both salt concentrations, the adsorption strength and stability of this second C-terminal hot spot was very high because of, inter alia, the formation of a salt bridge between the $-\text{NH}_3^+$ headgroups of the SAM and the negatively charged glutamic acids of the loop.

The adsorption behavior of the cyt *b5* domain in the C2 conformation undoubtedly depends on the ion concentration of the buffer solution, as clearly indicated by the corresponding number of contact plots. First, whereas under a low ion concentration the cyt *b5* domains establish stable contacts within 1 ns, this requires more than 5 ns for adsorption onto the SAM in 750 mM IS (Figure 5). Besides this initial adsorption delay, a large discrepancy in the number of contacts was monitored under different ion concentrations. An analysis of the last 20 ns of the MD simulation revealed 218 ± 49 and 96 ± 19 contacts on average for each system at 100 and 750 mM, respectively. The factor of 2 can be explained by monitoring the behavior of each monomer separately. Under high ion concentrations, only the cyt *b5* domain of one monomer adsorbs on the SAM whereas the cyt *b5* domain of the other monomer showed a

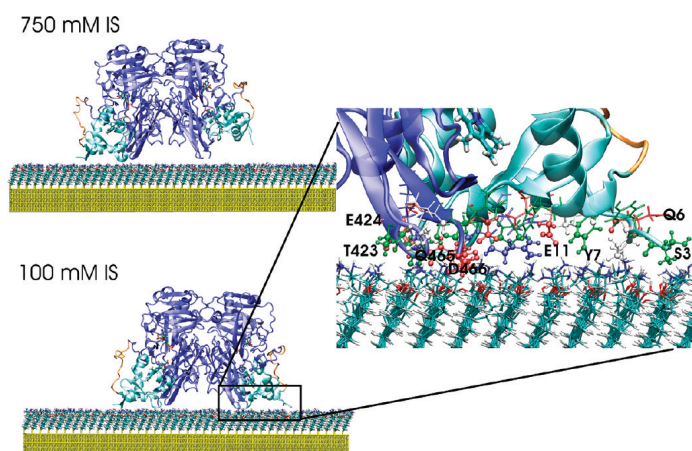


Figure 7. Orientation of the SO after 30-ns-long MD simulations for the C2 conformation under 100 mM (top) and 750 mM (bottom) IS conditions. On the right, the adsorption interface between one monomer of the SO and the surface is shown. In this representation, all protein atoms within 5 Å of the surface are indicated (ball and sticks) and the corresponding amino acids are marked as sticks.

Table 1. Average Electrostatic Interaction Energies (kcal/mol) between SO and the Surface at 100 and 750 mM Ionic Strengths (IS)^a

	C1		C2	
	100 mM IS	750 mM IS	100 mM IS	750 mM IS
SO–surface	-3820 ± 743	-1793 ± 558	-3969 ± 723	-1811 ± 668
SO–SAM	-4613 ± 294	-1143 ± 280	-5138 ± 219	-2899 ± 249
cyt b5–surface	-1747 ± 527	-16 ± 312	-2426 ± 490	-784 ± 438
cyt b5–SAM	-3274 ± 209	-387 ± 175	-3266 ± 117	-1897 ± 141
Moco–surface	-2097 ± 345	-1837 ± 367	-1485 ± 369	-1082 ± 439

^aThe surface is defined as the SAM together with a 5 Å adlayer of ion and water molecules.

very weak, sporadic interaction with the surface before desorbing into the bulk solution (Figures 5 and 7). The discrepancy in adsorption between the two monomers on the SAM is most probably caused by the lack of symmetry of the system and the distinct orientation of the two monomers with respect to the SAM. In addition, the initial random distribution of ions and the protonation pattern of the SAM may lead to differences in the simulations.

3.2.3. Interaction Energies between SO and a Surface. The strength of adsorption of SO onto a SAM can be quantified through the computation of the interaction energies between the surface and the enzyme, which are listed in Table 1. For these calculations, the surface is defined as the SAM together with the 5 Å adlayer of water molecules and ions. The interaction energies were averaged over the last 10 ns of the MD trajectories.

According to our calculations, the interaction energies between SO and the surface computed at 100 mM are significantly higher than those computed at 750 mM, independently of the initial configuration of the enzyme. For both configurations, we predict at 100 mM final average interaction energies on the order of -3900 kcal/mol. At high ionic strength, however, these interaction energies decrease by ca. 54%. The positive contribution to the total interaction energy between the enzyme and the surface ($E_{\text{SO-surface}} - E_{\text{SO-SAM}}$) coming from the water and ion adlayers reflect the repulsive character of the ion–enzyme and water–enzyme interactions. For the C2 conformation, this repulsive interaction does not vary significantly

with the ionic strength of the buffer solution (1169 kcal/mol at 100 mM IS, 1088 kcal/mol at 750 mM IS). Here, the largest difference in the average interaction energy arises mainly from the interaction of the enzyme with the SAM, which is predicted to be -5138 kcal/mol at 100 mM IS and -2899 at 750 mM IS. Interestingly, in contrast to the other simulation models, for the C1_750 model the negative interaction energy computed between the SO and the adlayer reflects the attractive character of this interaction.

An analysis of the separate contributions from the SO–Moco/dimerization domain and the cyt b5 units to the total interaction energy between the enzyme and the surface demonstrates that the adsorption of the cyt b5 units, in contrast to that from the Moco/dimerization domain, strongly depends on the ionic strength of the buffer solution. In the case of the C1 conformation, the interaction energies decrease by more than 99% if the concentration of ions in the buffer increases from 100 to 750 mM. In the case of the C2 form, the effect of the ion concentration is not as severe. Here, a decrease of only 68% of the cyt b5–surface interaction energy is predicted.

For the interaction energies between the Moco/dimerization domain and the surface, we observe only a slight difference between the two initial conformations ($-2097/-1837$ kcal/mol for the C1_100 and C1_750 models vs $-1484/-1082$ kcal/mol for the C2_100 and C2_750 models). In addition, the effect of the ionic strength is significantly smaller than that predicted for the cyt b5 units. For the Moco/dimerization domain–surface interaction,

we predict 12 and 27% lowerings of the corresponding interaction energies for the C1 and C2 conformations, respectively.

In summary, the values computed for the interaction energies between the enzyme and the surface show quantitatively that (a) SO adsorbs more strongly to the SAM surface when the ionic strength of the buffer solution is low and (b) this distinct adsorption behavior at different ionic strengths is mainly dominated by the interaction of cyt *b5* with the water–ion adlayer.

4. DISCUSSION

Although a detailed understanding of the molecular mechanism enabling the electron-transfer chain in SO is lacking,³⁷ it has been experimentally proven that its catalytic activity, resulting from efficient intramolecular ET between the Moco and the heme cofactor and intermolecular ET to ferricytochrome *c*, depends not only on the integral protein structure but also on the flexibility of the tether connecting the Moco/dimerization and the cyt *b5* domains.^{12,14} This becomes evident when immobilizing the enzyme onto surfaces, where the catalytic turnover rates significantly decrease from 100 s⁻¹ for SO in solution to 2–20 s⁻¹ for the surface-bound enzyme. The loss of catalytic activity of the immobilized SO can be interpreted as a result of the reduction of the flexibility of the tether when it interacts with a material surface.

According to the MD simulations, the overall structure of the SO enzyme and its individual domains in the C1 and C2 conformations are not particularly affected by adsorption onto positively charged SAMs. However, the strong adsorption of the cyt *b5* domains on the SAMs were predicted, in particular, at low ionic strengths, to be responsible for the loss of the mobility of the cyt *b5* units and for the significant decrease in the flexibility of the interdomain linker. Thus, as observed experimentally, we would consequently expect a reduction in the catalytic activity of the immobilized SO compared to that in solution. Furthermore, we predict similar adsorption behavior in the nanosecond time range for both conformations; the adsorption begins with the attachment of the C-termini in the Moco/dimerization domains, which act as an anchor for the latter attachment of the cyt *b5* units. Finally, only minor variations of the C-termini adsorption for 100 and 750 mM IS are observed.

In contrast, the affinity of the cyt *b5* domains toward the SAM is largely affected by the ionic strength of the buffer solution. Under high ionic strength conditions, the contact time between the cyt *b5* units and the SAM is largely decreased by a factor of 4. This effect could also be directly seen in surface-enhanced Raman spectroscopy (SERS) measurements of SO immobilized on SAM-coated Ag electrodes.¹⁹ Here the SERS intensity of the heme chromophore was reversibly decreased by a factor of 1.5 upon going from 5 to 750 mM IS in a Tris-acetate buffer solution, which indicates a larger average distance of the heme to the surface under high ionic strength conditions. The authors explained their results by assuming an immobilization mainly via the Moco/dimerization domain at high ionic strengths and an immobilization of the entire protein, including the cyt *b5* units, at low ionic strengths.

The strong adsorption of the cyt *b5* domains on the SAMs, in particular, at low ionic strengths, is responsible for the loss of mobility of the cyt *b5* units and for the significant decrease in the flexibility of the interdomain linker. Thus, from our calculations, we would consequently expect a reduction of the IET and thus a decrease in the catalytic activity of the immobilized SO compared to that in solution. Again, this is in line

with the experimental findings from the spectroelectrochemical measurements where only at ionic strengths above 100 mM are catalytic sulfite oxidation and subsequent heme reduction observed. The catalytic efficiency of SO is limited under low ionic strength by the strong binding of cyt *b5* to the surface that hinders the interdomain motion, consequently preventing electron flow away from the catalytic Moco center. In the experiments, a constant increase of both the IET and catalytic turnover rates was observed upon increasing the ionic strength, which further underlines the tight correlation between these two processes.

The analysis of our MD simulations performed at two different ionic strengths (IS), namely, at 100 and 750 mM, agrees very well with the experimental data collected by Sezer et al.¹⁹ Independently of the starting conformation of the enzyme, we observed that at low ionic strength there is not only adsorption of the C-terminal loop of the Moco/dimerization domain onto the positively charged SAM but also a strong, stable interaction of the cyt *b5* with the surface. Besides, the flexibility of the linker region is reduced at 100 mM IS compared to that of the 750 mM IS, as indicated by the root-mean-square-fluctuation (rmsf) plots in Figure 8. The rmsf

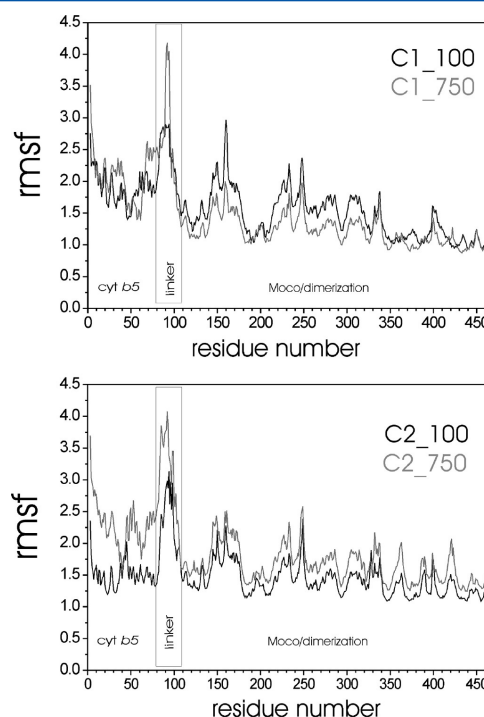


Figure 8. Root-mean-square fluctuations of $C\alpha$ atoms calculated from the MD simulation for the C1 conformation (top) and the C2 conformation (bottom) of the SO in buffer solution at 100 mM (black) and 750 mM (gray) ionic strengths.

describes the fluctuations of the $C\alpha$ atoms of each protein residue during the MD simulation with respect to their average position. The presence of double the number of chloride ions in the surface adlayers is responsible for the weak adsorption of SO at high ionic strength, compared to the situation at low ionic strength, which shields the attractive interaction forces between the enzyme and the positively charged surface.

Although the theoretical calculations presented in this work are in good agreement with experimental data, one must be aware of the deficiencies of the approach. With atomistic-MD simulations, only an early stage of the protein adsorption process can be performed because this technique becomes computationally expensive when predicting the dynamic behavior of large and complex systems beyond the nanosecond timescale. Furthermore, our theoretical results are biased by the initial conformations and orientations of the enzyme with respect to the surface. Although other initial orientations of the SO could result in other adsorption patterns, sampling the entire phase space is not computationally affordable.

5. CONCLUSIONS

The atomistic MD simulations support the assumption that high ionic strength conditions of the buffer solution inhibit, at least on the nanosecond timescale, the adsorption of the cyt *b5* domains on the SAM by competitive adsorption between ions and the cytochrome units and the shielding of the electrostatic attractive forces between the enzyme and surface. Results show that the inhibition of the adsorption process does not occur at lower ionic strengths where the cyt *b5* units are immobilized through strong surface interactions. This adsorption process most likely avoids domain motion events that are essential for intramolecular and intermolecular electron transfer. In addition, we did not observe any significant difference between the early adsorption behavior (30 ns) of the two initial conformations, C1 and C2, characterizing the SO in a catalytically inactive and a catalytically active form, respectively. Finally, these atomistic simulations further emphasize the importance of a flexible tether connecting the Moco and the cyt *b5* domains for efficient electron transfer in surface-bound SO, as already suggested by Sezer et al.¹⁹

AUTHOR INFORMATION

Corresponding Author

*E-mail: andrea.mroginski@tu-berlin.de

Notes

The authors declare no competing financial interest.

ACKNOWLEDGMENTS

We thank the cluster of excellence “Unifying Concepts in Catalysis (UniCat)” and the Fonds der Chemie (IW) for financial support and the North-German Supercomputing Alliance (HLRN) for providing computational resources.

REFERENCES

- Macleod, R. M.; Handler, P.; Fridovich, I.; Farkas, W. *J. Biol. Chem.* **1961**, *236*, 1841–1846.
- Hille, R. *Chem. Rev.* **1996**, *96*, 2757–2816.
- Johnson-Winters, K.; Tollin, G.; Enemark, J. H. *Biochemistry* **2010**, *49*, 7242–7254.
- Dublin, A. B.; Hald, J. K.; Wootton-Gorges, S. L. *Am. J. Neuroradiol.* **2002**, *23*, 484–485.
- Veldman, A.; Santamaria-Araujo, J. A.; Sollazzo, S.; Pitt, J.; Gianello, R.; Yapliito-Lee, J.; Wong, F.; Ramsden, C. A.; Reiss, J.; Cook, I.; Fairweather, J.; Schwarz, G. *Pediatrics* **2010**, *125*, E1249–E1254.
- Kisker, C.; Schindelin, H.; Rees, D. C. *Annu. Rev. Biochem.* **1997**, *66*, 233–267.
- Sullivan, E. P.; Hazzard, J. T.; Tollin, G.; Enemark, J. H. *Biochemistry* **1993**, *32*, 12465–12470.
- Pacheco, A.; Hazzard, J. T.; Tollin, G.; Enemark, J. H. *J. Biol. Inorg. Chem.* **1999**, *4*, 390–401.
- Feng, C. J.; Tollin, G.; Enemark, J. H. *Biochim. Biophys. Acta* **2007**, *2007*, 527–539.
- Emesh, S.; Rapson, T. D.; Rajapakse, A.; Kappler, U.; Bernhardt, P. V.; Tollin, G.; Enemark, J. H. *Biochemistry* **2009**, *48*, 2156–2163.
- Johnson-Winters, K.; Nordstrom, A. R.; Emesh, S.; Astashkin, A. V.; Rajapakse, A.; Berry, R. E.; Tollin, G.; Enemark, J. H. *Biochemistry* **2010**, *49*, 1290–1296.
- Feng, C. J.; Kedia, R. V.; Hazzard, J. T.; Hurley, J. K.; Tollin, G.; Enemark, J. H. *Biochemistry* **2002**, *41*, 5816–5821.
- Pushie, M. J.; George, G. N. *J. Phys. Chem. B* **2010**, *114*, 3266–3275.
- Utesch, T.; Mroginski, M. A. *J. Phys. Chem. Lett.* **2010**, *1*, 2159–2164.
- Spriego, R.; Dronov, R.; Rajagopalan, K. V.; Lisdat, F.; Leimkuhler, S.; Scheller, F. W.; Wollenberger, U. *Soft Matter* **2008**, *4*, 972–978.
- Elliott, S. J.; McElhaney, A. E.; Feng, C. J.; Enemark, J. H.; Armstrong, F. A. *J. Am. Chem. Soc.* **2002**, *124*, 11612–11613.
- Feng, J. J.; Murgida, D. H.; Kuhlmann, U.; Utesch, T.; Mroginski, M. A.; Hildebrandt, P.; Weidinger, I. M. *J. Phys. Chem. B* **2008**, *112*, 15202–15211.
- Millo, D.; Pandelia, M. E.; Utesch, T.; Wisitruangsakul, N.; Mroginski, M. A.; Lubitz, W.; Hildebrandt, P.; Zebger, I. *J. Phys. Chem. B* **2009**, *113*, 15344–15351.
- Sezer, M.; Frielingsdorf, S.; Millo, D.; Heidary, N.; Utesch, T.; Mroginski, M. A.; Friedrich, B.; Hildebrandt, P.; Zebger, I.; Weidinger, I. M. *J. Phys. Chem. B* **2011**, *115*, 10368–10374.
- Utesch, T.; Daminelli, G.; Mroginski, M. A. *Langmuir* **2011**, *27*, 13144–13153.
- Latour, R. A. *Biointerphases* **2008**, *3*, FC2–FC12.
- Zhou, J.; Zheng, J.; Jiang, S. Y. *J. Phys. Chem. B* **2004**, *108*, 17418–17424.
- Brooks, B. R.; Brooks, C. L.; MacKerell, A. D.; Nilsson, L.; Petrella, R. J.; Roux, B.; Won, Y.; Archontis, G.; Bartels, C.; Boresch, S.; Cafilisch, A.; Caves, L.; Cui, Q.; Dinner, A. R.; Feig, M.; Fischer, S.; Gao, J.; Hodosek, M.; Im, W.; Kuczera, K.; Lazaridis, T.; Ma, J.; Ovchinnikov, V.; Paci, E.; Pastor, R. W.; Post, C. B.; Pu, J. Z.; Schaefer, M.; Tidor, B.; Venable, R. M.; Woodcock, H. L.; Wu, X.; Yang, W.; York, D. M.; Karplus, M. *J. Comput. Chem.* **2009**, *30*, 1545–1614.
- MacKerell, A. D. Jr.; Bashford, D.; Bellott, M.; Dunbrack, R. L. Jr.; Evanseck, J. D.; Field, M. J.; Fischer, S.; Gao, J.; Guo, H.; Ha, S.; Joseph-McCarthy, D.; Kuchnir, L.; Kuczera, K.; Lau, F. T. K.; Mattos, C.; Michnick, S.; Ngo, T.; Nguyen, D. T.; Prodhom, B.; Reiher, W. E. I.; Roux, B.; Schlenkrich, M.; Smith, J. C.; Stote, R.; Straub, J.; Watanabe, M.; Wiorkiewicz-Kuczera, J.; Yin, D.; Karplus, M. *J. Phys. Chem. B* **1998**, *102*, 3586–3616.
- Leu, B. M.; Zhang, Y.; Bu, L. T.; Straub, J. E.; Zhao, J. Y.; Sturhahn, W.; Alp, E. E.; Sage, J. T. *Biophys. J.* **2008**, *95*, 5874–5889.
- Metz, S.; Thiel, W. *J. Am. Chem. Soc.* **2009**, *131*, 14885–14902.
- Fears, K. P.; Creager, S. E.; Latour, R. A. *Langmuir* **2008**, *24*, 837–843.
- Strong, L.; Whitesides, G. M. *Langmuir* **1988**, *4*, 546–558.
- Bizzarri, A. R.; Costantini, G.; Cannistraro, S. *Biophys. Chem.* **2003**, *106*, 111–123.
- Jorgensen, W. L.; Chandrasekhar, J.; Madura, J. D.; Impey, R. W.; Klein, M. L. *J. Chem. Phys.* **1983**, *79*, 926–935.
- Rudiger, O.; Abad, J. M.; Hatchikian, E. C.; Fernandez, V. M.; De Lacey, A. L. *J. Am. Chem. Soc.* **2005**, *127*, 16008–16009.
- Phillips, J. C.; Braun, R.; Wang, W.; Gumbart, J.; Tajkhorshid, E.; Villa, E.; Chipot, C.; Skeel, R. D.; Kale, L.; Schulten, K. *J. Comput. Chem.* **2005**, *26*, 1781–1802.
- Feller, S. E.; Zhang, Y. H.; Pastor, R. W.; Brooks, B. R. *J. Chem. Phys.* **1995**, *103*, 4613–4621.
- van Gunsteren, W. F.; Berendsen, H. J. C. *Mol. Phys.* **1977**, *34*, 1311–1327.
- Darden, T.; York, D.; Pedersen, L. *J. Chem. Phys.* **1993**, *98*, 10089–10092.
- Humphrey, W.; Dalke, A.; Schulten, K. *J. Mol. Graphics* **1996**, *14*, 33–38.
- Rajapakse, A.; Meyers, K. T.; Berry, R. E.; Tollin, G.; Enemark, J. H. *J. Biol. Inorg. Chem.* **2011**, *17*, 345–352.

10.4 Insights into the structure of the active site of the O₂ tolerant membrane bound [NiFe] hydrogenase of *R. eutropha* H16 by molecular modelling

Tillmann Utesch, Yvonne Rippers, Peter Hildebrandt, Ingo Zebger, and Maria Andrea Mroginski

published in *Phys. Chem. Chem. Phys.* (2011), 13, 16146-16149

Reproduced by permission of the PCCP Owner Societies.

Overview

The construction and validation of a homology model of the MBH is described. The model was based on known structures of standard [NiFe] hydrogenases. It is important to note that the work was carried out without the knowledge of the now resolved crystallographic structures of oxygen tolerant [NiFe] hydrogenases and was, therefore, more than a proof of principle. At that time, the homology model represented the first three-dimensional model of the MBH.

In order to validate the modelled structure, a combined approach of classical MD simulations and an IR spectra calculation with a QM/MM setup was performed. The approach was able to reproduce experimentally observed spectral shifts induced by mutants adjacent to the active site [209]. This observation indicates a structurally well conserved and unchanged active site between the oxygen tolerant and sensitive species. Further, it was stated that variations in the active site are not the reason for the oxygen tolerance in the MBH.

Cite this: DOI: 10.1039/c1cp21045a

www.rsc.org/pccp

COMMUNICATION

Insights into the structure of the active site of the O₂-tolerant membrane bound [NiFe] hydrogenase of *R. eutropha* H16 by molecular modelling†

Yvonne Rippers,‡ Tillmann Utesch,‡ Peter Hildebrandt, Ingo Zebger and Maria Andrea Mroginski

Received 4th April 2011, Accepted 27th July 2011

DOI: 10.1039/c1cp21045a

Structural models for the Ni-B state of the wild-type and C81S protein variant of the membrane-bound [NiFe] hydrogenase from *Ralstonia eutropha* H16 were derived by applying the homology model technique combined with molecular simulations and a hybrid quantum mechanical/molecular mechanical approach. The active site structure was assessed by comparing calculated and experimental IR spectra, confirming the view that the active site structure is very similar to those of anaerobic standard hydrogenases. In addition, the data suggest the presence of a water molecule in the second coordination sphere of the active centre.

Hydrogenases are enzymes which catalyse the reversible heterolytic cleavage of molecular hydrogen. In the focus of our study are [NiFe] hydrogenases, in which the catalytic site is a bimetallic complex, with two Ni bound terminal cysteine residues, three exogenous diatomic inorganic ligands (one CO and two CN⁻) at the Fe atom, and two further cysteines bridging the two metal atoms.¹ Depending on the particular redox state another, different ligand may occupy an additional bridging position between Ni and Fe. Most members of this enzyme family are oxygen-sensitive and form under electron-deficient conditions with O₂ the so-called ‘unready inactive’ Ni_u-A state, that requires a rather long time (up to several hours) for a reductive (re-)activation by molecular hydrogen, a property that impairs practical applications.¹ The membrane-bound [NiFe] hydrogenase (MBH) from *Ralstonia eutropha* H16 (*ReH16*), however, is capable of oxidizing hydrogen even at atmospheric oxygen levels. Under these conditions only the so-called ‘ready inactive’ Ni_r-B state is formed which is rapidly reactivated on the (sub-)second time scale, while the Ni_u-A state has never been observed for the wild type MBH.^{2,3} Therefore, this enzyme appears to be a promising candidate in the field of biotechnological energy storage and conversion as an alternative to fossil fuels.⁴ Ni_r-B harbors a hydroxide in

the bridging position between Ni and Fe,^{5,6} while a hydroperoxide is suggested to be the bridging ligand in Ni_u-A.⁷ These two states can be distinguished by IR spectroscopy which, in general, is a particularly instructive method for the identification of the various redox states involved in the catalytic cycle by probing the stretching modes of the CO and CN⁻ ligands.^{8,9}

So far, however, no crystallographic structures of oxygen tolerant [NiFe] hydrogenases have been reported, which would facilitate a more detailed investigation of the underlying reaction mechanism at the active site. In this work, we have constructed a homology model for the MBH from *ReH16* using the known three-dimensional (3D) structures of the standard [NiFe] hydrogenases as a template. The homology model was further refined by molecular dynamics (MD) simulations and quantum-mechanics/molecular mechanics (QM/MM) geometry optimizations of the active site, followed by the calculation of the IR spectra. Three structural models of the oxidized MBH in the Ni_r-B state were generated: MBH wild type (*MBH* model), MBH wild type including a water molecule in the second coordination sphere of the [NiFe] center as detected in other 3D structures of oxygen-sensitive hydrogenases (*MBH-H₂O* model) and the C81S variant MBH (*MBH-C81S-H₂O* model) which also contains the extra water. The latter protein variant was chosen because the mutation induces a significant 8 cm⁻¹ shift of the CO stretching in the experimental IR spectrum.¹⁰ Hence, the reproduction of a mutation-induced shift is considered as a more reliable criterion for the quality of the homology model in the active site than a comparison between the wild type MBH and the template enzyme *D. gigas* for which the frequency difference was only 2 cm⁻¹ and thus close to the experimental accuracy. The quality of the resulting structures was further evaluated via a Ramachandran plot analysis¹¹ (see Fig. S2 in the ESI†).

The far-reaching sequence identity between the template and the target of 44% leads to an initial model structure with a low overall root-mean-square deviation (with respect to the template) of 0.8 Å for the backbone atoms of both the small and the large subunit. This is particularly true for the environment of the bimetallic center, constituted by highly conserved amino acids. As a consequence, the active structure in the homology model is essentially the same as for the template. In this region only minor structural differences were observed due

Institut f. Chemie, Sekr. PC14, Technische Universität Berlin, Straße des 17. Juni 135, D-10623 Berlin, Germany.
E-mail: andrea.mroginski@tu-berlin.de; Fax: +49 30 31421122;
Tel: +49 30 31426403

† Electronic supplementary information (ESI) available. See DOI: 10.1039/c1cp21045a

‡ These authors contributed equally to the work and are listed alphabetically.

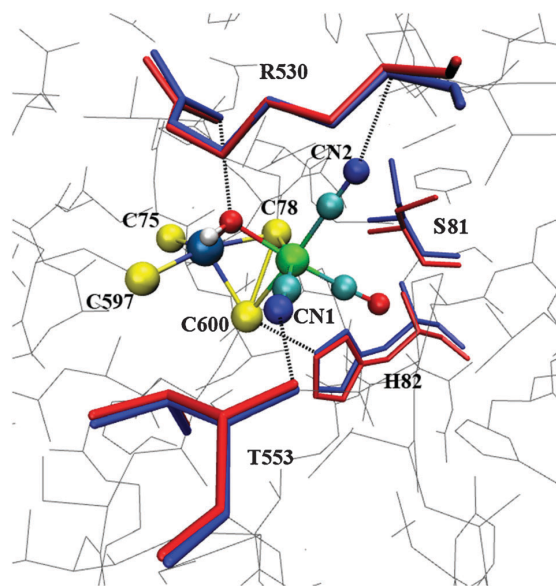


Fig. 1 Active site structure of *MBH-C81S* including a water molecule in the second coordination sphere (not displayed for the sake of clarity) and the amino acids R530, T553, H82 and S81 in two conformations (blue and red). Dashed lines indicate hydrogen bonds. The atoms of the bimetallic centre are represented by balls (S, yellow; O, red; C, cyan; N, blue; H, white; Ni, dark blue; Fe, green). Grey lines represent the protein matrix; all amino acids are shown without hydrogen atoms.

to the replacement of threonine by a serine at position 553. Larger deviations in the homology models are noted in surface loop regions. In all three structural models, important secondary structure elements are conserved (see Fig. S3 in the ESI†).

As observed in standard hydrogenases, the active sites in all our calculated models are embedded in the protein forming coordinative bonds between the metals and cysteine residues. Furthermore, the bimetallic centre is stabilized by a hydrogen bond network including, among others, interactions between the cyanide ligands CN and CN2 to the backbone nitrogens of T553 and R530, respectively. Except for the *MBH* model stable hydrogen bonds are established between the OH⁻ bridge and the side-chain nitrogen of R530. For all models only weaker hydrogen bonds are formed between the bridging sulfur of C78 or C600, respectively, and the N_ε of H82 located in the first coordination sphere, as described previously¹² (Fig. 1). It is interesting to note that the analysis of the MD trajectories for the *MBH-C81S-H₂O* model reveals two distinct conformations associated with Ser81 (Fig. 1).

The active site optimized by QM/MM calculations is a very rigid construct reflected by very low standard deviations computed over the series of snapshots (see Table S3 in the ESI†). A comparison with the crystallographic structure of *D. gigas* (2FRV),¹³ also harboring two CN⁻ and one CO ligands, indicates a shortening of the Fe–OH⁻, the Ni–S(C78), the Ni–S(C597) and the Ni–S(C600) bonds in the optimized structure. The length of the Fe–CO bond is reduced from 1.87 Å in the crystallographic structure to around 1.72 Å in our model. The Fe–CN1 bond is very similar in length to

the crystallographic structure, while the Fe–CN2 bond is elongated to 1.90 Å in our model (2FRV: 1.67 Å). This comparison further supports the view of a standard hydrogenase-like catalytic centre in the MBH. Compared to previous theoretical calculations performed on the active site of *D. gigas* in the Ni–B state,¹⁴ the differences in the crystallographic structures are reduced in the present model except for a slightly larger difference for the Ni–S(C533) and Ni–OH⁻ bonds. Earlier theoretical models presented by Stein and Lubitz¹⁵ display even higher differences, which might be related to the exclusion of the protein charge cloud (see Table S5 in the ESI†).

To validate the derived structural model of the catalytic centre IR spectra of the [NiFe] centre were computed (see Methods) and compared with the corresponding experimental data.¹⁰ A similar procedure has been employed in the past for determining the structure of a guanosine triphosphate (GTP) ligand bound to a Ras protein.¹⁶ Calculated spectra were obtained from 25 snapshots of the MD trajectory. The average frequencies and their standard deviations are listed in Table 1. The experimental IR spectrum in the region between 1890–2110 cm⁻¹ exclusively displays the stretching modes of the inorganic ligands with a prominent band at 1947 cm⁻¹ originating from the CO stretching vibration, and two weaker bands at 2080 cm⁻¹ and 2098 cm⁻¹ assigned to the asymmetric and symmetric CN stretching modes, respectively.² In the IR spectrum of the C81S MBH mutant, the CO stretching mode is shifted to higher wavenumbers by 8 cm⁻¹ whereas the CN stretching modes remain largely unchanged.¹⁰

In the *MBH* model consisting of a QM partition of 26 atoms (*vide infra*), analysis of the calculated spectra shows an overestimation of the vibrational frequencies of the CO and CN stretching modes, $\nu(\text{CO})$ and $\nu(\text{CN})$, compared to the experimental values (Table 1). Incorporation of water adjacent to the [NiFe] centre significantly improves the estimated $\nu(\text{CO})$ frequency, which is now predicted at 1950 cm⁻¹ and thus very close to the experimental value. However, the frequencies of the CN stretching modes are still overestimated. In presence of water, C81 is forced towards the CO ligand such that the CO–HS distance decreases from 6.4 Å in the *MBH* model to only 2.4 Å in the *MBH-H₂O* model. A further improvement is achieved by enlarging the QM partition to 75 atoms, including R530, T553, and H82 which are involved in hydrogen bond interactions with the CN ligands and the OH bridging ligand. With this model, not only the CO stretching is very well reproduced but also the CN stretching modes are predicted at much lower frequencies such that they coincide distinguished with the experimental values. The difference between

Table 1 Calculated and experimental frequencies (in cm⁻¹) for the wild type MBH and the C81S mutant. The calculated average frequencies are accompanied by the standard deviations computed over 25 spectra

		$\nu(\text{CO})$	$\nu(\text{CN})_{\text{asym}}$	$\nu(\text{CN})_{\text{sym}}$
Exp.	MBH-WT	1947	2080	2098
Calc.	MBH (QM26)	1970 ± 4	2106 ± 4	2120 ± 4
	MBH-H ₂ O (QM26)	1950 ± 5	2097 ± 6	2128 ± 5
	MBH-H ₂ O (QM75)	1954 ± 5	2078 ± 4	2098 ± 3
Exp.	MBH-C81S	1955	2080	2097
Calc.	MBH-C81S-H ₂ O (QM75)	1959 ± 8	2081 ± 12	2110 ± 5

the $\nu(\text{CN})$ frequencies computed for the *MBH* and *MBH-H₂O* models appear to be related to minor structural changes of the environment, such as the twisting of the R530 and the T553 side chains.

Also the IR spectra calculated for the *MBH-C81S-H₂O* model exhibit a very good agreement with the experimental IR spectrum. The experimental frequency upshift of 8 cm⁻¹ compared to the WT protein is very well reproduced by the calculations. The good agreement also holds for the asymmetric CN stretching while only the symmetric CN stretching is overestimated by the calculations. The frequency upshift of the CO stretching can be explained as a consequence of the higher polarity of the serine side chain, which is represented by a larger negative point charge, reducing the backbonding from the iron and strengthening the CO bond (blue-shifted).⁸ On the other hand, the CO stretching frequency calculated for the *MBH-C81S-H₂O* model is lower by 10 cm⁻¹ compared to that of the *MBH* model lacking the internal water molecule. Thus, the comparison of the experimental and calculated spectra for the WT and C81S variants provides strong support for a water molecule close to the [NiFe] centre. Note that the variations of the CN stretching frequencies for the *MBH-C81S-H₂O* model are larger than for the WT model, which is attributed to the fluctuations of the hydrogen bond network involving the CN⁻ ligands.

For the *MBH-H₂O* model and the *MBH-C81S-H₂O* model, calculated potential energy distributions show that the asymmetric $\nu(\text{CN})$ mode is dominated by the stretching of the CN1 ligand, while the symmetric $\nu(\text{CN})$ mode mainly contains the stretching of the CN2 ligand. Interestingly, there is a change of the hydrogen bond network involving H82 and the bridging cysteines. For the WT *MBH*, the hydrogen bond is formed with the sulfur atom of C78 whereas for the C81S mutant, it is formed with the bridging sulfur atom from C600. Analysis of the 25 snapshot structures with their corresponding vibrational spectra shows that there is a linear correlation between the strength of this hydrogen bond and the $\nu(\text{CO})$ frequency: a stronger hydrogen bond is reflected by an increase of the $\nu(\text{CO})$ frequency.

In summary, the theoretical 3D structural models of the *MBH* show only minor structural rearrangements of the active site and its vicinity compared to standard hydrogenases. These results confirm previous suggestions^{2,3,24} of a very similar catalytic centre in oxygen-tolerant and -sensitive [NiFe] hydrogenases, ruling out that the molecular origin of the oxygen-tolerance of *MBH* is related to a specific modification at the catalytic centre. The reliability of the present structural model for the active site of *MBH*, with a high similarity to oxygen-sensitive “standard” [NiFe] hydrogenases, is supported by the distinguished agreement between experimental and the QM/MM calculated IR spectra and specifically by the reproduction of the IR spectroscopic changes related to a single mutation of C81 to serine located in the second coordination sphere of the active site. In addition, these calculations indicate a water molecule close to C81, which influences the IR spectra. The present results constitute another example¹⁶ where the combination of molecular modelling with a spectroscopic validation represents a valuable tool for the structural analysis of enzymes for which no crystal structures are available.

Methods

Homology modeling

The *MBH* homology models were constructed with Modeller v9.5¹⁷ using the structures of the standard hydrogenases of *inter alia* *D. vulgaris* Miyazaki F¹⁸ and *D. gigas*¹³ as a template for the overall protein and the active site structure, respectively. Based on spectroscopic studies, the structure of the Ni-B state of the active site includes one CO, and two CN⁻ ligands and an OH⁻ bridging ligand.^{5,6} In the *MBH-H₂O* model, one water molecule was added adjacent to the active site. The C81S variant structure was constructed by replacing C81 by a serine followed by a short energy minimization run. Following the same procedure as for the *MBH-H₂O* model, a water molecule was placed in the active site cavity of the C81S mutant. MD simulations were performed to relax and to equilibrate the three structural models in TIP3P water boxes.¹⁹ The internal motions of the [NiFe] centre and the Fe-S clusters were strongly constrained during the MD simulations (see ESI 1†).

Geometry optimization of the active site

25 snapshots were extracted from the MD trajectory. The respective geometries were optimized at the QM/MM level of theory by combining density functional theory (DFT) calculations using the BP86 functional with CHARMM22 force field. The QM part consists either of 26 atoms containing the bimetallic centre with Ni(III) and Fe(II), the exogenous ligands, and the side chains of the four coordinating cysteines, or of 75 atoms by including R530, T553, and H82. The 6-31g(d) basis set was applied for all atoms excluding Ni and Fe for which Ahlrichs triple-zeta polarization all electron basis set (TZVP) was employed.²⁰ Covalent bonds at the QM/MM border were cut and saturated by hydrogen link atoms. The coupling between QM and MM was computed using electrostatic embedding with a charge-shift scheme.²¹ Final models were constructed by averaging over the 25 individual structures (see ESI 4†).

Spectra calculation

IR spectra of the active site were calculated for each snapshot using the normal mode analysis approximation following the procedure described previously by Mroginski *et al.*²² The final IR spectra for each model were computed using the instantaneous normal mode analysis (INMA) approach.²³

Acknowledgements

We thank the DFG (Cluster of Excellence “UniCat”) for financial support and the “Norddeutscher Verbund für Hoch- und Höchstleistungsrechnen” (HLRN) for providing computer resources.

Notes and references

- J. C. Fontecilla-Camps, A. Volbeda, C. Cavazza and Y. Nicolet, *Chem. Rev.*, 2007, **107**, 4273–4303.
- M. Saggi, I. Zebger, M. Ludwig, O. Lenz, B. Friedrich, P. Hildebrandt and F. Lendzian, *J. Biol. Chem.*, 2009, **284**, 16264–16276.
- O. Lenz, M. Ludwig, T. Schubert, I. Bürstel, S. Ganskow, T. Goris, A. Schwarze and B. Friedrich, *ChemPhysChem*, 2010, **11**, 1107–1119.

10.4 Insights into the structure of the active site of the O₂ tolerant membrane bound [NiFe] hydrogenase of *R. eutropha* H16 by molecular modelling

[View Online](#)

- 4 K. A. Vincent, J. A. Cracknell, O. Lenz, I. Zebger, B. Friedrich and F. A. Armstrong, *Proc. Natl. Acad. Sci. U. S. A.*, 2005, **102**, 16951–16954.
- 5 A. J. Pierik, W. Roseboom, R. P. Happe, K. A. Bagley and S. P. J. Albracht, *J. Biol. Chem.*, 1999, **274**, 3331–3337.
- 6 M. van Gastel, M. Stein, M. Brecht, O. Schröder, F. Lenzian, R. Bittl, H. Ogata, Y. Higuchi and W. Lubitz, *J. Biol. Inorg. Chem.*, 2006, **11**, 41–51.
- 7 A. Volbeda, L. Martin, C. Cavazza, M. Matho, B. W. Faber, W. Roseboom, S. P. Albracht, E. Garcin, M. Rousset and J. C. Fontecilla-Camps, *J. Biol. Inorg. Chem.*, 2005, **10**, 239–249.
- 8 A. L. De Lacey, V. M. Fernandez, M. Rousset and R. Cammack, *Chem. Rev.*, 2007, **107**, 4304–4330.
- 9 M. E. Pandelia, H. Ogata and W. Lubitz, *ChemPhysChem*, 2010, **11**, 1127–1140.
- 10 M. Saggi, M. Ludwig, B. Friedrich, P. Hildebrandt, R. Bittl, F. Lenzian, O. Lenz and I. Zebger, *ChemPhysChem*, 2010, **11**, 1215–1224.
- 11 R. W. W. Hoof, G. Vriend, C. Sander and E. E. Abola, *Nature*, 1996, **381**, 272–272.
- 12 C. Stadler, A. L. de Lacey, Y. Montet, A. Volbeda, J. C. Fontecilla-Camps, J. C. Conesa and V. M. Fernandez, *Inorg. Chem.*, 2002, **41**, 4424–4434.
- 13 A. Volbeda, E. Garcin, C. Piras, A. L. de Lacey, V. M. Fernandez, E. C. Hatchikian, M. Frey and J. C. Fontecilla-Camps, *J. Am. Chem. Soc.*, 1996, **118**, 12989–12996.
- 14 P. Jayapal, M. Sundararajan, I. H. Hillier and N. A. Burton, *Phys. Chem. Chem. Phys.*, 2008, **10**, 4249–4257.
- 15 M. Stein and W. Lubitz, *Phys. Chem. Chem. Phys.*, 2001, **3**, 2668–2675.
- 16 M. Klähn, J. Schlitter and K. Gerwert, *Biophys. J.*, 2005, **88**, 3829–3844.
- 17 A. Sali and T. L. Blundell, *J. Mol. Biol.*, 1993, **234**, 779–815.
- 18 H. Ogata, S. Hirota, A. Nakahara, H. Komori, N. Shibata, T. Kato, K. Kano and Y. Higuchi, *Structure*, 2005, **13**, 1635–1642.
- 19 W. L. Jorgensen, J. Chandrasekhar, J. D. Madura, R. W. Impey and M. L. Klein, *J. Chem. Phys.*, 1983, **79**, 926–935.
- 20 F. Weigend and R. Ahlrichs, *Phys. Chem. Chem. Phys.*, 2005, **7**, 3297–3305.
- 21 D. Bakowies and W. Thiel, *J. Phys. Chem.*, 1996, **100**, 10580–10594.
- 22 M. A. Mroginiski, F. Mark, W. Thiel and P. Hildebrandt, *Biophys. J.*, 2007, **93**, 1885–1894.
- 23 M. Nonella, G. Mathias and P. Tavan, *J. Phys. Chem. A*, 2003, **107**, 8638–8647.
- 24 J. Fritsch, S. Löscher, O. Sanganas, E. Sieber, I. Zebger, M. Stein, M. Ludwig, A. L. De Lacey, H. Dau, B. Friedrich and O. Lenz, *Biochemistry*, 2011, **50**, 5858–5869.

10.5 Effect of the protonation degree of a self-assembled monolayer on the immobilization dynamics of a standard [NiFe] hydrogenase.

Tillmann Utesch, Diego Millo, Maria Ana Castro, Peter Hildebrandt, Ingo Zebger, and Maria Andrea Mroginski

Reprinted with permission from *Langmuir* (2013), 29 (2): 673–682

Copyright 2013 American Chemical Society.

Overview

The immobilization of the standard [NiFe] hydrogenase of *D. gigas* on amino-terminated SAMs was analysed by classical MD simulations and complementary SEIRA measurements.

The main point was to investigate the effect of the pH dependent protonation level of the SAM on the initial adsorption dynamics. To avoid long reorientation dynamics, the initial placing of the [NiFe] hydrogenase on the surface was chosen according to the protein dipole moment. This orientation agrees with the energetically most favourable conformation of the enzyme on the modified electrode. On the one hand, augmenting charge density of the monolayer resulted in an increased adsorption strength of the enzyme on the SAM. On the other hand, the strong electric field of the surface affected protein stability beyond a threshold of pH 6.5. Thus, a suitable trade-off between these two parameters, namely, protein stability and adsorption strength, promised the best success for applications. The supporting SEIRA measurements confirmed these observations, but revealed again the limitations of MD simulations concerning the simulated time scale and the phase space sampling.

Effect of the Protonation Degree of a Self-Assembled Monolayer on the Immobilization Dynamics of a [NiFe] Hydrogenase

Tillmann Utesch,[†] Diego Millo,^{†,‡} Maria Ana Castro,[§] Peter Hildebrandt,[†] Ingo Zebger,[†] and Maria Andrea Mroginski^{*,†}

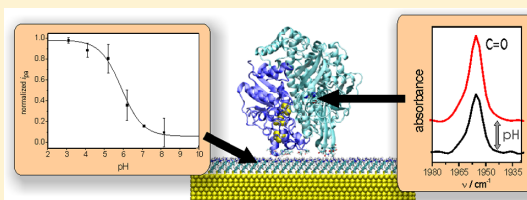
[†]Institut für Chemie, Technische Universität Berlin, Sekretariat PC 14, 10623 Berlin, Germany

[‡]Biomolecular Spectroscopy/LaserLaB Amsterdam, Vrije Universiteit Amsterdam, De Boelelaan 1083, NL-1081 HV Amsterdam, The Netherlands

[§]Departamento de Química Inorgánica, Analítica y Química Física/INQUIMAE-CONICET, Facultad de Ciencias Exactas y Naturales, Universidad de Buenos Aires, Ciudad Universitaria, Pabellón 2, Piso 1, C1428EHA Buenos Aires, Argentina

Supporting Information

ABSTRACT: Understanding the interaction and immobilization of [NiFe] hydrogenases on functionalized surfaces is important in the field of biotechnology and, in particular, for the development of biofuel cells. In this study, we investigated the adsorption behavior of the standard [NiFe] hydrogenase of *Desulfovibrio gigas* on amino-terminated alkanethiol self-assembled monolayers (SAMs) with different levels of protonation. Classical all-atom molecular dynamics (MD) simulations revealed a strong correlation between the adsorption behavior and the level of ionization of the chemically modified electrode surface. While the hydrogenase undergoes a weak but stable initial adsorption process on SAMs with a low degree of protonation, a stronger immobilization is observable on highly ionized SAMs, affecting protein reorientation and conformation. These results were validated by complementary surface-enhanced infrared absorption (SEIRA) measurements on the comparable [NiFe] standard hydrogenases from *Desulfovibrio vulgaris* Miyazaki F and allowed in this way for a detailed insight into the adsorption mechanism at the atomic level.



INTRODUCTION

Adsorption and immobilization of biomolecules on support materials play an important role in a wide field of research. *Inter alia*, catalysis involving immobilized enzymes on conductive surfaces is of particular interest in biotechnology and sustainable energy production. With respect to biofuel production, hydrogenases are interesting candidates, because of their ability to reversibly cleave hydrogen in several aerobic (and anaerobic) microorganisms.^{1–3} In particular, a biological activity in the presence of oxygen will offer promising applications for clean technological fuel production with hydrogen as an energy carrier.^{2,4,5} Hydrogenases are classified by their metal composition of the active site as [NiFe], [FeFe], and [Fe] hydrogenases.^{6,7} The [NiFe] hydrogenase of *Desulfovibrio gigas* is a heterodimer consisting of a small and a large subunit, which are not covalently bound to each other.⁸ It belongs to the standard or oxygen-sensitive hydrogenases, where small amounts of oxygen inhibit their catalytic activity.⁹ At the active center of [NiFe] hydrogenases, four cysteine residues coordinate the Ni atom, two of them bridge the Ni and the Fe. In addition to these two bridging cysteines, the Fe atom is bound to one CO and to two CN⁻ ligands, which have been validated by infrared spectroscopy.¹⁰ The open-coordination position is occupied by a small ligand, such as OH⁻, H⁻, or presumably OOH⁻, characteristic of the different redox states

of the hydrogenase.¹¹ Details of the catalytic cycle and the bridging ligands are still under discussion.^{12,13}

For the development of biofuel cells, the interaction of the [NiFe] hydrogenase with bare or chemically modified electrode surfaces is a crucial point.² First successful applications have been achieved but with small turnover rates and limited stability over time.^{4,14} Therefore, studies dedicated to the optimization of such systems are required.^{15,16}

Because structural information on the atomic level is difficult to obtain experimentally, molecular dynamics (MD) simulations are an approved and well established technique to investigate the initial adsorption processes of biomolecules on surfaces.^{17–23} This theoretical technique may be in many cases computationally demanding, because all protein and surface atoms and often the solvent molecules are taken explicitly into account. In addition, dependent upon the size of the protein and surface properties, the length of these simulations may even go beyond several hundreds of nanoseconds. For example, it has been shown by Wei et al.²² that lysozyme requires at least 70 ns to adsorb on polyethylene surfaces. In a similar way, Zuo et al.²³ demonstrated that 500 ns simulations are necessary for

Received: September 10, 2012

Revised: November 1, 2012

Published: December 7, 2012

properly predicting the adsorption properties of a villin headpiece onto graphene.

In this work, we applied MD simulations on a standard [NiFe] hydrogenase, serving as a relative simple and well-studied test system, which is placed on a gold electrode chemically modified with a self-assembled monolayer (SAM), to investigate the influence of the electric field strength resulting from different degrees of SAM terminal functional group ionization. Higher levels of protonation leading to a stronger electric field are expected to enhance the adsorption of the [NiFe] hydrogenase. This, however, might be on costs of the protein stability, as reported for cytochrome *c*.²¹ Goals of this study combining experimental and theoretical techniques are, *inter alia*, to identify important binding patterns and the optimal surface configuration at an initial stage of the protein adsorption process that allow for a stable biomolecule immobilization on the monolayer system.

MATERIALS AND METHODS

Experimental Work. SAM Titration. The pK_a value of the amino-terminated SAM was determined by cyclic voltammetry (CV), according to the procedure described by Degefa et al.²⁴ Briefly, the SAM-coated Au electrode exposed to a 10 mM buffered solution at the pH of interest was incubated for 10 min with a 10 μ M solution of the electroactive compound $K_3Fe(CN)_6$. Afterward, the $K_3Fe(CN)_6$ solution was replaced with the corresponding buffer solution at the same pH, so that the electroactive compound was only present in the adsorbed state. The amount of the negatively charged $[Fe(CN)_6]^{3-}$ complex adsorbed on the SAM is dependent upon the protonation state of the SAM itself and was determined by CV measurement. Given the electrochemical reversibility of the surface-confined $[Fe(CN)_6]^{3-}$ anions (see Figure S1A of the Supporting Information), the normalized peak currents of the baseline-corrected CV traces (see Figure S1B of the Supporting Information) are plotted versus the pH (Figure 1) to yield the titration curve of the SAM.

Surface-Enhanced Infrared Absorption (SEIRA) Measurements. SEIRA experiments were carried out in a Kretschmann attenuated total reflection (ATR) configuration using a silicon crystal coated with a nanostructured gold film, formed by electroless deposition. This surface was covered with a SAM formed by immersing the Au electrode for 18 h in a 1 mM solution of 6-amino-1-hexanethiol

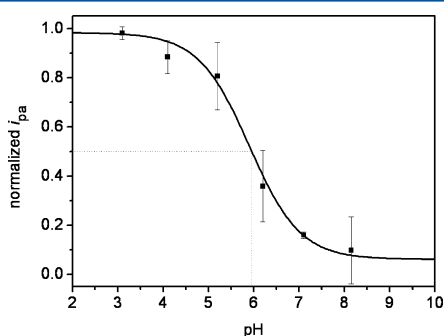


Figure 1. Normalized peak intensities i_{pa} (■), as derived from the CV traces obtained for the $K_3Fe(CN)_6$ adsorbed onto the SAM-coated Au electrode at different pH values (see Figure S1 of the Supporting Information). The line represents the fit to the experimental data points. An estimate of the degree of SAM protonation at different pH values has been inferred from the fit of the normalized i_{pa} versus pH plot, assuming that i_{pa} is proportional to the amount of protonated terminal functional groups of the SAM. These percentages are 52 ± 9 , 30 ± 9 , and $16 \pm 5\%$ for pH 6.0, 6.5, and 7.0, respectively.

containing 80% ethanol and 20% water (volume percent). Subsequently, the coated electrode was rinsed with ethanol and gently dried with Ar. The protein was immobilized by covering the electrode with a 1 μ M solution of *Desulfovibrio vulgaris* Miyazaki F (DvMF) dissolved in 10 mM phosphate buffer at pH values of 6.0 and 7.0. After a 45 min immobilization (i.e., when 90% of the adsorption process is completed),¹⁵ the protein solution was exchanged by a 10 mM phosphate buffer at pH 6.0. To determine the nature of the interaction between the protein and the surface, the intensity of the amide bands was followed spectroscopically for 3.5 h, and afterward, increasing concentrations of KCl (0.1, 0.5, 1, 1.5, 2, and 3 M) were successively added. Finally, the solution was exchanged for a 10 mM phosphate buffer at pH 6.0 for a better comparison to the initial conditions.

Theoretical Studies. Protein. The theoretical adsorption study was performed with the [NiFe] hydrogenase of *Desulfovibrio gigas*.⁸ This species shows a high similarity, more than 67%, to the homologous [NiFe] hydrogenase in DvMF and has already been proven to predict adequately the behavior of the DvMF on biocompatible surfaces.¹⁵ The active site was modeled in the Ni_2-S state. In this configuration, the bridging position between Fe and Ni of the active site is unoccupied. The initial conformation of one heterodimeric standard [NiFe] hydrogenase containing the small subunit that accommodates three iron sulfur (FeS) clusters and the large subunit harboring the active site was extracted from the X-ray structure (2FRV)⁸ (Figure 2A). Despite the relatively low resolution

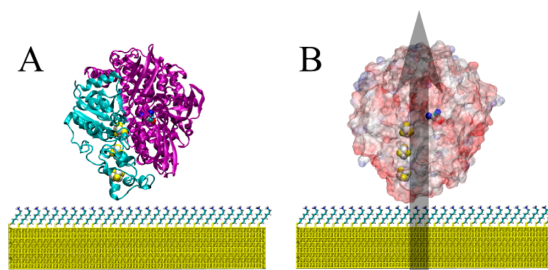


Figure 2. Initial positioning of the [NiFe] hydrogenase on the SAM-coated gold surface. Panel A shows the hydrogenase backbone and secondary structure elements indicating the large and small subunits in violet and cyan, respectively. Panel B shows the electrostatic potential surface of the enzyme in the same orientation with respect to the surface as in panel A. Negatively charged regions are colored in red, and positively charged areas are colored in blue. The shaded gray arrow in panel B indicates the dipole moment of the enzyme. FeS clusters and the active site are displayed as spheres in both illustrations.

(2.54 Å) of this structure compared to other anaerobic hydrogenases, we selected this topology, because it exhibits the inorganic ligand configuration at the active site that has been validated by spectroscopy¹⁰ and theory.²⁵

For the MD simulations, the titrable amino acid site chains were protonated according to pH 7.0 with the CHARMM package²⁶ and PROPKA.²⁷ This last one did not predict strong pK_a changes adjacent to the SAM. According to PROPKA, the highest stability of the [NiFe] hydrogenase is predicted to be at pH 7.2.²⁸ Histidine residues were protonated on their N_δ (HSD state) unless the environment suggests another configuration, such as the double-protonated histidines (H193 of the small subunit and H525 of the large subunit) and the N_ϵ -protonated residues (H45 and H185 of the small subunit and H20, H106, H114, H179, H322, H335, and H349 of the large subunit). Glutamic acids (Glu) and aspartic acids (Asp) were taken to be deprotonated, while lysine (Lys) and arginine (Arg) residues were protonated. The C-terminal residues Ala-264 of the small subunit and His-536 of the large subunit were modeled as deprotonated, and the N-termini as protonated. Given the high stability of the protonation state of most residues to variations of the pH value, all MD simulations were performed using the same protonation configuration. In total,

this protonation setting results in a total charge of $-10 e^-$ for the enzyme, including its cofactors, which reasonably agrees with the PROPKA prediction,²⁸ and a strong dipole moment of ~ 1050 D. The predicted electrostatic properties lead to the assumption of a strong Coulombic interaction with charged devices and a favorable orientation following the overall dipole moment of the hydrogenase.^{15,16}

For electrostatic interactions, we applied the partial charges derived by Teixeira et al.,²⁹ while the van der Waals parameters were transferred from the universal force field.³⁰ Because of the lack of bonding parameters in the CHARMM27 force field, we treated the active site and the iron sulfur clusters as rigid bodies with strongly restricted internal motions during all calculations.

Surface. The model surface used for the simulations consists of a ca. $121 \times 120 \text{ \AA}^2$ large Au(111) slab coated with a SAM. The sulfur atoms of the alkanethiol monolayer were placed in a $\sqrt{3} \times \sqrt{3}$ lattice on the Au(111), resulting in a herringbone structure with a minimal separation of 4.98 \AA between two sulfur atoms.³¹ All SAM backbones were initially tilted by ca. 30° to the surface normal. In total, the Au(111) was covered by 672 monolayer chains, which were chemisorbed via their sulfur atoms to the gold surface. Each chain of the SAM was composed of six carbon backbone atoms and terminated by an amino group (see Figure S2 of the Supporting Information). The level of ionization of the SAM was set to 0, 8, 33, and 50%, which resulted in a total charge of +0, +56, +224, and +336 e^- for the SAM, respectively. For clarity, the corresponding models were named sim0, sim8, sim33, and sim50 according to the protonation level of the SAM. The SAM amino groups were protonated in a systematic and homogeneous way, avoiding islands of charged or uncharged SAMs. The levels of ionization chosen for the theoretical models were approximated according to the experimentally determined pK_a values at pH 6.0, 6.5, and 7.0 (52, 30, and 16% ionization levels, respectively). To avoid systems of different ionic strength resulting from the charge neutralization of the SAMs with unequal protonation levels, the bottom layer of the gold slab was slightly charged to neutralize the SAM charge of all systems. In doing so, the z dimension of the cell had to be increased by 50 \AA to avoid artificial interactions of the hydrogenase with the surface of the image cell.

To maintain the coverage pattern during the MD simulations, the gold and sulfur atoms of the SAMs were kept fixed to their positions. Thus, only non-bonding parameters derived by Bizzarri et al.³² were required for the gold atoms. The monolayer was handled with the CHARMM force field for lipids, as reported earlier.^{19,33}

Simulation. The initial protein–surface configurations were constructed by placing the enzyme in a minimal separation distance of 5 \AA with respect to the corresponding surface, defined as the closest contact between enzyme and SAM. In addition, the protein is initially oriented with its dipole moment normal to the gold layer (Figure 2B). The choice of this initial configuration is supported by the energy landscapes shown in Figure 3 for the sim33 model and in Figure S3 of the Supporting Information for the remaining models. These plots were obtained by computing the *in vacuo* interaction energy between the SAM surface and the protein in different orientations. Each conformation was constructed by stepwise rotating the enzyme around the x axis (Φ angle) and the y axis (Ψ angle), maintaining the separation distance to the SAM at 5 \AA . As expected, the two most favorable energy regions correspond to conformations of the hydrogenase, where its dipole moment lies normal to the surface. In this orientation, the small subunit is facing the monolayer with its distal iron sulfur cluster and its negatively charged patch containing several glutamate residues, namely, Glu-195, Glu-198, Glu-207, and Glu-216.^{15,16}

For the all-atom MD simulations, the NAMD 2.7 code³⁴ with the CHARMM32 force field³⁵ was used. The protein–surface system was solvated in a $120 \times 120 \times 235 \text{ \AA}^3$ large TIP3P water box,³⁶ which was added with VMD 1.8.7.³⁷ The ionic strength mimicked by Na^+Cl^- was set to 18 mM , as used in experiments. The resulting models included more than 310 000 atoms.

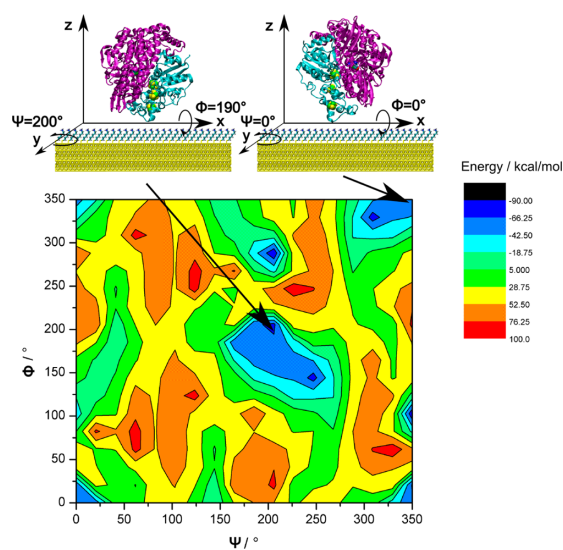


Figure 3. Interaction energy between hydrogenase and the SAM surface in model sim33 for different orientations of the enzyme obtained by stepwise rotating it around the x and y axes (Φ and Ψ angles). Negative energy wells, in blue, show favorable conformations of the hydrogenase on the surface. The two most favorable geometries in interaction energy are depicted above. These two regions correspond to the same orientation of the enzyme on the surface but rotated by 180° along the surface normal. In both conformations, the dipole moment of the enzyme is normal to the surface.

All simulations were carried out under periodic boundary conditions with a time step of 2 fs , and all bonds to hydrogen atoms were kept fixed by the SHAKE algorithm.³⁸ For van der Waals interactions and real space electrostatics, a simple cutoff of 12 \AA was applied, while long-range electrostatics were calculated with the particle mesh Ewald summation.³⁹ Recently, the stability of this method has been evaluated and validated for systems containing charged particles.⁴⁰

At first, the energy of the systems was minimized by applying the conjugated gradient algorithm for 30 000 steps until a constant total energy was achieved. During this step, the initial position constraints of $25 \text{ kcal mol}^{-1} \text{ \AA}^{-2}$ on all heavy atoms, except the fixed gold film and SAM sulfur atoms, were decreased stepwise to $5 \text{ kcal mol}^{-1} \text{ \AA}^{-2}$. Then, the systems were heated for 20 ps to 300 K by constraining the motions of the heavy atoms of the protein and SAM by a force of $5 \text{ kcal mol}^{-1} \text{ \AA}^{-2}$. Afterward, the water and the cell size in the z direction were carefully equilibrated for 60 ps by further decreasing the position constraints to $2.5 \text{ kcal mol}^{-1} \text{ \AA}^{-2}$. This step is important to obtain thermal ambient temperature properties, because the following 20 ns long MD simulations were performed in a NVT ensemble. During this production run, the protein was allowed to move freely but the SAM backbone in systems with charged monolayers was lightly constrained by $2.5 \text{ kcal mol}^{-1} \text{ \AA}^{-2}$ to maintain the coverage pattern. As stated recently, these restrictions on the monolayer should not strongly influence the adsorption behavior of enzymes⁴¹ and were necessary to avoid SAM defects caused by the attraction between SAM head groups and the charged gold, especially under high SAM protonation. Simulations of the hydrogenase in the absence of the surface, the so-called bulk model, were performed using the same protocol as previously described. The total energy of each model is plotted as a function of time in Figure S4 of the Supporting Information. For all models, with the exception of model sim50, the steady curves reflect equilibrated systems that can be used for investigating the very early steps of the adsorption dynamics.

In all production runs, various protein properties, such as the root-mean-square deviation (rmsd) and root-mean-square fluctuation

(rmsf), dipole moment, and radius of gyration, as well as interaction forces, energies, number of contacts, and separation distances to the surface were evaluated in intervals of 25 ps.

RESULTS AND DISCUSSION

Experiments. SAM Titration. The titration curve of the amino-terminated SAM over the whole pH value scale provides the relationship between the experimentally applied pH value and the corresponding level of SAM protonation (Figure 1). This information is required for generating an appropriate theoretical model, where a fixed protonation configuration is adopted during the calculation.

The course of the titration curve (Figure 1) displays a nearly constant value for the level of ionization above pH 7.0 and reveals a pK_a value of about 6.0 ± 0.2 for the amino-terminated SAM. In contrast to this observation, the change in protonation around pH 6.0 is sensitive to very small pH variations, as reflected by the steep slope in this region. While at pH 7.0, the percentage of SAM protonation is $16 \pm 5\%$, and it is strongly increased at pH 6.0, reaching a value of $52 \pm 9\%$.

SEIRA Adsorption Study. In the context of our studies, the SEIRA spectroscopic measurements offer details about three important points. They afford information about (a) the protein adsorption and changes in the competitive binding with buffer ions, (b) the possible reorientation as well as possible structural reorganization at different binding conditions, and (c) the type of binding interaction with the SAM.

Figure 4 displays the IR intensities of the amide I band, which is characteristic of the protein backbone, as a function of

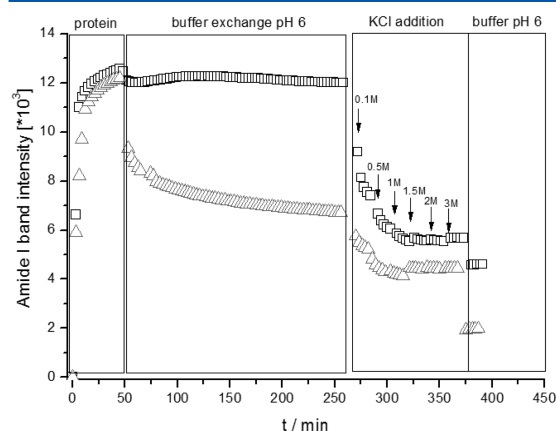


Figure 4. Intensity of the amide I band of the (DvMF [NiFe]) hydrogenase derived from SEIRA spectra. The first period of 45 min displays the immobilization of the enzyme at two different pH values of 6.0 (Δ) and 7.0 (\square). In a second step, the effect of a buffer replacement at pH 6.0 is demonstrated. Afterward, KCl is added stepwise before the buffer is again exchanged with fresh solution at pH 6.0.

time, pH value, and ionic strength of the buffer solution. For the initial immobilization period of 45 min, a similar time course of the protein adsorption can be observed at pH 6.0 and 7.0. However, the amount of residual immobilized hydrogenase differs significantly after replacing the protein solution by pure buffer at pH 6.0 for the two different incubation pH conditions. The hydrogenase immobilized at pH 7.0 remains on the SAM, while the ratio between the amide I and amide II bands

decreases slightly after the replacement of the buffer solution (see Figure S5 of the Supporting Information), suggesting minor protein reorientation (*vide infra*).

In contrast to the stable adsorption at pH 7, a significant fraction of the enzyme immobilized at pH 6.0 desorbs after exchanging the buffer (Figure 4). This observation might be related to an increased buffer adsorption on the SAM under these conditions (Figure 5). While only small amounts of the

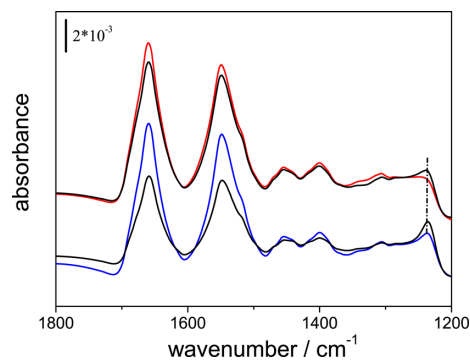


Figure 5. SEIRA spectra of the immobilized hydrogenase after replacement of the solution to a buffer at pH 6 (black), for an initial solution at pH 7 (red) and pH 6 (blue), respectively. Of particular interest are the amide I and amide II absorptions at 1660 and 1549 cm^{-1} as well as the band at 1240 cm^{-1} , assigned tentatively to a $\nu_s(\text{P}=\text{O})$ vibration of the phosphate buffer.

negatively charged buffer ions adsorb at pH 7.0, their respective electrostatic binding to the SAM is clearly detectable during the immobilization phase at pH 6.0, as indicated by the increase of the symmetric $\nu_s(\text{P}=\text{O})$ at about 1240 cm^{-1} . The observed buffer ion immobilization is further enhanced in the following buffer exchange, which is performed to establish equal conditions in the two systems after the immobilization period. The result is a strongly competitive adsorption between hydrogenase and buffer, which leads to partial desorption in the enzyme immobilized at pH 6.0 (Figure 4), while the amount of protein immobilized at pH 7.0 stays nearly unchanged. This behavior reflects the ionic strength sensitivity of the adsorption process, as observed for other charged proteins.¹⁹

In contrast to pH 7.0, the subsequent buffer exchange does not lead to any detectable changes in the amide I/amide II ratio for the hydrogenase immobilized at pH 6.0. During the immobilization period, the ratio is larger at pH 7.0, but after the buffer exchange, it drops to similar values as observed for pH 6.0 (see Figure S5 of the Supporting Information). This observation suggests a reorientation of the enzyme at pH 6.0 relative to the surface that might be tentatively ascribed to the structural reorganization predicted by MD simulations at pH 6.0 (sim50, *vide infra*).

Another important insight from the SEIRA measurements is the relative intensity of the CO bands, which can be taken as a measure of the distance d of the active site of the protein to the Au surface, as the surface enhancement decreases with $1/d^6$ (Figure 6).⁴² The clear difference between the respective intensities for hydrogenase immobilized at pH 6.0 and 7.0 indicates that the relative distance between the gold surface and active site is pH-dependent, suggesting that the distance is larger after immobilization at pH 7.0.

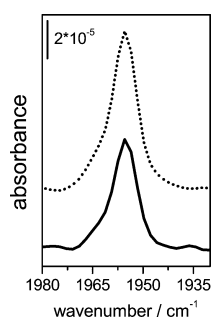


Figure 6. Comparison of the CO absorption band of the immobilized (DvMF [NiFe]) hydrogenase recorded with SEIRA spectroscopy after 45 min at pH 6 (···) and pH 7 (—).

The subsequent addition of KCl leads to enzyme desorption, proving the predominantly electrostatic type of interactions between the hydrogenase and the SAM (Figure 4). In fact, the stepwise increasing KCl concentration results in a decreasing amount of immobilized protein in both systems. Furthermore, stronger changes in the amide I/amide II ratio are visible in both systems, which may reflect changes in the orientation of the hydrogenase relative to the surface induced by the high ionic strength or partial desorption (see Figure S5 of the Supporting Information).

MD Simulations. Interacting Residues. The initial adsorption of the [NiFe] hydrogenase on the SAM is analyzed by three descriptors: the minimal separation distance between selected amino acids of the [NiFe] hydrogenase and the SAM,

the number of contacts between the enzyme and the SAM, and the interaction energy between the two interaction partners. Because these theoretical calculations are restricted to the nanosecond time scale, they only provide information of the first contacts that can be established between the two interaction partners.

For the sake of consistency and in line with previously employed procedures,^{18,19} we denote those protein residues in a minimal separation distance of 5 Å to the SAM as “adsorbed” and define the number of contacts as all protein atoms in a range of 5 Å from the SAM.

Analysis of the MD simulations indicates that, in all simulations, the negatively charged patch of the small subunit facing the surface is attracted by the SAM. Because of the favorable electrostatics, the first adsorption step occurred within ca. 2 ns. Evaluation of the minimal SAM distance of selected amino acids and the number of contacts (Figure 7) clearly reveals the importance of the glutamic acid cluster and the carboxylated C-terminal Ala-264 for adsorption (Figure 8). The glutamic acids, namely, Glu-195, Glu-198, Glu-207, and Glu-216, are located adjacent to the distal [FeS] cluster and might be important for electron transfer.^{9,43} Their adsorption is a key event for immobilization. Particularly in the simulations with a high degree of protonation (sim33 and sim50), they act as an anchor for other residues, which adsorb subsequently.

Additionally, the number-of-contacts analysis explicitly reveals the dependence of the adsorption strength on the degree of SAM ionization, which reaches a maximum at a certain point and does not increase any further beyond this level. For example, the number of contacts in sim33 reaches its

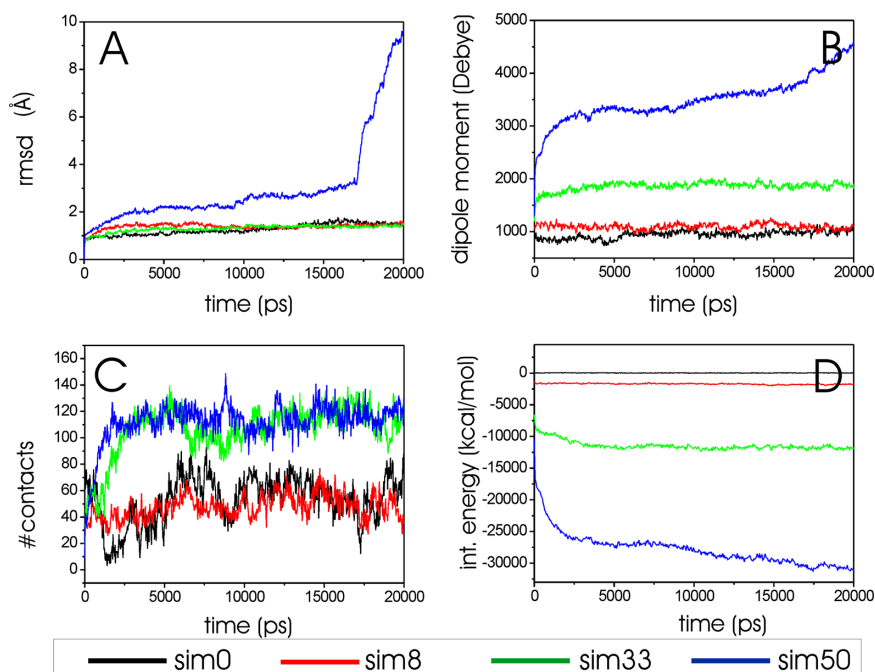


Figure 7. Evolution of the rmsd of the (A) hydrogenase backbone, (B) dipole moment of the enzyme, (C) number of contacts between the protein and the SAM, and (D) interaction energy between the hydrogenase and the surface, over time. The different model systems, sim0, sim8, sim33, and sim50, are colored in black, red, green, and blue, respectively.

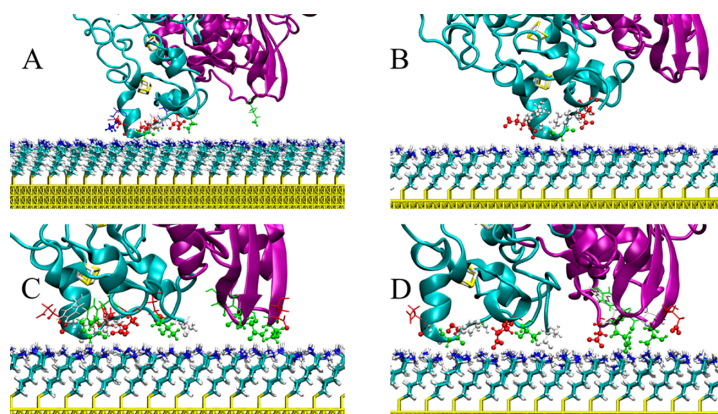


Figure 8. Enzyme–SAM interface after 20 ns MD simulation for models (A) sim0, (B) sim8, (C) sim33, and (D) sim50. The protein backbones of the large and small subunits are colored in violet and cyan, respectively. Protein side chains within 5 Å of the SAM are denoted as spheres, and their corresponding bonds are indicated by the stick representation according to their type.

maximum of around 115 contacts after ca. 2.5 ns and then fluctuates around this value.

The systems without (sim0) and with (sim8) low SAM ionization shows initially a weak adsorption of the small subunit with 58 ± 12 and 51 ± 9 contacts on average, respectively. Furthermore, the two models with a higher protonation level exhibit an increase in the number of contacts to 87 ± 8 and 74 ± 6 for the 33 and 50% protonated SAMs, respectively (Table 1). It is remarkable that the number of contacts under low

and the level of ionization (Table 1). While under low levels of SAM protonation, the large subunit interacts only sporadically with the surface; it is immobilized in conjunction with the small subunit on a highly charged SAM. The most important residues in this adsorption process under a high degree of ionization are Glu-452 and Asp-446 (see Figure 8), while the adsorption of the latter is delayed by ca. 1 ns in sim33.

In general, it is clearly visible that the total number of contacts strongly depends upon the ionization level of the SAM. A higher surface charge leads to an increasing number of contacts (Table 1). This observation is an outcome of two facts. At first, the hydrogenase is pulled closer to the SAM with an increasing surface charge (Table 2), and second, the large subunit is only, at least on this time scale, adsorbing on the surface under high electric field conditions, triggered by a high SAM ionization level. Additionally, the strong adsorption of the large subunit leads to a tilting of the [NiFe] hydrogenase and a slight weakening of the interaction between the small subunit and the monolayer. This conclusion can be drawn by comparing the adsorption interfaces of sim33 and sim50 shown in Figure 8. While the very strong interaction between the small subunit and the SAM in sim33 is weakened in sim50, the loose contact of the large subunit with the surface in sim33 is tightened further in sim50 (Table 1). Possibly, this reduced interaction between the small subunit and SAM in sim50 might affect the electron transfer between the [NiFe] hydrogenase and the surface as a result of a slightly increased separation distance between the distal FeS cluster and the monolayer.

Protein Stability. Previous studies dealing with the adsorption of cytochrome *c* on carboxyl-terminated SAMs showed, on the one hand, a positive correlation between the

Table 1. Average Values of the Number of Contacts between the Hydrogenase and the SAM, the Small Subunit and the SAM, and the Large Subunit and the SAM^a

	number of contacts		
	hydrogenase–SAM	small subunit–SAM	large subunit–SAM
sim0	59 ± 13	58 ± 12	1 ± 1
sim8	51 ± 9	51 ± 9	0 ± 1
sim33	115 ± 10	87 ± 8	29 ± 5
sim50	115 ± 9	74 ± 6	41 ± 6

^aThe average values are obtained from the last 10 ns of the MD simulations.

(sim0 and sim8) and high (sim33 and sim50) ionization levels differs considerably, but within the two clusters (sim0–sim8 and sim33–sim50), it is nearly equal and the values lie within the error bars.

Additionally, it is noticeable that the mainly electrostatic driven adsorption dynamics of the large subunit is strongly dependent upon the charge density of the SAM, which is reflected in positive correlation between the number of contacts

Table 2. Average Values of the Interaction Force between Hydrogenase and SAM, the Interaction Energy between Hydrogenase and SAM, and the Distance between the Ni Atom of the Active Site and the Gold Surface^a

	interaction force (hydrogenase–SAM) ($\text{kcal mol}^{-1} \text{Å}^{-1}$)	interaction energy (hydrogenase–SAM) (kcal mol^{-1})	distance (Au–Ni) (Å)
sim0	-13 ± 6	19 ± 17	51 ± 0.8
sim8	-71 ± 7	-1777 ± 83	49.3 ± 1.2
sim33	-324 ± 17	-11840 ± 246	44.4 ± 0.5
sim50	-599 ± 23	-29775 ± 877	44.5 ± 0.3

^aThe average values are obtained from the last 10 ns of the simulations.

adsorption strength and the level of ionization of the monolayer but, on the other hand, stronger conformational changes of the protein with an increasing charge density of the SAM.²¹ This effect has to be considered carefully to obtain strongly bound but intact and catalytically active enzyme molecules on the surface. Therefore, one has to find a trade-off between the adsorption strength and protein stability by changing the pH of the system. To analyze protein stability, we take into account the radius of gyration, the rmsd, and the evolution of the dipole moment.

Radius of Gyration. The radius of gyration is a measure for the size and shape of a protein. Changes in the radius of gyration indicate variations in the protein conformation. Our simulations demonstrate a slight increase of the radius of gyration of the [NiFe] hydrogenase in the initial phase of all simulations, which is also observed when the hydrogenase is exposed to solvent only (see Figure S6 of the Supporting Information). Contacts of the enzyme with the solvent molecules and the surface induce a small increase of the radius of gyration from initially 24.8 to ca. 25.3 Å (see Figure S6 of the Supporting Information). These conformational changes appear within ca. 100 ps and are a result of the interplay of mostly hydrophilic amino acids and the solvent. Afterward, the radius of gyration remains stable in all systems, except for sim50, where we observed a steady increase during the simulation until it jumps abruptly to values greater than 27 Å after approximately 17 ns. This evolution reflects structural rearrangements within the [NiFe] hydrogenase in sim50, starting with small but steady changes and eventually resulting in a significant reorganization, particularly in the remote region of the large subunit (130–165) (see the rmsf section).

In all other systems, the changes in the radius of gyration are very similar to the behavior of the enzyme in solution without any adsorption-induced effects.

Dipole Moment. Analysis of the dipole moment of the [NiFe] hydrogenase indicates a strong effect of the surface ionization on the protein side chains. During the first step of the adsorption (0–100 ps), the dipole moment of the hydrogenase increases as a function of the charge density of the SAM. While protonation levels of 0 and 8% lead to no or only to a slight increase of the dipole moment to ~1100 D, respectively, the dipole moment of the hydrogenase in sim50 goes up to more than 2500 D (Figure 7B). The prompt change in the dipole moment strength in the beginning of the simulation, similar to the effect described for the radius of gyration, results from reorientations of the protein side chains located at the protein surface, indicating very high flexibility. From the interaction with the electric field induced by the SAM, these chains are attracted or repelled by the surface according to their electrostatic properties. During the MD of sim50, a further increase in the dipole moment of the hydrogenase to more than 3000 D indicates additional structural rearrangements besides the initial reorientation of the protein side chains and is mainly related to the interaction of the large subunit with the SAM. The resulting tilting of the enzyme is partially noticed in sim33 but without a further increase in the dipole moment, which stays relatively stable at ca. 1900 D.

A comparison of the dipole moment of the protein in bulk solution and immobilized on the uncharged SAM (sim0) confirms the hypothesis that a neutrally charged SAM does not perturb the protein structure. Evolution of the dipole moments

in sim0 and in bulk exhibit a very similar behavior (see Figure S7 of the Supporting Information).

rmsd. The rmsd is a measure of the structural similarity between two structures. Evaluation of the rmsd of all heavy atoms of the protein during the MD simulations confirms the observed correlation between the surface charge density of the SAM and protein stability (Figure 7A). In all systems, except in sim50, the [NiFe] hydrogenase stays very close to its initial structure and the corresponding rmsd values do not exceed the 2.5 Å borders. The rmsd of the hydrogenase in bulk solution lies below 2 Å. This difference reflects the influence of the surface on the protein and especially on the side chains of the protein. In addition, the analysis of the rmsd of the protein backbone confirms the high stability of secondary structure elements monitoring a fluctuation around 1.5 Å, which indicates a stable protein and is matching the value obtained in bulk solution. These findings clearly show that, except for sim50, only the protein side chains are affected upon immobilization and that the secondary structure remains nearly unchanged, at least during an early adsorption phase.

In contrast to these observations, the hydrogenase in sim50 undergoes a stronger structural reorganization on the highly charged surface. The rmsd increases to more than 3 Å within 5 ns of simulation, where it stays stable for another 5 ns until it increases again and reaches 10 Å after 20 ns. These findings indicate that a high surface charge has a noticeable influence on the protein stability and even secondary structure elements are affected by the strong electric field induced by the highly protonated SAM.

rmsf. The rmsf of the C_α atoms of all amino acids gives information about the flexibility of single residues in the protein. By computing rmsf, one can specifically identify regions of the macromolecule that undergo high structural changes and fluctuations during time. Analysis of the rmsf of the [NiFe] hydrogenase on the SAMs with different protonation levels reveals that only sim50 exhibits prominent fluctuations (see Figure S8 of the Supporting Information). On top of the overall rather strong fluctuations, a region of the large subunit (130–165) shows a prominent rmsf value of more than 20 Å. Surprisingly, this region is not located adjacent to the surface but in a remote position more than 70 Å away from the gold film (see Figure S9 of the Supporting Information). Because of the large number of lysine and arginine residues, namely, Lys-133, Arg-136, Lys-144, Lys-145, Lys-152, Lys-157, and Lys-159, the region exhibits a high positive charge, which accounts for a strong repulsion from the surface. After ca. 17 ns, the region spanned by two helices, which are connected by a loop region, flips away from its initial position into the bulk solution and points away from the surface. During this process, the helical structure is partially conserved but the embedment in the protein is altered.

A comparison of the fractions of residues located in secondary structure elements in the simulations under different pH values monitors very similar results for sim0, sim8, and sim33 (α -helices, ca. 42–43%; β -sheets, ca. 15%) but slightly decreasing fractions for sim50 (α -helices, ca. 36%; β -sheets, ca. 12%). This loss of structural elements is another indicator for protein rearrangements at low pH.

Interaction Energies between the Hydrogenase and Surface. The strength of adsorption of the hydrogenase onto a SAM can be quantified through the computation of the interaction energies (E_{int}) between the surface and the enzyme. The evolution of the interaction energies during the MD

simulation are plotted for the four model system in Figure 7D. For these calculations, the surface is defined as the SAM together with the 5 Å adlayer of water molecules and ions.

For all models, with the exception of model sim50, the interaction energies remain practically constant, reflecting once again the stability of the protein and its interaction with the SAM. As expected, the strength of the interaction is proportional to the degree of protonation of the SAM: for a neutral SAM, E_{int} is almost negligible (on average, only 22 kcal/mol); for sim8, we predict an E_{int} of only -1700 kcal/mol, which significantly increases to -12 000 kcal/mol in sim33; and for sim50, E_{int} reaches a value of ca. 30 000 kcal/mol after 20 ns. Furthermore, for the neutral SAM, the positive sign of the interaction energy reflects the repulsive character of the very weak interaction. For all positive-charged SAMs, however, attractive interactions between the surface and protein are predicted.

Comparison between Experiment and Theory. The determination of the pK_a value of the amino-terminated SAM allows for a direct comparison between the immobilization conditions and the results of the SEIRA experiments to the theoretical prediction obtained from the MD simulations.

At pH 7.0, the SEIRA measurements are in good agreement with theory (sim8) and validate the weak but stable adsorption of the hydrogenase. At pH 6.0, however, the interpretation is much more complex but, anyway, consistent among the two techniques. The SEIRA measurements monitor a similar amount of immobilized protein under both low and high pH conditions during the immobilization phase, which is, upon a first glance, in conflict with the MD simulations (sim50), where the number of contacts between the enzyme and SAM is higher under lower pH conditions. Closer analysis suggests that this discrepancy is most likely due to competitive buffer adsorption, which is not taken into account in the MD simulations, where equal ionic strength conditions are used in all systems. The buffer effect is clearly observed in the SEIRA experiment, where at pH 6.0, a partial desorption of the immobilized hydrogenase is observed after replacing the buffer solution, accompanied by binding of phosphate ions. At pH 7.0, this effect is much weaker, resulting in an observed stable immobilization. Another reason for discrepancies between theory and experiment might be that possible changes in the protonation state of individual amino acids, brought about by the transition from the dissolved to the immobilized state, cannot be considered in the simulations.

Furthermore, changes in the hydrogenase orientation with respect to the SAM are observed in the MD simulations as well as in the experiments (*vide supra*). The pH-dependent reorientation of the enzyme is reflected in the simulations by the decreasing distance between the gold and the active site (Table 2), which can be related to the increase of the CO band intensity with a decreasing pH (Figure 6) in the experiments. In addition, the structural reorganization within the enzyme and the related initial reorientation simulated for sim50 (pH 6.0) may be related to the variations in the amide I spectral region compared to the spectra measured at pH 7 (see Figure S10 of the Supporting Information), and the different amide I/amide II ratios monitored at the two pH values indicate different protein orientations relative to the surface (see Figure S5 of the Supporting Information). Despite this good qualitative agreement between the structural changes derived from experiment and simulation, two specific methodological restrictions have to be pointed out to adequately assess the potential and

limitations of the present combined theoretical and experimental analysis. First, the two methods refer to different time scales (minutes versus nanoseconds). Thus, potential slow structural rearrangements of the immobilized protein, leading to the final state of the protein monitored by SEIRA spectroscopy, are not covered by the MD simulations. That means that, with MD simulations, we are only able to investigate a very early stage of the protein adsorption process. Second, SEIRA spectroscopy probes the protein structural changes in close vicinity to the surface such that the major changes predicted in the MD simulations of sim50 are presumably not detectable in the experiment.

CONCLUSION

The present study has shown that the combination of MD simulations and SEIRA spectroscopy may be used to guide a rational design of biocompatible surface coatings for the immobilization of enzymes under preservation of their native structure. Although the experimental method does not provide information about the three-dimensional structure of the adsorbed protein, it allows for qualitative conclusions about the secondary and tertiary structure changes and protein reorientations. Such conclusions may be related to the protein structural changes predicted by the MD simulations, although only in the first nanosecond time scale. The prerequisite for such correlations is, however, that experiments and simulations are carried out under “similar conditions”. In the present case of a predominantly electrostatic binding of the target enzyme, the crucial parameter is the surface charge density. This quantity has been derived from electrochemical experiments yielding the effective pK_a of the SAM. Thus, the protonation state of the SAM head groups in the MD simulations can be adjusted according to the pH to which the individual SEIRA measurements are referred. In this way, the present case study on the immobilization of hydrogenase afforded a good qualitative agreement between the MD simulations and spectroscopic experiments such that the present combined experimental and theoretical approach promised to become an important tool for optimizing immobilization conditions for enzymes on solid supports.

ASSOCIATED CONTENT

Supporting Information

Figures containing the CV traces for SAM titration, additional SEIRA spectra, evolution of the radius of gyration, rmsf during the MD simulation, and structural alignment of the initial and end conformations of hydrogenase in sim50. This material is available free of charge via the Internet at <http://pubs.acs.org>.

AUTHOR INFORMATION

Corresponding Author

*E-mail: andrea.mroginski@tu-berlin.de.

Notes

The authors declare no competing financial interest.

ACKNOWLEDGMENTS

This research has been financed by the Deutsche Forschungsgemeinschaft Cluster of Excellence “Unicat”. The authors are grateful to Prof. Wolfgang Lubitz for kindly supplying the DvMF enzyme. The authors thank the “Senat Berlin” for financial support (Nachhaltige Chemie), the “Norddeutscher Verbund für Hoch- und Höchstleistungsrechnen” (HLRN) for

providing computer power, the Alexander-von-Humboldt Foundation (to Diego Millo), and The Netherlands Organisation for Scientific Research (NWO), Grant 722.011.003 (to Diego Millo).

■ ABBREVIATIONS USED

SAM, self-assembled monolayer; SEIRA, surface-enhanced infrared absorption; CV, cyclic voltammetry; MD, molecular dynamics; *DvMF*, *Desulfovibrio vulgaris* Miyazaki F; rmsd, root-mean-square deviation; rmsf, root-mean-square fluctuation

■ REFERENCES

- (1) Adams, M. W. W.; Mortenson, L. E.; Chen, J. S. Hydrogenase. *Biochim. Biophys. Acta, Rev. Bioenerg.* **1980**, *594*, 105–176.
- (2) Lojou, E. Hydrogenases as catalysts for fuel cells: Strategies for efficient immobilization at electrode interfaces. *Electrochim. Acta* **2011**, *56*, 10385–10397.
- (3) Vignais, P. M.; Billoud, B. Occurrence, classification, and biological function of hydrogenases: An overview. *Chem. Rev.* **2007**, *107*, 4206–4272.
- (4) Vincent, K. A.; Cracknell, J. A.; Lenz, O.; Zebger, I.; Friedrich, B.; Armstrong, F. A. Electrocatalytic hydrogen oxidation by an enzyme at high carbon monoxide or oxygen levels. *Proc. Natl. Acad. Sci. U.S.A.* **2005**, *102*, 16951–16954.
- (5) Vincent, K. A.; Cracknell, J. A.; Clark, J. R.; Ludwig, M.; Lenz, O.; Friedrich, B.; Armstrong, F. A. Electricity from low-level H₂ in still air—An ultimate test for an oxygen tolerant hydrogenase. *Chem. Commun.* **2006**, 5033–5035.
- (6) Lyon, E. J.; Shima, S.; Boecher, R.; Thauer, R. K.; Grevels, F. W.; Bill, E.; Roseboom, W.; Albracht, S. P. J. Carbon monoxide as an intrinsic ligand to iron in the active site of the iron–sulfur–cluster-free hydrogenase H₂-forming methylenetetrahydromethanopterin dehydrogenase as revealed by infrared spectroscopy. *J. Am. Chem. Soc.* **2004**, *126*, 14239–14248.
- (7) Vignais, P. M.; Billoud, B.; Meyer, J. Classification and phylogeny of hydrogenases. *FEMS Microbiol. Rev.* **2001**, *25*, 455–501.
- (8) Volbeda, A.; Garcin, E.; Piras, C.; De Lacey, A. L.; Fernandez, V. M.; Hatchikian, E. C.; Frey, M.; Fontecilla-Camps, J. C. Structure of the [NiFe] hydrogenase active site: Evidence for biologically uncommon Fe ligands. *J. Am. Chem. Soc.* **1996**, *118*, 12989–12996.
- (9) Fontecilla-Camps, J. C.; Volbeda, A.; Cavazza, C.; Nicolet, Y. Structure/function relationships of [NiFe]- and [FeFe]-hydrogenases. *Chem. Rev.* **2007**, *107*, 4273–4303.
- (10) Pierik, A. J.; Roseboom, W.; Happe, R. P.; Bagley, K. A.; Albracht, S. P. J. Carbon monoxide and cyanide as intrinsic ligands to iron in the active site of [NiFe]-hydrogenases. *J. Biol. Chem.* **1999**, *274*, 3331–3337.
- (11) Stein, M.; Lubitz, W. Quantum chemical calculations of [NiFe] hydrogenase. *Curr. Opin. Chem. Biol.* **2002**, *6*, 243–249.
- (12) De Lacey, A. L.; Fernandez, V. M.; Rousset, M.; Cammack, R. Activation and inactivation of hydrogenase function and the catalytic cycle: Spectroelectrochemical studies. *Chem. Rev.* **2007**, *107*, 4304–4330.
- (13) Ogata, H.; Lubitz, W.; Higuchi, Y. [NiFe] hydrogenases: Structural and spectroscopic studies of the reaction mechanism. *Dalton Trans.* **2009**, 7577–7587.
- (14) Cracknell, J. A.; Vincent, K. A.; Armstrong, F. A. Enzymes as working or inspirational electrocatalysts for fuel cells and electrolysis. *Chem. Rev.* **2008**, *108*, 2439–2461.
- (15) Millo, D.; Pandelia, M. E.; Utesch, T.; Wisitruangsakul, N.; Mroginski, M. A.; Lubitz, W.; Hildebrandt, P.; Zebger, I. Spectroelectrochemical study of the [NiFe] hydrogenase from *Desulfovibrio vulgaris* Miyazaki F in solution and immobilized on biocompatible gold surfaces. *J. Phys. Chem. B* **2009**, *113*, 15344–15351.
- (16) Rüdiger, O.; Abad, J. M.; Hatchikian, E. C.; Fernandez, V. M.; De Lacey, A. L. Oriented immobilization of *Desulfovibrio gigas*

hydrogenase onto carbon electrodes by covalent bonds for non-mediated oxidation of H₂. *J. Am. Chem. Soc.* **2005**, *127*, 16008–16009.

- (17) Raut, V. P.; Agashe, M. A.; Stuart, S. J.; Latour, R. A. Molecular dynamics simulations of peptide–surface interactions. *Langmuir* **2005**, *21*, 1629–1639.
- (18) Utesch, T.; Daminelli, G.; Mroginski, M. A. Molecular dynamics simulations of the adsorption of bone morphogenetic protein-2 on surfaces with medical relevance. *Langmuir* **2011**, *27*, 13144–13153.
- (19) Utesch, T.; Sezer, M.; Weidinger, I. M.; Mroginski, M. A. Adsorption of sulfite oxidase on self-assembled monolayers from molecular dynamics simulations. *Langmuir* **2012**, *28*, 5761–5769.
- (20) Wang, Q.; Zhao, C.; Zhao, J.; Wang, J.; Yang, J. C.; Yu, X.; Zheng, J. Comparative molecular dynamics study of A β adsorption on the self-assembled monolayers. *Langmuir* **2009**, *26*, 3308–3316.
- (21) Zhou, J.; Zheng, J.; Jiang, S. Molecular simulation studies of the orientation and conformation of cytochrome *c* adsorbed on self-assembled monolayers. *J. Phys. Chem. B* **2004**, *108*, 17418–17424.
- (22) Wei, T.; Carignano, M. A.; Szleifer, I. Lysozyme adsorption on polyethylene surfaces: Why are long simulations needed? *Langmuir* **2011**, *27*, 12074–12081.
- (23) Zuo, G.; Zhou, X.; Huang, Q.; Fang, H.; Zhou, R. Adsorption of villin headpiece onto graphene, carbon nanotube, and C60: Effect of contacting surface curvatures on binding affinity. *J. Phys. Chem. C* **2011**, *115*, 23323–23328.
- (24) Degefa, T. H.; Schön, P.; Bongard, D.; Walder, L. Elucidation of the electron transfer mechanism of cytochrome *c* at SAMs with charged head groups. *J. Electroanal. Chem.* **2004**, *574*, 49–62.
- (25) Rippers, Y.; Utesch, T.; Hildebrandt, P.; Zebger, I.; Mroginski, M. A. Insights into the structure of the active site of the O₂-tolerant membrane bound [NiFe] hydrogenase of *R. eutropha* H16 by molecular modelling. *Phys. Chem. Chem. Phys.* **2011**, *13*, 16146–16149.
- (26) Brooks, B. R.; Bruccoleri, R. E.; Olafson, B. D.; States, D. J.; Swaminathan, S.; Karplus, M. CHARMM: A program for macromolecular energy, minimization, and dynamics calculations. *J. Comput. Chem.* **1983**, *4*, 187–217.
- (27) Olsson, M. H. M.; Sondergaard, C. R.; Rostkowski, M.; Jensen, J. H. PROPKA3: Consistent treatment of internal and surface residues in empirical pK_a predictions. *J. Chem. Theory Comput.* **2011**, *7*, 525–537.
- (28) Li, H.; Robertson, A. D.; Jensen, J. H. Very fast empirical prediction and rationalization of protein pK_a values. *Proteins* **2005**, *61*, 704–721.
- (29) Teixeira, V. H.; Baptista, A. M.; Soares, C. M. Pathways of H₂ toward the active site of [NiFe]-hydrogenase. *Biophys. J.* **2006**, *91*, 2035–2045.
- (30) Rappe, A. K.; Casewit, C. J.; Colwell, K. S.; Goddard, W. A.; Skiff, W. M. UFF, a full periodic table force field for molecular mechanics and molecular dynamics simulations. *J. Am. Chem. Soc.* **1992**, *114*, 10024–10035.
- (31) Widrig, C. A.; Alves, C. A.; Porter, M. D. Scanning tunneling microscopy of ethanethiolate and *N*-octadecanethiolate monolayers spontaneously adsorbed at gold surfaces. *J. Am. Chem. Soc.* **1991**, *113*, 2805–2810.
- (32) Bizzarri, A. R.; Costantini, G.; Cannistraro, S. MD simulation of a plastocyanin mutant adsorbed onto a gold surface. *Biophys. Chem.* **2003**, *106*, 111–123.
- (33) Feller, S. E.; Gawrisch, K.; MacKerell, A. D. Polyunsaturated fatty acids in lipid bilayers: Intrinsic and environmental contributions to their unique physical properties. *J. Am. Chem. Soc.* **2001**, *124*, 318–326.
- (34) Phillips, J. C.; Braun, R.; Wang, W.; Gumbart, J.; Tajkhorshid, E.; Villa, E.; Chipot, C.; Skeel, R. D.; Kale, L.; Schulten, K. Scalable molecular dynamics with NAMD. *J. Comput. Chem.* **2005**, *26*, 1781–1802.
- (35) MacKerell, A. D., Jr.; Bashford, D.; Bellott, M.; Dunbrack, R. L., Jr.; Evanseck, J. D.; Field, M. J.; Fischer, S.; Gao, J.; Guo, H.; Ha, S.; Joseph-McCarthy, D.; Kuchnir, L.; Kuczera, K.; Lau, F. T. K.; Mattos, C.; Michnick, S.; Ngo, T.; Nguyen, D. T.; Prodhom, B.; Reiher, W. E.,

III; Roux, B.; Schlenkrich, M.; Smith, J. C.; Stote, R.; Straub, J.; Watanabe, M.; Wiorkiewicz-Kuczera, J.; Yin, D.; Karplus, M. All-atom empirical potential for molecular modeling and dynamics studies of proteins. *J. Phys. Chem. B* **1998**, *102*, 3586–3616.

(36) Jorgensen, W. L.; Chandrasekhar, J.; Madura, J. D.; Impey, R. W.; Klein, M. L. Comparison of simple potential functions for simulating liquid water. *J. Chem. Phys.* **1983**, *79*, 926–935.

(37) Humphrey, W.; Dalke, A.; Schulten, K. VMD: Visual molecular dynamics. *J. Mol. Graphics* **1996**, *14*, 33–38.

(38) van Gunsteren, W. F.; Berendsen, H. J. C. Algorithms for macromolecular dynamics and constraint dynamics. *Mol. Phys.* **1977**, *34*, 1311–1327.

(39) Darden, T.; York, D.; Pedersen, L. Particle mesh Ewald: An $N\log(N)$ method for Ewald sums in large systems. *J. Chem. Phys.* **1993**, *98*, 10089–10092.

(40) Kastenholz, M. A.; Hünenberger, P. H. Influence of artificial periodicity and ionic strength in molecular dynamics simulations of charged biomolecules employing lattice-sum methods. *J. Phys. Chem. B* **2003**, *108*, 774–788.

(41) Soliman, W.; Bhattacharjee, S.; Kaur, K. Adsorption of an antimicrobial peptide on self-assembled monolayers by molecular dynamics simulation. *J. Phys. Chem. B* **2010**, *114*, 11292–11302.

(42) Osawa, M. Surface-enhanced infrared absorption. *Top. Appl. Phys.* **2001**, *81*, 163–187.

(43) Marr, A. C.; Spencer, D. J. E.; Schröder, M. Structural mimics for the active site of [NiFe] hydrogenase. *Coord. Chem. Rev.* **2001**, *219–221*, 1055–1074.

10.6 An integral, rational strategy for immobilizing oxygen tolerant [NiFe] hydrogenases on electrode surface

Nina Heidary, Tillmann Utesch, Johannes Fritsch, Oliver Lenz, Peter Hildebrandt, Anna Fischer, Maria Andrea Mroginski, and Ingo Zebger

PRELIMINARY RESULTS! THIS MANUSCRIPT IS NOT THE FINAL VERSION! THE SUBMITTED VERSION WILL BE MODIFIED!

Overview

A combined approach of classical MD simulations, electrochemistry, and SEIRA measurements was carried out to investigate the immobilization of the MBH on modified surfaces. The complement techniques offered insights from different points of view to gain a complete picture of the system. Electrochemistry probes the activity of the enzyme, SEIRA spectroscopy provides information about the active site structure and MD simulations offer dynamics on an atomic level. Here, the immobilization of the MBH on two different surfaces, amino- and carboxyl-terminated SAMs, was investigated. In order to adapt similar conditions in theory and experiments, the crystal structure of the MBH dimer serving as starting geometry in MD simulations was elongated by its C-terminal membrane anchor carrying a *StrepTag II*.

On amino-terminated SAMs, the MD simulations predicted a strong immobilization of the stable MBH dimer. This observation agreed very well with the strong SEIRA signals of the active site and the good electrical communication between protein and surface in the electrochemical experiments. According to the experiments, a termination with carboxyl-groups weakened the immobilization of the MBH. The simulations suggested that only the modelled C-terminal tail prevented desorption from the SAM. The distance between the active site and the electrode was strongly increased in this scenario. This dynamics explained the disturbed electronic communication and decreased signals of the active site measured in experiments.

The demonstrated concept of combining theory and experiment allows a deeper insight in the behaviour of enzymes on surfaces and is, therefore, a promising approach for the rational design of enzyme-surface systems.

An integral strategy for the rational immobilization of oxygen tolerant [NiFe] hydrogenases on biocompatible electrode surfaces **

Nina Heidary[#], Tillmann Utesch[#], Diego Millo, Johannes Fritsch, Oliver Lenz, Peter Hildebrandt, Anna Fischer^{*}, Maria Andrea Mroginski^{*} and Ingo Zebger^{*}

[NiFe] hydrogenases catalyze the reversible cleavage of molecular hydrogen into electrons and protons. In view of the raising importance of H₂-based technologies in energy storage and conversion, the biotechnological potential of these enzymes is being extensively explored. Particularly interesting in this context are the oxygen-tolerant hydrogenases capable of H₂ cycling in the presence of oxygen, such as the membrane-bound [NiFe]-hydrogenase (MBH) from *Ralstonia eutropha* (*Re*) H16, *Aquifex aeolicus* and *E-coli*.^[1-4] The MBH is a heterodimeric protein consisting of a large subunit (HoxG), harboring the [NiFe] active site and a small subunit (HoxK) carrying the corresponding electron transfer chain, made of one [3Fe4S]-, one [4Fe4S]- and an unusual proximal [4Fe3S] cluster, which is responsible for the oxygen tolerance.^[5-7] The Ni and the Fe of the bimetallic catalytic center are coordinated by four cysteine residues. In addition, one CO and two CN⁻ molecules bind to the Fe atom as exogenous ligands.^[7,8]

In order to exploit the full potential of oxygen tolerant hydrogenases as biocatalysts for technological applications, and in particular for bio-fuel cell development, it is a prerequisite to immobilize these enzymes on electrode surfaces under conditions, where their function and integrity are preserved. Furthermore, an efficient electrical coupling between the catalytic centre and the conducting support material has to be insured. A standard method for probing the electrical communication between enzyme and electrode is protein film voltammetry (PFV)^[9] This technique per se neither provides insights into the enzymatic adsorption process at the material interface nor structural insights on the the catalytic processes, which is essential information for a rational design of hydrogenase-based bio-electronic devices.

Recently, an extensive systematic study based on Atomic Force Microscopy, PFV and polarization modulation-

infrared reflection absorption spectroscopy (PM-IRRAS) investigations were carried out to elucidate the most efficient immobilization conditions for the oxygen tolerant, membrane-bound [NiFe] hydrogenases from *Aquifex aeolicus* onto Au-electrodes, covered with different self-assembled monolayers (SAM)^[10]. The thereby chosen IR spectroscopic technique could however not provide any structural information of the active site. In this context, surface enhanced infrared absorption (SEIRA) spectroscopy has been proven to be a powerful tool, to monitor the integrity of both the protein backbone and its catalytic centre within the immobilization process via their characteristic IR absorption bands. Furthermore, the underlying catalytic processes at the active site can be unravelled in a similar way by probing specific shifts of the stretching vibrations of the diatomic ligands.^[11-13]

Unfortunately, detailed structural information on a molecular level of proteins adsorbed on surfaces cannot be obtained experimentally. For this reason, theoretical approaches have been shown to be a suitable tool. In particular, classical molecular dynamics (MD) simulations are being successfully employed to investigate the adsorption properties of biomolecules onto surfaces, taking advantageously all protein-, surface- and solvent- atoms explicitly into account. Although, these all-atom simulations are restricted, in most cases, to the ns – μ s regime, they can be used to predict initial orientation and eventual conformational changes of the biomolecule upon adsorption and identify relevant interaction hot-spots governing the early adsorption process.^[14,15]

In this communication, we present an integrated approach of theory, spectroscopy, electrochemistry and surface chemistry for the rational design of an appropriate immobilization strategy for enzymes on conductive surfaces, as exemplified for the oxygen tolerant *Re* MBH HoxGK heterodimer. Thereby, SAM modified, hydrophilic charged Au electrodes were used, serving as models for alternative, low cost bio-fuel cell electrode materials, such as conductive metal oxides or conductive carbon materials. In a broader sense, the integrated strategy hereby presented may provide the general guidelines for the rational design of biocompatible surfaces for practical applications and fundamental studies.^[16]

Compared to standard (i.e. O₂-sensitive) hydrogenases, the MBH exhibits only a weak dipole moment (figure S1), so that a prediction of its adsorption behaviour is not straightforward. Starting from the recently solved crystal structure of the purified *Re* MBH heterodimer in its reduced state with the correct configuration of the diatomic ligands in the active site^[7,8], we simulated, using classical MD, the adsorption process of the MBH on Au surfaces modified with self-assembled monolayers (SAMs) carrying either positively charged amino- or negatively charged carboxyl-terminal

[*] [#]N.Heidary, T. Utesch, contributed equally to the paper
Dr. D. Millo, Prof. Dr. O.Lenz, Prof. Dr. P. Hildebrandt, Prof. M.A. Mroginski, Dr. A. Fischer, Dr. I. Zebger
Institut f. Chemie, Sekr. PC14
Technische Universität Berlin
Straße des 17. Juni 135, D-10623 Berlin (Germany)
Fax: +49-30-31421122
E-mail: anna.fischer@tu-berlin.de
andrea.mroginski@tu-berlin.de
ingo.zebger@tu-berlin.de

Dr. J. Fritsch
Institut f. Biologie/Mikrobiologie, Humboldt
Universität zu Berlin, Chausseestr. 117, D-10115
Berlin (Germany)

[**] Financial support by the DFG (Cluster of Excellence “UniCat”), HLRN for computer time

10.6 An integral, rational strategy for immobilizing oxygen tolerant [NiFe] hydrogenases on electrode surface

groups with a spacer length of 6 and 5 methylene units, respectively.

In our structural model we included the hydrophobic tail and the StrepTag II fused to the C-terminus of the MBH in order to cover all possible interaction sites with the different surface charges, contributing to a higher complexity of the absorption process (see SI for details on the construction of the molecular models, the setup of the MD simulation and on the stability of the resulting structures).

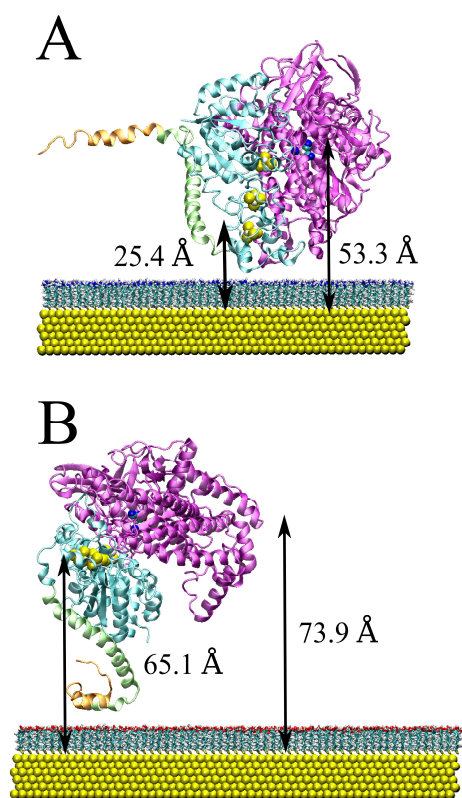


Figure 1. Predicted structure of MBH adsorbed on Au slabs coated with A) amino terminated SAM ($C_6NH_3^+$) and B) carboxyl terminated SAM (C_5COO^-) after 15 and 100 ns of immobilization, respectively. The protein backbones of the large and small subunits are colored in violet and cyan, respectively, the FeS-clusters in yellow and the [NiFe] active site in dark blue. The tail region and the Strep-tag II are highlighted in green and orange, respectively.

The results of the 15 and 100 ns long MD simulations are depicted in Figure 1. According to these simulations, the enzyme is adsorbed onto the 6-amino-1-hexanethiol ($C_6NH_3^+$) SAM (Figure 1A) via its small subunit while the hydrophobic tail is repelled by the surface (Figure S7). The minimal distances between the Ni-atom of the active site and the distal FeS cluster with respect to the Au upper layer are of $53.3 \pm 0.4 \text{ \AA}$ and $25.4 \pm 0.6 \text{ \AA}$, respectively, indicating that the enzyme is located closely to the surface in a favourable orientation for an efficient electron transfer. Contrary to this scenario, the MD simulations predict a weak adsorption of the MBH via the positively charged strep-tag (Figure S7) when the enzyme is placed on the 5-carboxyl-1-pentanethiol

(C_5COO^-) SAM (Figure 1B). In this case, the distances between the Ni atom and the distal FeS centre with respect to the Au surface are $73.9 \pm 1.0 \text{ \AA}$ and $65.1 \pm 1.2 \text{ \AA}$, i.e. more than 20 \AA larger when compared to the previous case.

This large difference in the protein-surface separation distance should have a significant effect on the intensity of the spectroscopic signals of both the protein backbone and the active site as well as on the observable catalytic currents. None of these simulations indicate a denaturation of the protein structure, which is mirrored in rmsd value of less than 3.5 \AA (figure S5). This suggests that the MBH immobilization on a positive charged surface would be more efficient for both, electrochemical and spectroscopic investigations. However, it is anticipated that a binding on negatively charged surfaces can be also potentially accomplished via the slightly positive charged strep-tag, without losing the catalytic function.

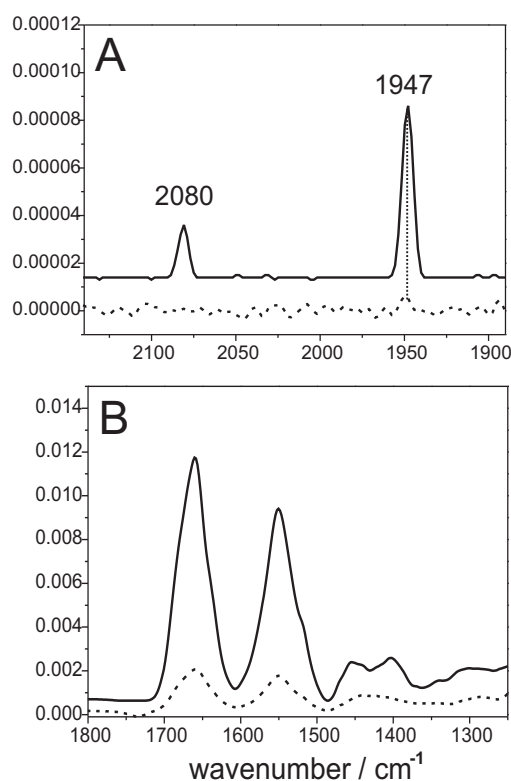


Figure 2. SEIRA spectra in selected wavenumber regions characteristic for the $\nu(CN)$ and $\nu(CO)$ stretching vibrations of the diatomic ligands (A) and the amide I and amide II (B) absorption bands of the strep-tagged MBH from Re immobilized on a negatively charged carboxyl-terminated SAM (5-carboxyl-1-pentanethiol, dashed lines) and a positively charged amino-terminated SAM (6-amino-1-hexanethiol, solid lines), respectively.

In order to verify the theoretically predicted different enzyme adsorption behaviour and orientations on the oppositely charged SAMs, IR spectroscopic and electrochemical control experiments have been carried out. Thereby, the acquisition of SEIRA spectra was accomplished in the attenuated total reflection (ATR) mode with a silicon prism, which is coated by a nanostructured Au layer.^[11,17] The metal surface was functionalized with amino terminated

and carboxyl-terminated SAMs, respectively, followed by enzyme immobilization (for experimental details, see SI). In this setup, Au serves both as spectroscopic signal amplifier and working electrode allowing spectroscopic and electrochemical studies on the same electrode sample. The protein backbone (amide I, amide II bands) and the diatomic ligands of the active site (CO, CN bands) of the Re MBH were monitored by their characteristic IR signatures, as displayed in Figure 2 A and B, respectively. For both immobilization strategies the band positions characteristic for backbone and active site are comparable with those observed previously, confirming the integrity of enzyme and active site.^[5,11] Notably, the intensity of the Re MBH related amide I and II bands (Figure 2A) are as well as the corresponding stretching modes of the CO and CN active site ligands (Figure 2B) about one order of magnitude higher for the Re MBH immobilized on the C6NH3⁺ SAM than for the Re MBH immobilized on the C5COO⁻ SAM. In the latter case CN and CO stretching vibrations are in the noise level. As the surface enhancement drops as function of the distance d from the Au surface by $1/d^6$ ^[18], the displayed spectral intensities are in line with the theoretically predicted enzyme orientation on the respective electrode surfaces. However, even though the amino terminated SAM offers an optimized surface for improved spectroscopic signals, the CN absorption with the highest wavenumber at 2098 cm⁻¹ appears to be too weak for spectral detection. This might be related to an unfavourable active site orientation with respect to the gold surface. In fact, according to the selection rule only vibrations with dipole moment changes preferentially perpendicular to the metal surface can be observed by SEIRAS.^[18]

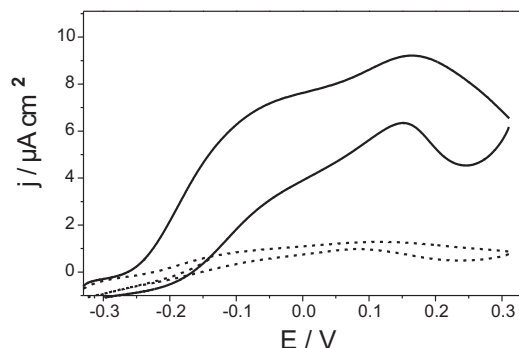


Figure 3. CV trace of the MBH from Re immobilized on Au electrodes, chemically modified with 6-amino-1-hexanethiol (solid line) and 5-carboxyl-1-pentanethiol (dashed line). The measurements were carried out at room temperature with a scan rate of 5 mV s⁻¹. Potentials are referred vs. the standard hydrogen electrode (SHE).

The sigmoid-shaped PFV traces shown in Figure 3 under H₂ atmosphere are ascribed to enzymatic H₂ oxidation. The overall shape of the traces is similar and closely resembles that of Re MBH on graphite and Ag electrodes.^[19,20] These findings prove that for both immobilization strategies the Re MBH heterodimer is catalytically active and exchanges electrons with the Au working electrode. The catalytic currents obtained for the MBH immobilized on the amino terminated gold electrode are, in line with the previously described SEIRA results, one order of magnitude higher

(when) compared to the carboxyl-terminated surface. This confirms, as suggested by theory, a more efficient binding interaction between the MBH and the C6NH3⁺ SAM than between the MBH and the C5COO⁻ SAM. In both cases, the addition of mediators did not show significant increase of the catalytic currents, proving that regardless the distance of the distal cluster from the electrode, the electron transfer between the enzyme and the Au electrode is direct. Therefore, the lower currents observed for the carboxyl-terminated SAM are more likely related to an enlarged distance of the distal cluster to the electrode surface, than from an unfavourable orientation of the latter relative to the electrode surface.^[10]

In summary, we applied for the first time an integral approach of MD simulations, SEIRA spectroscopy and PFV for an efficient, rational immobilization of an oxygen tolerant [NiFe] hydrogenase on SAM coated Au electrodes with varying surface charges. It has to be emphasized, that all constituents of the purified enzymes, including the hydrophobic C-terminus, which acts as membrane anchor and the affinity-tag used for enzyme purification were both included in the simulations and have been shown by MD to play, depending on the particular electrode surface charge a crucial role in the binding process.

Although theory suggest possible enzyme-surface interactions on a molecular level and resulting enzyme orientation on hydrophilic and charged Au model electrodes only in the ns time regime, combined SEIRAS and PFV experiments on the same enzyme film can be used to verify or disprove the calculated models. These combined experiments reveal fundamental insights into the material-enzyme interface and its influence on the resulting catalytic currents.

Based on this “proof of principle” more detailed immobilization studies will be carried out in the future, in order to design in a comprehensive manner the optimal chemical composition of the material interface for the immobilization of the MBH in view of both bioelectrocatalytic applications and in depth mechanistic studies of the underlying catalytic and interaction mechanisms. Furthermore, this approach can be further extended to other, alternative electrode materials, such as the above mentioned transparent conducting metal oxides, suitable for both spectroscopy and electrochemistry.

Keywords: [NiFe] hydrogenase · oxygen tolerance · molecular dynamics · SEIRA spectroscopy · protein film voltammetry · bioelectrocatalysis · biocompatibility

- [1] K. A. Vincent, J. A. Cracknell, O. Lenz, I. Zebger, B. Friedrich, F. A. Armstrong, *Proc Natl Acad Sci USA* **2005**, *102*, 16951–16954.
- [2] J. A. Cracknell, K. A. Vincent, F. A. Armstrong, *Chem Rev* **2008**, *108*, 2439–2461.
- [3] E. Lojou, *Electrochim Acta* **2011**, *56*, 10385–10397.
- [4] A. Parkin, F. Sargent, *Curr Opin Chem Biol* **2012**, *16*, 26–34.
- [5] M. Saggi, I. Zebger, M. Ludwig, O. Lenz, B. Friedrich, P. Hildebrandt, F. Lenzian, *J Biol Chem* **2009**, *284*, 16264–16276.
- [6] T. Goris, A. F. Wait, M. Saggi, J. Fritsch, N. Heidary, M. Stein, I. Zebger, F. Lenzian, F. A. Armstrong, B. Friedrich, et al., *Nat Chem Biol* **2011**, *7*, 310–318.
- [7] J. Fritsch, P. Scheerer, S. Frielingsdorf, S. Kroschinsky, B. Friedrich, O. Lenz, C. M. T. Spahn, *Nature* **2011**, *479*, 249–252.
- [8] Y. Rippers, M. Horch, P. Hildebrandt, I. Zebger, M. A. Mroginski, *ChemPhysChem* **2012**, *13*, 3852–3856.
- [9] K. A. Vincent, A. Parkin, F. A. Armstrong, *Chem Rev* **2007**, *107*, 4366–4413.

- [10] A. Ciaccafava, P. Infossi, M. Ilbert, M. Guiral, S. Lecomte, M. T. Giudici-Ortoni, E. Lojou, *Angew Chem Int Ed* **2012**, *51*, 953–956.
- [11] N. Wisitruangsakul, O. Lenz, M. Ludwig, B. Friedrich, F. Lenzian, P. Hildebrandt, I. Zebger, *Angew Chem Int Ed* **2009**, *48*, 611–613.
- [12] D. Millo, M.-E. Pandelia, T. Utesch, N. Wisitruangsakul, M. A. Mroginski, W. Lubitz, P. Hildebrandt, I. Zebger, *J Phys Chem B* **2009**, *113*, 15344–15351.
- [13] D. Millo, P. Hildebrandt, M.-E. Pandelia, W. Lubitz, I. Zebger, *Angew Chem Int Ed* **2011**, *50*, 2632–2634.
- [14] R. Latour, *Biointerphases* **2008**, *3*, FC2–FC12.
- [15] T. Utesch, D. Millo, M. A. Castro, P. Hildebrandt, I. Zebger, M. A. Mroginski, *Langmuir* **2013**, *29*, 673–682.
- [16] Y. Aksu, S. Frasca, U. Wollenberger, M. Driess, A. Thomas, *Chem Mater* **2011**, *23*, 1798–1804.
- [17] H. Miyake, S. Ye, M. Osawa, *Electrochem Commun* **2002**, *4*, 973–977.
- [18] M. Osawa, *Top Appl Phys* **2001**, *81*, 163–187.
- [19] K. A. Vincent, A. Parkin, O. Lenz, S. P. J. Albracht, J. C. Fontecilla-Camps, R. Cammack, B. Friedrich, F. A. Armstrong, *J Am Chem Soc* **2005**, *127*, 18179–18189.
- [20] M. Sezer, S. Frielingsdorf, D. Millo, N. Heidary, T. Utesch, M.-A. Mroginski, B. Friedrich, P. Hildebrandt, I. Zebger, I. M. Weidinger, *J Phys Chem B* **2011**, *115*, 10368–10374.

10.7 The linker pivot in Ci-VSP: the key to unlock catalysis

Kirstin Hobiger, Tillmann Utesch, Guiscard Seebohm, Maria Andrea Mroginski, and Thomas Friedrich

published in *PLoS ONE* (2013), 8(7): e70272. doi:10.1371/journal.pone.0070272

Overview

The hybrid approach of classical MD simulations on a Ci-VSP homology model embedded in the plasma membrane and electrophysiological measurements gave new insights into the dynamics and functionality of the biomolecule on the atomic level. In particular, the dynamic behaviour of the linker region connecting the voltage sensor with the catalytic phosphatase was of interest in this study.

It was demonstrated that the linker plays a crucial role in two interactions, namely, the membrane recruitment and the coupling between the sensor and the phosphatase. The latter one comprehended the essential contact between the positively charged linker and the anionic TI loop. In the WT model, this contact was stabilized by alternating salt bridges, which were interrupted by inserting several mutants into the TI loop. Surprisingly, a triple alanine mutant exhibited nearly the same activity as the WT enzyme, while neutralization of the three negative charges of the TI loop and a D400A single mutant strongly decreased the catalytic activity of Ci-VSP.

These observations were attributed to conformational changes in the PD adjacent to the TI loop and to the active site. With respect to the WT, this region was only weakly changed in the alanine triple mutant, where the linker-TI loop interaction was mostly stabilized by hydrophobic contacts. In the other two mutants larger rearrangements in this part of the structure were indicated.

The Linker Pivot in Ci-VSP: The Key to Unlock Catalysis

Kirstin Hobiger^{1*}, Tillmann Utesch^{1,9}, Maria Andrea Mroginski¹, Guiscard Seebohm², Thomas Friedrich¹

1 Institute of Chemistry, Max-Volmer-Laboratory of Biophysical Chemistry, Technische Universität Berlin, Berlin, Germany, **2** Department of Cardiovascular Medicine, Institute for Genetics of Heart Diseases, Myocellular Electrophysiology, University Hospital Münster, Münster, Germany

Abstract

In the voltage-sensitive phosphatase Ci-VSP, conformational changes in the transmembrane voltage sensor domain (VSD) are transduced to the intracellular catalytic domain (CD) leading to its dephosphorylation activity against membrane-embedded phosphoinositides. The linker between both domains is proposed to be crucial for the VSD-CD coupling. With a combined approach of electrophysiological measurements on *Xenopus* oocytes and molecular dynamics simulations of a Ci-VSP model embedded in a lipid bilayer, we analyzed how conformational changes in the linker mediate the interaction between the CD and the activated VSD. In this way, we identified specific residues in the linker that interact with well-defined amino acids in one of the three loops forming the active site of the protein, named T1 loop. With our results, we shed light into the early steps of the coupling process between the VSD and the CD, which are based on fine-tuned electrostatic and hydrophobic interactions between the linker, the membrane and the CD.

Citation: Hobiger K, Utesch T, Mroginski MA, Seebohm G, Friedrich T (2013) The Linker Pivot in Ci-VSP: The Key to Unlock Catalysis. PLoS ONE 8(7): e70272. doi:10.1371/journal.pone.0070272

Editor: Steven Barnes, Dalhousie University, Canada

Received: February 5, 2013; **Accepted:** June 17, 2013; **Published:** July 29, 2013

Copyright: © 2013 Hobiger et al. This is an open-access article distributed under the terms of the Creative Commons Attribution License, which permits unrestricted use, distribution, and reproduction in any medium, provided the original author and source are credited.

Funding: This work was funded by grants from the Cluster of Excellence Unifying Concepts in Catalysis, and the Berlin International Graduate School of Natural Science and Engineering, both launched by the German federal and state governments. The funders had no role in study design, data collection and analysis, decision to publish, or preparation of the manuscript.

Competing Interests: The authors have declared that no competing interests exist.

* E-mail: kirstin.hobiger@tu-berlin.de

⁹ These authors contributed equally to this work.

Introduction

The different species of phosphoinositides play crucial roles in diverse signaling cascades [1]. Proteins that intervene in these pathways are of huge interest in medical research, because their insufficient functionality is associated with serious diseases, e.g. cancer [2] or neurodegenerative disorders like Alzheimer [3]. In this context, the *Ciona intestinalis* voltage sensitive phosphatase (Ci-VSP) is one of the model systems for investigating phosphoinositide-selective enzymatic catalysis on a molecular level.

In voltage sensitive phosphatases, the modular protein structure enables, in a unique manner, the direct transduction of an electrical signal across the plasma membrane into an intracellular chemical reaction.

For this, a transmembrane voltage sensor domain (VSD) is coupled to a cytosolic catalytic domain (CD), which integrates a C2- and the enzymatic phosphatase domain (PD) (Fig. 1A, B). In Ci-VSP, the VSD-CD modules are coupled via a linker sequence of 18 amino acids (M240–K257, Fig. 1C).

Analogously to voltage-gated ion channels, the VSD consists of four putative α -helices, S1–S4, from which S4 contains several positively charged amino acids in a typical periodicity (Fig. 1A), which are responsible for voltage sensing of the protein [4].

The CD of Ci-VSP shares an overall amino acid homology of ~40% to the human tumor suppressor PTEN (phosphatase and tensin homolog deleted on chromosome 10) [5], but the substrate specificities of both proteins are different. PTEN dephosphorylates membranous phosphoinositides selectively at the 3'-site position of the inositol ring [6,7]. For Ci-VSP, a 3'-site selectivity was also demonstrated [8,9]. However, its main substrate preference seems

to be against the 5'-site position of phosphorylated phosphoinositides [8–10].

Since the discovery in 2005 [4], research on Ci-VSP has been focused on the intermodular coupling mechanisms that are responsible for the voltage-dependent activity of the protein. Upon depolarization of the membrane, conformational changes that occur in the VSD are transduced to the CD, which leads to the activation of the enzymatic domain [4,10,11]. The molecular processes that enable this VSD-CD interaction are dependent on the properties of the linker. Several studies revealed the importance of positively charged residues in the linker for electrostatic interactions with negatively charged membrane surfaces [11–13]. Thus, these interactions presumably lead to the binding of the linker to the membrane after the conformational change in the VSD has occurred. But what happens afterwards in the CD? Is the CD constitutively active, and does it just have to be recruited to the membrane in a diffusion-limited way? Or does it have to change its conformation during binding to the membrane-bound substrate? In both cases, the linker might be the crucial key in mediating mechanisms which lead to the activation of the CD.

The diffusion-limited recruitment of a constitutively active domain is supported by several studies about the isolated CD of Ci-VSP that shows catalytic activity against water-soluble substrates without the need of any membrane binding event [4,12]. However, other results pointed out that the isolated CD completely lacks its dephosphorylation activity against water-soluble substrates in case the linker sequence M240–Y255 is deleted [12]. This suggests an active role for the linker in the VSD-CD coupling, rather than just acting as recruiting element of a constitutively active CD to the membrane. Quite recently,

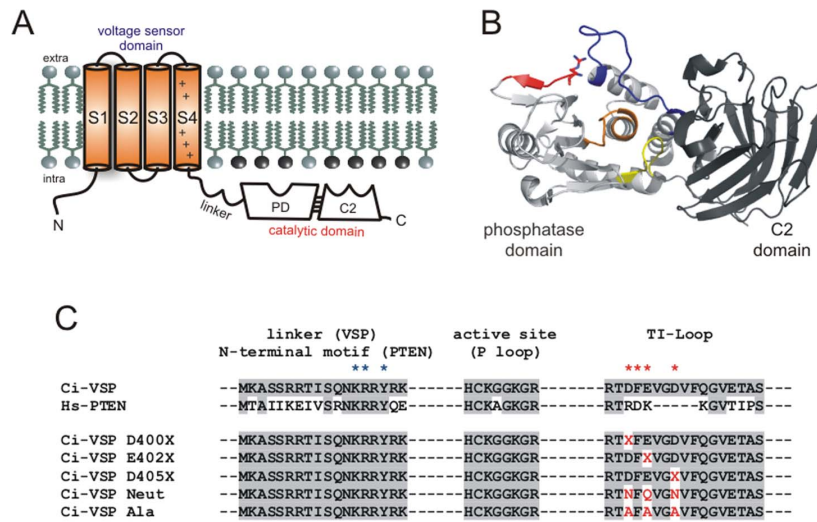


Figure 1. Topology scheme of Ci-VSP. (A) Topology scheme of Ci-VSP with the transmembrane voltage sensor (VSD) and the intracellular catalytic domain (CD), which comprises the phosphatase (PD) and the C2-domain. VSD and CD are connected via the linker sequence M240–K257. (B) Three-dimensional structure of the Ci-VSP CD based on the crystal structure by Liu et al. (PDB entry 3V0H) [14]. The P- (orange), the TI- (blue), and the WPD loop (yellow) form the active site of the CD. The linker (colored in red, with R253 shown as sticks) is oriented toward the TI loop, as proposed by Liu et al. [14]. (C) Amino acid alignment of Ci-VSP's linker (M240–K257), active site (H362–R369), and the TI loop (R398–S414) with regions of the homolog PTEN (Hs, Homo sapiens). Amino acid identities are highlighted with a gray background. Putative interacting partners in the linker and the TI loop are denoted with blue and red asterisks, respectively. Single and multiple altered Ci-VSP mutants are aligned as well (in red letters: mutated positions). In the single neutralization mutants, the X stands for N (in case aspartate was the native residue) or for Q (in case of glutamate). doi:10.1371/journal.pone.0070272.g001

a special role of the linker position K252 regarding the VSD-CD interaction has been proposed [13]. Functional analysis of K252 mutants indicated that this position might interact with the CD instead of binding to the membrane. Accordingly, Liu et al. confirmed these observations with results of crystal structures of the isolated CD [14]. These authors suggested interactions between linker positions K252 and R253 with D400 in the CD. Interestingly, D400 is located in one of the three loops forming the active site of the protein, named TI loop (Fig. 1B, C) [6,15]. However, the results obtained by the crystallographic structures are very limited, because of the poor resolution of the very flexible linker structure leading to ambiguous interpretations. Therefore, several questions still remain unanswered. If direct interactions really exist between linker and CD, including residue K252 and R253, which role do they play in coupling?

To close this gap of information, we performed atomistic molecular dynamics (MD) simulations on a homology model of the Ci-VSP and three TI loop mutants embedded in a lipid bilayer containing PI(4,5)P₂ molecules (Fig. S1A). These MD-simulations were complemented with a mutagenesis approach, in which several TI loop mutants (Fig. 1C) were functionally analyzed by electrophysiological measurements on *Xenopus* oocytes. With this combined strategy we are now able to elucidate the dynamics of the VSD-PD interaction in more detail, which would have been difficult to access with classical mutagenesis studies and incomplete crystallographic structures alone. Taken together, our results expand the previous knowledge about molecular mechanisms that enable the inter-domain coupling within the Ci-VSP protein including not only the CD but also the VSD and the linker region.

Results

MD Simulations

In this study, classical MD simulations were used to investigate whether the VSD-CD linker of the Ci-VSP protein interacts with putative binding partners in its immediate environment. For this purpose, the number of contacts is defined as all atoms within a 3.5 Å sphere of the corresponding interaction partners. This definition allows the characterization of relevant interactions according to their strength and stability during the MD simulations. While the strength is directly related to the number of contacts (Table 1), the stability is evaluated by their populations and maximal lifetimes (Table 2). The population is discriminating between bound (number of contacts >0) and unbound (number of contacts = 0) states and the maximal lifetime gives information about the maximal length of a contact during the 50 ns of the entire MD simulation.

Interaction linker – membrane. The MD simulations performed on all model systems predict a strong interaction between the linker and the PI(4,5)P₂ molecules at the membrane surface, which is reflected by the high number of contacts between the interacting partners (Table S1). The main contacts are established at an early stage of the simulations and remain stable throughout.

For the wild type (WT) and the TI loop mutants modeled in this work (Fig. 1C), the linker-membrane interaction is predicted to be of electrostatic nature and primarily stabilized by salt bridges (Fig. S1B, C). In particular, positively charged residues of the linker, namely R245, R246, R254, R256 and K257, are identified as main interaction partners for the PI(4,5)P₂ head groups. While R245 and R246 are located in the N-terminal part of the linker, the other residues (R254, R256 and K257) reside in the C-terminal section. The fact that contacts to PI(4,5)P₂ molecules are

Table 1. Mutations in the TI-loop affect the number of contacts with the linker during the MD simulation.

Model	#contacts linker-TI	#contacts N-term-TI	#contacts C-term-TI	#contacts K252-TI	#contacts R253-TI	#contacts Y255-TI
WT	37.2±7.2	0.2±0.8	37.1±7.0	4.7±5.2	29.4±4.5	5.7±3.1
NEUT	14.5±6.4	–	14.5±6.4	–	–	14.4±6.3
ALA	34.1±11.9	–	34.1±11.9	2.8±5.8	10.9±5.1	18.7±5.3
D400A	35.6±6.5	0.1±0.8	35.5±6.5	1.5±3.3	26.4±7.0	9.7±5.8

Interactions between the complete linker, its N- and C-terminal parts (240–249 and 250–257, respectively), K252, R253 and Y255 with the TI loop are summarized in terms of average contacts during the last 30 ns of simulation. Contacts are defined as atoms within a sphere of 3.5 Å.
doi:10.1371/journal.pone.0070272.t001

predicted for N- and C- terminal linker residues (Table S1) highlights the importance of the complete linker structure for its interaction with the plasma membrane.

Among the cationic residues of the linker, only K241, K252 and R253 do not establish stable contacts in the form of salt bridges with the PI(4,5)P₂ head groups. Only in the NEUT model, R253 forms a stable contact to the membrane, which increases the number of membrane interactions for the linker of this mutant (Table S1).

Besides the positively charged residues, uncharged linker positions (*inter alia* M240, A242, S243, S244, S249 and Q250) contribute to the interaction with the membrane either through van der Waals contacts or via hydrophobic interactions. However, these interactions show increased fluctuations and a reduced stability.

Interaction linker – CD. Besides the interaction with the membrane, the interplay of the linker with the enzymatic domain, particularly with the TI loop in the CD, is a main objective of this work.

In the WT model, a strong and stable connection between these two regions is observed. This interaction is reflected by the relatively high number of contacts (Table 1). Here, the C-terminal part of the linker plays the most essential role, since it participates in almost 100% of the contacts to the CD (37.2 average contacts against 0.2 coming from the N-terminal linker part). These contacts are mainly characterized by two salt bridges formed between K252, R253 in the linker, and E402, D400 in the TI loop (Fig. 2). Additionally, hydrophobic contacts between Y255 and F401 play a minor, but not negligible role (Table 1, Fig. 3A).

The most stable contact is predicted between R253 and D400 (Fig. 2A), which has a maximal lifetime of 24.3 ns (Table 2). This configuration is further stabilized by the favorable electrostatics between K252 and E402 (Fig. 2A). Occasionally, however, the salt bridge breaks and the guanidino group of R253 flips toward E402, pushing K252 into the solvent (Fig. 2B). In this configuration, R253 weakly interacts with D400 through a hydrogen bond (H-bond) involving the N_ε of the arginine. So the interactions R253-D400 and R253-E402 are not mutually exclusive. After a limited life span in this state (with a maximal lifetime of 16.6 ns, Table 2), R253 flips back to D400 due to the electrostatic repulsion by K252, which enables the re-establishment of the salt bridges R253-D400 and K252-E402. The salt bridges described for the WT are interrupted in the NEUT model (Fig. 3B). The lack of appropriate interaction partners in the TI loop for the cationic residues K252 and R253 strongly weakens the interaction between the linker and CD. As shown in Fig. 3B, these two residues either move into the bulk solution or interact with the membrane surface. The decreased coupling between linker and TI loop is primarily

characterized by hydrophobic contacts between Y255 and F401 with a maximal lifetime of 13.8 ns, which is shorter than the R253-D400 salt bridge in the WT (Table 2).

Interestingly, in contrast to the NEUT structure, the ALA model displays a rather strong interaction between linker and TI loop, which is reflected by the large number of contacts being in fact comparable to those predicted for the WT model (Table 1). This observation is the result of strong and stable hydrophobic and π -stacking interactions, which involves, *inter alia*, Y255 and the

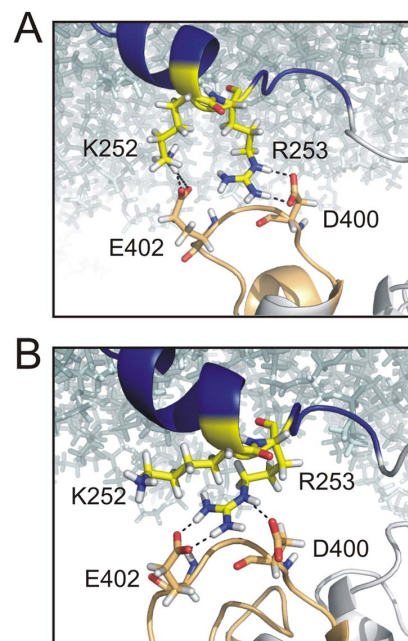


Figure 2. Flipping mechanism of R253 between D400 and E402 in the WT model. Interaction interface between the linker (blue backbone) and the TI loop (beige backbone) in the WT model. Membrane lipids are represented as cyan-colored sticks. A typical snapshot of the most frequently occurring state is shown in (A). Here, salt bridges between R253 and D400 strongly stabilize the contact between linker and TI loop. In this state, K252 is able to interact with E402. (B) The stable configuration between R253 and D400 breaks several times during the 50 ns long MD simulation whereby R253 gets in contact with E402. In this constellation of salt bridges, the interaction between K252 and the TI loop is interrupted.
doi:10.1371/journal.pone.0070272.g002

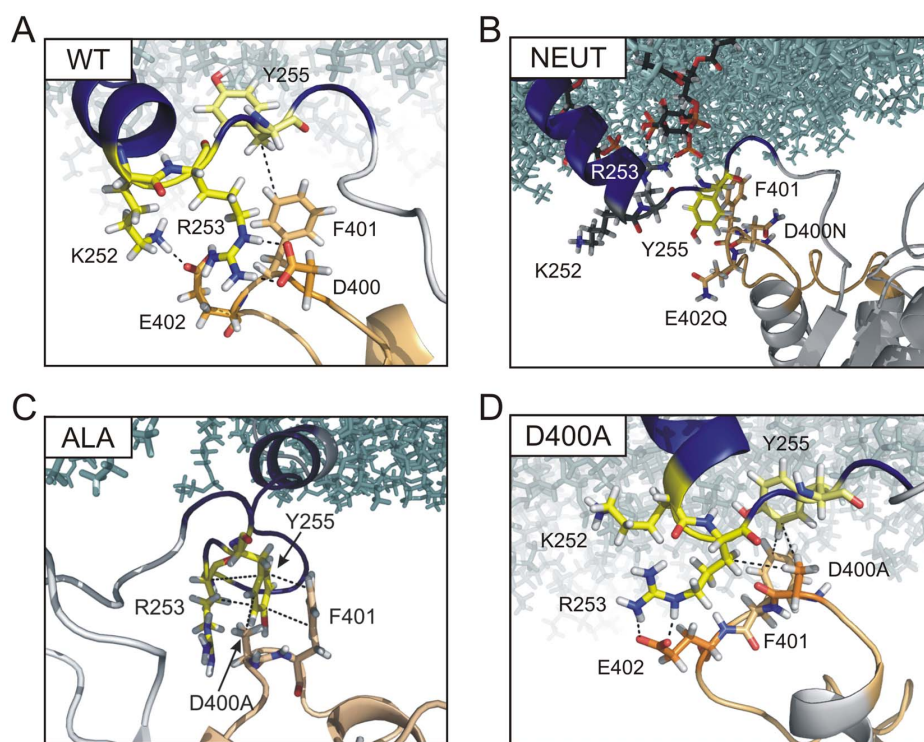


Figure 3. Models of WT and mutants reveal differences in the interface between linker and TI loop. Representative snapshots showing the linker-TI loop interface of (A) the WT, (B) NEUT, (C) ALA, and (D) D400A model. For clarity, only K252, R253, Y255, D400X, E402X (X denotes the inserted mutation residue, Fig. 1C) and F401 are shown as indicated in ball-and-stick representation. Furthermore, the backbones of the linker and the TI loop are represented as blue and beige cartoon, respectively. For a better orientation, the membrane lipids are shown as cyan sticks. For the NEUT model, PI(4,5)P₂ molecules interacting with R253 are indicated, with C atoms in black.
doi:10.1371/journal.pone.0070272.g003

hydrophobic part of R253 in the linker, and D400A, F401 and E402A in the TI loop (Fig. 3C, Table 2). Thus, hydrophobic contacts compensate for the electrostatic interactions which are predominant in the WT protein. Moreover, the important role of

electrostatics is nearly abrogated in this mutant, as reflected by the low average number of contacts involving residues K252 and R253 with the TI loop (2.8 ± 5.8 and 10.9 ± 5.1 , respectively, Table 1) that are based mainly on hydrophobic interactions

Table 2. Relevant calculated populations and maximal contact lifetimes between linker and TI loop residues.

Model	K252-X400	K252-X402	R253-X400	R253-X402	Y255-X400	Y255-F401
States (bound – unbound)						
WT	49–451	202–298	497–3	431–69	0–500	460–40
NEUT	0–500	0–500	0–500	6–494	285–215	460–40
ALA	27–473	81–419	454–46	8–492	497–3	478–22
D400A	4–496	78–422	480–20	488–12	285–215	441–59
Maximal contact lifetime (ns)						
WT	0.6	1.9	24.3	16.6	–	6.9
NEUT	–	–	–	0.2	4.1	13.8
ALA	1.0	4.3	8.9	0.3	24.5	12.4
D400A	0.1	2.0	17.3	21.9	7.7	7.5

Relation of connected and broken states (population) and maximal contact lifetimes for each interaction during the whole simulation of 50 ns are listed. For determining the population, the existence of a contact was checked in 100-ps-steps. Thus, the total number of possible states is 500. For the contact definition, a cut-off sphere of 3.5 Å is used. Beyond this value, a contact is defined as broken.
doi:10.1371/journal.pone.0070272.t002

(Fig. 3C). Furthermore, the maximal interaction lifetimes of these contacts are drastically reduced in comparison to the WT model (Table 2). This finding is striking considering the fact that the properties of the TI loop in the ALA mutant should be more disruptively changed than in the NEUT model.

In the D400A variant, the interaction between linker and CD can be described as a combination of elements from the WT and the ALA model. Thus, the most stable interaction is characterized by hydrophobic contacts involving Y255, D400A and F401, as observed in the ALA mutant and further by a salt bridge involving R253 and E402, as found in the WT model (Fig. 3D). However, while in the WT the maximal contact lifetime is 24.3 ns for the salt bridge between R253 and D400, this interaction is shortened to 17.3 ns for the D400A mutant and mainly of hydrophobic nature (Table 2, Fig. 3D). This is not surprising, since the salt bridge formation is precluded by the mutated residue. In return, the contact lifetime of the salt bridge between R253 and E402 is increased compared to the WT (21.9 ns vs. 16.6 ns, respectively). These changes in interactions decrease the chance of K252 to build up salt bridges with E402 in the D400A model, because E402 is mostly occupied by interactions with R253, so that the postulated flipping mechanism is blocked (Fig. 3D).

Due to the increased hydrophobicity in the D400A compared to the WT model, stronger hydrophobic contacts could be assumed which may compensate for the changes in interactions, as it has been observed in the ALA model. However, also the hydrophobic connections between linker and TI loop are diminished in comparison to the ALA model (Table 1) and the lifetime of these contacts is strongly shortened to less than 8 ns, which is an indicator of the increased fluctuation at the linker-TI loop interface (Table 2).

Structural integrity of the linker. The structural integrity of the linker regarding its initial α -helical conformation is differently affected in the four models, due to the variability in electrostatic conditions of the adjacent TI loop.

In the WT model, the α -helix ranging from H237 to R253 is nearly maintained. The only structural deviation occurs at R245, where the helix is bent in agreement with recent predictions (Fig. S1C) [13].

In the NEUT model, the helix remains straight at R245 and stays nearly unchanged with respect to its initial geometry, which is reflected by the low root-mean-square deviation (rmsd) of only 2.1 Å (Table S2). While the helical structure of the linker in the single mutant D400A is mostly conserved and comparable to the WT, it is completely distorted in the ALA model, where the helix is totally disrupted after position R245.

These observations are reflected by the corresponding rmsd between the backbone atoms of the linker after 50 ns (Table S2). Taking the WT geometry as a reference, the D400A model exhibits an rmsd of 2.6 Å. The other models, namely NEUT and ALA, show much larger deviations of 3.2 and 3.5 Å, respectively. Compared to the initial conformation, the rmsd lies between 2.1 and 3.2 Å for all models, which indicates slight, but noticeable rearrangements (Table S2). These variations in the linker dynamics are ascribed to the different interactions with the TI loop, which additionally leads to diverging membrane-linker coupling.

Experimental Results

Phosphatase activities of TI loop mutants. With the results of the MD simulations at hand, we carried out site-directed mutagenesis of the TI loop positions D400, E402, and D405, which could be candidates for the formation of salt bridges with the linker positions K252, and R253. The functional activity of the

mutants was analyzed by co-expressing them with the PI(4,5)P₂-sensitive potassium channels KCNQ2/KCNQ3 in *Xenopus* oocytes. This system has been frequently described to be optimal for measuring the catalytic activity of Ci-VSP [4,11,13].

By conservative neutralization of individual negatively charged residues in the TI loop (D400N, E402Q, and D405N, Fig. 1C) the CD activities were only slightly reduced showing inhibition efficiencies of ca. 80–90% in comparison to 99% for the WT (Fig. 4B). Furthermore, these single mutants required similar stimulating periods as the WT to inhibit the channel currents to 50% (Fig. 4B).

The simultaneous neutralization of the three positions in the NEUT mutant decreases the CD activity significantly, which shows up in a ca. 10-fold longer stimulation interval the mutant requires to inhibit the KCNQ2/KCNQ3-currents compared to the WT (Fig. 4A, B).

In contrast, single alanine substitutions (D400A, E402A, and D405A) impair the CD activity more dramatically than the NEUT mutation (Fig. 4C). Remarkably, the substitution D400A causes the most destructive effect on the CD activity. This is reflected by the extensive increase of stimulation duration the mutant requires to inhibit the channel currents to 50%, and, moreover, by its lowest inhibition efficiency of ca. 60% compared to all other mutants studied in this work (Fig. 4A, C).

However, none of the single alanine mutations blocked the CD activity completely in a similar way as observed earlier for several linker mutants, e.g. K252C and Y255C [13]. Therefore, we generated the triple mutant ALA which contains D400A, E402A, and D405A simultaneously. Since these mutations were expected to change the TI loop structure and hydrophilicity drastically, we suspected that they would abolish the interaction with the linker completely and, as a consequence, also the catalytic activity.

Surprisingly, the CD activity of the ALA-mutant is more similar to the WT than to all mutants investigated in this work (Fig. 4A, C). Thus, it inhibited the KCNQ/KCNQ3-currents with efficiency of ~90% and in a similar stimulation interval as the WT (Fig. 4C). Based on these functional data together with the simulation results, we propose for the ALA-mutant that the increased hydrophobicity of the TI loop enables similarly favorable conditions for the interaction with the linker as in the WT, which fully compensate for the lacking salt bridge interactions and, in turn, preserve the catalytic activity of the protein.

VSD off-kinetics of TI loop mutants. We further studied the effect of mutations on the VSD kinetics by measuring the “off”-sensing currents of Ci-VSP, since it has been proposed that these signals reflect the strength of binding of the CD to the membrane which occurs during a test potential phase [11,13]. This interpretation is based on the assumption that the membrane binding of the CD has to be overcome by the VSD during its off-motion, which in return leads to a slow-down in the VSD off-kinetics [11,13].

As described earlier [13], the translocation of off-sensing charges in the WT can be described either by mono- or biexponential functions depending on the preceding potential pulse. Therefore, the respective amount of off-sensing charges ($Q_{\text{off,all}}$) also consists of a fast ($Q_{\text{off,fast}}$) and a slow ($Q_{\text{off,slow}}$) component. Whereas $Q_{\text{off,fast}}$ is observable after potentials steps between -40 and $+80$ mV (Fig. 5A), $Q_{\text{off,slow}}$ appears after potential pulses from 0 to at least $+160$ mV. Remarkably, $Q_{\text{off,slow}}$ dominates the WT off-kinetics the more positive the preceding potential pulse was (Fig. 5A).

In a previous study, we were able to show that the VSD off-currents decay fast when the CD is deleted [13]. Therefore, we concluded that the slow component in the off-kinetics is caused by

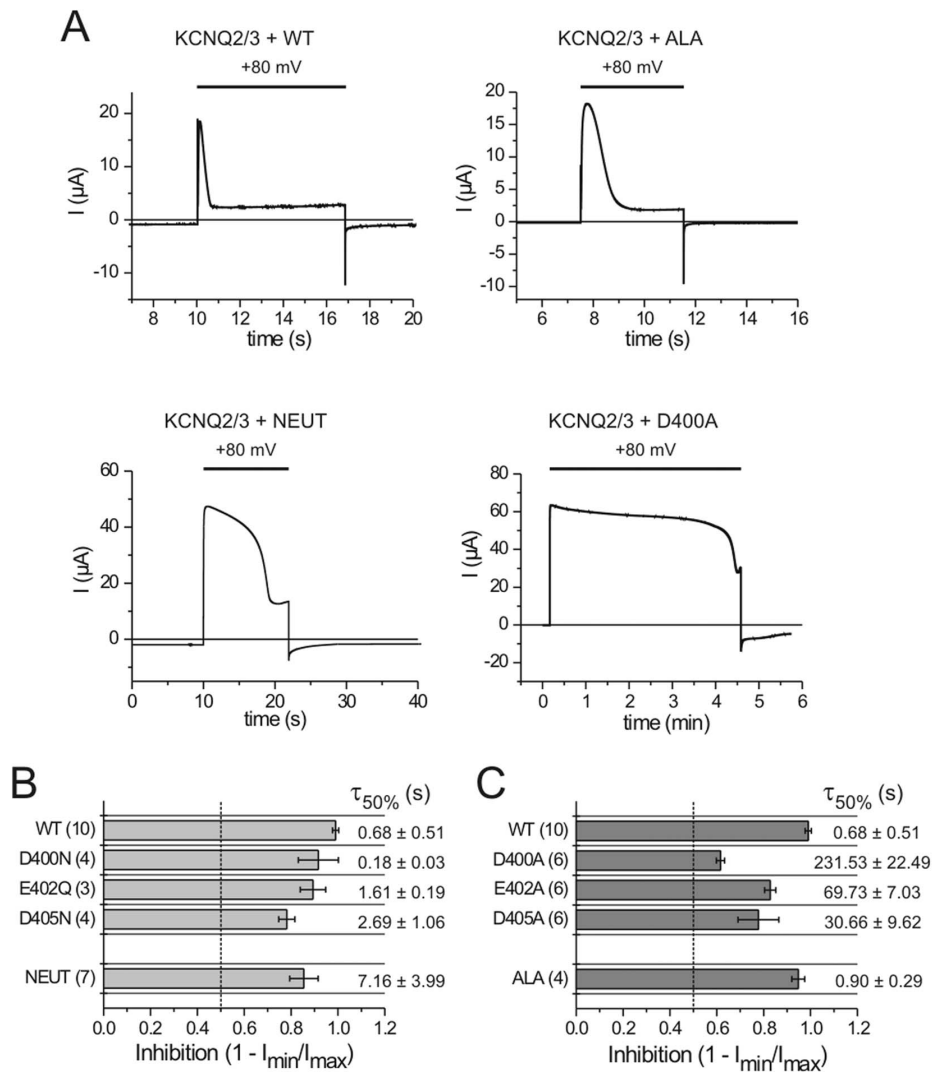


Figure 4. Phosphatase activities of TI loop mutants. (A) Representative currents traces of Ci-VSP WT and denoted mutants that were co-expressed with KCNQ2/KCNQ3 potassium channels in *Xenopus* oocytes. Channel currents were recorded in response to a depolarization pulse from a holding potential of -80 to $+80$ mV for the indicated time interval. (B–C) From the resulting current traces, maximal and minimal current amplitudes (I_{max} and I_{min}) were determined during the depolarization phase at $+80$ mV. Inhibition ratios calculated with the values of I_{min} and I_{max} are plotted with the corresponding time durations required for each mutant to inhibit the channel currents to 50% ($\tau_{50\%}$). Inhibition ratio of 0.5 (corresponding to 50%) is highlighted as dashed line. doi:10.1371/journal.pone.0070272.g004

processes that are related to the cytosolic part of the protein and, in particular, by its dissociation from the membrane.

Since the occurrence of the $Q_{off,slow}$ -fraction at voltages above 0 mV correlates with the appearance of the enzymatic activity in the WT protein [13], we initially assumed that the slow-down in the VSD off-motion is an indicator for having the CD in an active conformation. Interestingly, the kinetic data of the inactive linker mutant K252C contradicted this assumption, since this mutant showed VSD off-kinetics similar to the WT, with a dominating $Q_{off,slow}$ -fraction at positive potentials [13]. Thus, a dominating

slow fraction in the VSD off-motion is obviously not sufficient to conclude that the CD is in an active conformation.

However, a dominating fast component in the VSD off-kinetics seems to be consistently correlated with a reduction in the enzymatic activity [11,13]. Therefore, we assume that a proper coupling between VSD and CD is impaired in mutants which show fast VSD off-currents after potential pulses above 0 mV.

In the following, we analyzed the VSD off-dynamics of the TI loop mutants for this correlation. For the single neutralization mutants E402Q and D405N, slower VSD off-kinetics as for the WT are observable, which are mirrored by the moderate increase

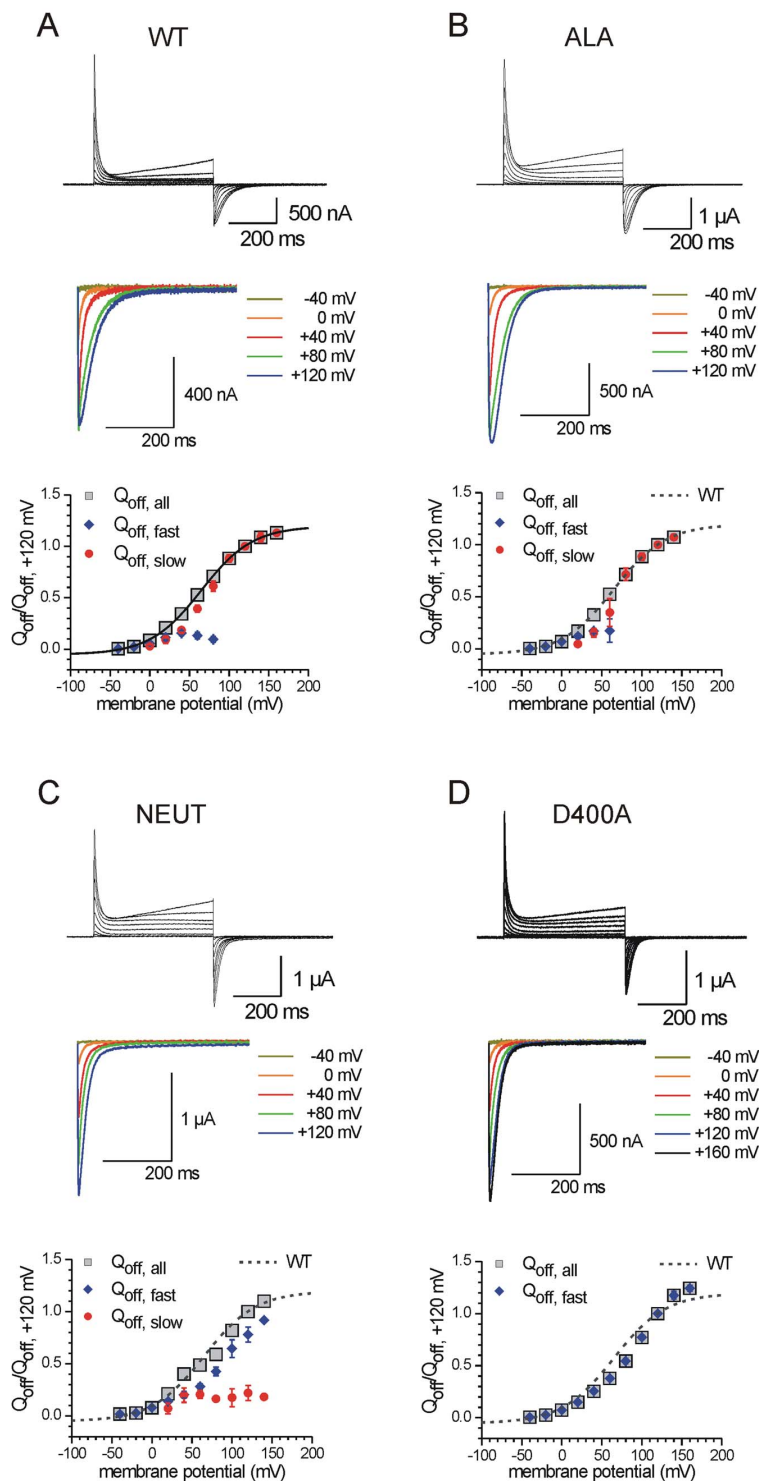


Figure 5. TI loop mutations differently affect the voltage sensor dynamics. On-sensing currents of Ci-VSP were recorded from a holding potential of -60 mV in response to variable test pulses between -40 to $+160\text{ mV}$ at maximum (increment: 20 mV , duration: 500 ms). Off-sensing currents were monitored by stepping back to -50 mV after the test potential phase (off-pulse duration: 500 ms). (A–D) Representative full current

traces are shown for the WT and the denoted mutants. From these signals, selected off-currents are zoomed out (40 mV increments). As described in Materials and Methods, $Q_{\text{off,all}}$ -V-distributions were calculated by integrating the off-sensing currents. These distributions are plotted against the potential of the preceding test pulse phase. From the whole amount of translocated sensing charges ($Q_{\text{off,all}}$), the fast ($Q_{\text{off,fast}}$) and the slow ($Q_{\text{off,slow}}$) component was determined as described in Materials and Methods. All calculated Q_{off} -values were normalized to the $Q_{\text{off,all}}$ -value corresponding to the test potential of +120 mV. $Q_{\text{off,all}}$ -V-distributions were approximated with a Boltzmann-type function (see Materials and Methods). Parameters of voltage-dependence ($V_{0.5}$, z_q) are given in Table S3.
doi:10.1371/journal.pone.0070272.g005

of the slow time constants ($\tau_{\text{off,slow}}$) in the off-currents (Fig. S2). Additionally, both mutants have slightly larger slope factors (z_q) in the voltage-dependence of translocated sensing charge ($Q_{\text{off,all}}$ -V-distribution, Table S3), which reflects an earlier saturation of the VSD off-motion at less positive potentials than in the WT (Fig. S3). All these results imply a marginally enhanced binding of the CD at the membrane in comparison to the WT.

In case of D400N, the off-kinetics is speeded up at potentials above +60 mV, which is reflected by faster time constants compared to the WT (Fig. S2). In addition, the midpoint potential of the $Q_{\text{off,all}}$ -V-distribution ($V_{0.5}$) is remarkably positively shifted by ca. +15 mV, although the z_q -value is in a similar range as for the WT (Table S3). The kinetic data of D400N corresponds to the special role of this position in the VSD-CD coupling, because the neutralization of D400 obviously leads to less restricted VSD off-motion.

For the single substitutions E402A and D405A, a similar behavior as for the neutralizing mutations E402Q and D405N is observed. The $\tau_{\text{off,slow}}$ -values are a bit larger as for the WT (Fig. S2) as well as the z_q -values (Table S3), which also indicates a slight increase in membrane binding of their catalytic domains.

In case of D400A, the VSD off-kinetics is most profoundly affected in comparison to all other mutants studied in this work. The $Q_{\text{off,all}}$ -V-distribution is significantly positive-shifted by about +30 mV (Fig. 5D, Table S3). Furthermore, the off-currents decay monoexponentially with very fast time constants compared to the WT (Fig. 5D, Fig. S2). These results indicate a disruption of the CD-mediated slow-down in the VSD off-motion for this mutant.

Interestingly, in line with the MD-simulations and CD activities, the $Q_{\text{off,all}}$ -V-distribution of the ALA-mutant is most similar to the WT compared to all other mutants (Fig. 5B). Thus, their τ_{off} -values are nearly identical for both, the fast and the slow time constants (Fig. S2). Additionally, the midpoint potential $V_{0.5}$ of the $Q_{\text{off,all}}$ -V-distribution is almost the same as for the WT (Table S3). Only the difference in z_q -values between the WT and ALA (with 0.78 and 0.90, respectively) indicates an earlier onset of saturation of the $Q_{\text{off,all}}$ -V-distribution for the ALA-mutant, which suggests a slightly stronger binding of the CD in the mutant.

As predicted from the MD simulation, reduced interaction between TI loop and linker in the NEUT-mutant is also supported by the corresponding VSD off-kinetics. Thus, the off-currents are speeded up similar to the D400A mutant (Fig. 5C, D). However, in contrast to D400A, the $Q_{\text{off,all}}$ -V-distribution contains both, a slow and a fast Q_{off} -fraction over the whole potential range (Fig. 5C), which correlates with a reduction in the catalytic activity, but not to the same extent as for D400A (Fig. 4).

As described earlier for several linker mutants, a reduction in their catalytic activity is correlated with a dominant fast Q_{off} -component [13]. Here, such a correlation between catalytic activity and VSD off-kinetics is again observed for the NEUT-mutant and, even more pronounced, for D400A.

In summary, the VSD off-kinetics obtained for all TI loop mutants are consistent with the results of their CD activities. Thus, the more dominant the fast component of the off-currents becomes, the more the catalytic activity is reduced. According to

the analysis of the CD activity, the VSD off-kinetics of the D400 mutants refers to the special role of this residue in the interaction between the linker and the TI loop, and, therefore, also on the VSD-CD coupling.

Discussion

The efficiency of the voltage-dependent activity of Ci-VSP depends on the quality of coupling between the VSD and the CD. For these processes, the region that links both modules is assumed to play a crucial role [4,11–13]. Particularly, the positively charged character of the linker suggests that it interacts electrostatically with negatively charged counterparts in its immediate environment. Several studies support the hypothesis that the binding of the linker to the membrane surface is crucial for coupling in Ci-VSP, since it might result in the recruiting of the CD to its substrate [11–13]. Besides that, previous results further suggested interactions between the linker positions K252 and R253 with residues inside the CD [13,14]. However, the knowledge about the dynamic VSD-CD interaction is still limited.

In this study, we gain more insight into this aspect with a combined approach of MD simulations and electrophysiology. We created a three-dimensional homology model of the Ci-VSP structure which includes the VSD and CD, both connected by an α -helical linker as proposed earlier [13]. This was done for the WT structure as well as for the three mutants NEUT, ALA and D400A (Fig. 1C).

In our classical MD simulations, interactions between the linker and the negatively charged membrane surface are observed for all models that confirms suggestions of previous studies [11–13]. It should be mentioned that we analyzed in our MD simulation only the interactions of the linker with PI(4,5)P₂, but not with other PIP-species, such as PI(3,4)P₂, PI(3,5)P₂ or PI(3,4,5)P₃. Thus, we cannot conclude whether the linker residues might exhibit a binding preference for one of these membrane lipids or not. This question must be addressed in forthcoming studies.

As suggested earlier, we observed a bending of the linker structure in the WT. However, the kink did not occur at position S249 as proposed earlier [13], but at position R245. Interestingly, this structural interruption enables stable interactions between the C-terminal linker residues K252, R253 and Y255 with D400, F401 and E402 in the TI loop of the CD. Remarkably, a mixture of electrostatic and hydrophobic interactions seems to be important for the linkage between linker and TI loop. Whereas K252 and R253 in the WT model form salt bridges with E402 and D400, respectively, Y255 contributes with hydrophobic contacts to F401.

These model predictions are supported by the electrophysiological data. Thus, single mutations in the TI loop affect the activity of the CD and the VSD off-kinetics depending on the properties of amino acids used for the replacement. Thereby, single conservatively neutralizing mutations have less impact on the coupling between the protein modules, presumably because they form H-bonds with the linker instead of salt bridges. Contrary, single alanine mutations interfere dramatically with these processes, probably because the formation of H-bonds and salt bridges are disrupted. Moreover, hydrophobic interactions

with one introduced hydrophobic residue alone seem to be insufficient to compensate for the lack of electrostatic interactions.

Interestingly, all single alanine mutations in the TI loop lead to a CD activity as it was observed earlier for most of the C-terminal cysteine linker mutants N251C-K257C [13]. These results suggest that TI loop- and C-terminal linker mutations similarly affect the VSD-CD-interaction.

From all positions mutated individually in the TI loop, D400 seems to be most crucial for maintaining the coupling. Thus, both D400Q and D400A cause the most dramatic effect on the VSD-off-kinetics and, especially D400A, also on the CD activity. Finally, the MD simulations provided a clue for understanding the importance of this position. While in the WT model a flipping of R253 between D400 and E402 is observed, this process is inhibited in the D400A model, where R253 preferentially binds to E402. If the stable interaction between R253 and E402 is the reason for the almost complete lack of catalytic activity of the D400A mutant, it seems to be obvious that the connection between R253 and D400 is essential for an efficient coupling between the VSD and the CD. In this way, it is also now possible to rationalize why the mutation K252C abolished the CD activity completely [13]. The presence of K252 seems to be crucial to push R253 towards D400, while forming the salt bridge K252-E402.

This interpretation agrees with results obtained recently from crystal structures of the Ci-VSP CD by Liu et al. [14]. These authors also suggested interactions between K252 and R253 with D400. Controversially, they observed other interaction modes between these three residues for their different crystal structures. Thus, K252 seemed to interact with D400, similar as R253. Furthermore, the competition between K252 and R253 for D400 was described to be stabilized by interactions via H-bonds to the G365 backbone carbonyl. This interaction is not observable in our simulation of the WT model, where the distance between K252 or R253 to the G365 backbone carbonyl was predicted to be 15 Å through the entire simulation.

It is important to note that during crystallization of the M240-I576-fragments of Ci-VSP's soluble cytosolic domain by Liu et al., the linker motif inevitably lacked the structural stabilization mediated by the VSD and the membrane surface allowing unconstrained movements of this flexible region. In the present study, the influence of the membrane surface on the structural integrity of the linker becomes obvious. In particular, in the MD-simulation of the NEUT model, where the polarity of the neutralized TI loop is no longer able to compensate for the attractive force mediated by the phosphate groups of the $PI(4,5)P_2$ molecules, the linker residue R253 is oriented towards the membrane surface rather than to the TI loop, which induces different structural rearrangements in the C-terminal linker compared to the WT. This reorientation seems to cause both, a reduction of catalytic activity and a disrupted coupling of the Ci-VSP modules as mirrored by the acceleration of the VSD off-currents (Fig. 5C). Hence, it can be assumed that the electrostatic attraction by the membrane is crucial for keeping the linker in a configuration that enables stable interactions with the TI loop. Taking these results into account, the interpretation of Liu et al. about flexible linker movements based on rigid crystal structures alone remains elusive.

Another indicator for the complexity of the interaction between the linker and the TI loop is observable in the dynamics of the ALA mutant. Here, due to the lack of salt bridges between K252, R253 with E402A and D400A, the linker structure is also completely reorganized compared to the WT. However, the increased hydrophobicity of the TI loop is able to compensate for the loss of electrostatic attractions by forming stable contacts

between Y255, D400A and F401, which are occasionally mediated by π -stacking interactions between the two phenyl rings of Y255 and F401 (Fig. 3C). These contacts are further stabilized by interactions of the hydrophobic parts of the side chains from K252 and R253 with D400A and E402A. Although the C-terminal linker's α -helical conformation is disrupted, the hydrophobic linkage to the TI loop obviously enables similar VSD-CD-interactions as in the WT, which is mirrored by the maintained CD activity as well as in almost identical VSD off-currents. Concordantly, the importance of the phenyl ring at linker position Y255 for Ci-VSP function was proven quite recently. While the mutation Y255C completely abolished phosphatase activity, the Y255F substitution preserved enzyme function [13].

Here, the results of the NEUT and ALA mutants illustrate the importance of balanced electrostatic and hydrophobic interactions between linker, membrane and CD. This complex interaction pattern is only revealed by considering the dynamics of the molecule and reaches beyond the previous concept of electrostatic repulsion or attraction between different regions of the Ci-VSP protein.

However, the question remains which processes lead to the activation of the CD after the linker has bound to the membrane. Two models of the activation process have been proposed: (1.) a recruitment of a constitutively active phosphatase to the membrane, and (2.) a 'gating' process, in which the CD in addition has to undergo conformational changes to enable catalysis. These processes can be illustrated in more detail by examining the substrate binding pocket of Ci-VSP based on the available crystal structures and our modeling data (Fig. 6, Fig. S4). Our results clearly show a highly negative electrostatic potential of the membrane-facing surface of the phosphatase domain in the initial state (Fig. 6A). Such a pattern can similarly be observed for the crystal structures of the Ci-VSP CD when no substrate molecule is bound to the active site (Fig. S4A) [14,15]. This raises the question why the highly negatively charged PIP-substrate should get access to the active site under such unfavorable electrostatic conditions.

For the WT and all TI loop mutants studied here, the positively charged residues around the catalytic cysteine C363 emerge from the substrate binding pocket during the MD simulations (Fig. 6A, Fig. S4B–D). The aforementioned results of the NEUT model imply that these structural rearrangements are caused by the electrostatic attraction mediated by the $PI(4,5)P_2$ -head groups during the recruitment of the CD to the membrane. We presume that the conformations obtained at the end of the MD simulations for the WT and the TI loop mutants represent intermediate open states of the substrate binding pocket, because the active site configuration in the crystal structure with an $I(1,4,5)P_3$ -molecule bound in the substrate binding pocket [14] suggests a further concentration of positively charged amino acids around the catalytic center (Fig. 6B). Interestingly, the binding pocket seems to adapt to the substrate, since the positive charges are even more concentrated, when a small PO_4^{3-} molecule is bound instead of $I(1,4,5)P_3$ (Fig. 6C). This suggests a certain degree of flexibility in the substrate binding pocket.

However, the exposure of cationic residues, which appears as prerequisite for substrate binding, requires that all negatively charged amino acids surrounding the active site in the initial state need to be pushed away from the substrate binding pocket by dynamic interactions with the membrane or with the linker.

In case of the Ci-VSP homolog PTEN, it has already been suggested that the flexible TI loop could aid in adapting the size of the active site to its substrate [6]. Moreover, it was proposed that the reorientation of this loop away from the substrate binding

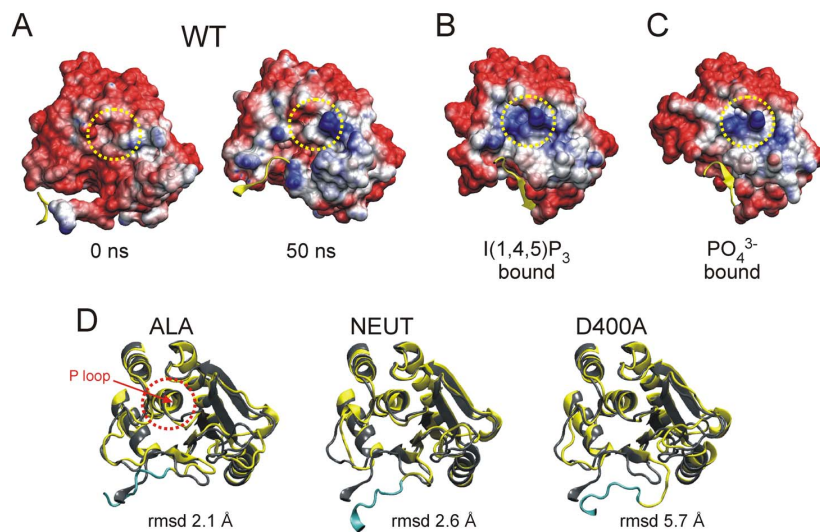


Figure 6. Interaction between linker and TI loop influences the structural integrity of the active site. (A–C) Electrostatic potential surfaces of the phosphatase domain calculated with the APBS tool [26] are shown. Representations of (A) the wild type model at 0 and after 50 ns of the MD simulation, (B) the crystallographic structures by Liu et al. of the IP₃ bound conformation (PDB 3V0H) and (C) the PO₄³⁻ bound state (3V0G) [14]. Negatively and positively charged regions are colored in red and blue, respectively. The yellow element marks the linker residues 252–257. Encircled in yellow is the immediate environment of the catalytic cysteine C363. (D) The aligned backbone structures of the phosphatase domain of the WT (grey) and the corresponding TI loop mutant (yellow) are shown. The P loop containing C363 is highlighted with a dashed circle in red. The linker motif K252–K257 of the mutants is indicated in cyan. Additionally, the figure contains the rmsd values for the structural deviation between wild type and the respective mutant.
doi:10.1371/journal.pone.0070272.g006

pocket might enable the dephosphorylation of the sterically demanding PIP-head groups [6].

For Ci-VSP, Liu et al. suggested that residue E411 is one of the candidates in the TI loop for switching between an open and a closed state of the Ci-VSP CD since it could compete with the substrate for binding at the active site [14]. In our model simulations, however, E411 does not dramatically change its position on a 50 ns time scale. This could be due to the fact that we here observe only an intermediate open conformation of the active site. To observe all structural rearrangements in the substrate binding pocket, a simulation of the entire docking process might be required. Substrate docking takes place on a large time scale, which is impossible to simulate by our present computational resources.

Nonetheless, our study sheds light on several details regarding the role of the interaction between linker and TI loop for the early conformational changes that need to occur in the substrate binding pocket during the recruitment of the CD to the membrane. Although the electrostatic potential surface for the WT and the TI loop mutants does not differ dramatically at the end of our simulations (Fig. 6A, Fig. S4B–D), a close-up view of the interaction zone between linker and TI loop reveals more clearly the role of both flexible regions for the coupling process. In Fig. 6D the coordination of the backbones of the phosphatase domain is shown, which includes the flexible regions of linker, TI and WPD loop surrounding the active site motif around C363 (named as P-loop). According to the structural deviation of the region that is oriented towards the linker, the ALA model shows the highest similarity with respect to the WT, which is mirrored in the lowest rmsd value of 2.1 Å. For the NEUT and the D400A model, the values increase from 2.6 to 5.7 Å, respectively. This corresponds to

the differently decreased phosphatase activities of both mutants. Therefore, the reduced interaction strength between linker and TI loop in the NEUT and, even more so, in the D400A model apparently destabilizes one of the boundaries of the substrate binding pocket, which might explain the impaired catalytic activity of these mutants.

In summary, the multifaceted interplay between linker and TI loop seems to invoke structural rearrangements in the substrate binding pocket, which are crucial to switch on catalytic activity. This, in effect, would reject the hypothesis of a constitutively active phosphatase in Ci-VSP. Since the formation of stable salt bridges and hydrophobic interactions between linker and TI loop is coupled to the activation state of the VSD, we propose that the linker acts as a dynamic scaffold during the voltage-dependent coupling mechanism, and - in effect - serves as a key to unlock the enzymatic activity of the Ci-VSP protein.

Materials and Methods

Model Building

To investigate the dynamics of Ci-VSP in the plasma membrane with MD simulations, an initial geometry is required. Because a complete crystallographic structure of Ci-VSP is lacking, a homology model of the protein embedded in the plasma membrane was developed. For this procedure, the programs YASARA (<http://www.yasara.org>) and VMD 1.8.7 [16] were used. The crystallographic structures of the voltage-dependent Shaker family K⁺ channel (PDB entry 2R9R) [17] and the Ci-VSP phosphatase-C2 domain complex (3AWE) [15] served as templates for the sensory and PD-C2 domains, respectively. Since the structural template for the VSD was taken from a

K_V-channel structure representing the activated configuration [17], the VSD-CD linker and the CD should encounter the structural constraints present during the activation process of the enzymatic domain.

The unknown or very poorly resolved linker was modeled as α -helix as predicted earlier [13]. Small gaps in the structural templates, such as the flexible TI loop in the crystal structure of the PD-C2-complex by Matsuda et al. [15], were inserted into the geometry and energy minimized *in vacuo*. Although several crystal structures by Liu et al. contain the TI loop, an alignment of this region derived from the different crystals revealed high structural fluctuations in the loop while the position of the neighboring helices were conserved (Fig. S5A). Comparison of the TI loop in our initial WT model with the different structures resolved by Liu et al. shows that our model fits well into the variety of possible conformations represented in the various crystals (Fig. S5A). Together with the high B-values of the TI loop elements from the structural data by Liu et al. (Fig. S5B), we assume that the loop is flexible and not restricted to a certain conformation. Because of these observations, there is no obvious reason why one of the conformations from the different crystal structures by Liu et al. should be preferred for the modeling. Therefore, we chose to continue with our initial model based upon the PD-C2-complex by Matsuda et al. [15].

The cytosolic N-terminus preceding the VSD (107 amino acids) was omitted in our model due to the lack of an appropriate template structure.

The corresponding double layer membrane consists of 291 neutrally charged POPE (1-palmitoyl-2-oleoyl- sn-glycerol-3-phosphatidylethanolamine) chains and 13 negatively charged PI(4,5)P₂ (phosphatidylinositol-4,5-bisphosphate) molecules located at the in the cytosolic leaflet. The PI(4,5)P₂ chains were modeled facing the linker and PD-C2 complex, which are both positively charged at physiological pH. This initial placing of the PI(4,5)P₂ molecules was adopted to speed up the electrostatic interactions with the positively charged regions of Ci-VSP and to avoid long rearrangement processes within the membrane. The PI(4,5)P₂ head groups were treated with the partial charges derived by Lupyan et al. [18].

To investigate changes in the dynamics and the interaction between the membrane and Ci-VSP and, furthermore, to resolve more details about the coupling between the linker and the TI loop, we generated, additionally to the wild type (WT), three mutants by selectively replacing the negatively charged amino acids of the TI loop (D400, E402, D405). In the first mutant (NEUT model), we simply neutralized the charges of the loop region simultaneously while keeping the amino acid side chains as similar as possible (D400N, E402Q, D405N, Fig. 1C). In the second model (ALA model), we mutated all indicated residues to alanines (D400A, E402A, D405A), which strongly alters the electrostatic nature of the region. To demonstrate the importance of D400A, we constructed a third modification of Ci-VSP by changing D400 into alanine (D400A model).

In order to approximate experimental conditions, we solvated the Ci-VSP-membrane models in a TIP3P water box [19]. Additionally, we added Na⁺ and Cl⁻ ions to obtain a neutrally charged system with an ionic strength of 100 mM mimicking the experimental conditions. In total, each system contains more than 153,000 atoms and has a dimension of ca. 177 × 101 × 147 Å³.

Molecular Dynamics Simulations

Atomistic molecular dynamics simulations were performed with NAMD2.7 [20] using the CHARMM27 force field including the CHARMM force field for lipids [21].

In a first step, the energy of the models containing Ci-VSP, the membrane and the solution was energy minimized with the conjugated gradient routine in 30,000 steps. During the minimization, all heavy atoms were constrained with 25 kcal·mol⁻¹ Å⁻² to their positions. Afterwards, the systems were heated up to 300 K in 60 ps, while the position constraints were decreased stepwise from 7.5 to 2.5 kcal·mol⁻¹ Å⁻².

In the following solvent equilibration, the water and ions were allowed to translate and rotate without any restrictions and the constraints on the protein and the membrane were further decreased until all atoms in the systems were allowed to move freely in the cell. After this preparation, an unconstrained production MD run of 50 ns was carried out to investigate the dynamics of the system. The simulations were run on 128 CPUs (16 nodes with 8 tasks) in parallel and required in total more than 6,400 CPU hours.

To obtain a realistic behavior of the membrane, periodic boundary conditions in all dimensions were applied keeping the cell size in the membrane directions constant. This cell setup was realized by an NPaT ensemble, where besides the surface area the numbers of particles (N), the pressure (P) and the temperature (T) were kept constant during the simulation. Langevin piston dynamics [22] enabled these conditions. Furthermore, an integration time step of 2 fs was employed, which was enabled by the SHAKE algorithm treating all bonds including hydrogen atoms as rigid [23].

Short-range electrostatics and van der Waals interactions were simulated with a cut-off of 12 Å, while long-range electrostatics was calculated with the particle mesh Ewald summation [24].

Mutagenesis

Ci-VSP cDNA was subcloned into the plasmid vector pFROG3, which has been optimized for heterologous protein expression in *Xenopus* oocytes [25]. All mutations were generated using the QuikChange site directed mutagenesis kit (Stratagene, La Jolla, CA), and verified by sequencing (Eurofins MWG Operon, Germany).

cRNA Synthesis and Injection of *Xenopus* Oocytes

Ci-VSP cDNA was linearized with *Ksp*AI (Fermentas). Afterwards, cRNA was synthesized with the T7 mMessage mMachine kit (Ambion, USA). KCNQ2 and KCNQ3 cDNA (subcloned into the plasmid vector pTLN) were linearized with *Not*I (Fermentas) and transcribed into cRNA with the SP6 mMessage mMachine kit (Ambion). The preparation of *Xenopus* oocytes was done as described in detail recently [13].

For measuring transient sensing currents, 50 nL of 0.5 µg/µL Ci-VSP cRNA were injected per cell; for CD-activity measurements, 50 nL of a KCNQ2:KCNQ3:Ki-VSP cRNA mixture (0.05:0.05:0.5 µg/µL) were injected. After injection, oocytes were stored for 3–4 days at 18°C in ORI buffer containing 50 mg/L gentamycin, as described previously [13].

Electrophysiology

3–4 days after injection, currents were recorded at 21–23°C with the two-electrode voltage-clamp technique using a Turbotec 10CX amplifier (NPI instruments, Tamm, Germany). The experimental solutions and procedures for analyzing VSD-kinetics (from Ci-VSP's "off" sensing currents) and CD-activities (from the inhibition of KCNQ2/KCNQ3 currents) used in this study were recently described in detail [13]. Measuring protocols are denoted at the respective positions in the results section.

Data Acquisition and Analysis

Currents were acquired using the pClamp 10 software (Axon Instruments, USA). Data were analyzed with pClampfit 10 (Axon Instruments), Excel (Microsoft, USA) and Origin 7.0 (Microcal, USA). As described previously [13], the time constants τ_{off} for the VSD off-currents were determined by exponential approximation:

$$I(t) = I_0 + \sum_{i=1}^N I_i \times \exp\left(-\frac{t}{\tau_i}\right) \quad (1)$$

with $N=1$ for monoexponential and $N=2$ for biexponential kinetics.

The decisive criteria for using a mono- or biexponential approximation was the χ^2 -value determined with a χ^2 -minimization of the respective data set, without applying a weight to individual experimental data points. The parameters of the function that gave the minimal χ^2 -value during the fitting session were used subsequently, because this function described the VSD off-kinetics most precisely.

According to Eq. 1, the data set used for the fitting session started from $t=5$ ms to calculate the initial current amplitudes at the onset of the off-pulse directly from the fitted function, and to eliminate residual capacitive artefacts. The charge translocated during the VSD off-motion, $Q_{\text{off,all}}$, was determined from the fitting parameters from Eq. 1 with:

$$Q_{\text{off,all}} = \sum_{i=1}^N I_i \times \tau_i \quad (2)$$

$Q_{\text{off,fast}}$ was calculated from the product of $\tau_{\text{off,fast}}$ and its corresponding initial current amplitude $I_{\text{off,fast}}$. $Q_{\text{off,slow}}$ was determined analogously with the values of $\tau_{\text{off,slow}}$ and $I_{\text{off,slow}}$.

The values which describe the voltage-dependence of the VSD off-kinetics, $V_{0.5}$ (midpoint potential) and z_q (slope factor), were determined by fitting the $Q_{\text{off,all}}$ -V-relationship with a Boltzmann-type function:

$$\frac{Q_{\text{off,all}}}{Q_{\text{off,all,+120mV}}} = A_{\text{max}} + \frac{A_{\text{min}} - A_{\text{max}}}{1 + \exp\left[\frac{z_q F}{RT} (V - V_{0.5})\right]}$$

with the applied test potential V , the Faraday constant F , the gas constant R , the absolute temperature T in K , and A_{min} , A_{max} as the minimal and maximal values the function adopts during approximation.

For statistics, at least three independent measurements were analyzed. Oocytes were obtained from at least two different cell batches. Unless mentioned differently, means \pm standard deviations are presented.

Supporting Information

Figure S1 Three-dimensional Ci-VSP model with the VSD embedded in a lipid bilayer and with interactions between linker residues and PI(4,5)P₂ molecules. (A) Structural model of the protein backbone for the wild type before (0 ns) and after (50 ns) the MD-simulation. The VSD (colored in dark gray) is embedded in the lipid bilayer containing 291 neutrally charged POPE chains (cyan) and 13 negatively charged PI(4,5)P₂ molecules (yellow). The CD is coupled to the VSD via the linker motif M240–K257 (blue). PD and C2 domain are marked in medium and light gray, respectively. (B, C) Structural

geometries between single linker residues (yellow, and N251 in orange) and PI(4,5)P₂ molecules at the inner membrane surface (B) before and (C) after the MD-simulation. Heavy atoms are marked in the following colors: nitrogen, blue; oxygen, red; phosphorus, orange; hydrogen, white. (The structure coordinates of our wild type model will be available upon request.)

(TIF)

Figure S2 Differences in voltage-dependent time constants of the VSD off-motion for TI loop mutants.

Transient off-currents of Ci-VSP were approximated with mono- or biexponential functions as described earlier [13]. Fast and slow time constants (τ_{off}) for the VSD-off-kinetics were determined depending on the membrane potential applied during the test pulse phase. Averaged τ_{off} -values are given as filled symbols. For comparison, the corresponding voltage-dependent time constants of the WT are shown as dotted lines.

(TIF)

Figure S3 Voltage-dependence of translocated off-sensing charges for TI loop mutants.

Sensing charges translocated during the off-motion of the VSD were calculated as described earlier [13]. The averaged fast ($Q_{\text{off,fast}}$ in blue) and slow fraction ($Q_{\text{off,slow}}$ in red) of the off-sensing charge are plotted against the membrane potential as well as the sum of both ($Q_{\text{off,all}}$ in gray). The individual Q_{off} -values, which were obtained per oocyte, were normalized to the respective $Q_{\text{off,all}}$ -value at +120 mV. $Q_{\text{off,all}}$ was approximated with a Boltzmann-type function as described in Materials and Methods. Fitting parameters $V_{0.5}$ and z_q are given in Table S3.

(TIF)

Figure S4 Electrostatic potential surfaces for the catalytic domain of Ci-VSP in the substrate-unbound conformation and the modeled TI loop mutants.

Electrostatic potential surfaces for the phosphatase domain of Ci-VSP were calculated with the APBS tool [26]. Representations of (A) the unbound conformations based on the crystal structures by Matsuda et al., 2011 [15] (left panel) and Liu et al., 2012 [14] (right panel; PDB entries are given, respectively) as well as (B–D) for the denoted TI loop mutants before (0 ns) and after (50 ns) of MD simulation. It should be noted that the differences in electrostatic potentials between the WT (Fig. 6A) and the mutants at 0 ns is due to the reduction of the negatively charged character in the TI loop caused by the respective mutation.

(TIF)

Figure S5 Structural alignment between the TI loop region of the initial Ci-VSP WT model and crystallographic structures.

(A) The TI loop of our initial Ci-VSP WT model (red) is structurally aligned with the respective region from the crystallographic structures by Liu et al. [14] (cyan). To obtain a suitable alignment, the neighboring α -helices were superimposed, with helix a and b containing the residues T386–T399 and T412–Y429, respectively. (B) The B-values of the C_α-atoms for all residues resolved in the crystallographic structures by Liu et al. [14] are plotted. The red box marks the strongly fluctuating region of the TI loop.

(TIF)

Table S1 Averaged number of contacts between linker and PI(4,5)P₂ residues.

Number of contacts (#contacts) between the linker and PI(4,5)P₂ residues averaged over the last 30 ns. Additionally, the interaction of the N-terminal (240–249) and the C-terminal (250–257) parts of the linker and PI(4,5)P₂ residues is shown. As in Table 1, contacts are defined as atoms within a sphere of 3.5 Å.

(DOC)

Table S2 Structural changes of the linker in terms of the root-mean-square deviation. The differences between the end geometries in comparison to the WT enzyme after 50 ns are shown. Additionally, the over the last 30 ns averaged rmsd to the initial conformation is displayed. All rmsd values refer to the backbone atoms of the linker region (240 to 257). (DOC)

Table S3 Boltzmann-parameters for the voltage-dependent translocation of sensing charges in Ci-VSP. Amount of voltage-dependent sensing charges ($Q_{\text{off,all}}-V$ -values) were determined from the transient off-currents of Ci-VSP as described in detail earlier [13]. The resulting $Q_{\text{off,all}}-V$ -distributions were approximated with a Boltzmann-type function (see Material and Methods) to determine the parameters $V_{0.5}$ (midpoint potential) and z_q (slope factor) which describe the voltage-dependence of the

off-currents (n: numbers of independently performed measurements). (DOC)

Acknowledgments

The authors thank Dr. Yoshimichi Murata for providing the Ci-VSP cDNA, and the “North-German Supercomputing Alliance” (HLRN) for the computational resources.

Author Contributions

Conceived and designed the experiments: KH TU MAM GS TF. Performed the experiments: KH TU. Analyzed the data: KH TU. Contributed reagents/materials/analysis tools: MAM GS TF. Wrote the paper: KH TU MAM TF. Supervised the experimental part: TF. Supervised the modelling part: MAM.

References

- Falkenburger BH, Jensen JB, Dickson EJ, Suh B-C, Hille B (2010) Phosphoinositides: lipid regulators of membrane proteins. *J Physiol* 588: 3179–3185.
- Bunney TD, Katan M (2010) Phosphoinositide signalling in cancer: beyond PI3K and PTEN. *Nat Rev Cancer* 10: 342–352.
- Shi Y, Azab A, Thompson M, Greenberg M (2006) Inositol Phosphates and Phosphoinositides in Health and Disease. *Subcell Biochem* 39: 265–292.
- Murata Y, Iwasaki H, Sasaki M, Inaba K, Okamura Y (2005) Phosphoinositide phosphatase activity coupled to an intrinsic voltage sensor. *Nature* 435: 1239–1243.
- Li J, Yen C, Liaw D, Podyspanina K, Bose S, et al. (1997) PTEN, a Putative Protein Tyrosine Phosphatase Gene Mutated in Human Brain, Breast, and Prostate Cancer. *Science* 275: 1943–1947.
- Lee J-O, Yang H, Georgescu M-M, Di Cristofano A, Maehama T, et al. (1999) Crystal Structure of the PTEN Tumor Suppressor: Implications for Its Phosphoinositide Phosphatase Activity and Membrane Association. *Cell* 99: 323–334.
- Vazquez F, Sellers WR (2000) The PTEN tumor suppressor protein: an antagonist of phosphoinositide 3-kinase signaling. *Biochim Biophys Acta* 1470: M21–M35.
- Iwasaki H, Murata Y, Kim Y, Hossain MI, Worby CA, et al. (2008) A voltage-sensing phosphatase, Ci-VSP, which shares sequence identity with PTEN, dephosphorylates phosphatidylinositol 4,5-bisphosphate. *Proc Natl Acad Sci USA* 105: 7970–7975.
- Kurokawa T, Takasuga S, Sakata S, Yamaguchi S, Horie S, et al. (2012) 3' Phosphatase activity toward phosphatidylinositol 3,4-bisphosphate [PI(3,4)P2] by voltage-sensing phosphatase (VSP). *Proc Natl Acad Sci USA*.
- Halaszovich CR, Schreiber DN, Oliver D (2009) Ci-VSP Is a Depolarization-activated Phosphatidylinositol-4,5-bisphosphate and Phosphatidylinositol-3,4,5-trisphosphate 5'-Phosphatase. *J Biol Chem* 284: 2106–2113.
- Villalba-Galea CA, Miceli F, Tagliatalata M, Bezanilla F (2009) Coupling between the voltage-sensing and phosphatase domains of Ci-VSP. *J Gen Physiol* 134: 5–14.
- Kohout SC, Bell SC, Liu L, Xu Q, Minor DL, et al. (2010) Electrochemical coupling in the voltage-dependent phosphatase Ci-VSP. *Nat Chem Biol* 6: 369–375.
- Hobiger K, Utesch T, Mroginiski MA, Friedrich T (2012) Coupling of Ci-VSP Modules Requires a Combination of Structure and Electrostatics within the Linker. *Biophys J* 102: 1313–1322.
- Liu L, Kohout SC, Xu Q, Müller S, Kimberlin CR, et al. (2012) A glutamate switch controls voltage-sensitive phosphatase function. *Nat Struct Mol Biol* 19: 633–641.
- Matsuda M, Takeshita K, Kurokawa T, Sakata S, Suzuki M, et al. (2011) Crystal structure of the cytoplasmic PTEN-like region of Ci-VSP provides insight into substrate specificity and redox regulation of the phosphoinositide phosphatase activity. *J Biol Chem*.
- Humphrey W, Dalke A, Schulten K (1996) VMD: Visual molecular dynamics. *J Mol Graph* 14: 33–38.
- Long SB, Tao X, Campbell EB, MacKinnon R (2007) Atomic structure of a voltage-dependent K⁺ channel in a lipid membrane-like environment. *Nature* 450: 376–382.
- Lupyan D, Mezei M, Logothetis DE, Osman R (2010) A Molecular Dynamics Investigation of Lipid Bilayer Perturbation by PIP2. *Biophys J* 98: 240–247.
- Jorgensen WL, Chandrasekhar J, Madura JD, Impey RW, Klein ML (1983) Comparison of simple potential functions for simulating liquid water. *J Chem Phys* 79: 926–935.
- Phillips JC, Braun R, Wang W, Gumbart J, Tajkhorshid E, et al. (2005) Scalable molecular dynamics with NAMD. *J Comput Chem* 26: 1781–1802.
- MacKerell AD, Bashford D, Dunbrack RL, Evanseck JD, Field MJ, et al. (1998) All-Atom Empirical Potential for Molecular Modeling and Dynamics Studies of Proteins. *The Journal of Physical Chemistry B* 102: 3586–3616.
- Feller SE, Zhang Y, Pastor RW, Brooks BR (1995) Constant pressure molecular dynamics simulation: The Langevin piston method. *J Chem Phys* 103: 4613–4621.
- Van Gunsteren WF, Berendsen HJC (1977) Algorithms for macromolecular dynamics and constraint dynamics. *Mol Phys* 34: 1311–1327.
- Darden T, York D, Pedersen L (1993) Particle mesh Ewald: An N log(N) method for Ewald sums in large systems. *J Chem Phys* 98: 10089–10092.
- Koenderink JB, Zifarelli G, Qiu LY, Schwarz W, De Pont JJHMM, et al. (2005) Na,K-ATPase mutations in familial hemiplegic migraine lead to functional inactivation. *Biochim Biophys Acta* 1669: 61–68.
- Baker NA, Sept D, Joseph S, Holst MJ, McCammon JA (2001) Electrostatics of nanosystems: Application to microtubules and the ribosome. *Proc Natl Acad Sci* 98: 10037–10041.

11 Conclusions and Outlook

This study demonstrates the successful application and potential of all-atom MD simulations combined with different experimental techniques to investigate the interaction dynamics of biomolecules with different surfaces. Although the simulations are limited to the nanosecond time-scale, the characteristics of the interaction between enzyme and surface were demonstrated and agree very well with the observations obtained experimentally. This approach investigating immobilization processes with two techniques connects the microscopic information of MD simulations with the macroscopic observables gained by experiments and allows in this way a detailed and directed modification of the treated system.

11.1 Cytochrome *c*

Cytochrome *c* served as test system for fundamental research and showed a high stability in solution and upon immobilization. The gained trajectories were analysed to explain changes in the electrostatics and to proof basic principles, such as the Stark effect [10, 11].

11.2 Bone morphogenetic protein-2

The adsorption SMD/MD simulations of BMP-2 on two implant surfaces, namely, graphite and titanium dioxide, revealed two very different results. On graphite, BMP-2 showed a relatively weak and unspecific binding and the protein structure was only slightly affected by the adsorption. In contrast to this observation, BMP-2 did not adsorb on titanium dioxide showing much favourable interaction energies *in vacuo*. This surprising result was an outcome of the competitive adsorption of water forming an adlayer on the metal oxide.

11.3 Sulfite oxidase

In sulfite oxidase science, two proposed models were confirmed by SMD and MD simulations. First, a hybrid approach of SMD and pure MD simulations demonstrated that the proposed domain motion of the cytochrome *b5* unit resulted in a (at least on the nanosecond time scale) stable activated conformation enabling fast IET between the redox centres. Second, immobilization MD simulations validated the inhibitory effect of a positively charged surface on the IET. This effect was based on the strong immobilization of the cytochrome *b5*, which lost its flexibility upon the ionic strength dependent adsorption. Taken together, these results affirm the experimental predictions and offer a detailed insight into the underlying molecular processes, which are meaningful for the biosensor application.

11.4 [NiFe] hydrogenases

The work on the standard [NiFe] hydrogenase of *D. gigas* demonstrated the importance of the pH conditions for the electrostatically driven adsorption dynamics of the enzyme on amine terminated SAMs. At low pH leading to a high protonation degree of the SAM, the hydrogenase adsorbed firmly on the surface, but exhibited major rearrangements with respect to its initial structure. These structural disruption might affect the proper functionality. By increasing the pH value the protein became more stable which correlated with a decreased adsorption strength.

The immobilization of the oxygen tolerant MBH was more complex, because the structure is elongated by a hydrophobic membrane anchor and exhibits only a weak dipole moment. While the adsorption on amino-terminated SAMs was comparable to standard hydrogenases, the tail region played a key role in the interaction with anionic carboxyl-terminated monolayers and prevented desorption from the surface.

In the future, the immobilization study will be further extended to mixed and hydrophobic monolayers. The idea behind this plan is to regulate the electrostatic interactions by diluting the SAMs with polar hydroxyl groups. The hydrophobic monolayer will be used to further reduce the Coulombic contribution for the adsorption dynamics.

11.5 *Ciona intestinalis* voltage sensing phosphatase

By means of MD simulations based on a homology model, the complex dynamics of Ci-VSP embedded in the plasma membrane were explored. In particular, the dynamics of the linker region connecting VSD and CD were analysed. Its roles in membrane recruitment as well as in coupling between the two domains were shown and shed light into the comprehensive observations performed by electrophysiological research. We demonstrated that the coupling dominated by electrostatics in the wild type (WT) enzyme can be compensated by hydrophobic interactions in TI loop triple Ala-mutants, while neutralization and single mutants led to noticeable decreased phosphatase activity.

11.6 Outlook

The rapidly increasing computer power and the beginning application of graphic card processors for the calculation of biological problems will allow longer MD simulations and enlarge the complexity of the treated systems. This fact will boost the importance of theoretical calculations and further establish their predictions.

Furthermore, the ongoing improvement of coarse-grained MD simulations offers another way to extend the time scale of simulations. In the future, a combination of coarse-grained and classical all-atom MD simulations could be a promising technique to investigate surface interaction of biomolecules even if larger reorientations are predicted.

12 Danksagung

Ich danke allen, die mich während meiner Promotion in unterschiedlicher Weise unterstützt haben. Besonderer Dank gilt folgenden Personen:

- Prof. Dr. Maria Andrea Mroginki für die hervorragende Betreuung meiner Arbeit und die sehr angenehme Arbeitsatmosphäre
- Dr. Peter Hildebrand für die Begutachtung meiner Arbeit
- Prof. Dr. Roderich Süßmuth für die Übernahme des Prüfungsvorsitzes
- Dr. Steve Kaminski für seine ausführliche und sehr geduldige Einführung in den Umgang mit CHARMM und dem Alibaba Rechencluster
- Prof. Dr. Peter Hildebrandt für die lockere Art und seine Hilfe und Ratschläge
- Dr. Grazia Daminelli für die interessante Zusammenarbeit an BMP-2
- Yvonne Rippers für die stets freundliche Odyssee zur Validierung des MBH Modells
- Dr. Inez Weidiger und Dr. Murat Sezer für die erfolgreiche Zusammenarbeit an der Sulfitoxidase
- Dr. Ingo Zebger, Dr. Diego Millo, Nina Heidary und Prof. Dr. Anna Fischer für die Einblicke in SEIRA Spektroskopie und sehr gute Zusammenarbeit an [NiFe] Hydrogenasen
- Prof. Dr. Thomas Friedrich und Dr. Kirstin Hobiger für die konstruktive Zusammenarbeit an Ci-VSP, die trotz einiger Rückschläge viel Spass gemacht hat
- Dr. Gal Schkolnik für die erfolgreiche Kombination von Theorie und Spektroskopie zur Stark-Effekt-Berechnung
- der 11-Uhr-Mittags-Crew, die das Essen immer wieder lustig und abwechslungsreich gestaltet hat: Steve Kaminski, Miguel Saggu, Matthias Schenderlein, Marius Horch, Francisco Velazquez, Khoa Ly, Stefan Wahlefeld, Jacek Kozuch, Lars Paasche, Kirstin Hobiger, Ina Seuffert, Susan Spiller, Nesslihan Tavraz, Sara Bruun, Daria Tombolelli, Thomas Hildebrandt, Steffen Sarstedt und allen anderen Gelegenheitsgästen
- Jürgen Krauss, Hendrik Naumann und David von Stetten für allerlei Computerangelegenheiten
- dem Büro 316 und der gesamten MVL Belegschaft für die angenehme Zeit
- dem HLRN und Alibaba-Cluster Teams für die vielen Rechenstunden und die Instandhaltung der Rechenzentren
- dem Unicat für die Finanzierung
- Alex und Cassie für die Tipps
- meinen Freunden außerhalb des Instituts (Stammtisch, Fussball- und anderen Freunden) für die Abwechslung zur Arbeit
- Nadine für die Ruhe und Geduld, wenn ich mich mal wieder „Einwählen“ musste
- meiner Familie, die mich immer unterstützt und mir die Promotion ermöglicht hat

Bibliography

- [1] A. Kleinert. “Der messende Luchs.” *NTM Zeitschrift für Geschichte der Wissenschaften, Technik und Medizin* **2009** 17: 199–206
- [2] J. N. Talbert, J. M. Goddard. “Enzymes on material surfaces.” *Colloids and Surfaces, B: Biointerfaces* **2012** 93: 8–19
- [3] A. R. Leach. *Molecular Modelling: Principles and Applications*. Addison Wesley Longman Ltd. **1996**
- [4] T. Schlick. *Molecular Modeling and Simulation: An Interdisciplinary Guide (2nd Edition)*. Springer New York Dordrecht Heidelberg London **2010**
- [5] R. A. Latour. “Molecular simulation of protein-surface interactions: benefits, problems, solutions, and future directions.” *Biointerphases* **2008** 3(3): FC2–F12
- [6] G. Raffaini, F. Ganazzoli. “Protein adsorption on biomaterial and nanomaterial surfaces: a molecular modeling approach to study non-covalent interactions.” *J Appl Biomater Biomech* **2010** 8: 135 – 145
- [7] L. M. Szott, T. A. Horbett. “Protein interactions with surfaces: Computational approaches and repellency.” *Curr Opin Chem Biol* **2011** 15(5): 683–689
- [8] D. Costa, P.-A. Garrain, M. Baaden. “Understanding small biomolecule-biomaterial interactions: A review of fundamental theoretical and experimental approaches for biomolecule interactions with inorganic surfaces.” *J Biomed Mater Res A* **2012**
- [9] J. C. Love, L. A. Estroff, J. K. Kriebel, R. G. Nuzzo, G. M. Whitesides. “Self-assembled monolayers of thiolates on metals as a form of nanotechnology.” *Chem Rev* **2005** 105(4): 1103–1169
- [10] G. Schkolnik, T. Utesch, J. Salewski, K. Tenger, D. Millo, A. Kranich, I. Zebger, C. Schulz, L. Zimányi, G. Rákhely, M. A. Mroginski, P. Hildebrandt. “Mapping local electric fields in proteins at biomimetic interfaces.” *Chem Commun (Camb)* **2012** 48(1): 70–72
- [11] H. K. Ly, T. Utesch, I. Díaz-Moreno, J. M. García-Heredia, M. Ángel De La Rosa, P. Hildebrandt. “Perturbation of the Redox Site Structure of Cytochrome *c* Variants upon Tyrosine Nitration.” *J Phys Chem B* **2012**
- [12] V. Rosen. “BMP2 signaling in bone development and repair.” *Cytokine Growth Factor Rev* **2009** 20(5-6): 475–480
- [13] M. S. Bretscher. “Asymmetrical lipid bilayer structure for biological membranes.” *Nat New Biol* **1972** 236(61): 11–12

- [14] T. Pomorski, A. K. Menon. "Lipid flippases and their biological functions." *Cell Mol Life Sci* **2006** 63(24): 2908–2921
- [15] Y. Shi, A. N. Azab, M. N. Thompson, M. L. Greenberg. "Inositol phosphates and phosphoinositides in health and disease." *Subcell Biochem* **2006** 39: 265–292
- [16] B.-C. Suh, B. Hille. "PIP₂ is a necessary cofactor for ion channel function: how and why?" *Annu Rev Biophys* **2008** 37: 175–195
- [17] B. H. Falkenburger, J. B. Jensen, E. J. Dickson, B.-C. Suh, B. Hille. "Phosphoinositides: lipid regulators of membrane proteins." *J Physiol* **2010** 588(Pt 17): 3179–3185
- [18] C. Eriksson, H. Nygren. "The initial reactions of graphite and gold with blood." *J Biomed Mater Res* **1997** 37(1): 130–136
- [19] T. Albrektsson, M. Jacobsson. "Bone-metal interface in osseointegration." *J Prosthet Dent* **1987** 57(5): 597–607
- [20] U. Diebold. "The surface science of titanium dioxide." *Surf Sci Rep* **2003** 48(5-8): 53 – 229
- [21] A. V. Bandura, J. D. Kubicki. "Derivation of Force Field Parameters for TiO₂-H₂O Systems from ab Initio Calculations." *J Phys Chem B* **2003** 107(40): 11072–11081
- [22] L. H. Dubois, R. G. Nuzzo. "Synthesis, Structure, and Properties of Model Organic Surfaces." *Annu Rev Phys Chem* **1992** 43(1): 437–463
- [23] G. E. Poirier. "Mechanism of Formation of Au Vacancy Islands in Alkanethiol Monolayers on Au(111)." *Langmuir* **1997** 13(7): 2019–2026
- [24] X. Xie. "A Review of Recent Advances in Surface Defect Detection using Texture analysis Techniques." *ELCVIA* **2008** 7(3)
- [25] K. Rendulic. "The influence of surface defects on adsorption and desorption." *Appl Phys A* **1988** 47: 55–62
- [26] L. Strong, G. M. Whitesides. "Structures of self-assembled monolayer films of organosulfur compounds adsorbed on gold single crystals: electron diffraction studies." *Langmuir* **1988** 4(3): 546–558
- [27] R. A. Scott, A. G. Mauk. *Cytochrome c: A Multidisciplinary Approach*. University Science Books: Sausalito, CA **1995**
- [28] I. Bertini, G. Cavallaro, A. Rosato. "Cytochrome c: occurrence and functions." *Chem Rev* **2006** 106(1): 90–115
- [29] Y.-L. P. Ow, D. R. Green, Z. Hao, T. W. Mak. "Cytochrome c: functions beyond respiration." *Nat Rev Mol Cell Biol* **2008** 9(7): 532–542
- [30] F. C. Bernstein, T. F. Koetzle, G. J. Williams, E. F. M. Jr., M. D. Brice, J. R. Rodgers, O. Kennard, T. Shimanouchi, M. Tasumi. "The protein data bank: A computer-based archival file for macromolecular structures." *Arch Biochem Biophys* **1978** 185(2): 584 – 591

- [31] R. Kranz, R. Lill, B. Goldman, G. Bonnard, S. Merchant. "Molecular mechanisms of cytochrome *c* biogenesis: three distinct systems." *Mol Microbiol* **1998** 29(2): 383–396
- [32] J. W. A. Allen, N. Leach, S. J. Ferguson. "The histidine of the c-type cytochrome CXXCH haem-binding motif is essential for haem attachment by the *Escherichia coli* cytochrome *c* maturation (Ccm) apparatus." *Biochem J* **2005** 389(Pt 2): 587–592
- [33] W. H. Koppenol, J. D. Rush, J. D. Mills, E. Margoliash. "The dipole moment of cytochrome *c*." *Mol Biol Evol* **1991** 8(4): 545–558
- [34] J.-J. Feng, D. H. Murgida, U. Kuhlmann, T. Utesch, M. A. Mroginski, P. Hildebrandt, I. M. Weidinger. "Gated electron transfer of yeast iso-1 cytochrome *c* on self-assembled monolayer-coated electrodes." *J Phys Chem B* **2008** 112(47): 15202–15211
- [35] D. Alvarez-Paggi, D. F. Martín, P. M. DeBiase, P. Hildebrandt, M. A. Martí, D. H. Murgida. "Molecular basis of coupled protein and electron transfer dynamics of cytochrome *c* in biomimetic complexes." *J Am Chem Soc* **2010** 132(16): 5769–5778
- [36] D. A. Paggi, D. F. Martin, A. Kranich, P. Hildebrandt, M. A. Marti, D. H. Murgida. "Computer simulation and SERR detection of cytochrome *c* dynamics at SAM-coated electrodes." *Electrochim Acta* **2009** 54(22): 4963 – 4970
- [37] G. V. Louie, G. D. Brayer. "High-resolution refinement of yeast iso-1-cytochrome *c* and comparisons with other eukaryotic cytochromes *c*." *J Mol Biol* **1990** 214(2): 527–555
- [38] J. Massagué, L. Attisano, J. L. Wrana. "The TGF-beta family and its composite receptors." *Trends Cell Biol* **1994** 4(5): 172–178
- [39] B. L. Hogan. "Bone morphogenetic proteins in development." *Curr Opin Genet Dev* **1996** 6(4): 432–438
- [40] Z. S. Haidar, R. C. Hamdy, M. Tabrizian. "Delivery of recombinant bone morphogenetic proteins for bone regeneration and repair. Part A: Current challenges in BMP delivery." *Biotechnol Lett* **2009** 31(12): 1817–1824
- [41] Z. S. Haidar, R. C. Hamdy, M. Tabrizian. "Delivery of recombinant bone morphogenetic proteins for bone regeneration and repair. Part B: Delivery systems for BMPs in orthopaedic and craniofacial tissue engineering." *Biotechnol Lett* **2009** 31(12): 1825–1835
- [42] P. C. Bessa, M. Casal, R. L. Reis. "Bone morphogenetic proteins in tissue engineering: the road from laboratory to clinic, part II (BMP delivery)." *J Tissue Eng Regen M* **2008** 2(2-3): 81–96
- [43] J. M. Granjeiro, R. C. Oliveira, J. C. Bustos-Valenzuela, M. C. Sogayar, R. Taga. "Bone morphogenetic proteins: from structure to clinical use." *Braz J Med Biol Res* **2005** 38(10): 1463–1473
- [44] M. Namiki, S. Akiyama, T. Katagiri, A. Suzuki, N. Ueno, N. Yamaji, V. Rosen, J. M. Wozney, T. Suda. "A kinase domain-truncated type I receptor blocks bone morphogenetic protein-2-induced signal transduction in C2C12 myoblasts." *J Biol Chem* **1997** 272(35): 22046–22052

- [45] E. Chaloux, T. López-Rovira, J. L. Rosa, R. Bartrons, F. Ventura. “JunB is involved in the inhibition of myogenic differentiation by bone morphogenetic protein-2.” *J Biol Chem* **1998** 273(1): 537–543
- [46] T. Kirsch, W. Sebald, M. K. Dreyer. “Crystal structure of the BMP-2-BRIA ectodomain complex.” *Nat Struct Mol Biol* **2000** 7(6): 492–496
- [47] T. Kirsch, J. Nickel, W. Sebald. “BMP-2 antagonists emerge from alterations in the low-affinity binding epitope for receptor BMPR-II.” *EMBO J* **2000** 19(13): 3314–3324
- [48] J. Nickel, M. K. Dreyer, T. Kirsch, W. Sebald. “The crystal structure of the BMP-2:BMPR-IA complex and the generation of BMP-2 antagonists.” *J Bone Joint Surg Am* **2001** 83-A Suppl 1(Pt 1): S7–14
- [49] W. Sebald, J. Nickel, J.-L. Zhang, T. D. Mueller. “Molecular recognition in bone morphogenetic protein (BMP)/receptor interaction.” *Biol Chem* **2004** 385(8): 697–710
- [50] C. Mücksch, H. M. Urbassek. “Adsorption of BMP-2 on a hydrophobic graphite surface: A molecular dynamics study.” *Chem Phys Lett* **2011** 510: 252 – 256
- [51] G. Raffaini, F. Ganazzoli. “Molecular dynamics simulation of the adsorption of a fibronectin module on a graphite surface.” *Langmuir* **2004** 20(8): 3371–3378
- [52] G. Raffaini, F. Ganazzoli. “Sequential adsorption of proteins and the surface modification of biomaterials: A molecular dynamics study.” *J Mater Sci - Mater Med* **2007** 18: 309–316
- [53] D. J. Cole, M. C. Payne, L. C. Ciacchi. “Water structuring and collagen adsorption at hydrophilic and hydrophobic silicon surfaces.” *Phys Chem Chem Phys* **2009** 11(48): 11395–11399
- [54] G. Raffaini, F. Ganazzoli. “Protein adsorption on a hydrophobic surface: a molecular dynamics study of lysozyme on graphite.” *Langmuir* **2010** 26(8): 5679–5689
- [55] X. Dong, Q. Wang, T. Wu, H. Pan. “Understanding adsorption-desorption dynamics of BMP-2 on hydroxyapatite (001) surface.” *Biophys J* **2007** 93(3): 750–759
- [56] X.-L. Dong, H.-L. Zhou, T. Wu, Q. Wang. “Behavior regulation of adsorbed proteins via hydroxyapatite surface texture control.” *J Phys Chem B* **2008** 112(15): 4751–4759
- [57] R. Hille. “The Mononuclear Molybdenum Enzymes.” *Chem Rev* **1996** 96(7): 2757–2816
- [58] T. Eilers, G. Schwarz, H. Brinkmann, C. Witt, T. Richter, J. Nieder, B. Koch, R. Hille, R. Hänisch, R. R. Mendel. “Identification and biochemical characterization of *Arabidopsis thaliana* sulfite oxidase. A new player in plant sulfur metabolism.” *J Biol Chem* **2001** 276(50): 46989–46994
- [59] N. Schrader, K. Fischer, K. Theis, R. R. Mendel, G. Schwarz, C. Kisker. “The crystal structure of plant sulfite oxidase provides insights into sulfite oxidation in plants and animals.” *Structure* **2003** 11(10): 1251–1263

- [60] C. Kisker, H. Schindelin, A. Pacheco, W. A. Wehbi, R. M. Garrett, K. V. Rajagopalan, J. H. Enemark, D. C. Rees. “Molecular basis of sulfite oxidase deficiency from the structure of sulfite oxidase.” *Cell* **1997** 91(7): 973–983
- [61] A. B. Dublin, J. K. Hald, S. L. Wootton-Gorges. “Isolated sulfite oxidase deficiency: MR imaging features.” *Am J Neuroradiol* **2002** 23(3): 484–485
- [62] R. M. Macleod, W. Farkas, I. Fridovich, P. Handler. “Purification and properties of hepatic sulfite oxidase.” *J Biol Chem* **1961** 236: 1841–1846
- [63] A. Pacheco, J. T. Hazzard, G. Tollin, J. H. Enemark. “The pH dependence of intramolecular electron transfer rates in sulfite oxidase at high and low anion concentrations.” *J Biol Inorg Chem* **1999** 4(4): 390–401
- [64] C. Feng, H. L. Wilson, J. K. Hurley, J. T. Hazzard, G. Tollin, K. V. Rajagopalan, J. H. Enemark. “Essential role of conserved arginine 160 in intramolecular electron transfer in human sulfite oxidase.” *Biochemistry* **2003** 42(42): 12235–12242
- [65] C. Feng, H. L. Wilson, G. Tollin, A. V. Astashkin, J. T. Hazzard, K. V. Rajagopalan, J. H. Enemark. “The pathogenic human sulfite oxidase mutants G473D and A208D are defective in intramolecular electron transfer.” *Biochemistry* **2005** 44(42): 13734–13743
- [66] S. Emesh, T. D. Rapson, A. Rajapakshe, U. Kappler, P. V. Bernhardt, G. Tollin, J. H. Enemark. “Intramolecular electron transfer in sulfite-oxidizing enzymes: elucidating the role of a conserved active site arginine.” *Biochemistry* **2009** 48(10): 2156–2163
- [67] K. Johnson-Winters, A. R. Nordstrom, S. Emesh, A. V. Astashkin, A. Rajapakshe, R. E. Berry, G. Tollin, J. H. Enemark. “Effects of interdomain tether length and flexibility on the kinetics of intramolecular electron transfer in human sulfite oxidase.” *Biochemistry* **2010** 49(6): 1290–1296
- [68] M. Sezer, R. Spricigo, T. Utesch, D. Millo, S. Leimkuehler, M. A. Mroginski, U. Wollenberger, P. Hildebrandt, I. M. Weidinger. “Redox properties and catalytic activity of surface-bound human sulfite oxidase studied by a combined surface enhanced resonance Raman spectroscopic and electrochemical approach.” *Phys Chem Chem Phys* **2010** 12(28): 7894–7903
- [69] C. Feng, R. V. Kedia, J. T. Hazzard, J. K. Hurley, G. Tollin, J. H. Enemark. “Effect of solution viscosity on intramolecular electron transfer in sulfite oxidase.” *Biochemistry* **2002** 41(18): 5816–5821
- [70] N. A. Baker, D. Sept, S. Joseph, M. J. Holst, J. A. McCammon. “Electrostatics of nanosystems: application to microtubules and the ribosome.” *Proc Natl Acad Sci U S A* **2001** 98(18): 10037–10041
- [71] P. M. Vignais, B. Billoud, J. Meyer. “Classification and phylogeny of hydrogenases.” *FEMS Microbiol Rev* **2001** 25(4): 455–501
- [72] P. M. Vignais, B. Billoud. “Occurrence, classification, and biological function of hydrogenases: an overview.” *Chem Rev* **2007** 107(10): 4206–4272

- [73] K. A. Vincent, J. A. Cracknell, O. Lenz, I. Zebger, B. Friedrich, F. A. Armstrong. “Electrocatalytic hydrogen oxidation by an enzyme at high carbon monoxide or oxygen levels.” *Proc Natl Acad Sci U S A* **2005** 102(47): 16951–16954
- [74] K. A. Vincent, A. Parkin, O. Lenz, S. P. J. Albracht, J. C. Fontecilla-Camps, R. Cammack, B. Friedrich, F. A. Armstrong. “Electrochemical definitions of O₂ sensitivity and oxidative inactivation in hydrogenases.” *J Am Chem Soc* **2005** 127(51): 18179–18189
- [75] M.-E. Pandelia, H. Ogata, W. Lubitz. “Intermediates in the catalytic cycle of [NiFe] hydrogenase: functional spectroscopy of the active site.” *Chem Phys Chem* **2010** 11(6): 1127–1140
- [76] J. A. Cracknell, K. A. Vincent, F. A. Armstrong. “Enzymes as working or inspirational electrocatalysts for fuel cells and electrolysis.” *Chem Rev* **2008** 108(7): 2439–2461
- [77] J. Zhou, J. Zheng, S. Jiang. “Molecular Simulation Studies of the Orientation and Conformation of Cytochrome *c* Adsorbed on Self-Assembled Monolayers.” *J Phy Chem B* **2004** 108(45): 17418–17424
- [78] T. Wei, M. A. Carignano, I. Szeleifer. “Lysozyme adsorption on polyethylene surfaces: why are long simulations needed?” *Langmuir* **2011** 27(19): 12074–12081
- [79] G. Zuo, X. Zhou, Q. Huang, H. Fang, R. Zhou. “Adsorption of Villin Headpiece onto Graphene, Carbon Nanotube, and C60: Effect of Contacting Surface Curvatures on Binding Affinity.” *J Phys Chem C* **2011** 115(47): 23323–23328
- [80] A. Volbeda, E. Garcin, C. Piras, A. L. de Lacey, V. M. Fernandez, E. C. Hatchikian, M. Frey, J. C. Fontecilla-Camps. “Structure of the [NiFe] Hydrogenase Active Site: Evidence for Biologically Uncommon Fe Ligands.” *J Am Chem Soc* **1996** 118(51): 12989–12996
- [81] D. Millo, M.-E. Pandelia, T. Utesch, N. Wisitruangsakul, M. A. Mroginski, W. Lubitz, P. Hildebrandt, I. Zebger. “Spectroelectrochemical study of the [NiFe] hydrogenase from *Desulfovibrio vulgaris* Miyazaki F in solution and immobilized on biocompatible gold surfaces.” *J Phys Chem B* **2009** 113(46): 15344–15351
- [82] M. Stein, W. Lubitz. “DFT calculations of the electronic structure of the paramagnetic states Ni-A, Ni-B and Ni-C of [NiFe] hydrogenase.” *Phys Chem Chem Phys* **2001** 3: 2668–2675
- [83] M. Stein, W. Lubitz. “Quantum chemical calculations of [NiFe] hydrogenase.” *Curr Opin Chem Biol* **2002** 6(2): 243–249
- [84] W. Lubitz, E. Reijerse, M. van Gastel. “[NiFe] and [FeFe] hydrogenases studied by advanced magnetic resonance techniques.” *Chem Rev* **2007** 107(10): 4331–4365
- [85] M. Brecht, M. van Gastel, T. Buhrke, B. Friedrich, W. Lubitz. “Direct detection of a hydrogen ligand in the [NiFe] center of the regulatory H₂-sensing hydrogenase from *Ralstonia eutropha* in its reduced state by HYSORE and ENDOR spectroscopy.” *J Am Chem Soc* **2003** 125(43): 13075–13083
- [86] H. Ogata, S. Hirota, A. Nakahara, H. Komori, N. Shibata, T. Kato, K. Kano, Y. Higuchi. “Activation process of [NiFe] hydrogenase elucidated by high-resolution X-ray analyses: conversion of the ready to the unready state.” *Structure* **2005** 13(11): 1635–1642

- [87] A. J. Pierik, W. Roseboom, R. P. Happe, K. A. Bagley, S. P. Albracht. "Carbon monoxide and cyanide as intrinsic ligands to iron in the active site of [NiFe]-hydrogenases. NiFe(CN)₂CO, Biology's way to activate H₂." *J Biol Chem* **1999** 274(6): 3331–3337
- [88] J. Fritsch, S. Löscher, O. Sanganas, E. Siebert, I. Zebger, M. Stein, M. Ludwig, A. L. D. Lacey, H. Dau, B. Friedrich, O. Lenz, M. Haumann. "[NiFe] and [FeS] cofactors in the membrane-bound hydrogenase of *Ralstonia eutropha* investigated by X-ray absorption spectroscopy: insights into O₂-tolerant H₂ cleavage." *Biochemistry* **2011** 50(26): 5858–5869
- [89] Y. Shomura, K. Hagiya, K.-S. Yoon, H. Nishihara, Y. Higuchi. "Crystallization and preliminary X-ray diffraction analysis of membrane-bound respiratory [NiFe] hydrogenase from *Hydrogenovibrio marinus*." *Acta Crystallogr Sect F Struct Biol Cryst Commun* **2011** 67(Pt 7): 827–829
- [90] A. Volbeda, P. Amara, C. Darnault, J.-M. Mouesca, A. Parkin, M. M. Roessler, F. A. Armstrong, J. C. Fontecilla-Camps. "X-ray crystallographic and computational studies of the O₂-tolerant [NiFe]-hydrogenase 1 from *Escherichia coli*." *Proc Natl Acad Sci U S A* **2012** 109(14): 5305–5310
- [91] M. Ludwig, J. A. Cracknell, K. A. Vincent, F. A. Armstrong, O. Lenz. "Oxygen-tolerant H₂ oxidation by membrane-bound [NiFe] hydrogenases of *Ralstonia* species. Coping with low level H₂ in air." *J Biol Chem* **2009** 284(1): 465–477
- [92] M. Horch, L. Lauterbach, O. Lenz, P. Hildebrandt, I. Zebger. "NAD(H)-coupled hydrogen cycling - structure-function relationships of bidirectional [NiFe] hydrogenases." *FEBS Lett* **2012** 586(5): 545–556
- [93] M. Bernhard, T. Buhrke, B. Bleijlevens, A. L. D. Lacey, V. M. Fernandez, S. P. Albracht, B. Friedrich. "The H₂ sensor of *Ralstonia eutropha*. Biochemical characteristics, spectroscopic properties, and its interaction with a histidine protein kinase." *J Biol Chem* **2001** 276(19): 15592–15597
- [94] T. Buhrke, O. Lenz, A. Porthun, B. Friedrich. "The H₂-sensing complex of *Ralstonia eutropha*: interaction between a regulatory [NiFe] hydrogenase and a histidine protein kinase." *Mol Microbiol* **2004** 51(6): 1677–1689
- [95] M. Saggi, I. Zebger, M. Ludwig, O. Lenz, B. Friedrich, P. Hildebrandt, F. Lenzian. "Spectroscopic insights into the oxygen-tolerant membrane-associated [NiFe] hydrogenase of *Ralstonia eutropha* H16." *J Biol Chem* **2009** 284(24): 16264–16276
- [96] T. Goris, A. F. Wait, M. Saggi, J. Fritsch, N. Heidary, M. Stein, I. Zebger, F. Lenzian, F. A. Armstrong, B. Friedrich, O. Lenz. "A unique iron-sulfur cluster is crucial for oxygen tolerance of a [NiFe]-hydrogenase." *Nat Chem Biol* **2011** 7(5): 310–318
- [97] B. Schink, H. G. Schlegel. "The membrane-bound hydrogenase of *Alcaligenes eutrophus*. I. Solubilization, purification, and biochemical properties." *Biochim Biophys Acta* **1979** 567(2): 315–324
- [98] C. Kortlüke, K. Horstmann, E. Schwartz, M. Rohde, R. Binsack, B. Friedrich. "A gene complex coding for the membrane-bound hydrogenase of *Alcaligenes eutrophus* H16." *J Bacteriol* **1992** 174(19): 6277–6289

- [99] C. Kortlüke, B. Friedrich. “Maturation of membrane-bound hydrogenase of *Alcaligenes eutrophus* H16.” *J Bacteriol* **1992** 174(19): 6290–6293
- [100] M. Bernhard, E. Schwartz, J. Rietdorf, B. Friedrich. “The *Alcaligenes eutrophus* membrane-bound hydrogenase gene locus encodes functions involved in maturation and electron transport coupling.” *J Bacteriol* **1996** 178(15): 4522–4529
- [101] M. Bernhard, B. Benelli, A. Hochkoepler, D. Zannoni, B. Friedrich. “Functional and structural role of the cytochrome *b* subunit of the membrane-bound hydrogenase complex of *Alcaligenes eutrophus* H16.” *Eur J Biochem* **1997** 248(1): 179–186
- [102] K. A. Vincent, A. Parkin, F. A. Armstrong. “Investigating and exploiting the electrocatalytic properties of hydrogenases.” *Chem Rev* **2007** 107(10): 4366–4413
- [103] F. A. Armstrong, N. A. Belsey, J. A. Cracknell, G. Goldet, A. Parkin, E. Reisner, K. A. Vincent, A. F. Wait. “Dynamic electrochemical investigations of hydrogen oxidation and production by enzymes and implications for future technology.” *Chem Soc Rev* **2009** 38(1): 36–51
- [104] E. Lojou. “Hydrogenases as catalysts for fuel cells: Strategies for efficient immobilization at electrode interfaces.” *Electrochim Acta* **2011** 56(28): 10385 – 10397
- [105] O. Rüdiger, J. M. Abad, E. C. Hatchikian, V. M. Fernandez, A. L. D. Lacey. “Oriented immobilization of *Desulfovibrio gigas* hydrogenase onto carbon electrodes by covalent bonds for nonmediated oxidation of H₂.” *J Am Chem Soc* **2005** 127(46): 16008–16009
- [106] M. Sezer, S. Frielingsdorf, D. Millo, N. Heidary, T. Utesch, M.-A. Mroginski, B. Friedrich, P. Hildebrandt, I. Zebger, I. M. Weidinger. “Role of the HoxZ subunit in the electron transfer pathway of the membrane-bound [NiFe]-hydrogenase from *Ralstonia eutropha* immobilized on electrodes.” *J Phys Chem B* **2011** 115(34): 10368–10374
- [107] A. Ciaccafava, A. D. Poulpiquet, P. Infossi, S. Robert, R. Gadiou, M. Giudici-Ortoni, S. Lecomte, E. Lojou. “A friendly detergent for H₂ oxidation by *Aquifex aeolicus* membrane-bound hydrogenase immobilized on graphite and Self-Assembled-Monolayer-modified gold electrodes.” *Electrochim Acta* **2012** 82(0): 115 – 125
- [108] Y. Murata, H. Iwasaki, M. Sasaki, K. Inaba, Y. Okamura. “Phosphoinositide phosphatase activity coupled to an intrinsic voltage sensor.” *Nature* **2005** 435(7046): 1239–1243
- [109] Y. Murata, Y. Okamura. “Depolarization activates the phosphoinositide phosphatase Ci-VSP, as detected in *Xenopus* oocytes coexpressing sensors of PIP₂.” *J Physiol* **2007** 583(Pt 3): 875–889
- [110] H. Iwasaki, Y. Murata, Y. Kim, M. I. Hossain, C. A. Worby, J. E. Dixon, T. McCormack, T. Sasaki, Y. Okamura. “A voltage-sensing phosphatase, Ci-VSP, which shares sequence identity with PTEN, dephosphorylates phosphatidylinositol 4,5-bisphosphate.” *Proc Natl Acad Sci U S A* **2008** 105(23): 7970–7975
- [111] F. Bezanilla. “How membrane proteins sense voltage.” *Nat Rev Mol Cell Biol* **2008** 9(4): 323–332

- [112] S. B. Long, X. Tao, E. B. Campbell, R. MacKinnon. "Atomic structure of a voltage-dependent K^+ channel in a lipid membrane-like environment." *Nature* **2007** 450(7168): 376–382
- [113] M. Matsuda, K. Takeshita, T. Kurokawa, S. Sakata, M. Suzuki, E. Yamashita, Y. Okamura, A. Nakagawa. "Crystal structure of the cytoplasmic phosphatase and tensin homolog (PTEN)-like region of *Ciona intestinalis* voltage-sensing phosphatase provides insight into substrate specificity and redox regulation of the phosphoinositide phosphatase activity." *J Biol Chem* **2011** 286(26): 23368–23377
- [114] J. O. Lee, H. Yang, M. M. Georgescu, A. D. Cristofano, T. Maehama, Y. Shi, J. E. Dixon, P. Pandolfi, N. P. Pavletich. "Crystal structure of the PTEN tumor suppressor: implications for its phosphoinositide phosphatase activity and membrane association." *Cell* **1999** 99(3): 323–334
- [115] G. D. Paolo, P. D. Camilli. "Phosphoinositides in cell regulation and membrane dynamics." *Nature* **2006** 443(7112): 651–657
- [116] R. Endersby, S. J. Baker. "PTEN signaling in brain: neuropathology and tumorigenesis." *Oncogene* **2008** 27(41): 5416–5430
- [117] M. P. Wymann, R. Schneiter. "Lipid signalling in disease." *Nat Rev Mol Cell Biol* **2008** 9(2): 162–176
- [118] G. M. Blumenthal, P. A. Dennis. "PTEN hamartoma tumor syndromes." *Eur J Hum Genet* **2008** 16(11): 1289–1300
- [119] T. D. Bunney, M. Katan. "Phosphoinositide signalling in cancer: beyond PI3K and PTEN." *Nat Rev Cancer* **2010** 10(5): 342–352
- [120] D. Barford, A. K. Das, M. P. Egloff. "The structure and mechanism of protein phosphatases: insights into catalysis and regulation." *Annu Rev Biophys Biomol Struct* **1998** 27: 133–164
- [121] C. A. Villalba-Galea, F. Miceli, M. Tagliatela, F. Bezanilla. "Coupling between the voltage-sensing and phosphatase domains of Ci-VSP." *J Gen Physiol* **2009** 134(1): 5–14
- [122] S. C. Kohout, S. C. Bell, L. Liu, Q. Xu, D. L. Minor, E. Y. Isacoff. "Electrochemical coupling in the voltage-dependent phosphatase Ci-VSP." *Nat Chem Biol* **2010** 6(5): 369–375
- [123] M. I. Hossain, H. Iwasaki, Y. Okochi, M. Chahine, S. Higashijima, K. Nagayama, Y. Okamura. "Enzyme domain affects the movement of the voltage sensor in ascidian and zebrafish voltage-sensing phosphatases." *J Biol Chem* **2008** 283(26): 18248–18259
- [124] Y. Okamura. "Another story of arginines in voltage sensing: the role of phosphoinositides in coupling voltage sensing to enzyme activity." *J Gen Physiol* **2009** 134(1): 1–4
- [125] C. A. Villalba-Galea. "Voltage-Controlled Enzymes: The New JanusBifrons." *Front Pharmacol* **2012** 3: 161
- [126] K. Hobiger, T. Utesch, M. A. Mroginski, T. Friedrich. "Coupling of Ci-VSP modules requires a combination of structure and electrostatics within the linker." *Biophys J* **2012** 102(6): 1313–1322

- [127] N. L. Allinger. “Conformational analysis. 130. MM2. A hydrocarbon force field utilizing V1 and V2 torsional terms.” *J Am Chem Soc* **1977** 99(25): 8127–8134
- [128] B. R. Brooks, R. E. Bruccoleri, B. D. Olafson, D. J. States, S. Swaminathan, M. Karplus. “CHARMM: A program for macromolecular energy, minimization, and dynamics calculations.” *J Comput Chem* **1983** 4(2): 187–217
- [129] C. Oostenbrink, A. Villa, A. E. Mark, W. F. van Gunsteren. “A biomolecular force field based on the free enthalpy of hydration and solvation: the GROMOS force-field parameter sets 53A5 and 53A6.” *J Comput Chem* **2004** 25(13): 1656–1676
- [130] A. D. MacKerell, D. Bashford, Bellott, R. L. Dunbrack, J. D. Evanseck, M. J. Field, S. Fischer, J. Gao, H. Guo, S. Ha, D. Joseph-McCarthy, L. Kuchnir, K. Kuczera, F. T. K. Lau, C. Mattos, S. Michnick, T. Ngo, D. T. Nguyen, B. Prodhom, W. E. Reiher, B. Roux, M. Schlenkrich, J. C. Smith, R. Stote, J. Straub, M. Watanabe, J. Wiorkiewicz-Kuczera, D. Yin, M. Karplus. “All-Atom Empirical Potential for Molecular Modeling and Dynamics Studies of Proteins.” *J Phys Chem B* **1998** 102(18): 3586–3616
- [131] M. Levitt, R. Sharon. “Accurate simulation of protein dynamics in solution.” *Proc Natl Acad Sci U S A* **1988** 85(20): 7557–7561
- [132] V. Daggett, M. Levitt. “Realistic Simulations of Native-Protein Dynamics in Solution and Beyond.” *Annu Rev Biophys Biomol Struct* **1993** 22(1): 353–380
- [133] B. Xia, V. Tsui, D. A. Case, H. J. Dyson, P. E. Wright. “Comparison of protein solution structures refined by molecular dynamics simulation in vacuum, with a generalized Born model, and with explicit water.” *J Biomol NMR* **2002** 22(4): 317–331
- [134] M. Feig, C. L. Brooks. “Recent advances in the development and application of implicit solvent models in biomolecule simulations.” *Curr Opin Struct Biol* **2004** 14(2): 217–224
- [135] N. A. Baker. “Improving implicit solvent simulations: a Poisson-centric view.” *Curr Opin Struct Biol* **2005** 15(2): 137–143
- [136] J. Chen, C. L. Brooks, J. Khandogin. “Recent advances in implicit solvent-based methods for biomolecular simulations.” *Curr Opin Struct Biol* **2008** 18(2): 140–148
- [137] W. C. Still, A. Tempczyk, R. C. Hawley, T. Hendrickson. “Semianalytical treatment of solvation for molecular mechanics and dynamics.” *J Am Chem Soc* **1990** 112(16): 6127–6129
- [138] C. L. Brooks, M. Karplus. “Deformable stochastic boundaries in molecular dynamics.” *J Chem Phys* **1983** 79(12): 6312–6325
- [139] G. E. Uhlenbeck, L. S. Ornstein. “On the Theory of Brownian Motion.” *Phys Rev* **1930** 36: 823–841
- [140] S. A. Adelman, C. L. Brooks. “Generalized Langevin models and condensed-phase chemical reaction dynamics.” *J Phys Chem* **1982** 86(9): 1511–1524
- [141] M. P. Allen, D. J. Tildesley. *Computer Simulation of Liquids..* Oxford: Clarendon Press **1987**

- [142] L. Verlet. "Computer "Experiments" on Classical Fluids. I. Thermodynamical Properties of Lennard-Jones Molecules." *Phys Rev* **1967** 159: 98–103
- [143] T. Darden, D. York, L. Pedersen. "Particle mesh Ewald: An N log(N) method for Ewald sums in large systems." *J Chem Phys* **1993** 98(12): 10089–10092
- [144] C. Sagui, T. A. Darden. "Molecular dynamics simulations of biomolecules: long-range electrostatic effects." *Annu Rev Biophys Biomol Struct* **1999** 28: 155–179
- [145] L. Saiz, M. L. Klein. "Computer simulation studies of model biological membranes." *Acc Chem Res* **2002** 35(6): 482–489
- [146] R. Devane, W. Shinoda, P. B. Moore, M. L. Klein. "A Transferable Coarse Grain Non-bonded Interaction Model For Amino Acids." *J Chem Theory Comput* **2009** 5(8): 2115–2124
- [147] M. Seo, S. Rauscher, R. Pomes, D. P. Tieleman. "Improving Internal Peptide Dynamics in the Coarse-Grained MARTINI Model: Toward Large-Scale Simulations of Amyloid- and Elastin-like Peptides." *J Chem Theory Comput* **2012** 8(5): 1774–1785
- [148] W. L. Ash, M. R. Zlomislic, E. O. Oloo, D. P. Tieleman. "Computer simulations of membrane proteins." *Biochim Biophys Acta* **2004** 1666(1-2): 158–189
- [149] W. C. Swope, H. C. Andersen, P. H. Berens, K. R. Wilson. "A computer simulation method for the calculation of equilibrium constants for the formation of physical clusters of molecules: Application to small water clusters." *J Chem Phys* **1982** 76(1): 637–649
- [150] C. K. Birdsall, A. B. Langdon. *Plasma Physics via Computer Simulations*. McGraw-Hill Book Company **1985**
- [151] P. Schofield. "Computer simulation studies of the liquid state." *Comput Phys Commun* **1973** 5(1): 17 – 23
- [152] J. C. Phillips, R. Braun, W. Wang, J. Gumbart, E. Tajkhorshid, E. Villa, C. Chipot, R. D. Skeel, L. Kalé, K. Schulten. "Scalable molecular dynamics with NAMD." *J Comput Chem* **2005** 26(16): 1781–1802
- [153] K. A. Atkinson. *An Introduction to Numerical Analysis (2nd ed.)*. New York: John Wiley & Sons **1989**
- [154] P. Attard. *Thermodynamics and Statistical Mechanics*. Elsevier Ltd. **2002**
- [155] W. F. van Gunsteren, H. J. C. Berendsen. "Moleküldynamik-Computersimulationen; Methodik, Anwendungen und Perspektiven in der Chemie." *Angew Chem* **1990** 102(9): 1020–1055
- [156] H. J. C. Berendsen, J. P. M. Postma, W. F. van Gunsteren, A. DiNola, J. R. Haak. "Molecular dynamics with coupling to an external bath." *J Chem Phys* **1984** 81(8): 3684–3690
- [157] H. Eslami, F. Mojahedi, J. Moghadasi. "Molecular dynamics simulation with weak coupling to heat and material baths." *J Chem Phys* **2010** 133(8): 084105
- [158] S. Nose. "A unified formulation of the constant temperature molecular dynamics methods." *J Chem Phys* **1984** 81(1): 511–519

- [159] S. E. Feller, Y. Zhang, R. W. Pastor, B. R. Brooks. “Constant pressure molecular dynamics simulation: The Langevin piston method.” *J Chem Phys* **1995** 103(11): 4613–4621
- [160] J. D. Chodera, D. L. Mobley, M. R. Shirts, R. W. Dixon, K. Branson, V. S. Pande. “Alchemical free energy methods for drug discovery: progress and challenges.” *Curr Opin Struct Biol* **2011** 21(2): 150–160
- [161] J. D. Durrant, J. A. McCammon. “Molecular dynamics simulations and drug discovery.” *BMC Biol* **2011** 9: 71
- [162] B. Isralewitz, M. Gao, K. Schulten. “Steered molecular dynamics and mechanical functions of proteins.” *Curr Opin Struct Biol* **2001** 11(2): 224–230
- [163] S. A. Adcock, J. A. McCammon. “Molecular dynamics: survey of methods for simulating the activity of proteins.” *Chem Rev* **2006** 106(5): 1589–1615
- [164] S. Izrailev, A. R. Crofts, E. A. Berry, K. Schulten. “Steered molecular dynamics simulation of the Rieske subunit motion in the cytochrome bc(1) complex.” *Biophys J* **1999** 77(4): 1753–1768
- [165] L. Shen, J. Shen, X. Luo, F. Cheng, Y. Xu, K. Chen, E. Arnold, J. Ding, H. Jiang. “Steered molecular dynamics simulation on the binding of NNRTI to HIV-1 RT.” *Biophys J* **2003** 84(6): 3547–3563
- [166] H. Lu, B. Isralewitz, A. Krammer, V. Vogel, K. Schulten. “Unfolding of titin immunoglobulin domains by steered molecular dynamics simulation.” *Biophys J* **1998** 75(2): 662–671
- [167] H. Lu, K. Schulten. “Steered molecular dynamics simulations of force-induced protein domain unfolding.” *Proteins* **1999** 35(4): 453–463
- [168] J.-P. Ryckaert, G. Ciccotti, H. J. Berendsen. “Numerical integration of the cartesian equations of motion of a system with constraints: molecular dynamics of n-alkanes.” *J Comput Phys* **1977** 23(3): 327 – 341
- [169] H. C. Andersen. “Rattle: A \hat{v} elocity \hat{v} version of the shake algorithm for molecular dynamics calculations.” *J Comput Phys* **1983** 52(1): 24 – 34
- [170] S. Miyamoto, P. A. Kollman. “Settle: An analytical version of the SHAKE and RATTLE algorithm for rigid water models.” *J Comput Chem* **1992** 13(8): 952–962
- [171] W. L. Jorgensen, J. Chandrasekhar, J. D. Madura, R. W. Impey, M. L. Klein. “Comparison of simple potential functions for simulating liquid water.” *The Journal of Chemical Physics* **1983** 79(2): 926–935
- [172] F. C. Bernstein, T. F. Koetzle, G. J. Williams, E. F. Meyer, M. D. Brice, J. R. Rodgers, O. Kennard, T. Shimanouchi, M. Tasumi. “The Protein Data Bank: a computer-based archival file for macromolecular structures.” *J Mol Biol* **1977** 112(3): 535–542
- [173] T. J. Dolinsky, P. Czodrowski, H. Li, J. E. Nielsen, J. H. Jensen, G. Klebe, N. A. Baker. “PDB2PQR: expanding and upgrading automated preparation of biomolecular structures for molecular simulations.” *Nucleic Acids Res* **2007** 35(Web Server issue): W522–W525

- [174] M. H. M. Olsson, C. R. Sondergaard, M. Rostkowski, J. H. Jensen. "PROPKA3: Consistent Treatment of Internal and Surface Residues in Empirical pK_a Predictions." *J Chem Theory Comput* **2011** 7(2): 525–537
- [175] A. Cauchy. "Methodes generales pour la resolution des systemes d'equations simultanees." *C. R. Acad. Sci. Paris* **1847** 25: 536–538
- [176] T. A. Straeter. "On the Extension of the Davidon-Broyden Class of Rank One, Quasi-Newton Minimization Methods to an Infinite Dimensional Hilbert Space with Applications to Optimal Control Problems." *Technical report*, NASA Technical Reports Server. NASA. **1971**
- [177] M. D. Liptak, R. D. Fagerlund, E. C. Ledgerwood, S. M. Wilbanks, K. L. Bren. "The proapoptotic G41S mutation to human cytochrome *c* alters the heme electronic structure and increases the electron self-exchange rate." *J Am Chem Soc* **2011** 133(5): 1153–1155
- [178] G. E. Crooks, J. Wolfe, S. E. Brenner. "Measurements of protein sequence-structure correlations." *Proteins* **2004** 57(4): 804–810
- [179] M. Perutz, J. Kendrew, H. Watson. "Structure and function of haemoglobin: II. Some relations between polypeptide chain configuration and amino acid sequence." *J Mol Biol* **1965** 13(3): 669 – 678
- [180] A. M. Lesk, C. Chothia. "How different amino acid sequences determine similar protein structures: the structure and evolutionary dynamics of the globins." *J Mol Biol* **1980** 136(3): 225–270
- [181] M. Bajaj, T. Blundell. "Evolution and the tertiary structure of proteins." *Annu Rev Biophys Bioeng* **1984** 13: 453–492
- [182] C. Chothia, A. M. Lesk. "The relation between the divergence of sequence and structure in proteins." *EMBO J* **1986** 5(4): 823–826
- [183] G. N. Ramachandran, C. Ramakrishnan, V. Sasisekharan. "Stereochemistry of polypeptide chain configurations." *J Mol Biol* **1963** 7: 95–99
- [184] R. W. Hooft, G. Vriend, C. Sander, E. E. Abola. "Errors in protein structures." *Nature* **1996** 381(6580): 272
- [185] A. Sali, T. L. Blundell. "Comparative protein modelling by satisfaction of spatial restraints." *J Mol Biol* **1993** 234(3): 779–815
- [186] C. B. Anfinsen. "Principles that govern the folding of protein chains." *Science* **1973** 181(4096): 223–230
- [187] R. Bonneau, D. Baker. "AB INITIO PROTEIN STRUCTURE PREDICTION: Progress and Prospects." *Annu Rev Biophys Biomol Struct* **2001** 30(1): 173–189
- [188] D. E. Kim, D. Chivian, D. Baker. "Protein structure prediction and analysis using the Robetta server." *Nucleic Acids Res* **2004** 32(Web Server issue): W526–W531
- [189] D. T. Jones. "Protein secondary structure prediction based on position-specific scoring matrices." *J Mol Biol* **1999** 292(2): 195–202

- [190] K. Karplus, C. Barrett, R. Hughey. "Hidden Markov models for detecting remote protein homologies." *Bioinformatics* **1998** 14(10): 846–856
- [191] S. F. Altschul, T. L. Madden, A. A. Schäffer, J. Zhang, Z. Zhang, W. Miller, D. J. Lipman. "Gapped BLAST and PSI-BLAST: a new generation of protein database search programs." *Nucleic Acids Res* **1997** 25(17): 3389–3402
- [192] M. Holst. "Adaptive Numerical Treatment of Elliptic Systems on Manifolds." *Adv Comput Math* **2001** 15: 139–191
- [193] R. Bank, M. Holst. "A New Paradigm for Parallel Adaptive Meshing Algorithms." *SIAM Rev* **2003** 45(2): 291–323
- [194] T. Utesch, D. Millo, M. A. Castro, P. Hildebrandt, I. Zebger, M. A. Mroginski. "Effect of the Protonation Degree of a Self-Assembled Monolayer on the Immobilization Dynamics of a [NiFe] Hydrogenase." *Langmuir* **2013** 29(2): 673–682
- [195] R. Marcus, N. Sutin. "Electron transfers in chemistry and biology." *Biochim Biophys Acta - Rev Bioenerg* **1985** 811(3): 265 – 322
- [196] D. N. Beratan, J. N. Onuchic, J. N. Betts, B. E. Bowler, H. B. Gray. "Electron tunneling pathways in ruthenated proteins." *Journal of the American Chemical Society* **1990** 112(22): 7915–7921
- [197] D. N. Beratan, J. N. Betts, J. N. Onuchic. "Protein electron transfer rates set by the bridging secondary and tertiary structure." *Science* **1991** 252(5010): 1285–1288
- [198] M.-L. Tan, I. Balabin, J. N. Onuchic. "Dynamics of electron transfer pathways in cytochrome *c* oxidase." *Biophys J* **2004** 86(3): 1813–1819
- [199] F. Siebert, P. Hildebrandt. *Vibrational Spectroscopy in Life Science*. Wiley-VCH, Berlin **2007**
- [200] M. Kerker. "Resonances in electromagnetic scattering by objects with negative absorption." *Appl Opt* **1979** 18(8): 1180–1189
- [201] M. Kerker, D. S. Wang, H. Chew. "Surface enhanced Raman scattering (SERS) by molecules adsorbed at spherical particles: errata." *Appl Opt* **1980** 19(24): 4159–4174
- [202] M. Kerker, D. S. Wang, H. Chew. "Surface enhanced Raman scattering (SERS) by molecules adsorbed at spherical particles." *Appl Opt* **1980** 19(19): 3373–3388
- [203] W. Stühmer. "Electrophysiologic recordings from *Xenopus* oocytes." *Methods Enzymol* **1998** 293: 280–300
- [204] A. Warshel, M. Levitt. "Theoretical studies of enzymic reactions: Dielectric, electrostatic and steric stabilization of the carbonium ion in the reaction of lysozyme." *J Mol Biol* **1976** 103(2): 227 – 249
- [205] H. M. Senn, W. Thiel. "QM/MM methods for biomolecular systems." *Angew Chem Int Ed Engl* **2009** 48(7): 1198–1229
- [206] M. J. Field, P. A. Bash, M. Karplus. "A combined quantum mechanical and molecular mechanical potential for molecular dynamics simulations." *J Comput Chem* **1990** 11(6): 700–733

- [207] I. Antes, W. Thiel. “Adjusted Connection Atoms for Combined Quantum Mechanical and Molecular Mechanical Methods.” *J Phys Chem A* **1999** 103(46): 9290–9295
- [208] H. Zhang, C. He, X. Yan, T. Mirshahi, D. E. Logothetis. “Activation of inwardly rectifying K⁺ channels by distinct PtdIns(4,5)P₂ interactions.” *Nat Cell Biol* **1999** 1(3): 183–188
- [209] M. Saggu, M. Ludwig, B. Friedrich, P. Hildebrandt, R. Bittl, F. Lenzian, O. Lenz, I. Zebger. “Impact of amino acid substitutions near the catalytic site on the spectral properties of an O₂-tolerant membrane-bound [NiFe] hydrogenase.” *Chem Phys Chem* **2010** 11(6): 1215–1224

Selbständigkeitserklärung

Die selbständige und eigenhändige Anfertigung dieser Arbeit versichere ich an Eides statt.

Tillmann Utesch

Berlin, 4. März 2013